CHEMICAL VAPOUR TRANSPORT OF III-V SEMICONDUCTOR MATERIALS

A Thesis submitted for the degree of

Doctor of Philosophy of the

University of London

by

Mervyn Howard Davis

March 1983

Bourne Laboratory

Royal Holloway College

Egham Hill

Egham

Surrey

ABSTRACT

Chemical vapour transport of III-V semiconductor materials

Mervyn Howard Davis

The evaporation of liquid zinc has been studied using a modified entrainment method, and allows the determination of the diffusion coefficient of zinc in hydrogen within the temperature range 724 to 1027 K. The study also allowed the evaluation of a newly constructed apparatus.

Enthalpies and entropies for the transport reactions involved in the etching of gallium phosphide in hydrogen chloride and hydrogen bromide; and indium phosphide in hydrogen bromide, have been calculated using data assimilated from entrainment studies. The entrainment studies illustrate that for the transport of gallium phosphide over the temperature range 970 to 1300 K, a single chloride species is involved. Over the temperature range 770 to 1310 K, however, two bromides compete for prominence, dependent upon temperature. In both instances, it is shown that vapour transport becomes rate limited at low temperature. Further to the chemical vapour transport of indium phosphide, the dissociative sublimation of the compound has also been investigated.

Raman spectroscopy has been used to identify high temperature molecular species involved in vapour transport of III-V semiconductor materials.

Supplementary work has been performed on the thermochemistry of indium monobromide. The heat of formation of

indium bromide crystals has been determined using a solution calormetric technique. Differential scanning calorimetry was used to measure the heat capacity and heat of fusion of the salt. An entrainment study of the evaporation of liquid indium monobromide was undertaken to yield a value for its heat of vaporisation. Using a statistical thermodynamic approach, the heat capacity of the vapour was calculated. Collating the information, a value for the heat of formation of indium monobromide gas at 1000 K has been calculated for use in other thermodynamic calculations.

ACKNOWLEDGEMENTS

The work recorded in this Thesis was carried out under the supervision of Dr P J Gardner, to whom the author wishes to express his gratitude for guidance and encouragement. Sincere thanks are also due to Dr A Finch, for many valuable discussions.

The author also acknowledges the provision of laboratory facilities at Royal Holloway College, and a maintenance grant from the Science Research Council.

Thanks are due to the Chemistry Departments of Southampton University, and University College, (University of London), for the use of their respective Raman spectroscopic facilities.

Finally, the author wishes to thank Dr M M Faktor and his colleagues at the British Telecom Research Laboratories, for their help during the tenure of this CASE award.

Science is a very human form of knowledge. We are always at the brink of the known, we always feel forward for what is to be hoped. Every judgment in science stands on the edge of error, and is personal. Science is a tribute to what we can know although we are fallible.

J Bronowski

(1973)

TO MY WIFE, GILLIAN

CONTENTS

CHAPTER ONE

Introduction

The telecommunications industry is growing rapidly, and with increasing energy costs, is likely to grow more rapidly in the future. This century has seen the rise of many new technologies, notably that of semiconductors. Transistor action was first demonstrated in 1947 at Bell Laboratories, with the invention of the bipolar transistor. Since that time, technologies have evolved principally for the processing of silicon for the fabrication of bipolar and MOS devices. In recent years much interest has been expressed in a further group of electronic materials (III - V and II - VI) compound semiconductors.

Very complex systems are available for the processing of electronic signals, and the techniques required to form a sophisticated telecommunications network are well established. Most telecommunications systems used today operate by the transmission of electrical signals along coaxial metal conductors.

The first proposal for a wideband optical communications system was presented in 1966[1]. Today the term 'fibre optic communications' is in common usage. The development of dielectric waveguides[2,3,4,5], for use at optical frequencies has advanced very quickly.

Both the source and detector used in a fibre optic communication link take the form of solid state devices. The

sources may comprise of either a super-luminescent light emitting diode, or more importantly, a compound semiconductor laser. In late 1962, three independent groups[6,7,8] almost simultaneously announced that lasing in semiconductors had been demonstrated. Semiconductor lasers are similar to other lasers in that they emit radiation displaying both spatial and temporal coherence. Such lasers do, however, differ from other lasers in several important respects:

i) In conventional lasers, the quantum transitions occur between discrete energy levels, whereas in semiconductor lasers the transitions are associated with the band properties of materials.

ii) Because of the very compact dimensions of a semiconductor laser ($\approx$1 mm long, active region $\approx$1 μm thick), the divergence of the laser beam is far greater than that from a conventional laser.

iii) The spatial and spectral characteristics of a semiconductor laser are strongly influenced by the properties of the junction medium.

iv) For the p-n junction laser, the laser action is produced by simply passing a forward current through the diode itself. The result is a very efficient overall system that can be modulated easily by modulation of the current. Since these lasers have very short photon lifetimes, modulation at high frequencies can be obtained.

Because of its compact size and capability for high frequency modulation, the semiconductor laser has become one of

the most important light sources for optical-fibre communication. Three operational wavelengths are of particular interest[5]. Around 0.9 μm wavelength, the GaAs - $Al_xGa_{1-x}As$ heterostructure lasers serve as an optical source, and the Si photodiode or Si avalanche photodiode is used as the optical detector. Around 1.3 μm wavelength, modern fibres display low loss (0.6 $dBkm^{-1}$) and low dispersion; and around 1.55 μm, the loss reaches a minimum of 0.2 $dBkm^{-1}$. At these two wavelengths, III - V quarternary compound lasers, such as $Ga_xIn_{1-x}As_yP_{1-y}$ - InP lasers, are candidates for optical sources and Ge avalanche photodiodes, as well as photodiodes in tenary or quaternary compounds are the candidates for optical detectors[9]. Longer wavelengths, exploiting very low fibre losses have been considered[10]. To make such a system, efficient long wavelength optical sources (eg $PbS_{0.1}Se_{0.9}$ LEDs)[11] would require development. Injection lasers displaying resonance at useful frequencies may then be made using materials such as III - V compound semiconductors. Figure 1 shows a simplified structure of a p-n junction laser. A pair of parallel planes are cleaved or polished normal to the plane of the junction. In order to eliminate lasing in a direction perpendicular to that intended, the remaining faces of the diode are roughened. The structure shown is known as a Fabry-Perot cavity. When a forward bias is applied to the diode, a current flows. At low currents, spontaneous emission occurs in all directions. As the bias is increased, eventually a threshold current is reached, at which stimulated emission occurs and a monochromatic and highly directional beam of light is emitted from the junction.

Fig 1.1 Schematic Diagram of a Fabry-Perot cavity.

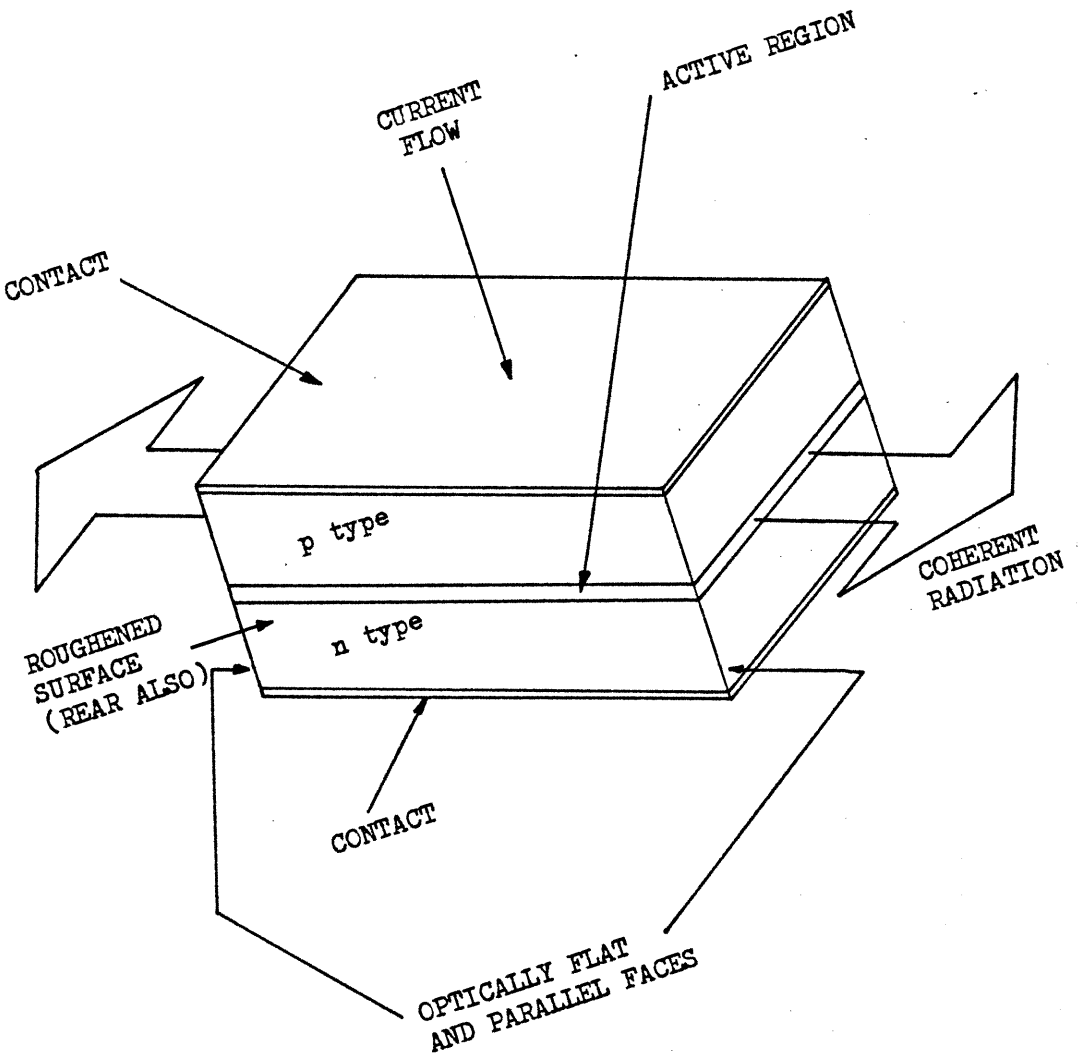

Literature relating to the structures and performance of various semiconductor lasers is expansive. The interested reader is referred to a review by C A Burrus et al[12]. Laser confinment is achieved by wave guide techniques and results in structures known as double-hetrostructure lasers. All structures use high quality binary semiconductors as the substrates (eg GaAs or InP). Successive epitaxial with different alloy compositions and dopings are grown by liquid-phase epitaxy, vapour-phase epitaxy or nuclear-beam epitaxy processes.

The very wide band width offered by optical transmission make such systems attractive alternatives to electrical coaxial systems for high volume communication traffic. Increasing traffic, particularly in the areas of machine-machine communications can quickly overload the capacity of conventional coaxial systems. Losses and propagation delay limit the data transmission rates using coaxial wire links. For overland communications then, the advantages of an optical system are primarily in the area of increased band width. When optical fibre transmission links are considered for submerged systems, some additional benefits come to light. Submarine transmission lines are expensive both to manufacture and install. High though these costs may be, they become quite insignificant when compared with the revenue earned from intercontinental communications traffic. For these reasons, very high standards of reliability are demanded of individual components and indeed, the system as a whole. To illustrate this, general consumer electronics would normally require a mean time between failures for individual components of two to five years. For components used in the

manufacture of submerged systems, this time is extended to a minimum of twenty five years.

Present day coaxial systems operating at 14 MHz require signal repeaters at intervals of 3 km. Losses involved in data transmission by optical fibres are sufficiently smaller than in coaxial systems that the distance between repeaters may be increased to 20 km. The first submerged optical systems will have a data rate of 256 Mbt using a carrier frequency of 353 GHz. This feature would also be of some benefit in land-line systems, as fibre-optic links between exchanges require few or no repeaters.

Optical systems have certain advantages that may be exploited in military applications. For example, data and control signalling on board air and marine craft require numerous back-up systems to guard against catastrophic failure. Current practice is to at least duplicate each link and use different routing circuits for both cables. Optical cables are intrinsically low in bulk and do not require Faraday shielding to prevent interference - such cables consequently may readily be embedded in resin and composite structures. At the present time, an optical data transmission line is largely dependent on conventional electrical systems for signal generation, modulation and decoding. Much effort is being directed towards the development of integrated optical circuits; when such technologies reach maturity, further benefits may be exploited.

Now, turning attention specifically towards the materials required to fabricate the optical sources for communications systems, (ie, semiconductor injection lasers), the various technologies will be briefly discussed. In order to exploit the

interesting phenomena displayed by these III - V compounds, single crystal material is required. These crystals must be grown in a manner to form the complicated structures required to make active devices. The general generic term for the method by which this is achieved is epitaxial growth. Starting with a single crystal substrate of GaAs, for example, various layers are successively grown above this, using the previous layer as an epitaxial key. The composition of the successive layers is dictated by the need to achieve a lattice match to the underlying material, and the desired performance charateristics of the device being grown.

Essentially, three technologies are available by which this end may be achieved:

i) Liquid-phase epitaxy (LPE).

ii) Vapour-phase epitaxy (VPE).

iii) Molecular-beam epitaxy (MBE).

These three techniques are listed in order of increasing complexity. Liquid-phase epitaxy is the technique that is, perhaps, the most developed, and will supply the lasers for the first submerged system. Molecular-beam epitaxy, as the name suggests, is a very exotic and expensive technique. MBE work is, however, being heavily funded in Japan, and the potential of the technique is undoubtabley great. Very abrupt transitions in alloy composition are difficult to achieve by LPE. Low temperature MBE, by contrast, allows extremely abrupt (a few monolayers) transitions in composition. This leaves the vapour-phase techniques in the middle, less expensive and complicated than MBE, but less well understood than LPE.

Practically all vapour deposition processes for epitaxial growth of III - V materials belong to one of the following three methods:

i) The hydride method where group V elements are introduced as hydrides, and group III elements are monochlorides which result from the HCl interaction with the appropriate metals, (other halides may also be used).

ii) The chloride method where group V trichlorides interact with the appropriate III - V compound or group III metal (again, other halides may be used).

iii) The organometallic method where group III elements are introduced as trimethyl or triethyl compounds, while group V elements are usually introduced as hydrides.

An interesting experimental difference between iii) and i) and ii) is that i) and ii) are performed in hot-walled systems while iii) uses a cold-walled heated system. The organometallic rate to epitaxial deposition is perhaps less exploited than the hydride and chloride processes. Difficulties can arise with carbon contamination in films grown in this manner.

Engineers in the field of crystal growth of III - V electronic materials are called upon to produce materials with close control over the following properties:

1) Defects: non-stoichiometry, dislocation density etc.
2) Impurity concentrations.
3) Concentrations of foreign atoms added intentionally, ie, dopants.

4) Geometry, eg very thin epitaxial layers.

Growth from the vapour has certain attractions. As the concentration and distribution of dopants, vertically through the laser structure, must be well controlled, the very high diffusion rates associated with the liquid state can be a disadvantage. Growth by vapour deposition allows the temperature to be reduced appreciably. Dopants may easily be introduced as volatile species in the background atmosphere during deposition, and their concentrations as a function of depth may be controlled by suitable manipulation of the gaseous concentrations. Hyper-abrupt junctions are a little more difficult to achieve, since under practical conditions, when a dopant flow is interrupted, a finite time is incurred before its gaseous concentration at the substrate falls to zero. At the Sony Corporation in Japan, this constraint has been largely overcome. Using a vertical furnace arrangement, abrupt changes in alloy composition (and/or dopant inclusion), are achieved by rotating the substrate from one gaseous environment to another. Indeed, Sony now grow all their laser material using VPE methods, (primarily the chloride and hydride processes).

Semicondutor lasers are complicated structures that are fabricated using complicated techniques and systems. In order to exercise control over the rate, composition, stoichiometry and surface morphology of crystal growth, (such control is desirable so that the precise nature of an epitaxial layer deposited by chemical vapour deposition may be characterised), a knowledge of the following is required:

1) What vapour species are present under conditions of

growth?

2) What is the equilibrium composition of the vapour over the crystal?
3) How far does the composition depart from equilibrium during growth?
4) How are surface kinetics altered by the individual partial pressures, and by changes in vapour species?
5) What species are present on the crystal surface?
6) What is the state of the surface, with respect to stoichiometry, dislocation density and orientation?

Crystal growth from the vapour may be considered as a number of sequential processes. By assuming that the chemical reactions involved in deposition of a binary semiconductor from the vapour are the reverse of those that etch a solid material, then the study of a chemical vapour transport (CVT) system becomes an attractive proposition. The simplest CVT system may be described by a reaction:

Solid + Transporting Agent = Volatile Product.

The position of the above equilibrium is dictated by temperature. Useful information pertaining to practical chemical vapour deposition (CVD) may be extracted from the study of CVT reactions. To make things easier still, the etching of the material may be investigated as opposed to their growth.

The work presented here is primarily a study involving selected III - V electronic materials undergoing chemical vapour transport under equilibrium conditions. The modified entrainment method (MEM) used in this thesis overcomes the limitations imposed by the techniques due to Knudsen and

Langmuir[13] and is suitable for studying heterogeneous reaction equilibria as well as for the determination of vapour or dissociation pressures. In this MEM the region over which diffusion occurs is defined by a narrow capillary of known dimensions and rates of weight loss are independent of the carrier gas flow rate.

Thermodynamic data afforded by MEM experiments are useful in assessing the efficiency of a crystal growth system. By using a suitable mathematical model, heats and entropies of reaction may be deduced from the weight-loss data from a MEM experiment. The ease of simulating the experimental results, combined with chemical intuition allows the composition of the gas phase over a transporting binary semiconductor to be inferred. Direct physical evidence for the existence of particular species is obviously preferable to the inferred presence in the vapour. Mass spectroscopy has been applied quite widely to the study of III - V compound growth in CVD reactors[14-18]. In this work, Raman spectroscopy has been applied to the study of gallium and indium halides in the vapour. Elaborate studies have been made using Raman spectroscopy in CVD systems involving the growth of single crystal silicon[19] and In_2Se_3[20].

REFERENCES TO CHAPTER ONE

1.1 K.C. Kao and G.A. Hockman, Proc. IEE 3, 1151, (1966)

1.2 C.P. Sandbank, Elec. Commun. 50, 20 (1975)

1.3 P.W. Black, ibid. 51, 4 (1976)

1.4 M. Chown and R. Worthington, ibid. 51, 242 (1976)

1.5 T. Miya, Y. Terunuma, T. Hasaka and W. Miyashita, Electron. Lett. 15, 108 (1979)

1.6 R.N. Hall, G.E. Genner, J.D. Kingsley, T.J. Soltys and R.O. Carston, Phys. Rev. Lett. 9, 366 (1962)

1.7 M.I. Nathan, W.P. Dumke, G. Burns, F.J. Dill and G.J. Lasker, Appl. Phys. Lett. 1, 62 (1962)

1.8 T.M. Quist, R.H. Rediker, R.J. Keyes, W.E. Krag, B. Lax, A.L. McWhorter and H.J. Leigler, Appl. Phys. Lett. 1, 91 (1962)

1.9 A.G. Foyt, IEEE Device Res. Conf. (1979)

1.10 C.H.L. Goodman, Solid State Electron. Devices, 2, 129 (1978)

1.11 W. Lo and D.E. Swets, Appl. Phys. Lett. 36, 450 (1980)

1.12 C.A. Burrus, H.C. Casey and T.Y. Li, 'Optical Sources' in S.E. Miller and A.G. Chynoweth (Eds.) Optical Fibre Communication (Academic Press 1979)

1.13 R.H. Moss, PhD Thesis, London (1975)

1.14 V.S. Ban, J. Electrochem. Soc. 118, 1473 (1971)

1.15 Idem., ibid., 119, 761 (1972)

1.16 V.S. Ban, H.F. Gossenberger and J.J. Tietjen, J. Appl. Phys. A3, 2471 (1972)

1.17 V.S. Ban, J. Cryst. Growth 17, 19 (1972)

1.18 V.S. Ban and M. Ettenburg, J. Phys. Chem. Solids 34, 1119 (1973)

1.19 T.O. Sedgwick, J.E. Smith, R. Ghez and M.E. Cawker, J. Cryst. Growth 31, 264 (1975)

1.20 Ja Kh. Grinberg, J. Inorg. Nucl. Chem. 38, 383 (1976)

CHAPTER TWO

Experimental

2.1 A Modified Entrainment Method for Measuring Vapour Pressures and the study of Heterogeneous Equilibria Involving Reactive Gases.

The technique employed in this work overcomes the limitations of those due to Knudsen and Langmuir[1] and is suitable for studying heterogeneous equilibria, as well as the measurement of vapour and dissociation pressures.

This capillary leak method described was first validated[2] by comparing vapour pressure measurements on water and lead with previously reported data. The technique is referred to as a modified entrainment method (MEM).

In this method a small silica bottle containing a condensed sample is suspended, in the hot zone of a vertically mounted tube furnace, from a recording microbalance. A carrier gas mixed, if required, with a reactive gas, flows over the bottle in the direction indicated in fig. 2.1. The orifice of the bottle takes the form of a narrow capillary, of known dimensions, typically 20 mm in length and 1 mm in diameter. This capillary, which acts as a diffusive resistance, serves to isolate the substrate from the irreproducible effects of the flowing transport gas, and if the capillary is sufficiently narrow, then equilibrium vapour pressures are attained in the bottle. This constraint ensures

Fig 2.1 Positioning of the Reaction Bottle Within the Furnace Tube.

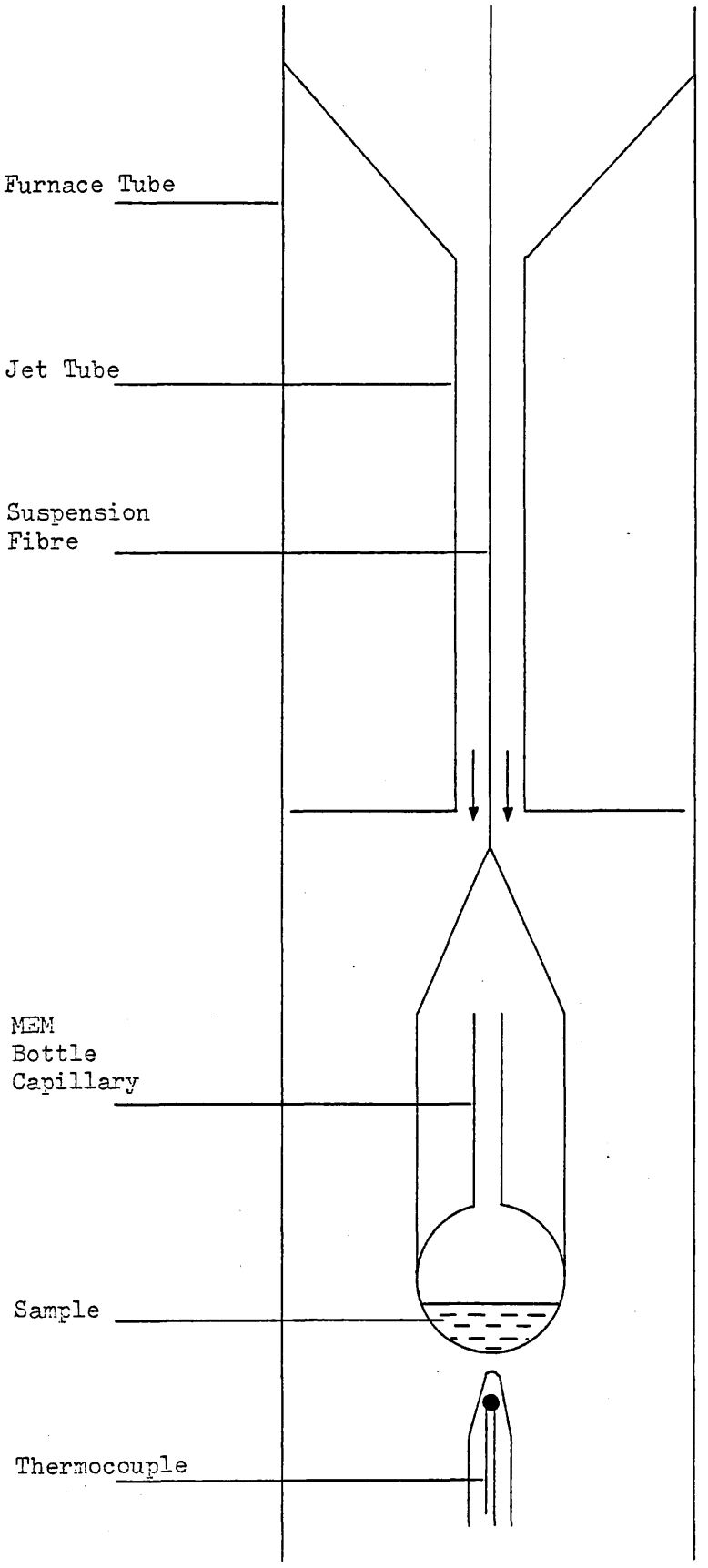

that the rate of weight loss from the sample is usually limited by transport kinetics within the capillary.

Two similar sets of apparatus have been used. The first is discussed elsewhere[3] and the second is described below. A schematic diagram of this apparatus appears in fig. 2.2.

The central feature of this apparatus is a recording electrobalance (Cahn R-100), from which is suspended the sample bottle, via a silica fibre. This balance has a maximum sample capacity of 100 g and an electrical lifting capacity of 10 g, with a sensitivity of 5×10^{-10} kg. Changes in sample weight are displayed on a chart recorder (Bryans 28000). The balance, suspension fibre and bottle are all enclosed in an evacuable glass system, having two gas inlets and a single outlet. The sample may be heated, and held under isothermal conditions, in the temperature range 500 to 1900 K by a single zone, 2.5 kW single 25 V winding tube furnace 250 mm long and having an internal diameter of 45 mm. The furnace is controlled by a linear temperature variable rate programmer (Stanton Redcroft LVP/CC20/R). The control thermocouple is located between the furnace and furnace tube. Sample temperatures are monitered by a second thermocouple, sheathed in a thin-walled silica tube, positioned immediately below the sample bottle. Both thermocouples are Pt/Pt 13% Rh fabricated from wire supplied by Johnson Matthey Metals Ltd. The EMF of the monitering thermocouple is displayed on a digital panel meter (Daystrom 1294) and cold junction temperatures are determined using a mercury in glass thermometer (-5 to 50°C). The positioning of the bottle and thermocouple bead within the furnace temperature profile may

Fig 2.2 Experimental MEM System

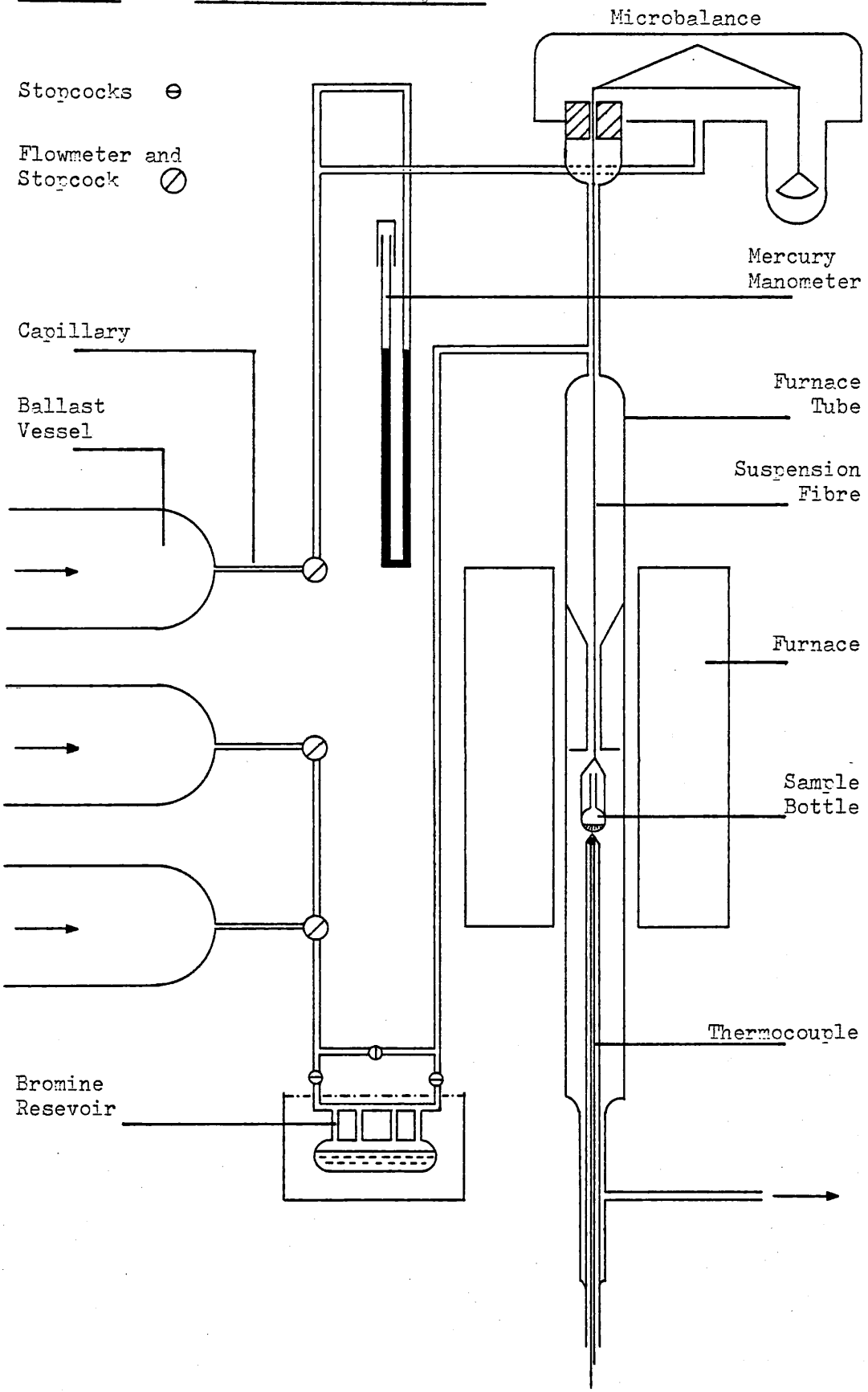

be altered by raising or lowering of the furnace accordingly.

Nitrogen is introduced to the system after drying by passing through molecular sieves (BDH type 4A 1/16 pellets), via the upper and lower gas inlets. Hydrogen may be introduced in a similar fashion following delivery from a palladium diffuser (Johnson Matthey & Co Ltd model H28/1). A third gas inlet line is available for the introduction of hydrogen chloride, again dried by its passage through molecular sieves (Union Carbide AW 300 1/16 pellets). Metering valves (Negretti & Zambra Ltd, type BS-LMV-L-V-4), are used to regulate the nitrogen and hydrogen flow rates. A twin needle valve (Nupro, type SS-4MGD) regulates the flow of hydrogen chloride if required. Flowmeters (Meterate RS1, ruby float), are used to moniter the gas flow rates. Use of the upper gas inlet ensures that the balance remains in a non corrosive environment. Reactive gases are introduced below a constriction through the lower inlet. Typically the operational pressure is maintained approximately 3 mbar above atmospheric pressure.

The lower gas inlet includes a bromine reservoir (fig. 2.3) through which a hydrogen flow may be diverted, so permitting entrainment of a reactive component in the carrier gas stream. The reservoir is immersed in a water thermostat (Grant SX10). At temperatures between 50° C and ambient, the bath temperature is stable to within 0.01° C. Plastic spheres are floated on the surface of the water to minimise evaporation losses. The temperature of the bath is measured using a calibrated mercury in glass thermometer (-10 to 50° C, 0.1 interval).

The glass system may be evacuated using a rotary pump

Fig 2.3 Bromine Reservoir

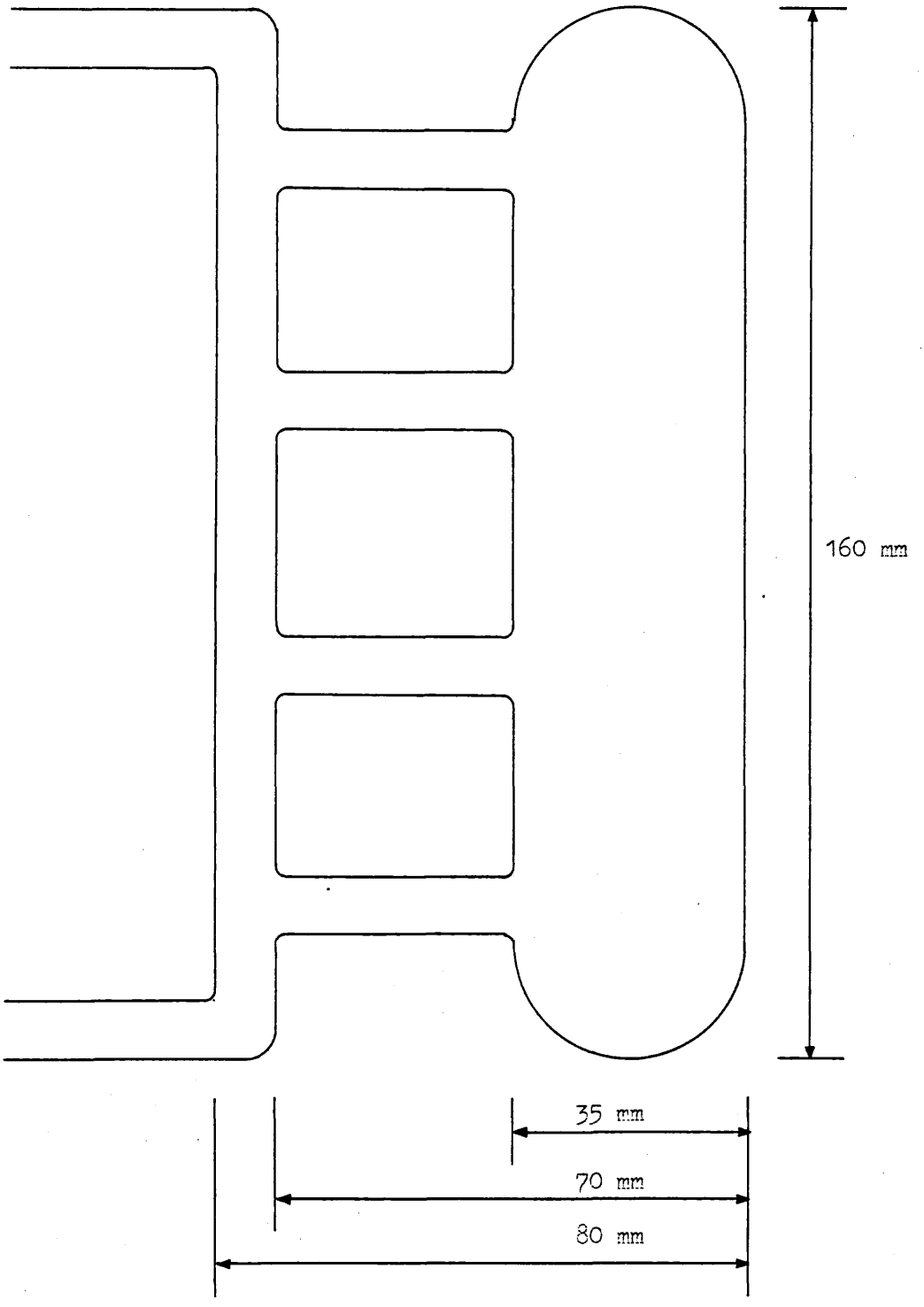

(Edwards Speedivac 2520). A mercury manometer is included in the system, and a vacuum gauge (Edwards Pirani 12, head PRCT10-C), is used for measurement of low pressures. Following prolonged evacuation a base pressure of 2×10^{-3} mbar may be attained.

Constructional Data.

The balance base plate is mounted 1.7 m from the floor on an aliminium bracket. The furnace in its operating position, is 0.7 m below the furnace. The gas inlet lines consist of the metering valves followed by ballast vessels (2 dm^{-3}) and then $\frac{1}{2}$ m of capillary tube ($1\frac{1}{2}$ mm ID). After this pressure-stabilizing stage, the gas stream passes throgh the flowmeters, and from there through 9 mm tube to the balance enclosure (upper inlet), and furnace tube (lower inlet). The metering valves, ballast vessels, flowmeters and bromine reservoir are all mounted at bench height. Provision is made to evacuate the system through the gas inlet lines and the bottom of the furnace tube, by means of a vacuum line beneath the bench. Stopcocks (J Young 5 mm, PTFE 'O' ring), are positioned between the vacuum line and gas inlet ballast vessels; the vacuum line and furnace tube, and also between the vacuum line and vacuum gauge head. The same design stopcocks are used at the top of each flowmeter, in the by-pass arrangement for the bromine reservoir and finally at the gas outlet.

Experimental Procedure.

The chosen bottle is cleaned, dried and loaded with the sample of interest, and the balance is calibrated. The suspension fibre is located and the furnace tube brought into position. The bottle is then introduced from the bottom of the

furnace tube and located on the fibre. With the bottle in position, the balance is tared, and the weight suspension dial on the balance control box set accordingly. Lastly, the thermocouple is inserted below the bottle and the glassware is connected to the vacuum line and gas outlet.

Once assembled, the apparatus is evacuated (typically 5×10^{-2} mbar), firstly through the gas inlets, to 10 mbar, and then also through the bottom of the furnace tube. Evacuation through the bottom of the apparatus is delayed until a low pressure has been attained, otherwise turbulence may seriously buffet the bottle and cause the suspension fibre to break. The system is next leak tested and then filled to atmospheric pressure with dry nitrogen. Evacuation is repeated and the apparatus filled with hydrogen. Leak detection follows, using a gas leak detector (Gow-Mac Inst Co model 21-212). The system is evacuated and back filled with hydrogen twice more before use.

Following the final filling, the gas outlet is opened and the hydrogen flow rates set to the desired levels, a delay is incurred before the flow rates stabilize while the diffuser re-establishes pressure behind the needle valves. While the hydrogen flow rates are settling, the furnace may be heated, and a reactive gas introduced if required, to such a temperature that 10% of the sample weight may be lost in a relatively short period of time. This exercise ensures that a clean surface is exposed ready for the accumulation of weight loss data.

Rates of weight loss are recorded under isothermal conditions over the desired temperature range. The rate of

weight loss is displayed on a chart recorder, the full scale deflection of which may be set to various values, usually 1 mg (1 or 0.4 mg using the Cahn RG balance). Four measurements of the rate of weight loss are usually recorded at each temperature.

When conducting transport experiments using hydrogen bromide below 770 K a preheater is required (set in excess of 870 K), around the furnace tube above the level of the furnace. This preheater is employed to effect near-quantative conversion of the hydrogen-bromine mixture to hydrogen bromide. Although the combination of the elements to form hydrogen bromide is thermodynamically favoured at the lower temperature, it is however kinetically limited[4]. The heater takes the form of a high temperature heating tape (Electrothermal HC 504, 800 W).

2.2 Solution Calorimetry.

The calorimeter used for the determination of heats of reaction in this work is of constant temperature environment (CTE), or isoperibol design. The calorimeter was designed and constructed at this laboratory. Operational procedures and constructional details are available[5,6]. The principle of operation is that the thermal energy liberated, or absorbed, during the reaction between a known amount of sample and the solvent is compared to that quantity of electrical energy required to produce a similar temperature change in the solution.

The apparatus as a whole, including ancillary electronic equipment, will be referred to as the 'calorimeter'. The evacuated unsilvered Dewar vessels, containing the reaction solution, will be referred to as the 'reaction vessels'. Two

similar reaction vessels (fig 2.4) are employed. The reaction vessel contains: a central stirrer, driven via a flexible cable from an electric motor (Parvalux Electric Motors Ltd, model SD8), an ampoule holder, cooling tube, thermistor (Standard Telephones & Cables Ltd, F53), and a heater. Two types of heater were used, each having a nominal resistance of 100 Ω, the first type were commercially available, PTFE encapsulated, solid state heaters, (Tronac Inc, R-24), and a second type were fabricated at this laboratory.

The laboratory-made heaters consist of $\frac{1}{2}$ W thick film resistors (RS Components Ltd, stock no. 145-131). These were chosen for their small bulk and low temperature coefficient, ($\pm$ 100 ppm max). The resistors are supported in thin walled glass tubes (NMR sample tubes) and immersed in oil (Midland Silicones MS200). Current is delivered to the resistors from a 6 V constant current source.

The thermistors constitute one arm of a Wheatstone bridge circuit and a chart recorder (Bryans 27000) is used to record the out of balance bridge voltage.

Two calibration curcuits were used; the first appears in fig 2.5.

The heater (H) is connected in parallel with a potential divider comprising resistors M and N (Croyden Precision Resistors 2 W, 0.025% tolerance), and in series with a standard resistance, S, (Cropico, type RSI 10 Ω, 1 A). The constant voltage source (Ether Ltd, model AA100) has nominal output of 6 Vd.c.

The potentials V_1 and V_2 were measured on a potentiometer (Tinsley, type 3387B) in conjunction with a Scalamp galvanometer

Fig 2.4 Reaction Vessel of Isoperibol Calorimeter

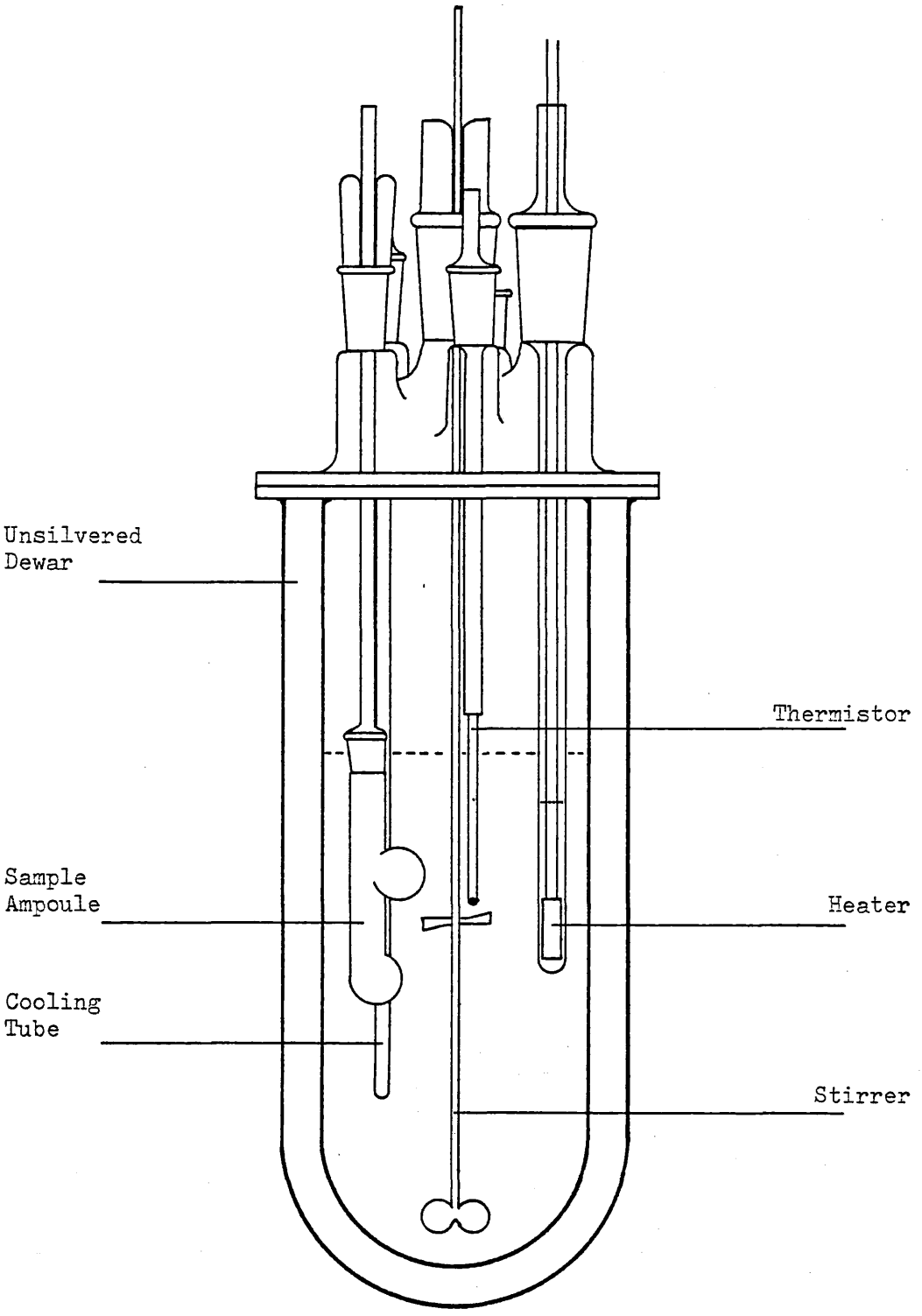

Fig 2.5 First Calibration Circuit

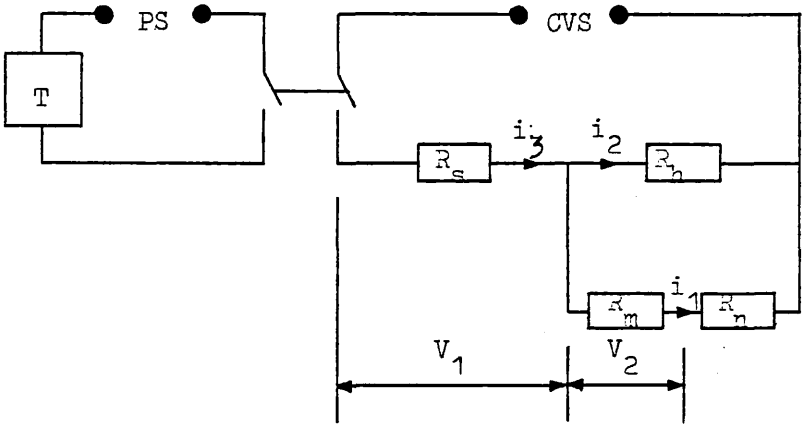

PS = Main power supply

CVS = Constant voltage source, 5.960 ± 0.001 V

R_s = 9.9998 Ω

R_m = 9.992 Ω

R_n = 99.955 Ω

$$i_3 = V_1/R_s = i_1 + i_2 = V_2/R_m + i_2$$

$$i_2 = V_1/R_s - V_2/R_m$$

$$V_h = (R_m + R_n)V_2/R_m$$

$$\text{Power, } P = i_2V_h = (R_m + R_n)V_2/R_m \; V_1/R_s - V_2/R_m$$

$$= 11.0035V_2(V_1/9.9998 - V_2/9.992)$$

Fig 2.6 Second Calibration Circuit

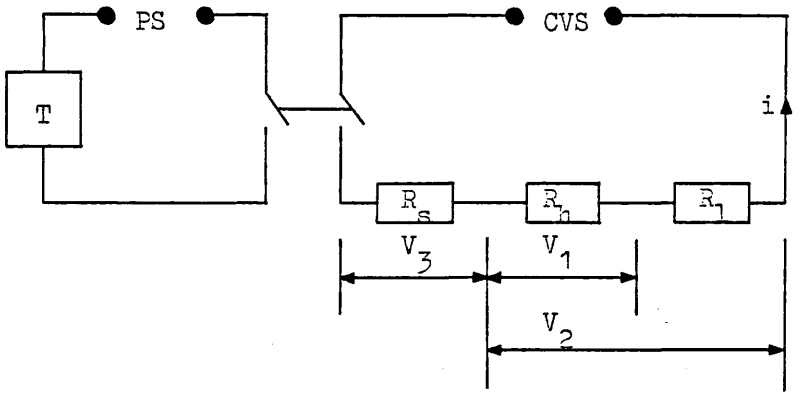

PS = Mains power supply

CVS = Constant voltage source, 5.960 ± 0.001 V

R_s = 9.9998 Ω

R_h = Heater resistance, (nominally, 100 Ω)

R_l = Heater lead resistance

$$i = V_3/R_s$$

$$\text{Power, } P = iV = V_1V_3/R_s$$

$$R_h = V_1R_s/V_3$$

NB V_2 is redundant, but may be used to determine R_l.

(Pye 110 Ω). Before use, the potentiometer was calibrated against a Western Standard Cell (Cambridge Instrument Co Ltd). The heating period was timed using an electric timer (J Hengstler & Co, model FO 43.4), coupled to the heater via a double pole switch.

The second calibration circuit appears in fig 2.6. Again, the heater (H), is connected in series with a standard resistance, S, as above, but a potential divider is not used. The same constant voltage source is employed with the same output as before. The potentials V_1, V_2 and V_4 are measured with a digital volt meter (Solartron LM 1440.3). The volt meter is calibrated against an internal reference.

Operation.

The ampoules are cleaned and oven dried. A known weight of sample is loaded into each ampoule under suitable experimental conditions. The reaction vessel is assembled and the solution loaded, preheated as required. The reaction vessel is next submerged in a thermostated water bath, ≈ 50 dm^3 in volume. The reaction vessel is then left for an extended period (usually overnight), to attain thermal equilibrium. The drive cable to the stirrer is attatched and the motor switched on, and a further two hours are allowed to re-establish equilibrium. Following the final equilibrium period the reaction experiment is performed. Once the after period is recorded, the reaction vessel is cooled and left for a further two hours prior to calibration. The two vessels were normally operated in tandem.

When the calorimeter is used to study reactions involving a bromine solution, the greased flange between the upper and

lower components of the reaction vessels is sealed using a fluorinated hydrocarbon grease (3M Voltalef).

The temperature-resistance relationship is given by:

$$R = A\exp(B/T)$$

where, R/ = resistance, T/K = temperature, and A and B are thermistor constants.

Actual temperatures were not used in this work since it may be shown that provided the temperature excursions are small, and the reactions are relatively fast (ca 5 min), then the resistance measurements are all that are required. Fig 2.7 shows temperature-time profiles for an exothermic reaction and its associated calibration. T_1 represents the temperature at the instant the ampoule is broken, and T_2 represents the temperature attained following complete reaction. The temperature change T_r accompanying the reaction is then given by $T_2 - T_1$. Resistance values corresponding to temperatures T_1 and T_2 may be labelled R_1 and R_2 respectively. Similarly for the calibration. $T_4 - T_3$ represent the temperature change T_c that accompanies the calibration, and have a corresponding resistance value $R_4 - R_3$.

Now,

$$T_r = T_2 - T_1 = \frac{B\ln(R_1/R_2)}{\ln(R_1R_2/A^2)}$$

and,

$$T_c = T_4 - T_3 = \frac{B\ln(R_3/R_4)}{\ln(R_3R_4/A^2)}$$

so,

$$T_r/T_c = \frac{\ln(R_1/R_2)}{\ln(R_3/R_4)} \cdot \frac{\ln(R_3R_4/A^2)}{\ln(R_1R_2/A^2)}$$

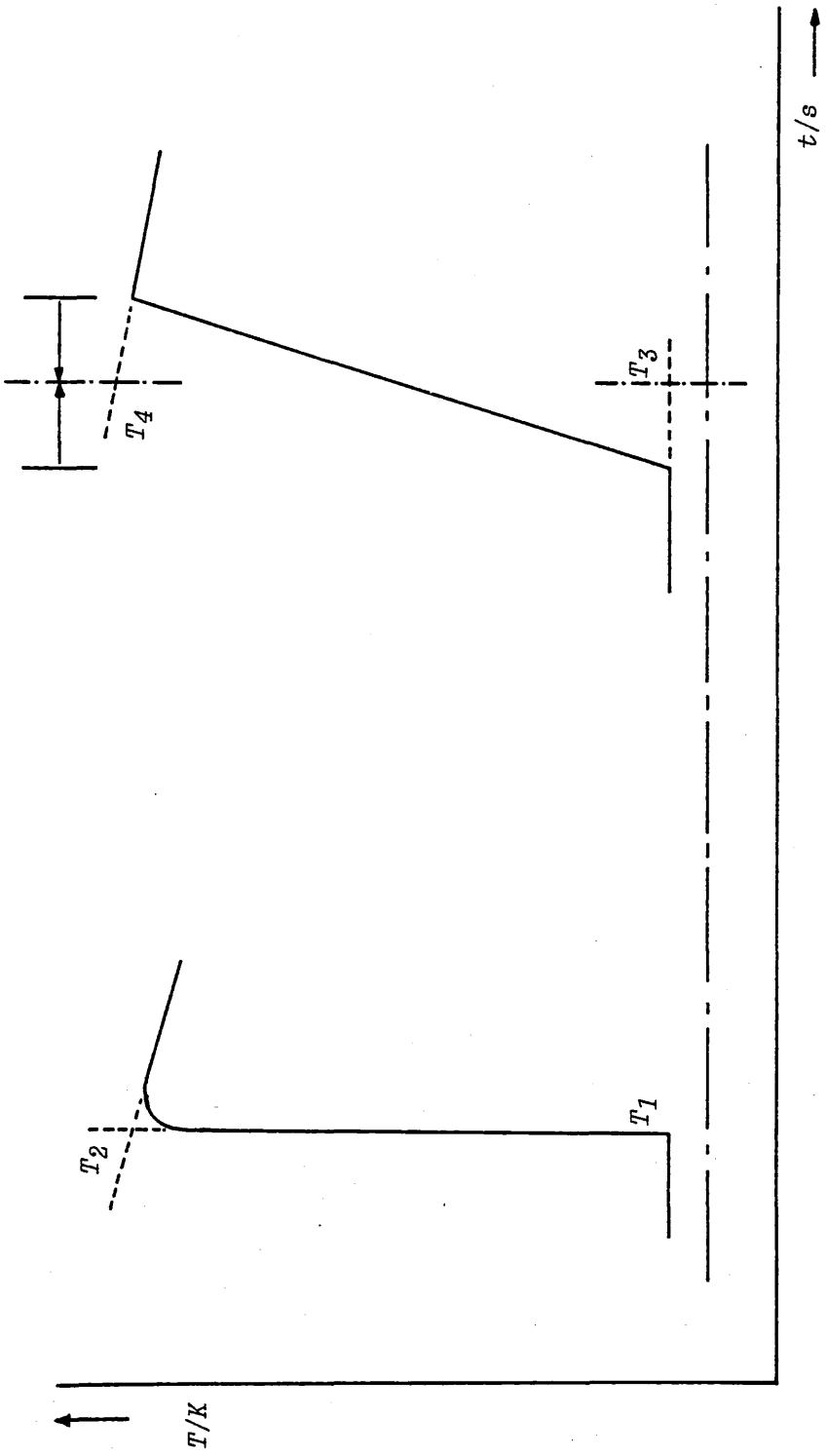

Fig. 2.7 Temperature time profile

Since the constant A in these expressions is the resistance of the thermistor at 25° C, (ie 5000 Ω), and provided that the reaction and calibration are initiated at very similar temperatures, and the value $R_2 - R_1$ is roughly equivalent to the value $R_4 - R_3$, then the second term in the above expression may be omitted as it becomes close to unity,

hence we have,

$$T_r / T_c = \frac{\ln(R_1/R_2)}{\ln(R_3/R_4)}$$

Then from fig 2.6,

$$\text{Power } (P) = V_1 V_3 / R_s$$

$$\Delta H/\text{kJmol}^{-1} = \frac{P.t.M.\ln(R_1/R_2)}{1000.w.\ln(R_3/R_4)}$$

where, P/W = electrical power

t/s = heating time

M/gmol^{-1} = molecular weight

w/g = weight of sample.

2.3 Differential Scanning Calorimetry.

Differential Scanning Calorimetry (DSC), is a useful and rapid technique for the measurement and characterisation of the thermal properties of materials. The technique involves bringing a sample and inert reference material to a common initial temperature, and selecting a suitable linear heating (or cooling) programme to raise or lower the sample and reference to a desired final temperature. DSC differs fundementally from the more conventional technique of

differential thermal analysis (DTA), in that the sample and reference are both maintained at the same temperature which is predetermined by the chosen programme even during a physical change in the sample. When a transition or reaction takes place in the sample, the accompanying endotherm or exotherm is detected as the change in power required to maintain the sample at the same temperature as the reference material.

The sample and reference are placed in identical environments; metal pans on individual bases which each contain a platinium resistance thermometer and a heater. The thermal mass of the holders is minimised so that the response of the resistance thermometer is rapid. The temperatures of the two thermometers are compared, and the electrical power supplied to each heater adjusted so that the temperatures of both the sample and the reference remain equal to the programmed temperature; ie any temperature difference which would result from a physical change in the sample is 'nulled'.

The ordinate signal, the rate of energy absorption by the sample, is proportional to the specific heat of the sample, since the specific heat at any temperature determines the amount of thermal energy necessary to change the sample temperature by a given amount. Any transition accompanied by a change in specific heat produces a discontinuity in the power signal, and exothermic or endothermic enthalpy changes give rise to peaks whose areas are proportional to the total enthalpy change.

The sample containers used in a DSC instrument are shallow metal pans which may be open, loose lidded or sealed. The sample and reference containers are placed on individual bases

Fig 2.8 Differential Scanning Calorimeter System

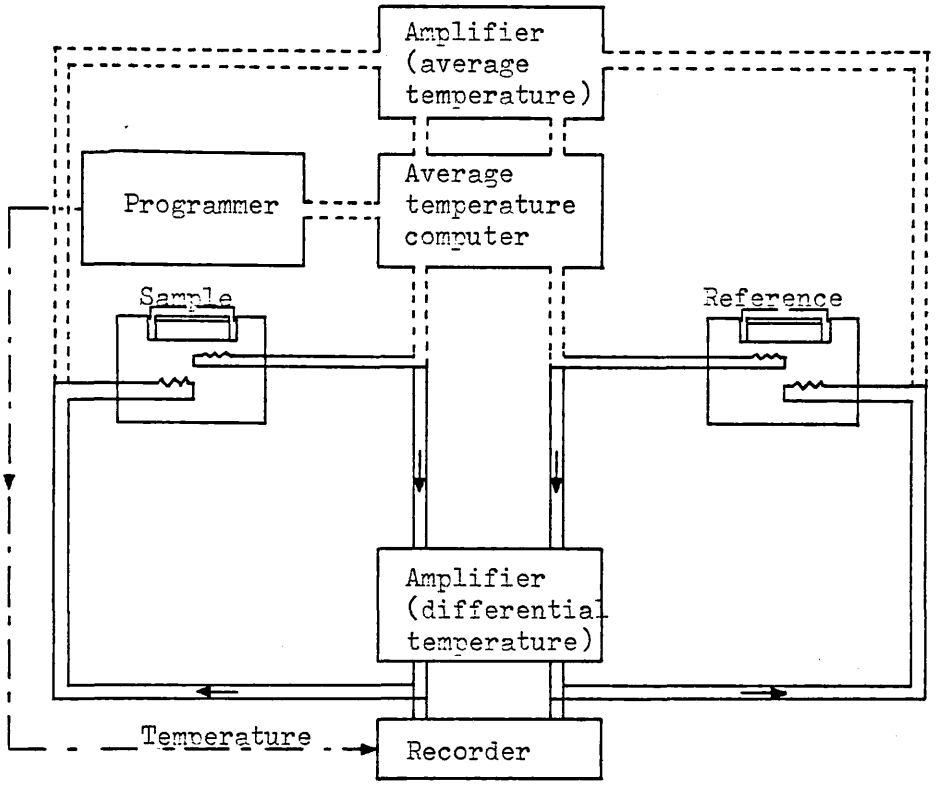

Fig 2.9 Form of DSC Output

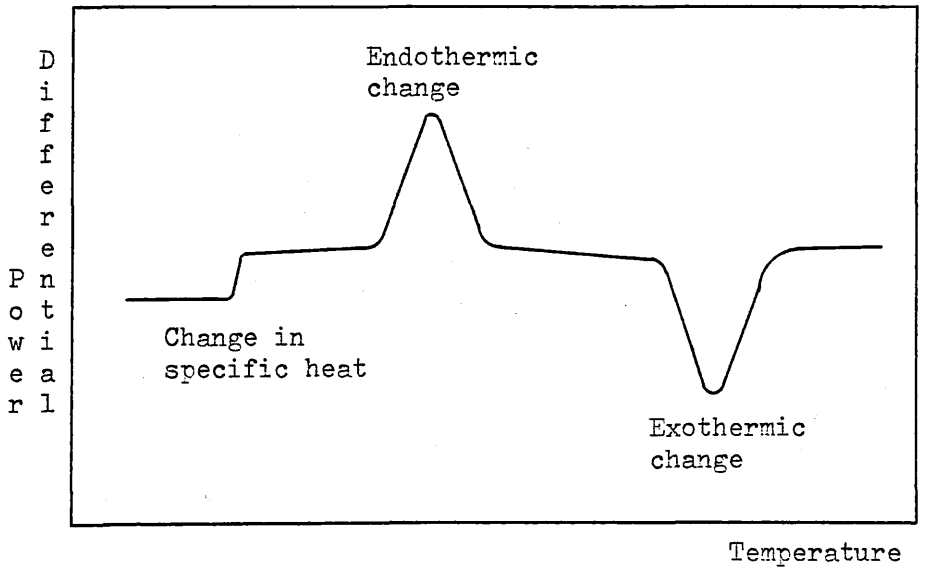

thermally isolated from each other, each base containing a separately controllable heater and thermal sensor (fig 2.8).

The Perkin-Elmer differential scanning calorimeter, (model DSC-2), used for this work, operates in the manner described below. Both programmed and balancing heating are performed by the single heaters encapsulated in each of the sample and reference bases (fig 2.8). These heaters are powered by alternating current. On one half cycle, power is supplied equally to sample and reference via the temperature programmer. Differing amounts of power may be applied to the sample and reference on the remaining half cycle, which are sufficient to nullify any temperature differential between the sample and reference pans. The heating system then responds to two control loops, one controlled by the temperature programme and the second by the different energy requirements of the sample and reference.

Any inert material may be used as a reference, but an empty sample pan is generally preferred. In this way, if the sample and reference pans are matched, the thermal capacity of the sample pan is balanced and the DSC trace records changes in only the sample. An arrangement was used where-by the differential power provided was recorded as ordinate versus programmed temperature as atscissa (fig 2.9).

The DSC-2 may be used to obtain specific heats directly from the ordinate displacement from the interpolated, empty pan, isothermal base line. The accuracy of such measurements depend upon the accuracy of the scanning rate. The method employed here was to compare this ordinate displacement of a sapphire

standard (Union Carbide Electronics) to the displacement for a known weight of sample.

The DSC-2 was also used to determine heats of transition. The peak area of a transition represents the energy liberated, or absorbed, during that transition and is independent of scanning speed temperature, nature of sample or mode of operation (heating, cooling or isthermal). Calibration is made using a material of precisely known thermal properties, usually indium metal.

Before any measurements are made using the instrument, a temperature calibration must be undertaken. This involves recording the melting endotherms of a number of reference materials.

Operation.

Prior to any sequence of experiments the crucible lids were removed and the DSC heaters cycled rapidly to maximum output (1000 K). This temperature is maintained for a period of about two minutes to remove dust and any organic residues. For heat capacity measurements three scans over a limited temperature range are made. The first is to record a base line and to ensure that the isothermal recorded before and after the temperature excursion lie within specified limits (they should display equal displacements). This trace is recorded with empty pans loaded in both the sample and reference crucibles. An isothermal line is recorded and the temperature programme engaged and a further isothermal recorded on its completion. The second scan is superimposed upon the first with the sample pan loaded with the sapphire calibrant. The third trace is superimposed upon the previous two, and is made with the sample

pan loaded with a weighed quantity of the material of interest, (fig 2.10). All materials were weighed by a null technique using an electrobalance (Cahn Gram).

In order to determine transition enthalpies one simply loads a weighed sample and records a temperature scan, over an appropriate range, against an empty reference pan. The area beneath any peak is proportional to the heat of transition and a value may be extracted directly from the trace using the known instrument settings. It is preferable, however, to relate the ordinate deflection to that of a reference material. The melting endotherm of indium metal is therefore recorded at the same instrument settings as those used for the sample of undetermined thermal properties.

Determination of Heat Capacity.

Using the comparison procedure the heat capacity of a sample, $C_p(s)$, may readily be obtained from the heat capacity of the sapphire calibrant, $C_p(c)$;

$$C_p(s) = \frac{C_p(c).m(c).x(s)}{m(s).x(c)}$$

where m(c) and m(s) are the weights of the calibrant and sample respectively, x(c) and x(s) are the corresponding ordinate deflections of calibrant and sample.

Determination of Transition Enthalpies.

The heat of fusion (or transition) of a sample is calculated from the general formula:

$$\Delta H_{fus}/Jmol^{-1} = \frac{M(s).A(s).W(In).(3263)}{W(s).A(In).(114.82)}$$

Fig 2.10 Typical Thermogram Trace for Heat Capacity Determination.

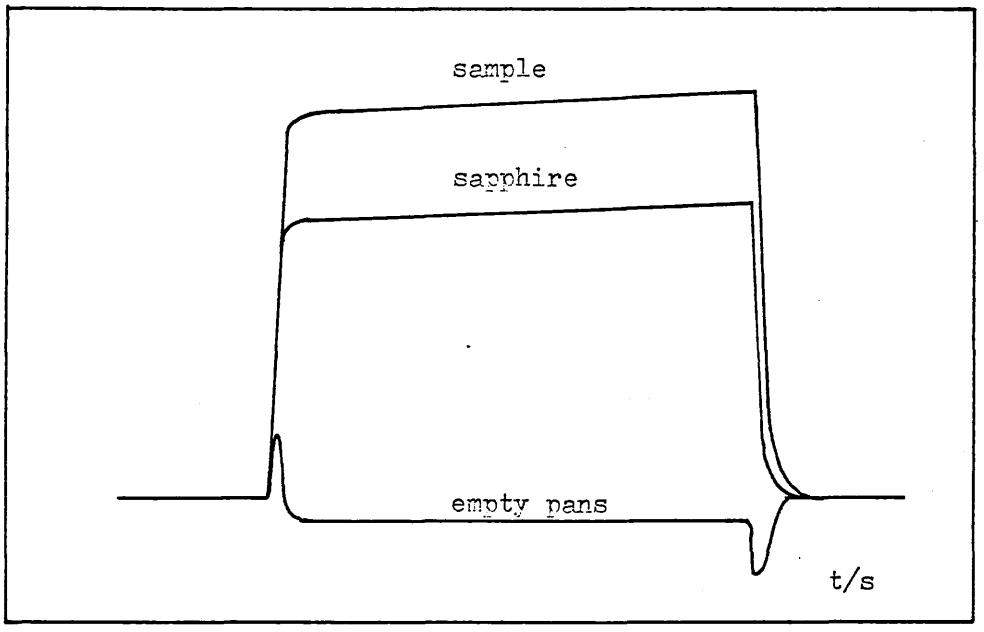

where $M(s)/gmol^{-1}$ = molecular weight of the sample

$W(s)/g$ = weight of sample

$W(In)/g$ = weight of indium

$A(s)/cm^2$ = area beneath sample endotherm

$A(In)/cm^2$ = area beneath indium endotherm

$114.82/gmol^{-1}$ = molecular weight of indium

$3263 \pm 41/Jmol^{-1}$ = ΔH_{fus} In, c-l [7]

Peak Areas are measured using a planimeter.

Aliminium, volatile sample pans were employed, as well as open gold pans. For heat capacity determinations, temperature scans (usually covering 40 K), were made over the temperature range of interest. For each scan, isothermal base lines were recorded for the empty sample pans, sapphire calibrant and the sample.

Throughout all measurements the sample and reference cavities were continually purged with dry nitrogen.

2.4 Raman.

2.4.1 Raman, solid samples.

The Raman spectra of solid samples were recorded using a Coberg (model PHO) monochromator equiped with a cooled RCA photomultiplier tube. Spectra were excited by the 647.1 nm line from a krypton ion laser (Coherent Radiation, model 52 K).

2.4.2 Raman, gas phase.

Preliminary gas phase studies were performed using a double monochromator (Spex 1401), equiped with an RCA photomultiplier tube. The spectra were excited by the 488.0 nm line

line from an argon ion laser (Spectre Physics, model 170).

Further studies employed the 514.5 nm line of another argon ion laser (Coherent Radiation, model CR-12), as an excitation source, and a Spex monochromator (Ramalog 6), again fitted with an RCA photomultiplier tube.

Samples were contained in silica ampoules for which a dumbell design was adopted because the preliminary experiments illustrated a flaw in a cylindrical design. The ampoules were held and heated by a small resistance furnace, which had a cold resistance of approximately 2 Ω, (fig 2.11).* The furnace in turn was mounted on a cooling plate (fig 2.12), which was constructed to suit the sample area of the Spex Ramalog 6 monochromator. Cooling water was passed continuously through the cooling plate and furnace end plates during operation. Furnace temperatures were regulated using a 20 A variable transformer and monitered (to within $\pm$ 2 K), by a chromel-alumel thermocouple. Incident radiation entered the sample from below via a narrow port in the furnace wall, and scattered radiation was collected horizontally through a quartz/fluorite collection lens.

The problem arising from cylindrical ampoule geometry was due to the nature of the optical path. At intermediate temperatures the laser beam entered the sample after passing through a melt. This melt boiled vigorously in the vicinity of the beam, causing unavoidable random fluctuations in the scattered light intensity.

The ampoules were loaded and sealed on a glass vacuum line (fig 2.13). The line may be evacuated (10^{-4} mbar) by means

* The furnace used was kindly lent by the Department of Chemistry, University of Southampton.

Fig 2.11 Raman Furnace

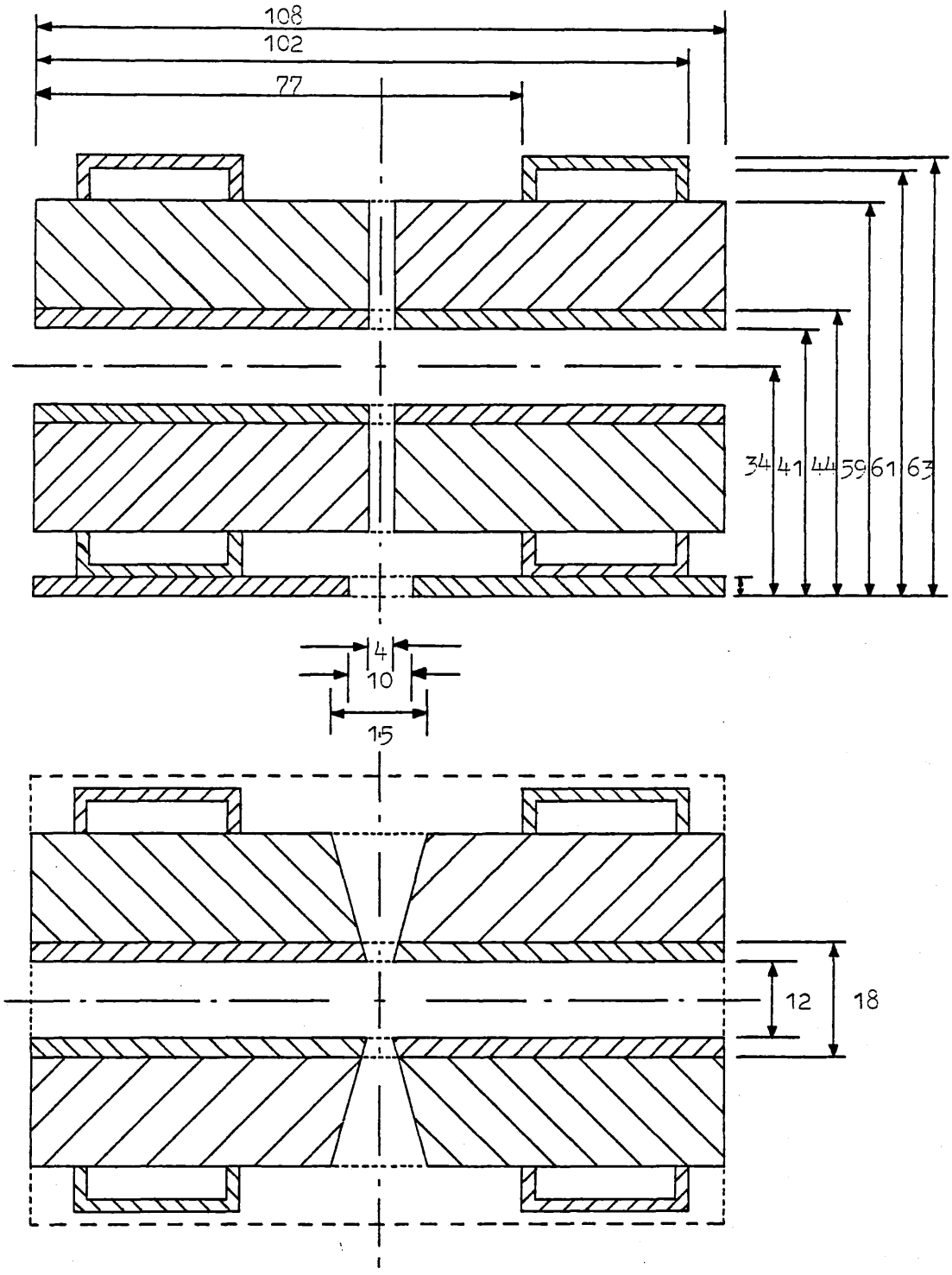

Dimensions in mm.

Fig 2.12 Raman Furnace Mounting Plate

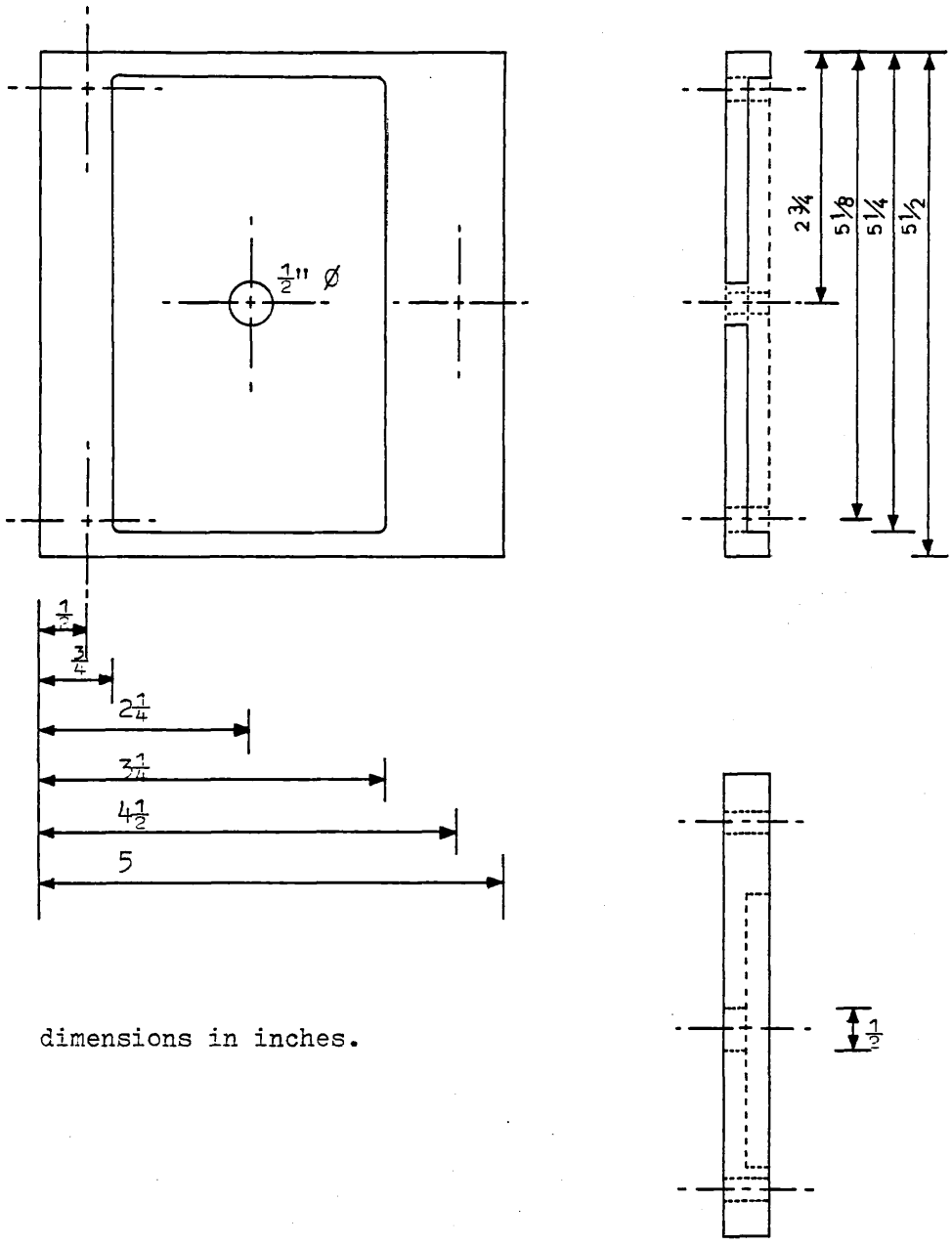

dimensions in inches.

of a mercury diffusion pump (D), with a two stage rotary backing pump (R).

Fig 2.13 Vacuum Line

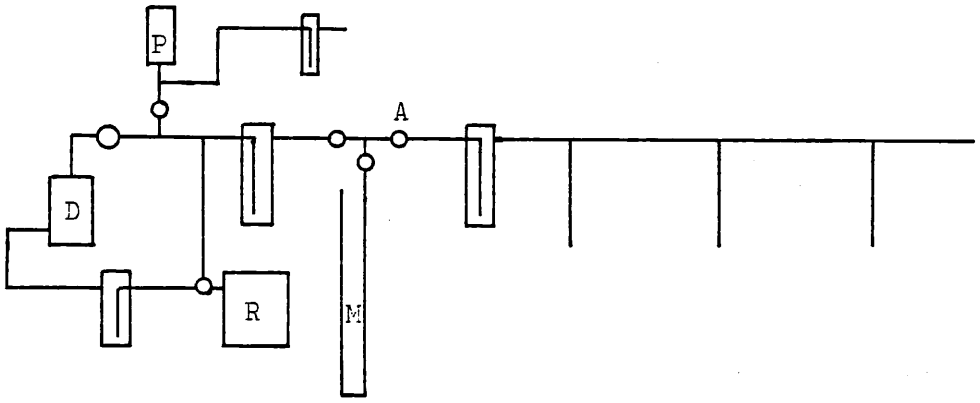

To the right of point A all stopcocks and seals are greaseless (J Young, PTFE). The manometer, M, allows for the measurement of pressure from 1 mbar to 10 mbar. An Edwards Pirani gauge, P, fitted with a 96C-2 head is used to moniter pressures below 1 mbar.

Attatched to the vacuum manifold, the ampoules may be evacuated, outgassed and sealed. Solid materials may be introduced by vacuum sublimation, and liquids by vacuum distillation. Gases may also be introduced at any desired pressure. Throughout all loading procedures the ampoules are maintained under rigorously anhydrous conditions.

Following preparation, the mechanical integrity of each ampoule is tested by heat cycling to 1000 K.

2.5 Preparations.

2.5.1 Indium Monobromide.

Various methods for the preparation of indium monobromide appear in the literature[6-14]. Most have utilized two main approaches: either direct combination of the elements (or hydrogen bromide instead of elemental bromine), or the reduction of higher bromides. Such methods usually require careful control in order to achieve the desired stoichiometry in the product.

The procedure first adopted in this work was chosen from the literature[14] and involved the following reaction:

$$2In + HgBr_2 = Hg + 2InBr$$

The reaction was carried out in an evacuated (10^{-3} mbar) thick-walled pyrex tube. Material prepared in this fashion proved difficult to purify. Immediately following preparation, visual inspection revealed gross contamination with mercury. Purification by vacuum sublimation resulted in very small yields of pure material. Inspection of Raman spectra of various samples proved a rapid technique for detecting the presence of higher bromides. Analysis[15] revealed 4.5% by weight mercury in the final product.

A second procedure provided a useful sample. This involved the addition of ammonium bromide to molten indium:

$$In + NH_4Br = InBr + NH_3 + \tfrac{1}{2}H_2$$

6.54 g of indium (BDH, AnalaR 99.9%) were loaded into a 50 cm^3 B29 conical flask and evacuated (10^{-3} mbar). Dry nitrogen was then bled into the flask, and evacuation and filling was repeated. The indium was then melted using a gentle Bunsen flame. Ammonium bromide (BDH, AnalaR) was added to the molten indium in small quantities (fig 2.14). With continued heating,

Fig 2.14 Indium Monobromide Preparation

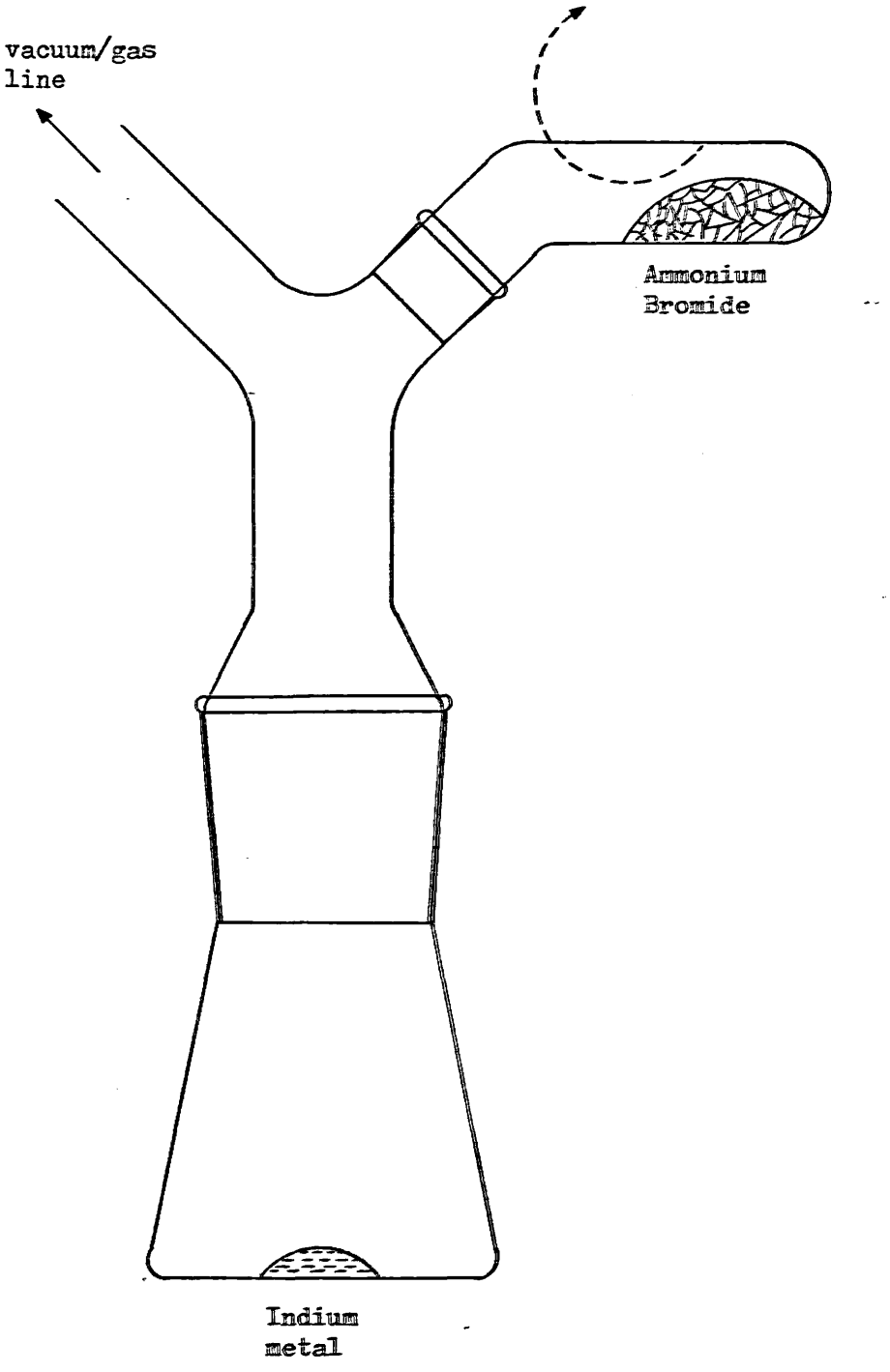

the surface of the indium takes on an orange colouration, then black. Shortly after blackening, the surface clears, exposing fresh indium metal, and so on. Between additions of ammonium bromide, the flask was evacuated and refilled with dry nitrogen. This procedure was adopted in order to remove the ammonia evolved in the reaction. Previous experience had shown that allowing the product to cool under an atmosphere of ammonia had a deleterious influence on the desired final product. In all a stoichiometric excess of ammonium bromide was added (5.62 g) but some sublimation to the neck of the flask was noticed. An excess of indium did in fact remain, this being considered desirable, and was apparent on visual inspection. The molten product exhibited a dark red colour. The red melt became orange on solidification under vacuum, darkening a little in colour on cooling to room temperature.

The material was removed from the flask under anhydrous conditions and pulverised using a pestle and mortar. The grinding procedure allows much of the remaining indium to be physically separated, and the fine orange powder was then further purified by vacuum sublimation.

Volumetric analysis of the sample, bromine by Volhard's[16] method and indium by an EDTA titration[17], revealed excess bromine (91% In, 114% Br). Three samples prepared as above and yielding similar analyses were mixed and sealed in a thick walled pyrex tube with 7 g indium metal. The tube was heated (ca 350° C) for an extended period (80 hours). While hot, it was agitated at intervals. The remaining excess indium was separated physically and the material again powdered. The bright orange

powder analysed as 99.74% of theoretical indium (mean of three results), and 98.37% of theoretical bromine (mean of eight results).

2.5.2 Gallium Tribromide.

Bromine (BDH AristaR), which had to be dried over activated acid resistant molecular sieves (Union Carbide AW 300/1/16), was entrained in a dry nitrogen gas flow over liquid gallium (MCP Electronics Ltd, 99.9999%). It was found necessary to heat the gallium in a fierce Bunsen flame to sustain a reasonable rate of reaction. The product, a white crystalline material, was purified by vacuum distillation.

2.6 Chemicals and Handling.

2.6.1 MEM

Nitrogen (BOC, oxygen free 99.94%) was dried by its passage through molecular sieves (BDH type 4A 1/16" pellets). Hydrogen (BOC high purity grade 99.994%) was purified by a palladium diffuser (Johnson Matthey & Co Ltd, model H28/1). Bromine (BDH AristaR) was dried over acid resistant molecular sieves (Union Carbide AW 300 1/16" pellets). The molecular sieves were reactivated at intervals by pumping for an extended period at an elevated temperature (ca 200° C).

Zinc (Goodfellow Metals Ltd, 99.95% foil .05 mm thick), was cut and loaded into an MEM bottle for the evaporation studies, (see chapter 3). Indium monobromide (as above), was used in the vapour pressure measurements detailed in chapter 7. Indium phosphide (MCP Electronics Ltd, polycrystalline platelets) was ground in an agate pestle and mortar prior to loading in a prepared MEM bottle. Each sample is loaded in

anhydrous conditions. MEM bottles were prepared for use in the following manner: The bottle is initially soaked in aqua regia for about two hours, followed by successive washes in distilled water and AnalaR methanol. Finally the bottle is dried for two hours at 115 °C and cooled in a vacuum desiccator.

2.6.2 Solution Calorimetry.

The accuracy and precision of the calorimeter was checked by measuring the neutralisation of tris(hydroxymethyl) aminomethane (BDH AristaR) in excess .1 M hydrochloric acid. The tris(hydroxymethyl)aminomethane (THAM) was ground, dried at 115 °C for two hours and cooled under vacuum prior to use. Hydrochloric acid was preheated to calorimeter temperature and delivered from a pipette.

Both indium monobromide and indium tribromide were handled under anhydrous conditions at all times. Indium metal (BDH 99.9%) was handled on a clean glass surface with stainless steel instruments.

The aqueous bromine used was prepared from distilled water, potassium bromide (BDH AnalaR) and bromine (BDH AnalaR). The solution was thermostated over-night before introduction to the reaction vessels. Delivery was made from a volumetric flask.

2.6.3 DSC.

Handling procedures of all sample pans used in these studies involved the use of forceps, in order to prevent the transfer of body oils. In the preliminary studies using aluminium pans, the pans were sealed using a crimping tool. Later studies employing gold pans did not feature the sealing

procedure. Gold pans used for indium monobromide were cleaned for recycling after each use.

The following regime was adopted in cleaning indium monobromide-fouled gold pans: Firstly, the pan was immersed in hot distilled water to dissolve the indium monobromide. The lid was not usually physically removeable directly following the DSC scan since the sample had been melted. Once the lid and pan were separated, and the indium monobromide dissolved, then the pan and lid were boiled in nitric acid. Following the acid cleansing, the pan was rinsed in water and then methanol (AristaR). The pans were dried in air and then heat cycled to 1000 K in the DSC head, under a dry nitrogen purge.

Indium monobromide is not markedly hydroscopic. The sample was, however, handled with care. Anhydrous handling procedures were relaxed once a small sample, nominally kept under dry nitrogen, was separated from the stock. The stock material was maintained under anhydrous conditions at all times.

Following the loading of a gold sample pan with indium monobromide, in air, the pan was placed in a small vacuum desiccator evacuated and then back-filled with dry nitrogen. This procedure was adopted in an attempt to exclude moisture otherwise enclosed when the lid was positioned. The pan was then transferred directly to the DSC head where it was placed under a dry nitrogen purge.

2.6.4 Raman Studies.

Gallium metal (MCP Electronics Ltd, 99.9999%) was made into thin wire by filling a PVC tube with a melt and stripping back the PVC sheath as required. In wire form, the metal was

easily weighed and loaded into the silica ampoules. Indium metal (BDH 99.9%) was handled on clean glass surfaces with stainless steel instruments. Gallium tribromide from the preparation previously mentioned was introduced to the ampoules by vacuum sublimation, as also were gallium trichloride, indium trichloride, indium tribromide and indium triiodide (all Ventron Alpha, ultra pure). Gallium arsenide (MCP Electronics Ltd), ground to a coarse powder, was loaded into an ampoule via a funnel in the absence of moisture. Bromine (BDH AristaR) was transferred to the ampoules by vacuum distillation. Hydrogen (BOC, high purity grade, 99.994%) entered the ampoule from the vacuum manifold as required.

REFERENCES TO CHAPTER TWO

2.1 R.H. Moss, PhD Thesis, London (1975)

2.2 D. Battat, M.M. Faktor, J. Garrett and R.H. Moss, J. Chem. Soc. Faraday I. 70, 2267 (1974)

2.3 E.J. Tarbox, PhD Thesis (1977)

2.4 P.J. Gardner, PhD Thesis, London (1963)

2.5 R.J. Coley, PhD Thesis, London (1971)

2.6 W. Klemm, Z. Anorg. u Allgem. Chem. 152, 252 (1926)

2.7 W. Klemm and F. Dierks, ibid., 219, 42 (1934)

2.8 L.F. Nilson and O. Petterson, Z. Physik. Chem. 2, 657 (1888)

2.9 A. Thiel, Z. Anorg. Chem. 40, 280 (1904)

2.10 J.K. Aiken, J.B. Haley and H. Terrey, Trans. Faraday Soc. 32, 1617 (1936)

2.11 M. Weherli and E. Miescher, Helv. Phys. Acta 7, 298 (1934)

2.12 R.J. Clarge, E. Griswold and J. Kleinberg, J. Am. Chem. Soc. 80, 4764 (1958)

2.13 W. Klemm and W. Tilk, Z. Anorg. u Allgem. Chem. 207, 175 (1932)

2.14 R.J. Clarke, E. Griswold and J. Kleinberg (Eds.) Inorganic Synthesis Vol. VII (McGraw-Hill pp. 18 (1963))

2.15 A. Vogel, Vogel's Textboook of Quantitative Inorganic Analysis, including Elementary Instrumental Analysis (Longman, 1978)

2.16 R. Belcher and A.J. Nutten, Quantitative Inorganic Analysis (Butterworth, 1970)

2.17 H. Flaschka and H. Abdine, Chemist Analyst 45, 58 (1956)

CHAPTER THREE

Evaporation of Zinc.

3.1 Introduction

The modified entrainment method (MEM) has been used to study hetrogeneous equilibria in various systems.[1,2,3] The method was first validated using the system to obtain vapour pressure results for water and lead, and comparing these with previously reported data[4]. The first MEM apparatus installed at the laboratory was similarly validated using water and zinc[5]. Following the construction of a second apparatus, described in chapter two, evaporation studies of zinc in hydrogen were repeated.

3.2 Simple theoretical description of the modified entrainment method.

A complete theoretical description of the MEM has been presented elsewhere[4], so only a brief account shall be given here.

For the evaporation of a liquid, or sublimation of a solid:

$$M(s) = M(g) \qquad (3.2.1)$$

$$M(l) = M(g) \qquad (3.2.2)$$

there is a net increase in molar volume in the system. The increase in volume accompanying vaporisation gives rise to a Stefan flow. Stefan proposed[6], and verified experimentally, that the volume V, of vapour passing through a unit cross-section of

a pipe per unit of time is given by:

$$V = \frac{D}{P-p} \cdot \frac{dp}{dx} \qquad (3.2.3)$$

when P is the total pressure, p the partial pressure of the vapour, and D its diffusion coefficient in the surrounding environment. The flux $J/molm^{-2}s^{-1}$, may be expressed as the sum of a flow term and a coefficient term,

$$J_i = n_i U - D \frac{dn_i}{dx} \qquad (3.2.4)$$

where U is the Stefan velocity, and $n/molm^{-3}$ is the molar density.

A one dimensional model may be used to describe gas transport in the channel of an MEM bottle (fig 3.1). At the base of the channel, x = 0, the vapour composition is assumed to be the same as that at the surface of the condensed phase. At the top of the channel, x = 1, where the vapour from the capillary is rapidly diluted by the bulk flow of the carrier gas, the vapour composition is assumed to be zero. These two assumptions are found to be valid under the experimental conditions employed[4].

Flow equations for the reactants, products and carrier gas (H_2) in the channel may be written in the following form:

$$J_i = n_i U - D_{i,H_2} \frac{dn_i}{dx} \qquad (3.2.5)$$

where J_i is the flux of the species i, n_i the concentration of species i, U is the mole average Stefan velocity and D_{i,H_2} the binary diffusion coefficient of species i in hydrogen. Assuming ideal gas behaviour, the molar densities in 3.2.5 may be replaced by partial pressures provided that the total pressure varies

Fig 3.1 MEM Reaction Bottle

a) stopered bottle

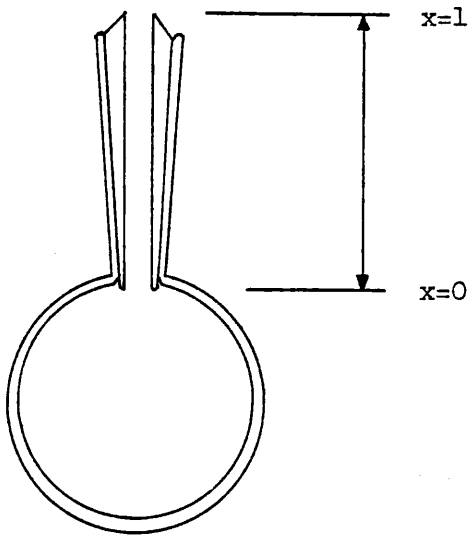

b) integral bottle

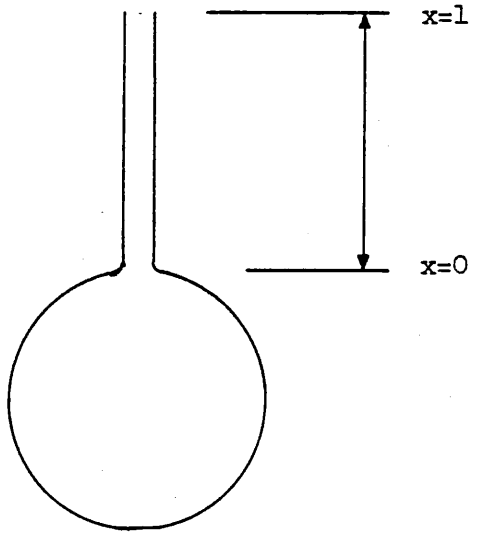

negligibly with x, (ie, there is a negligible pressure gradient), this holds unless the channel is very narrow.

Equation 3.2.5 may then be rewritten:

$$J_i = \frac{Up_i}{RT} - \frac{D_{(i,H_2)}}{RT}\frac{dp_i}{dx} \qquad (3.2.6)$$

For hydrogen, the carrier gas, there is no net flow so J_{H_2} = zero. On summation of the flux equations the diffusion terms cancel, if there is no pressure gradient in the channel, and:

$$\Sigma_i J_i = J = \frac{UP}{RT} \qquad (3.2.7)$$

where, $P = \Sigma_i p_i$, is the total pressure in the system.

Now substituting 3.2.7 in 3.2.6, U may be eliminated:

$$J_i = \frac{JRT}{P}\frac{p_i}{RT} - \frac{D_{(i,H_2)}}{RT}\frac{dp_i}{dx}$$

rearanging we obtain:

$$\frac{RT}{D_{(i,H_2)}} J_i + \frac{dp_i}{dx} = \frac{Jp_i}{P}\frac{RT}{D_{(i,H_2)}}$$

and

$$\frac{dp_i}{dx} = \frac{RT}{D_{(i,H_2)}}\left[\frac{dp_i}{P} - J_i\right] \qquad (3.2.8)$$

now separating the variables:

$$\frac{dp_i}{Jp_i/P - J_i} = \frac{RT}{D_{(i,H_2)}}\,dx$$

Integrating from, x=0 to x=1 we obtain:

$$\int_{P(0)}^{P(1)} \frac{dp_i}{Jp_i/P - J_i} = \int_0^1 \frac{RT}{D_{(i,H_2)}}\,dx$$

$$\frac{P}{J} \ln \left[\frac{Jp_i^{(1)}/P - J_i}{Jp_i^{(0)}/P - J_i} \right] = \frac{RTl}{D_{(i,H_2)}}$$

so

$$\ln \left[\frac{Jp_i^{(1)}/P - J_i}{Jp_i^{(0)}/P - J_i} \right] = \frac{JRTl}{D_{(i,H_2)}P}$$

In order to simplify matters let us introduce ξ_i, the transport function of species i.

$$\xi_i = \frac{JRTl}{PD_{(i,H_2)}} = \frac{\dot{w}RTl}{D_{(i,H_2)}AMP}$$

where, $J = \dot{w}/AM$

$\dot{w}/kgs^{-1}$ = the rate of weight loss from the sample.

$R/JK^{-1}mol^{-1}$ = is the gas constant.

T/K = temperature.

l/m = the length of the MEM capsule channel.

$D_{(i,H_2)}/m^2s^{-1}$ = the diffusion coefficient of species i in hydrogen.

A/m^2 = the cross-sectional area of the MEM capsule channel.

$M/kgmol^{-1}$ = the molecular weight of the condenced phase.

P/Pa = the total pressure.

Thus rearranging,

$$Jp_i^{(0)}/P - J_i = (Jp_i^{(1)}/P - J_i)\, e^{-\xi_i} \qquad (3.2.9)$$

Considering the evaporation of a single substance $J_i = J$, and for a minority species it is assumed that,

$$0 = p_i^{(1)}/P$$

ie that species i is quantitativly flushed away at the open end of the channel.

Then 3.2.9 becomes:

$$p_i^{(0)} = P(1 - e^{-\xi_i}) \qquad (3.2.10)$$

$p_i^{(0)}$ represents the vapour pressure of species i over the condensed phase. If the capillary is sufficiently narrow then $p_i^{(0)}$ represents the saturated vapour pressure of the sample.

The evaporation of zinc was studied over the temperature range 820 to 1150 K. The results are documented in table 3.1, and are presented graphically in fig 3.2.

From 3.2.10 the evaporation of a single substance, zinc, the rate of weight loss, $\dot{w}$, from an MEM capsule at temperature, T, is related to the equilibrium vapour pressure, p^o_{Zn}, by the expression:

$$p^o_{Zn} = P(1 - e^{-\xi})$$

where

$$\xi = \frac{\dot{w}RTl}{D_{(Zn,H_2)}PM_{Zn}A} \qquad (3.2.11)$$

An equation for the equilibrium vapour pressure of molten zinc (mpt 693 K) was adopted from a critical compilation by Nesmeyanov[7], is given below:

$$\log_{10}(p^o_{Zn}/Pa) = -5.7941 - \frac{5330.735}{T} - 0.00161644\ T + 5.59972\ \log_{10}T \qquad (3.2.12)$$

A more recent collection of thermodynamic data for the elements[8] includes no further reliable results over the temperature range of interest, although the recommended values for the vapour pressure of liquid zinc are 5% greater than those calculated

Table 3.1

Evaporation of Zinc in Hydrogen from an MEM Bottle, having nominal channel dimensions l = 0.02 m, and d = 0.002 m.

T/K	$10^9 \dot{w}/kgs^{-1}$	$\ln\dot{w}$
1148.8	82.675	-16.308
1148.8	83.047	-16.303
1148.8	83.047	-16.304
1141.2	72.632	-16.438
1138.0	68.762	-16.493
1137.2	68.208	-16.501
1136.4	66.507	-16.526
1130.8	59.920	-16.630
1130.8	59.169	-16.643
1130.8	60.383	-16.623
1130.8	58.575	-16.653
1112.9	44.177	-16.935
1112.9	44.587	-16.926
1112.1	43.763	-16.944
1112.1	42.820	-16.966
1111.0	42.036	-16.985
1111.0	42.238	-16.980
1110.2	41.597	-16.995
1110.2	41.434	-16.999
1061.4	19.415	-17.757
1061.4	19.402	-17.758
1061.1	19.415	-17.757
1059.4	19.116	-17.773
1060.7	19.420	-17.757
1060.7	19.461	-17.755
1060.7	19.495	-17.753
1060.7	19.558	-17.750

Table 3.1 continued

T/K	$10^9 \dot{w}/kgs^{-1}$	ln$\dot{w}$
1040.2	14.386	-18.057
1042.2	14.422	-18.054
1042.2	14.379	-18.058
1042.2	14.439	-18.053
991.8	6.619	-18.833
991.8	6.611	-18.835
991.8	6.612	-18.834
991.8	6.612	-18.835
989.4	6.410	-18.865
989.4	6.439	-18.861
989.4	6.494	-18.852
988.9	6.344	-18.876
958.2	3.900	-19.364
958.2	3.959	-19.347
958.2	3.929	-19.355
958.2	3.957	-19.348
944.1	3.074	-19.600
941.5	2.939	-19.645
941.5	2.935	-19.647
941.5	2.934	-19.647
916.2	1.863	-20.101
916.2	1.851	-20.107
911.9	1.716	-20.184
911.9	1.715	-20.184
911.8	1.718	-20.182
888.2	1.118	-20.611
888.2	1.116	-20.614
888.2	1.117	-20.612
869.2	0.776	-20.977
869.2	0.775	-20.978
869.2	0.773	-20.981

Table 3.1 continued

T/K	$10^9 \dot{w}/kgs^{-1}$	$\ln\dot{w}$
865.2	0.691	-21.093
864.1	0.700	-21.080
821.3	0.279	-22.001
821.3	0.280	-21.998
821.3	0.280	-21.996

Fig 3.2 Evaporation of Zinc
Graph of $\ln(\dot{w}/kgs^{-1})$ v $10^4 K/T$
Over the Temperature Range, 820 to 1150 K.

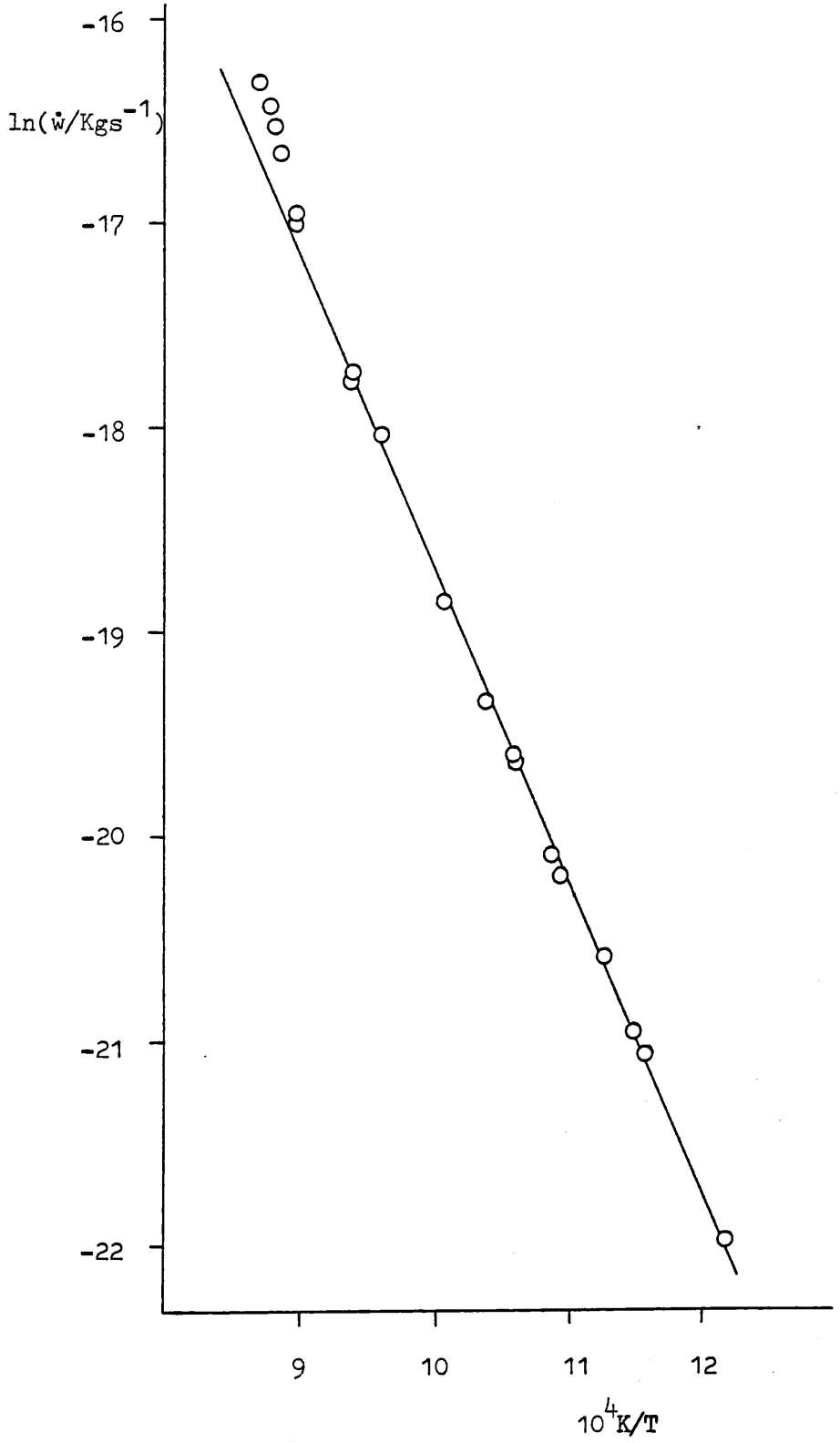

using the above equation.

Assuming the equilibrium vapour pressures of liquid zinc to be accurately represented by equation 3.2.12, values of D(T) for zinc in hydrogen were obtained by substitution in equations 3.2.11.

The temperature dependence of the diffusion coefficient was included by fitting the experimental results to the expression,

$$D_T = D_o(T/T_o)^{1+s}$$

where D_o is the diffusion coefficient at some arbitary reference temperature, T_o, chosen here as 273.15 K, and s is a constant usually between .5 and 1. The inverse pressure dependence of the diffusion coefficient could also have been included, but the small fluctuations in atmospheric pressure during the course of the experiment caused changes in D that were within the random scatter of the results.

Table 3.2 contains values of T, ξ, $\dot{w}$, and D_T calculated using equations 3.2.11 and 3.2.12. These results are illustrated in fig 3.3 as a plot of $\ln D_T$ against $\ln T$. The slope of the graph yields a value of 1+s, and D_o may be extracted from the intercept. The following formula was derived:

$$D_T/m^2s^{-1} = 5.23 \times 10^{-5} (T/273.15)^{1.72}$$
$$T/K = 820 - 1060 \text{ K}$$

The uncertainties in the quantities 1+s, and D_o may be expressed as standard deviations about their respective means. The uncertainty calculated in D_o is large due to the long extrapolation to the chosen reference temperature. The standard deviation of the slope, 1+s, is calculated to be 0.02 and in the intercept 0.14.

Table 3.2

Diffusion Data for Zinc in Hydrogen.

T/K	lnT	ξ	$10^9 \dot{w}/kgs^{-1}$	$10^4 D_T/m^2s^{-1}$	$\ln D_T$
1141.2	7.0398	1.0150	72.632	6.270	-7.375
1138.0	7.0370	0.9582	68.762	6.269	-7.372
1137.2	7.0364	0.9453	68.208	6.299	-7.370
1136.4	7.0356	0.9314	66.507	6.228	-7.381
1130.8	7.0307	0.8404	59.169	6.111	-7.400
1130.8	7.0307	0.8404	59.920	6.189	-7.388
1130.8	7.0307	0.8404	60.383	6.237	-7.380
1130.8	7.0307	0.8404	58.575	6.049	-7.410
1112.9	7.0147	0.6318	44.177	5.973	-7.423
1112.9	7.0147	0.6318	44.587	6.028	-7.414
1112.9	7.0147	0.6318	43.764	5.990	-7.420
1112.9	7.0147	0.6318	42.820	5.860	-7.442
1111.0	7.0130	0.6132	42.036	5.846	-7.445
1111.0	7.0130	0.6132	42.238	5.874	-7.440
1110.2	7.0123	0.6053	41.597	5.856	-7.443
1110.2	7.0123	0.6053	41.434	5.833	-7.447
1059.4	6.9655	0.2858	19.116	5.438	-7.517
1061.4	6.9673	0.2939	19.415	5.324	-7.538
1061.4	6.9673	0.2939	19.402	5.378	-7.528
1061.1	6.9671	0.2928	19.415	5.400	-7.524
1060.7	6.9667	0.2913	19.420	5.429	-7.519
1060.7	6.9667	0.2913	19.461	5.440	-7.517
1060.7	6.9667	0.2913	19.495	5.449	-7.515
1060.7	6.9667	0.2913	19.558	5.467	-7.512
1040.2	6.9472	0.2164	14.386	5.307	-7.541
1040.2	6.9472	0.2164	14.422	5.320	-7.539
1040.2	6.9472	0.2164	14.379	5.304	-7.542
1040.2	6.9472	0.2164	14.439	5.326	-7.538
991.8	6.8995	0.1057	6.619	4.766	-7.649
991.8	6.8995	0.1057	6.611	4.760	-7.650

Table 3.2 continued

T/K	lnT	ξ	$10^9 \dot{w}/kgs^{-1}$	$10^4 D_T/m^2s^{-1}$	$\ln D_T$
991.8	6.8995	0.1057	6.612	4.761	-7.650
991.8	6.8995	0.1057	6.612	4.761	-7.650
989.4	6.8971	0.1018	6.410	4.781	-7.646
989.4	6.8971	0.1018	6.439	4.802	-7.641
989.4	6.8971	0.1018	6.494	4.843	-7.633
988.9	6.8970	0.1012	6.344	4.760	-7.650
958.2	6.8651	0.0627	3.900	4.569	-7.691
958.2	6.8651	0.0627	3.959	4.646	-7.674
958.2	6.8651	0.0627	3.929	4.611	-7.682
958.2	6.8651	0.0627	3.957	4.644	-7.675
944.1	6.8502	0.0498	3.074	4.461	-7.713
941.5	6.8475	0.0478	2.939	4.446	-7.718
941.5	6.8475	0.0478	2.935	4.440	-7.720
941.5	6.8475	0.0478	2.935	4.440	-7.720
916.2	6.8202	0.0312	1.863	4.204	-7.774
916.2	6.8202	0.0312	1.851	4.178	-7.780
911.9	6.8155	0.0289	1.716	4.156	-7.786
911.9	6.8155	0.0289	1.715	4.154	-7.786
911.8	6.8154	0.0289	1.718	4.162	-7.784
888.2	6.7891	0.0189	1.118	4.026	-7.818
888.2	6.7891	0.0189	1.116	4.018	-7.820
888.2	6.7891	0.0189	1.117	4.022	-7.819
869.2	6.7675	0.0133	0.776	3.900	-7.849
869.2	6.7675	0.0133	0.775	3.895	-7.851
869.2	6.7675	0.0133	0.773	3.885	-7.853
865.2	6.763	0.0123	0.691	3.730	-7.894
864.1	6.762	0.0123	0.700	3.786	-7.879
821.3	6.711	0.0050	0.279	3.476	-7.965
821.3	6.711	0.0050	0.279	3.487	-7.961
821.3	6.711	0.0050	0.280	3.493	-7.960

Fig 3.3 Diffusion of Zinc in Hydrogen

$$D_T = 5.23 \times 10^{-5} (T/273.15)^{1.72} \quad m^2 s^{-1}$$

$$T = 820 - 1060K$$

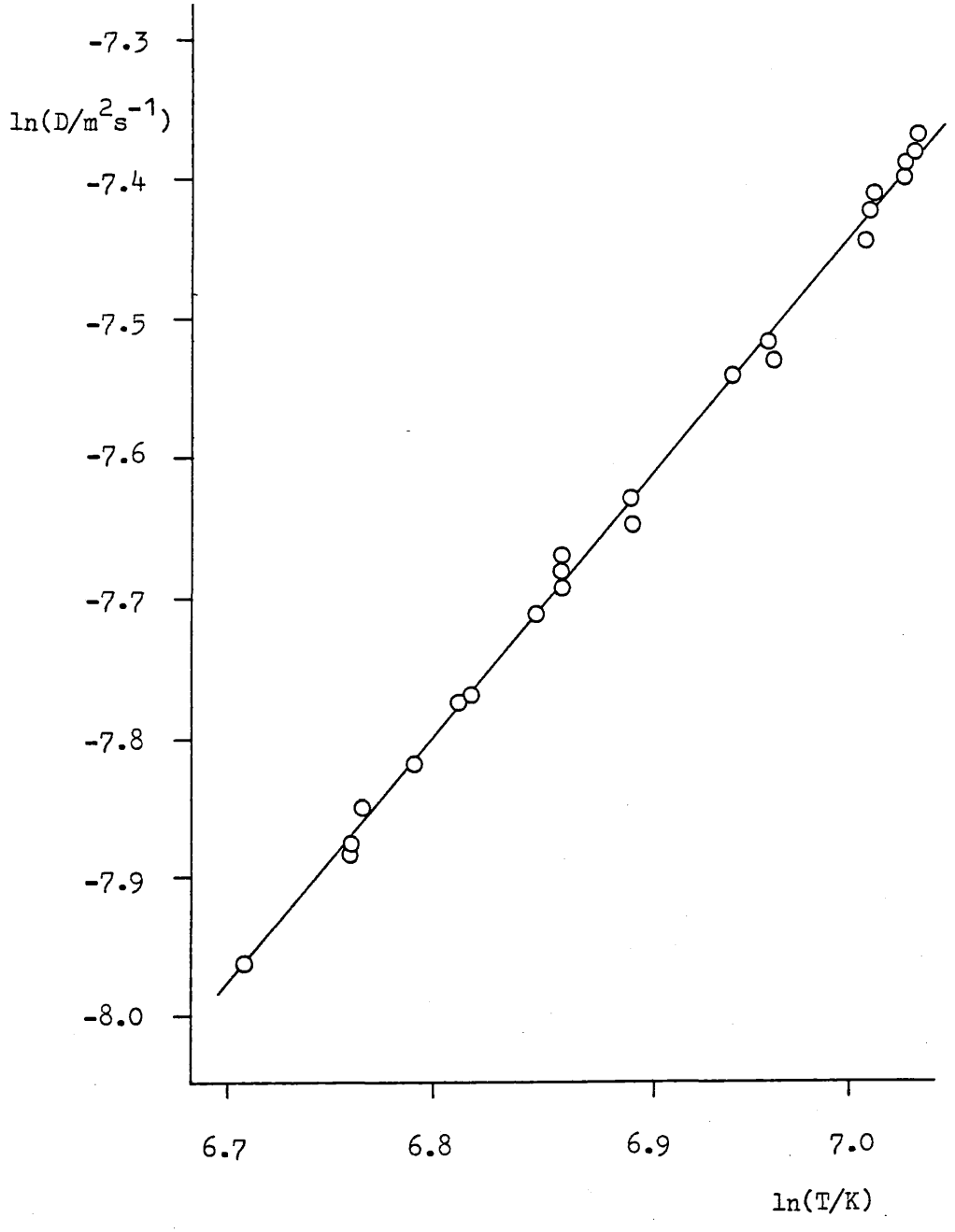

This error in the intercept gives rise to an artifically large uncertainty of ± 20% in D_T. It is therefore more useful to consider the rms error in D_T, over the experimental temperature range, which is calculated to be 0.01%.

In the upper temperature range, in excess of 1100 K, slight divergence from the expected rate of weight loss is noted. These higher values are certainly due to the breakdown of steady-state diffusion in the MEM bottle capillary. This results from the high Stefan velocity of zinc vapour in the channel at temperature approaching its boiling point, (bpt 1186 K). For this reason, only data collected below 1100 K was used in the linear regression from which the formula for D_T was extracted.

3.3 Discussion

Although hydrogen was metered into the system following delivery from a palladium diffuser some moisture is inevitably present. Since the experiment was conducted over a peroid of several days, and the sample communicating with a constant flow of hydrogen during this time, (at both elevated and ambient temperatures), the following equilibrium is relevant,

$$ZnO(c) + H_2(g) = Zn(l) + H_2O(g)$$

The standard free energy change, ΔG°, for this reaction may be expressed as follows[9],

$$\Delta G^\circ/Jmol^{-1} = 112340.4 + 47.61 \log_{10}T - 193.93\ T$$

Now $$\Delta G = \Delta G^\circ + RT\ln K_p$$

where $$K_p = \frac{a_{Zn} p_{H_2O}}{a_{ZnO} p_{H_2}}$$

Thus the position of the equilibrium may be assessed at any temperature given the moisture content of the hydrogen gas stream. Dew meter measurements would indicate the maximum water content of the hydrogen to be 20 vpm.

We have then: $p_{H_2O}/p_{H_2} = 2 \times 10^{-5}$

and $a_{Zn} = a_{ZnO} = 1$

therefore $\Delta G = \Delta G^{\circ} - 89.96(T)$

The table below (3.3) shows values of ΔG° and ΔG over a wide temperature range.

T/K	ΔG°/kJmol^{-1}	ΔG/kJmol^{-1}
300	89.5	62.5
400	84.3	48.3
500	79.6	34.6
600	75.3	21.3
700	71.4	8.4
800	67.8	-4.2
900	64.4	-16.6
1000	61.2	-28.8
1100	58.3	-40.7
1200	55.5	-52.5

It is clear from the table that over the experimental temperature range zinc oxide would be reduced by the hydrogen atmosphere. During heating the sample, when oxidation might prove a problem, the hydrogen has a beneficial influence on the equilibrium tending in accordance with Le Chatelier's principle to supress the formation of the oxide.

This work was undertaken for the purpose of validating a newly constructed MEM rig. It is therefore important to compare

these results with those obtained previously at this laboratory. From the previous work the following formula for D_T was derived;[5]

$$D_T/m^2s^{-1} = 6.86 \times 10^{-5} (T/273.15)^{1.71}$$
$$T/K = 724 - 1027\ K$$

The two values of s are in good agreement. The values of D_o differ markedly from one another, although bearing in mind the large error (≈20%) associated with D_o perhaps this is not to be unexpected.

In order to make a useful comparison between the two experiments $\ln\dot{w}/T^s$ is plotted against inverse temperature in fig 3.4. Both sets of data are plotted with many points ommitted for clarity. In both instances the data is scaled to common capillary dimensions, chosen to be, length 0.02 m and diameter 0.002 m.

The two sets of data are found to be in fair agreement. By scaling the results to a standard channel, uncertainties arising from the error in the channel conductances are, however, neccessarily introduced.

To allow visual comparison of the values of D_T obtained from this and the previous work, D_T is plotted as a function of temperature in fig 3.5. The open circles represent this work, the filled circles the upper limit. The open squares represent the previous work, and the filled-in squares the lower limit.

A further comparison is made in table 3.4 and fig 3.6, between varicus empirically and theoretically determined expresions for D_T.

The experimental results observed in this work using the Cahn R-100 electrobalance produce the lowest values of D_T, and as already shown may be considered to overlap the values determined

Fig 3.4 Correlation of Results

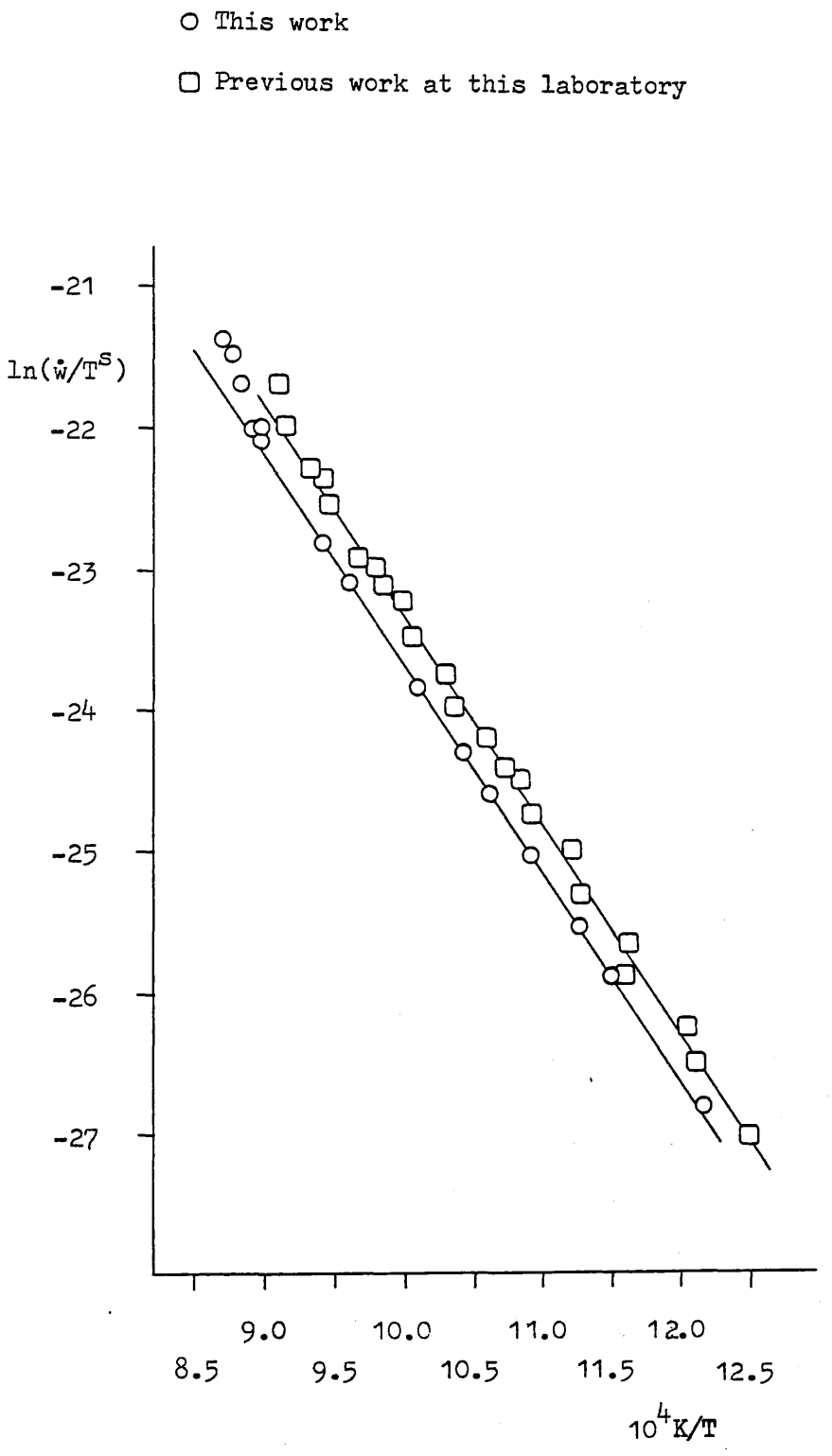

Fig 3.5 Diffusion Coefficient of Zinc in Hydrogen

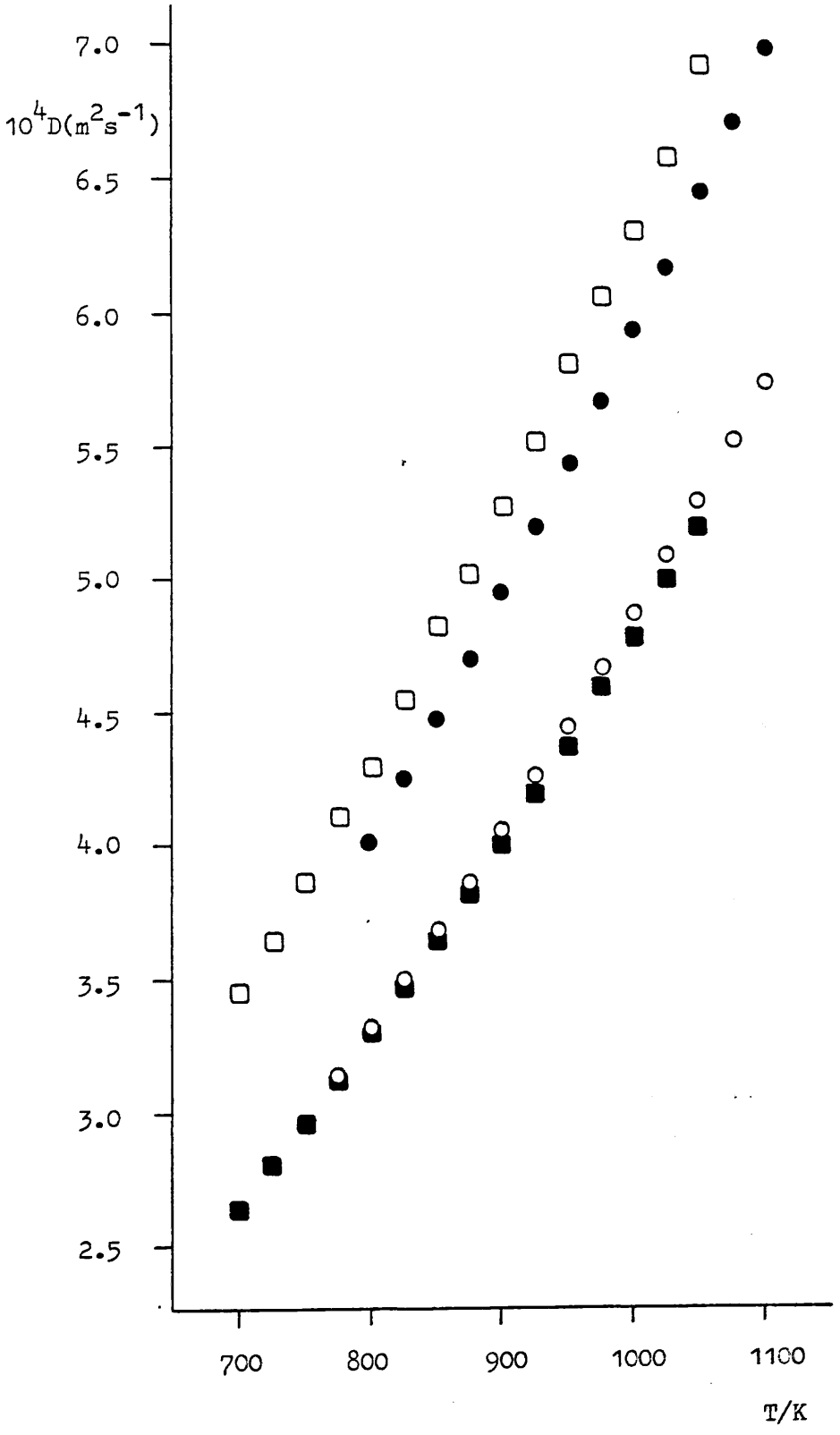

Table 3.4

A Comparison Between Empirically and Theoretically Determined Values of D_T, for Zinc in Hydrogen.

$10^5 D_o/m^2 s^{-1}$	(1+s)	$10^4 D_T/m^2 s^{-1}$	source	line
6.86	1.709	6.31	ref 5*	1
5.87	1.718	5.45	ref 10*	2
7.70	1.5	5.40	upper limit hard spheres calc^n	3
5.46	1.731	5.16	ref 11**	4
7.23	1.5	5.0	lower limit hard spheres calc^n	5
5.23	1.72	4.89	this work	6

T = 1000 K

previously at this laboratory. Recently the evaporation of zinc in hydrogen has been re-evaluated using the Cahn RG balance, these results are illustrated by line 2 of fig 3.6. The correlation between the results represented by lines 2 and 6 is evidently closer than that between lines 1 & 6. Theoretical calculations assuming a hard-spheres collision model are represented by lines 3 and 5. Estimation of the diffusion coefficient from the mass scaling of results for Ne/H_2 produce a line falling between the results obtained using the RG and R-100 balances.

In view of the close correlation between the coefficients calculated from expressions 2-6 at 1000 K, (5.18 ± 0.3 $m^2 s^{-1}$), the two MEM systems incorporating the Cahn RG and R-100 balances are considered to be in good and reliable agreement.

* These experimental data were obtained at this laboratory using a Cahn RG electrobalance.

** This data is calculated using a Graham's law scaling of values for the diffusion of Ne in H_2.

Fig 3.6 Graph of $\ln D_T$ v $\ln T$ for the Diffusion of Zinc in Hydrogen over the Temperature Range 810 to 1100 K.

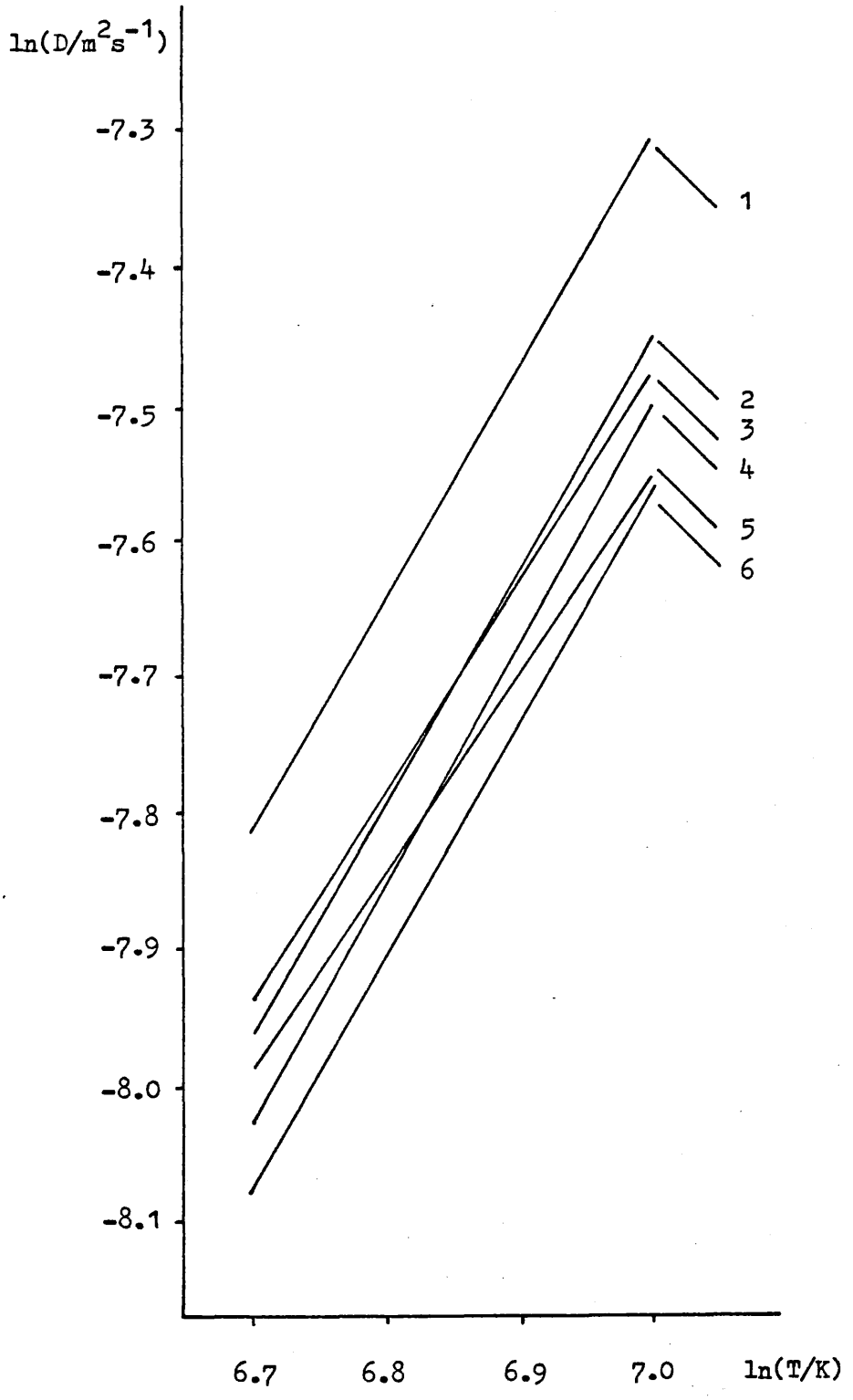

REFERENCES TO CHAPTER THREE

3.1 D. Battat, M.M. Faktor, J. Garrett and R.H. Moss, J. Chem. Soc. Faraday I, 70, 2302 (1974)

3.2 M.M. Faktor and J. Garrett, J. Cryst. Growth 38, 213 (1977)

3.3 E.J. Tarbox, PhD Thesis London (1977)

3.4 E. Battat, M.M. Faktor, J. Garrett and R.H. Moss, J. Chem. Soc Faraday I, 70, 2267 (1974)

3.5 A. Finch, P.J. Gardner, E.J. Tarbox and S.W. Yardley, J. Chem. Soc. Faraday I, 75, 545 (979)

3.6 J. Stefan, Annalen der Physik und Chemie, 17, 550 (1890)

3.7 A.N. Nesmeyanou, Vapour Pressure of the Chemical Elements (Elsevier, 1963)

3.8 R. Hultgren, P. Desai, D.T. Hawkins, M. Gleiser, K.K. Kelley and D.D. Wagmore, Selected Values of the Thermodynamic Properties of the Elements (American Society for Metals, 1975)

3.9 O. Kubaschewski, E.L. Evans and C.B. Alcock, Metallurgical Thermochemistry (Pergamon Press, 1967)

3.10 B.M. de Largy, to be published

3.11 T.R. Marrero and E.A. Mason, J. Chem. Phys. Ref. Data 1 (1972)

CHAPTER FOUR

Chemical Vapour Transport of Gallium Phosphide.

4.1 Introduction

Chemical vapour transport of gallium phosphide employing hydrogen chloride and hydrogen bromide as transporting agents has been studied using the modified entrainment method at this laboratory[1]. The results obtained using an apparatus previously described[2], appear at the end of this chapter.

Experimentally, the rate of weight loss is measured from a sample as a function of temperature. The results may be usefully visualised as a plot of $\ln\left[\dot{w}/kg\ e^{-1}\right]$ versus $1/(T/K)$.

Figure 4.1 displays a schematic representation typical of many MEM studies. Over a wide temperature range, spanning several hundred K, the graph is linear. Towards the highest temperatures, the rate of weight loss increases less rapidly. At the highest temperatures the curvature may be explained by diffusion limitation, since the equilibrium constant for the transport reaction is becoming large, and the rate of weight loss is determined by the flux of transporting gas down the channel of the reaction capsule. Ultimately, the slope in this region reflects the temperature dependence of the diffusion coefficient of the **transporting gas in the carrier gas.**

The modified entrainment method described here has been applied to the study of numerous heterogenous reaction equilibria involving binary III - V semiconductors[2,3,4,5]. Results for the systems GaAs/HCl, GaAs/HBr, as well as GaP/HBr display the

Fig 4.1 Typical plot of $\ln\dot{w}$ v 1/T

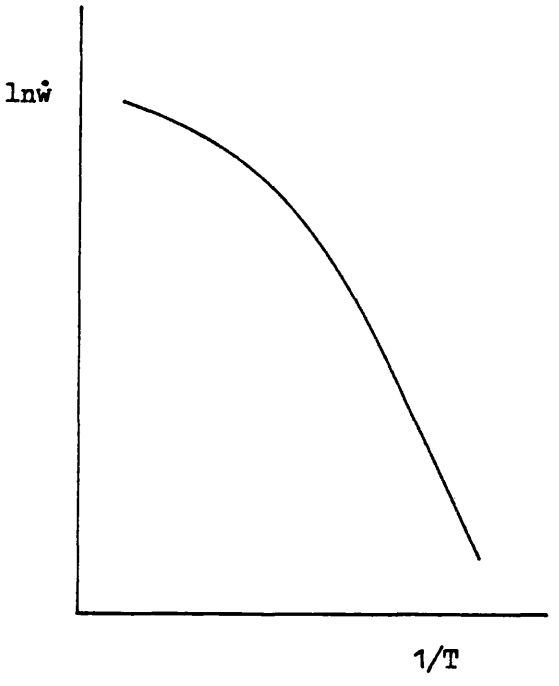

Fig 4.2 Illustration of the Type of $\ln\dot{w}$ v 1/T plot Obtained in some Systems

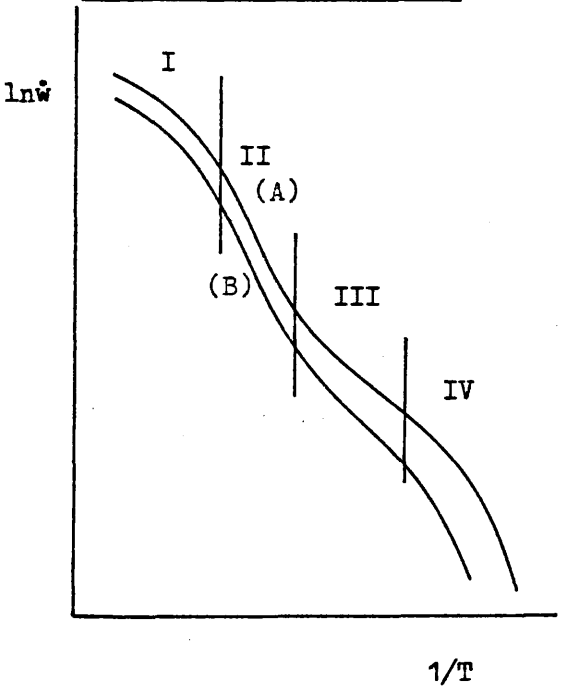

features illustrated in fig 4.2. This diagram may be divided into four regions, I - IV. The existance of these four regions is interpreted in the following manner: At high temperatures, (region I), the equilibrium constant for the dominant reaction is large, and diffusion becomes a limiting factor as explained above. Over the next temperature interval, labelled region II, the graph is linear. This represents the participation of a dominant transport reaction involving the formation of the metal monohalide:

$$MA(c) + HX(g) = MX(g) + \tfrac{1}{4}P_4(g) + \tfrac{1}{2}H_2(g) \qquad (4.1.1)$$

In this region, equilibrium partial pressures prevail in the bottle, and the slope of the graph **reflects the temperature dependence of the equilibrium constant of this dominating transport reaction.**

Region III spans a temperature range where mass transfer is dominated by a second CVT reaction,usually of larger stoichoimetry than the first. Again, equilibrium partial pressures obtain in the bottle, and the slope of the graph reflects the temperature dependence of the equilibrium constant of this second participating reaction.

Since the formation of the metal trihalides in such systems are generally exothermic reactions, the participation of the dibromide is invoked.

$$MA(c) + 2HX(g) = MX_2(g) + \tfrac{1}{4}P_4(g) + H_2(g) \qquad (4.1.2)$$

or

$$MA(c) + 2HX(g) = \tfrac{1}{2}(M_2X_4)(g) + \tfrac{1}{4}P_4(g) + H_2(g) \qquad (4.1.3)$$

Finally, the low temperature portion of the graph

depicted by region IV, again displays marked curvature. In this region, the rates of weight loss are found to be time dependant as well as a function of temperature. At these moderate temperatures it is belived that equilibrium partial pressures are not approached in the bottle, and that surface kinetics dictate the observed rate of weight loss[2].

Care should be taken when interpreting the results from MEM studies. Representing the results in the usual manner, ($\ln\dot{w}$ vs $1/T$), the graph may or may not display each of the features outlined above. The need for cautious interpretation is illustrated in the analysis of the gallium phosphide : hydrogen bromide system. Some of the pitfalls that may lead to erroneous conclusions are discussed later in this chapter.

The abrupt kink in the lines in the intermediate temperature range separates two regions where transport is dominated by two different chemical vapour transport reactions. An experiment yielding a line such as that in A (a single value of ε), permits the interpretation that a different chemical reaction is involved at high temperatures from that at low, and that both reactions are endothermic. Insufficient information may be extracted from a single experiment in order to infer any relationship between the relative stoichiometries of the species involved. An explanation of the change in slope may be sought in the dissociation of As_4, or P_4, or of polymeric GaCl (or GaBr).

A second experiment performed with a lower value of ε may yield, as for the systems mentioned, results illustrated by line B. In repeating the experiment at a second value of ε, the relative separation of lines A and B at high temperatures is

constant, within experimental error, and takes a larger, (not quite constant) value over the low temperature region. This may only be explained by invoking the participation of a second transport reaction, at lower temperature, involving the formation of a metal halide species of different metal : halogen ratio from that at a higher temperature.

Consider the generalised chemical reaction:

$$M(c) + nHX(g) = MX_n(g) + \tfrac{1}{2}nH_2(g) \qquad (4.1.4)$$

where n may take the values 1,2,3 or 4. Intuitively, the most probable value for n may be predicted having selected the metal.

The transport equations for the various vapour species may be written:

$$J_M = J = J_{MX_n} = \frac{UP_{MX_n}}{RT} - \frac{DdP_{MX_n}}{RTdx} \qquad (4.1.5)$$

$$J_{H_2} = \tfrac{1}{2}nJ = \frac{UP_{H_2}}{RT} - \frac{DdP_{H_2}}{RTdx} \qquad (4.1.6)$$

$$J_{HX} = -nJ = \frac{UP_{HX}}{RT} - \frac{DdP_{HX}}{RTdx} \qquad (4.1.7)$$

For simplicity the same diffusion coefficient is used for each species. Summing equations 4.1.5 - 4.1.7:

$$mJ = \frac{UP}{RT} \qquad (4.1.8)$$

where $$m = 1 - \tfrac{1}{2}n \qquad (4.1.9)$$

Thus, on substituting for U in equations 4.1.5 - 4.1.7:

$$J = m\frac{JP_{MX_n}}{P} - \frac{DdP_{MX_n}}{RTdx} \qquad (4.1.10)$$

$$\tfrac{1}{2}J = m\frac{JP_{H_2}}{P} - \frac{DdP_{H_2}}{RTdx} \qquad (4.1.11)$$

$$-nJ = m\frac{JP_{HX}}{P} - \frac{DdP_{HX}}{RTdx} \qquad (4.1.12)$$

Integrating from x=0, to x=1 (NB at the channel exit, $P_{MX}(1) = 0$)

$$p^{(0)}_{MX_n} = \frac{P}{m}(1 - \exp(-m\xi)) \qquad (4.1.13)$$

$$p^{(0)}_{H_2} = \frac{P}{m}\tfrac{1}{2}n - (\tfrac{1}{2}n - m\frac{p^{(1)}_{H_2}}{P})\exp(-m\xi) \qquad (4.1.14)$$

and

$$p^{(0)}_{HX} = \frac{P}{m}(n + m\frac{p^{(1)}_{HX}}{P})\exp(-m\xi) - m\xi \qquad (4.1.15)$$

where

$$\xi = \frac{JRTl}{DAP}$$

Now since $p_{HX}/P \ll 1$ (and hence $\xi \ll 1$) equations 4.1.13 - 4.1.15 may be simplified:

$$p^{(0)}_{MX_n} = P\xi \qquad (4.1.16)$$

$$p^{(0)}_{HX} = P(\varepsilon - n\xi) \qquad (4.1.17)$$

where

$$= \frac{p^{(1)}_{HX}}{P}$$

finally, we assume that the partial pressure of the carrier gas, hydrogen, is equal to the total pressure, so

$$\frac{p^{(0)}_{H_2}}{P} = 1 \qquad (4.1.18)$$

The general equation for the equilibrium constant, of reaction 4.1.4, is thus:

$$K_p = \frac{P_\xi}{\left[\varepsilon - n\xi\right]^n} \qquad (4.1.19)$$

When $K_p \ll 1$ (and hence $\xi \ll \varepsilon$) 4.1.19 may be simplified to give:

$$K_p = \frac{P_\xi}{\varepsilon^n}$$

Substituting for K_p and taking logarithms then the following expression is obtained:

$$(\frac{\Delta H}{R})\frac{1}{T} = \ln P_\xi - \left[n\ln\varepsilon - \frac{\Delta S}{R}\right] \qquad (4.1.20)$$

similarly simplification may be achieved when $K_p \gg 1$,

from 4.1.4 $$P^{(0)}_{MX_n} \approx \varepsilon/n \qquad (4.1.21)$$

therefore $$P \approx \varepsilon/n \qquad (4.1.22)$$

or $$\ln P_\xi = \ln\varepsilon - \ln n \qquad (4.1.23)$$

In theory, the value of n can be obtained directly from 4.1.22. Two difficulties belie this approach: firstly, it may not be possible to attain sufficiently elevated temperatures whereby equation 4.1.22 is appropriate, and secondly, any error in the physical constants used will distort the derived information. A more rational approach is then adopted where ε, the partial pressure of HX, is altered. If $(P^{(o)}_{HX}/P)$ were doubled, when $K \gg 1$, the effect will be to displace the $\ln\dot{w}$ vs $1/T$ plot by $\ln 2$. When $K \ll 1$, the displacement is $n\ln 2$. Thus, at temperatures where $K \ll 1$ it is possible to establish the value of n by the extent to which the trace is displaced by increasing or decreasing ε.

4.2 Results

The results of this study, using both 0.001 m and 0.002 m diameter channels are represented in figures 4.3 and 4.4. A total of eight experiments were performed; four with each reaction transport gas. Both systems (GaP/HCl and GaP/HBr) were studied using two values for the partial pressure of reactive gas, $p_{HX}^{(1)}/P$, this dimensionless quantity shall be denoted by the greek symbol ε. Both values for ε were used with each of the two chosen capillaries.

Values of ε for hydrogen chloride were calculated using the following expression to determine the flow rate[2]:

$$\text{flow rate } y/dm^3s^{-1} = 6.6796 \times 10^{-6}(x/mm) + 8.096 \times 10^{-5} \quad (4.2.1)$$

where x is the float height.

and those for hydrogen were taken from the same source[2].

4.3 Analysis of results.

Now in chapter three, it was shown that for the evaporation of a single species:

$$p_A^o = P(1 - e^{-\xi}) \quad (4.3.1)$$

In order to consider a hetrogeneous reaction equilibrium of the form:

$$MA(s) + HX(g) = MX(g) + \tfrac{1}{4}A_4(g) + \tfrac{1}{2}H_2(g) \quad (4.3.2)$$

further development of the theory is required.

Recall equation 3.2.9:

$$\frac{p_i^o}{P} = \frac{J_i}{J} + \frac{p_i^{(1)}}{P} - \frac{J_i}{J} e^{-\xi_i} \quad (4.3.3)$$

Fig 4.3 Graphs of $\ln\dot{w}$ v 1/T for Gallium Phosphide Using Hydrogen Chloride as the Reactive Gas.

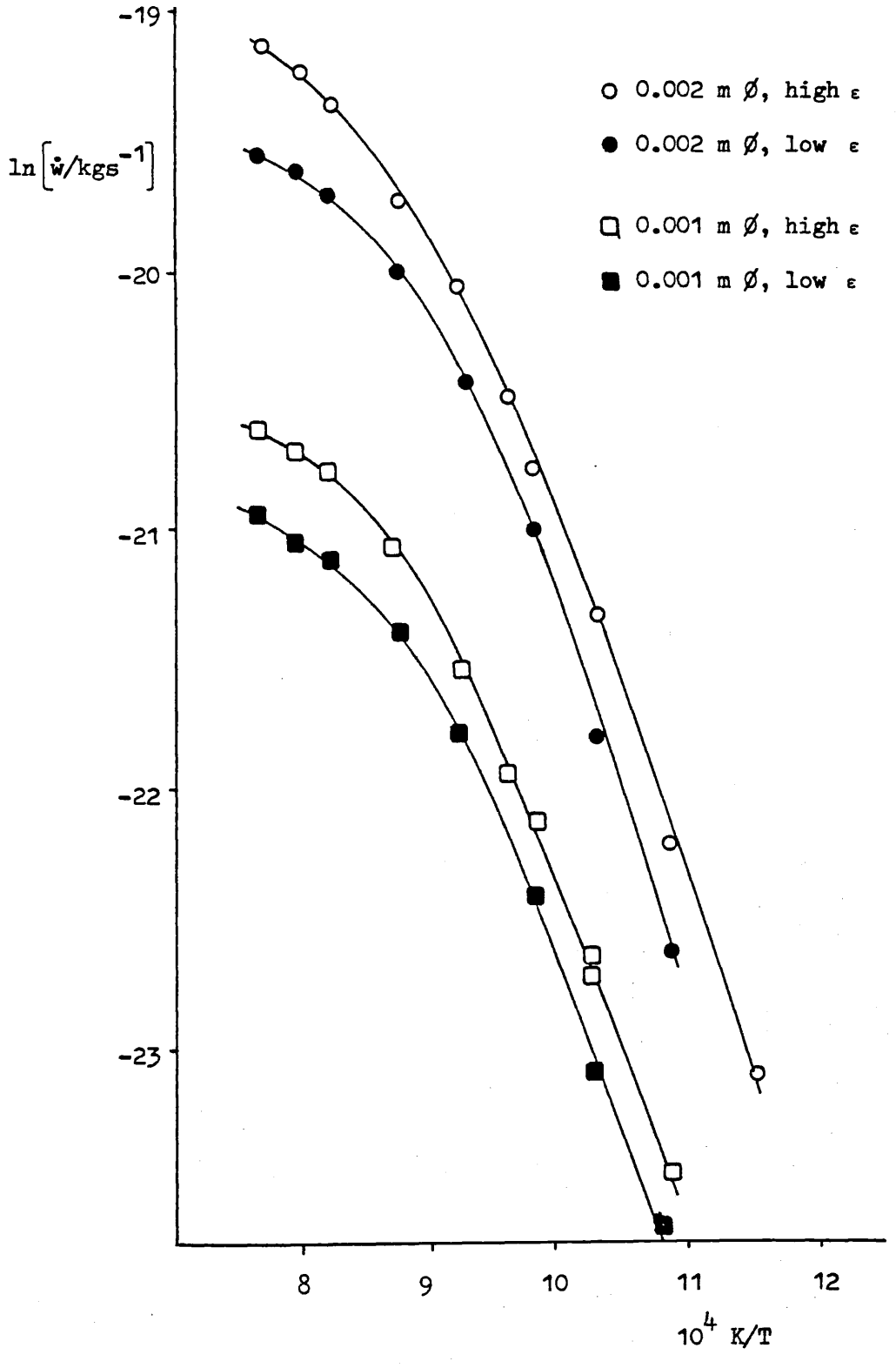

Fig 4.4 Graphs of $\ln \dot{w}$ v 1/T for Gallium Phosphide Using Hydrogen Bromide as the Reactive Gas.

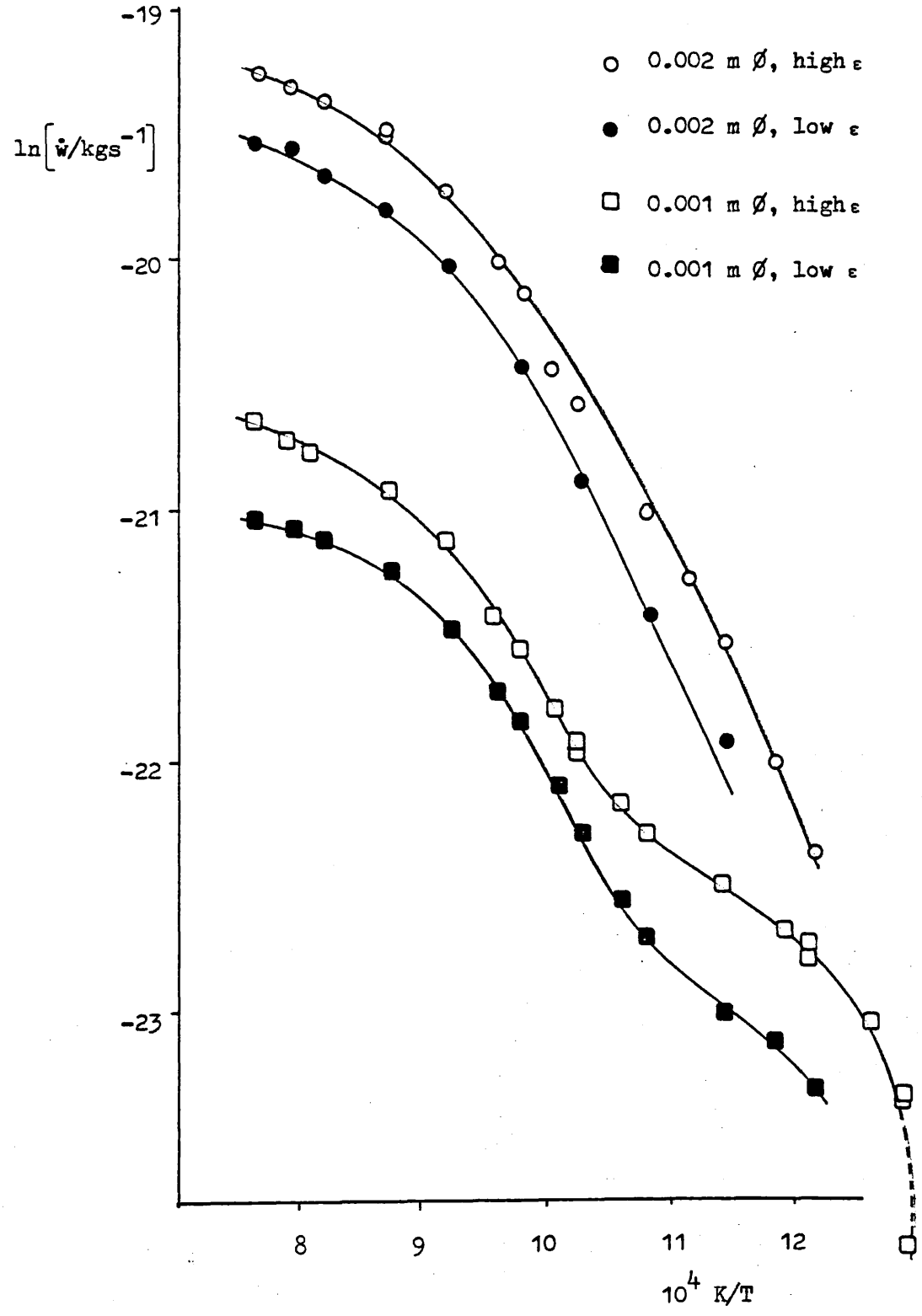

now ξ, the transport function, is at most the order of ε thus $\xi \ll 1$ and 4.3.3 may be rewritten as:

$$\frac{p_i^o}{P} = \frac{J_i}{J} + \frac{p_i^{(1)}}{P} - \frac{J_i}{J}(1-\xi_i) \qquad (4.3.4)$$

in this one-dimensional model $p_i^{(1)}/P$ is a boundary condition and is zero for a minority species.

Hence $$\frac{p_i^{(0)}}{P} = \frac{J_i}{J}\xi_i \qquad (4.3.5)$$

The results obtained for the transport of gallium phosphide using hydrogen chloride are interpreted as being dominated by a single CVT reaction over the whole temperature range studied. The system involving hydrogen bromide indicates that two reactions compete over the temperature range of interest.

When a single transport reaction is invoked in order to interpret the MEM results the scheme of analysis shall be referred to as "scheme - 1". Chemical intuition would suggest that the following reactions should be considered when dealing with the GaP : HCl system,

$$GaP(s) + HCl(g) = GaCl(g) + \tfrac{1}{4}P_4(g) + \tfrac{1}{2}H_2(g) \qquad (4.3.6)$$

$$P_4(g) = 2P_2(g) \qquad (4.3.7)$$

The equilibrium constant for reaction 4.3.6 may be written as:

$$K_1 = \frac{p^o_{GaCl}\,(p^o_{P_4})^{\frac{1}{4}}\,p^{o\,\frac{1}{2}}_{H_2}}{p^o_{HCl}\,P^{\frac{1}{4}}} \qquad (4.3.8)$$

Similarly for reaction 4.3.7

$$K_4 = p^{o\,2}_{P_2}/p^o_{P_4}P \qquad (4.3.9)$$

Now let the ratio of the fluxes of P_2 and P_4 be denoted by α:

Then $$\alpha = \frac{J_{P_2}}{J_{P_4}} \qquad (4.3.10)$$

Considering the conservation of mass, in respect to the transport fluxes, it is seen that:

for hydrogen $$J_{HCl} + 2J_{H_2} = 0 \qquad (i)$$

for chlorine $$J_{HCl} + J_{GaCl} = 0 \qquad (ii)$$

and $$J_{GaCl} = 4J_{P_4} + 2J_{P_2} = J_{GaP} \qquad (iii)$$

so $$J_{GaCl} = -J_{HCl} \qquad (iv)$$

$$\Sigma_i J_i = J_{HCl} + J_{H_2} + J_{P_2} + J_{P_4} + J_{GaCl} = J \qquad (v)$$

Thus: $$J_{H_2} = -\tfrac{1}{2}J_{HCl} \qquad (vi)$$

$$J_{HCl} = -J_{GaCl} \qquad (vii)$$

$$J_{GaCl} = J_{P_4}(4+2\alpha) = -J_{HCl} \qquad (viii)$$

so $$J_{P_4} = -\frac{J_{HCl}}{4+2\alpha} \qquad (ix)$$

and $$J_{P_2} = -\frac{J_{HCl}}{4+2\alpha}\,\alpha \qquad (x)$$

from (v) - (x) it is seen that (v) may be rewritten as

$$J = J_{HCl} - \frac{J_{HCl}}{2} - \frac{J_{HCl}}{4+2\alpha} - \frac{J_{HCl}\alpha}{4+2\alpha} - J_{HCl}$$

$$= J_{HCl}\left[-\tfrac{1}{2} - \left(\frac{1+\alpha}{4+2\alpha}\right)\right]$$

so $$\frac{J}{J_{HCl}} = \frac{-(2+\alpha) - (1+\alpha)}{4+2\alpha}$$

$$= - \frac{3+2\alpha}{4+2\alpha}$$

and hence $$\frac{J_{HCl}}{J} = - \frac{4+2\alpha}{3+2\alpha} \qquad \text{(xi)}$$

using (vi) - (x) and 4.3.5 the following equalities may be written.

$$\frac{p^{o}_{GaCl}}{P} = \frac{J_{GaCl}}{J} \xi_{GaCl} \qquad \text{(xii)}$$

$$\frac{p^{o}_{P_2}}{P} = \frac{J_{P_2}}{J} \xi_{P_2} \qquad \text{(xiii)}$$

$$\frac{p^{o}_{P_4}}{P} = \frac{J_{P_4}}{J} \xi_{P_4} \qquad \text{(xiv)}$$

$$\frac{p^{o}_{HCl}}{P} = \varepsilon + \frac{J_{HCl}}{J} \xi_{HCl} \qquad \text{(xv)}$$

$$\frac{p^{o}_{H_2}}{P} = 1 - \varepsilon \qquad \text{(xvi)}$$

but $$= \frac{JRTl}{PD_{(i,H_2)}} = \frac{J_{GaP}RTl}{PD_{(i,H_2)}} = \frac{J}{J_{GaP}}$$

$$= \underbrace{\frac{\dot{w}_{GaP}RTl}{AM_{GaP}PD_{(i,H_2)}}} \frac{3+2\alpha}{4+2\alpha} \qquad \text{(xvii)}$$

$$\bar{\xi}$$

where $\bar{\xi}_i$ is the reduced transport function of the i^{th} species.

(xii) - (xvi) may then be written:

$$\frac{p^{o}_{GaCl}}{P} = \bar{\xi}_{GaCl} \qquad \text{(xviii)}$$

$$\frac{p^{o}_{P_4}}{P} = \bar{\xi}_{P_4} \frac{1}{4+2\alpha} \qquad \text{(xix)}$$

$$\frac{p^{o}_{P_2}}{P} = \bar{\xi}_{P_2} \frac{\alpha}{4+2} \qquad \text{(xx)}$$

$$\frac{p^{o}_{HBr}}{P} = \varepsilon - \bar{\xi}_{HBr} \qquad \text{(xxi)}$$

The partial pressures in the equilibrium constant K_1 may now be replaced by expressions, $(f(\dot{w}))$, involving the reduced transport functions of the gasous species.

$$K_1 = \frac{\bar{\xi}_{GaCl} \left[1/(4+2\alpha)\ \bar{\xi}_{P_4}\right]^{\frac{1}{4}} (1-\varepsilon)^{\frac{1}{2}}}{\varepsilon - \bar{\xi}_{HCl}} \qquad (4.3.11)$$

In the systems considered here the lengthy and rigorous treatment of multicomponent diffusion[6] is not applied. Having confined the analysis to a system where one component is present in large excess it is permissible to consider the diffusion of each minority species in the majority species as an independent binary diffusion system. Such treatment may be justified for both ternary[7] and quarternary[8] systems. Second-order corrections to the binary diffusion coefficients may then be employed to more fully account for multicomponent diffusion. This may be applied in the following manner,[8]

$$\frac{p^{o}_{i}}{P} = \gamma_i \xi_i \frac{J_i}{J} \qquad (4.3.12)$$

$$\frac{p^{o}_{m_i}}{P} = \varepsilon + \gamma_{m_i} \xi_{m_i} \frac{J_{m_i}}{J} \qquad (4.3.13)$$

where γ_i and γ_{m_i} are the corrections for the minority species, (γ_{m_i} for the reactive gas). These corrections take the analytical forms:

$$\gamma_i = a_i - (1 - c_i)\,\xi_i/2 \qquad (4.3.14)$$

and

$$\gamma_{m_i} = a_{m_i} - (1 - c_{m_i})\,\xi_{m_i}/2 - \frac{J}{\xi_{m_i}} \qquad (4.3.15)$$

The expressions that form the coefficients a and c appear in appendix 3.

When CVT occurs via a single chemical equilibrium then $\bar{\xi}_i$ is proportional to ξ and J is proportional to $\dot{w}/AM$. However if a further reaction is involved, for example phosphorus dissociation, then the relationship between J and $\dot{w}$ becomes a function of α.

The British Telecoms derived programs[2] used previously express the term α as a function of the **reduced transport function of P_2, ξ_{P2}.**

$$K_4 = \frac{p^{o2}_{P_2}}{p^{o}_{P_4} P} = \frac{\bar{\xi}^2_{P_2}}{\bar{\xi}_{P_4}} \frac{\alpha^2}{4 + 2\alpha}$$

$$= \frac{D_{(P_4,H_2)}}{D_{(P_2,H_2)}} \frac{\bar{\xi}_{P_2}{}^2 \alpha^2}{4 + 2\alpha}$$

therefore

$$\frac{4 + 2\alpha}{3 + 2\alpha} = \frac{D_{(P_4,H_2)}}{D_{(P_2,H_2)}} \frac{\bar{\xi}_{P_2}}{K_4} = A$$

and

$$0 = A\alpha^2 - 2\alpha - 4$$

so

$$\alpha = 1 + \frac{\sqrt{1 + 4A}}{A} \qquad (4.3.16)$$

This quantity, fundamental to the computations requires that the experimentally observed weight loss data is used in order to simulate that very data.

Two variations of the British Telecom (BT) derived programs are available. The first is called a plotting program, and the second a sig program. Once experimental data is available, a plotting program may be run to evaluate, in a rudimentary manner, the fit obtained using selected values for the entropy and enthalpy of the CVT reaction. Typically, this program would be executed using six experimental data points and three combinations of H and S. The computations performed by the program require that experimental weight-loss is supplied as input data. In order to calculate a simulated datum point at a given temperature, the soft-ware requires values of α, (and θ according to the analysis scheme) at this temperature. These values are, however, formulated as functions of ξ, and ξ in turn is a function of $\dot{w}$. This cyclic arrangement is unsatisfactory, and probably biases the calculated values towards the experimental results. In addition, this arangement precludes any attempt of predicting the outcome of experiments.

The second program option is used to obtain a "best-fit" simulation, and extract best-values of ΔH and ΔS of the CVT reaction. In this instance, the experimental results are evidently required so that the assessment of fit between the calculated and measured rates of weight-loss may be made. It remains preferable that the soft-ware does not use the experimental values a priori in the computations.

A more rigorous approach has been adopted involving the simultaneous solution of two equations to yield α and $\dot{w}$.

Before presenting the algebra, some nomenclature will be defined to allow some simplification.

chemical species	species number
H_2	1
MX	2
A_2	3
MX_2	4
A_4	5
HX	6
MA	7

so now $\alpha = j_3/j_5$

and all partial pressures may be defined in terms of $\dot{w}_7$ and α:

eg: $$\frac{p_3^o}{P} = \frac{\alpha}{4 + 2\alpha} \cdot \bar{\xi}_3$$

where $$\bar{\xi}_3 = \frac{\dot{w}_7 RTl}{D_{3,1} A M_7 P} = \frac{x}{D_{3,1}}$$

and setting $P/P^{\ominus} = 1$

the chemical equilibria under consideration are:

$$MA(c) + HX(g) = MX(g) + \tfrac{1}{4}A_4(g) + \tfrac{1}{2}H_2(g) \qquad (4.3.19)$$

$$P_4(g) = 2P_2(g) \qquad (4.3.20)$$

hence $$K_1 = \frac{x/D_2 \; (1/(4+2\alpha)).(x/D_5)^{\frac{1}{4}} \; (1-\varepsilon)^{\frac{1}{2}}}{\varepsilon - (x/D_6)} \qquad (4.3.21)$$

and $$K_4 = \frac{\alpha^2}{(4 + 2\alpha)} \frac{D_5}{D_3^2} \cdot x \qquad (4.3.22)$$

Rearranging 4.3.21

$$A_1 = \frac{K_1 D_2 D_5^{\frac{1}{4}}}{(1 - \varepsilon)^{\frac{1}{2}}} = \frac{\left[1/(4 + 2\alpha)\right]^{\frac{1}{4}} x^{\frac{5}{4}}}{\varepsilon - (x/D_6)} \qquad (4.3.23)$$

Similarly from 4.3.22

$$A_2 = K_4 D_3^2 / D_5 = \frac{\alpha^2 x}{(4 + 2\alpha)} \qquad (4.3.24)$$

Taking the 4^{th} root of 4.3.24 and dividing this into 4.3.23,

$$\frac{A_1}{A_2^{\frac{1}{4}}} = \frac{x}{\left[\varepsilon - (x/D_6)\right]\alpha^{\frac{1}{2}}} \qquad (4.3.25)$$

Now taking x from 4.3.24 and substituting in 4.3.25, the following expression is obtained:

$$C_1 \alpha^{\frac{5}{2}} - 2C_2 \alpha^{\frac{3}{2}} - 2\alpha - 4C_2 \alpha^{\frac{1}{2}} - 4\alpha = 0 \qquad (4.3.26)$$

defining $C_o = K_1 D_2 D_5^{\frac{1}{2}} / ((1-\varepsilon)^{\frac{1}{2}} K_4^{\frac{1}{4}} D_3^{\frac{1}{2}})$

then $C_1 = C_o D_5 \varepsilon / (K_4 D_3^2)$

and $C_2 = C_o / D_6$

4.3.26 may be solved for α and the value substituted in a further equation to extract x, and thus $\dot{w}_7$.

Apparently, the procedure detailed above allows the calculation of $\dot{w}_7$ independently of the experimental data. There is, however, a minor complication. This involves the corrections to the binary diffusion coefficient, that take account of multicomponent diffusion. Recall,

$$\gamma_i = a_i - (1 + c_i)\, \xi_i/2$$
$$i = 1,2\ldots5$$

and

$$\gamma_i = a_6 - (1 + c_6)\, \xi_6/2 - \varepsilon \frac{J}{j_6}$$
$$i = 6$$

it is seen that the γ_i terms are functions of $\dot{w}_7$.

In order to calculate weight loss data for simulation purposes that very data is required once again to calculate the correction terms γ_i. Although the object of the exercise was to remove such a need, it may be argued that the use to calculate γ_i is not a serious flaw.

The approach taken has been to calculate approximate values for γ_i, ignoring their dependence upon $\dot{w}_7$ and extract values $\dot{w}_7'$. Values for $\dot{w}_7'$ are then used to refine γ_i and so reiteratively refine $\dot{w}_7$ to a predetermined precision. The functions are found to be well behaved and converge rapidly. This analysis is fine for a system involving a single CVT reaction and the inclusion of the dissociation of a group V component.

It was briefly discussed at the begining of this chapter that a scheme involving a single CVT reaction does not adequately describe both the systems of interest here. A treatment taking account of a second participating CVT reaction is presented below.

The following chemical equilibria will be considered as responsible for mass transfer in this scheme 2 analysis.

$$MA(c) + HX(g) = MX(g) + \tfrac{1}{4}A_4(g) + \tfrac{1}{2}H_2(g)$$

$$MA(c) + 2HX(g) = MX_2(g) + \tfrac{1}{4}A_4(g) + H_2(g)$$

$$A_4(g) = 2A_2(g)$$

Now using the same nomenclature as previously defined:

$$\alpha = j_3/j_5 \qquad \text{and also} \qquad \theta = j_2/j_4$$

The term θ is introduced to express the ratio of the metal monohalide to the dihalide.

As in the previous case by considering the conversation of mass, in respect to the transport fluxes, the following flux relationships may be derived.

$$\frac{j_6}{J} = -\frac{(4+2\alpha)(2+\theta)}{(\alpha+1)(1+2\theta)+\theta} \qquad (a)$$

$$\frac{j_1}{J} = \frac{(2+\alpha)(2+\theta)}{(\alpha+1)(1+2\theta)+\theta} \qquad (b)$$

$$\frac{j_2}{J} = \frac{\theta(4+2\alpha)}{(\alpha+1)(1+2\theta)+\theta} \qquad (c)$$

$$\frac{j_3}{J} = \frac{\alpha(1+\theta)}{(\alpha+1)(1+2\theta)+\theta} \qquad (d)$$

$$\frac{j_4}{J} = \frac{(4+2\alpha)}{(\alpha+1)(1+2\theta)+\theta} \qquad (e)$$

$$\frac{j_5}{J} = \frac{(1+\theta)}{(\alpha+1)(1+2\theta)+\theta} \qquad (f)$$

$$\frac{j_7}{J} = \frac{(4+2\alpha)(2+\theta)}{(\alpha+1)(1+2\theta)+\theta} \qquad (g)$$

These in turn lead to expressions for the partial pressures of each species in terms of the various reduced transport functions.

$$\frac{p_1^o}{P} \approx 1-\varepsilon \qquad (h)$$

$$\frac{p_2^o}{P} = \frac{\theta}{\theta+1}\,\bar{\xi}_2 \qquad (i)$$

$$\frac{p_3^o}{P} = \frac{\alpha}{4+2\theta}\,\bar{\xi}_3 \qquad (j)$$

$$\frac{p_4^o}{P} = \frac{1}{\theta+1}\,\bar{\xi}_4 \qquad (k)$$

$$\frac{p_5^o}{P} = \frac{1}{4+2\alpha}\,\bar{\xi}_5 \qquad (l)$$

$$\frac{p_6^o}{P} = \varepsilon - \left(\frac{2+\theta}{1+\theta}\right)\bar{\xi}_6 \qquad (m)$$

Now the British Telecoms derived treatment for such a system, uses 4.3.16 to define α, further more θ is defined as a function of $\dot{w}_7$.[2] This situation is again not ideal. The aim is to solve the problem and extract calculated weight loss data without the need for the experimental data, as in the previous case.

By suitable manipulation of the algebra it is found that three equations may be written that fully describe the system using the three variables α, θ, and x. The algebra is involved and shall not be presented fully here.

Considering the three chemical equilibria already given then the equilibrium constants K_1, K_2 and K_4 may be written:

$$K_1 = \frac{\frac{\theta}{\theta+1}\cdot\frac{x}{D_2}\left[\frac{1}{4+2\alpha}\frac{x}{D_5}\right]^{\frac{1}{4}}(1-\varepsilon)^{\frac{1}{2}}}{\varepsilon - \frac{\theta+2}{\theta+1}\frac{x}{D_6}} \qquad (4.3.27)$$

$$K_2 = \frac{\alpha^2}{4+2\alpha}\,\frac{D_5}{D_3^2}\,x \qquad (4.3.28)$$

$$K_4 = \frac{D_2}{D_4}\,\frac{(1-\varepsilon)^{\frac{1}{2}}}{\theta} \Big/ \left[\varepsilon - \frac{\theta+2}{\theta+1}\frac{x}{D_6}\right] \qquad (4.3.29)$$

Rearranging the above three equations in turn,

$$K_1 D_2 D_5^{\frac{1}{4}}/(1-\varepsilon)^{\frac{1}{2}} = A = \frac{\frac{\theta}{\theta+1} x \left[\frac{1}{4+2\alpha} x\right]^{\frac{1}{4}}}{\varepsilon - \frac{\theta+2}{\theta+1} \frac{x}{D_6}} \qquad (4.3.30)$$

$$K_2 D_3^2/D_5 = B = \frac{\alpha^2 x}{4+2\alpha} \qquad (4.3.31)$$

$$K_4 \frac{D_4}{D_2} \frac{1}{(1-\varepsilon)^{\frac{1}{2}}} = C = \frac{1}{\theta\left[\varepsilon - \frac{\theta+2}{\theta+1} \frac{x}{D_6}\right]} \qquad (4.3.32)$$

A,B,and C represent the three simultaneous equations which when solved will yield α, θ, and x.

$$Af(\alpha,\theta,x)$$

$$Bf(\alpha,x)$$

$$Cf(\theta,x)$$

A polynomial in θ may be derived from the above equations:

$$a_0 + a_1\theta + a_2\theta^2 + a_3\theta^3 + a_4\theta^4 + a_5\theta^5 + a_6\theta^6 + a_7\theta^7 + a_8\theta^8 + a_9\theta^9 + a_{10}\theta^{10} + a_{11}\theta^{11} = 0$$

The detailed form of various coefficients appearing in the 11^{th} order polynomial derived are collected in appendix 3, within the computer software.

Any computer program written to analyse a system according to scheme-1 or 2 may be used simply to calculate the rate of loss, from a given sample, as a function of temperature. It may also be written not only to perform the above, but also to compare the computed with experimental data. The fit between simulated and experimental points may be refined in a reiterative manner.

The criterion used to assess the integrity of fit is denoted by σ, and is defined in appendix 3.

4.4 Thermodynamic data.

Now the computer aided analysis presented has as input data, values for the enthalpies and entropies of the reactions participating in vapour transport. Values for these quantities must be obtained from a critical evaluation of literature data.

Below in table 4.1 are collected relevent thermodynamic parameters required in the estimation of ΔH_{1000} and ΔS_{1000} for the participating chemical reactions.

Table 4.1

Species	ΔH_f^o/kJ mol^{-1}	S_f^o/J K^{-1}mol^{-1}	C_p^o/J K^{-1}mol^{-1}
GaP(c)	-87.9[9] -104.6[10] -100.4[11]	50.6[11]	47.7[12]
Ga(c)	0	40.9[9]	25.9[9]
(l)	5.6[9]		
(g)	277.0[9]	169[9]	25.4[9]
Br(g)	118.0[9]	174.9[9]	20.8[9]
Br_2(l)	0	152.2[9]	75.7[9]
(g)	30.9	245.4[9]	36.0[9]
Cl_2(g)	0	223.0[9]	33.9[9]
HBr(g)	-36.4[9] -36.4[11] (-54.0[9])	198.6[9] (234.9[9])	29.2[9]
HCl(g)	-92.5[13] (-94.6[13])	186.7[13] (222.8[13])	
P(g)	314.6[9] 333.9[13] 246.9[13]	163.1[9] 163.1[13] 188.3[9]	

Table 4.1 cont.

Species	ΔH_f°/kJ mol^{-1}	S_f°/JK^{-1}mol^{-1}	C_p°/JK^{-1}mol^{-1}
$P_2(g)$	144.3[9] 178.6[13] (0[13])	218.0[9] 218.0[13] 260.2[9]	
$P_4(g)$	58.9[9] 128.9[13] (-223.4[13])	279.9[9] 179.9[13] (372.4[9])	
GaBr(g)	-49.8[9] 12.6[14] -29.3[2] 25.1[5]	251.9[9] 245.2[5]	36.4[9]
$GaBr_2(g)$	-128*	351.5[15]	
$Ga_2Br_4(g)$	-251*	343*	
$GaBr_3(g)$	-292.9[9]	361.1[16]	78.7[16]
GaCl(g)	-79.9[9] -67.8[16] -71.8[14]	240.2[4] 240.2[9] 243.3[15]	
$GaCl_2(g)$	-197*	301.7[17]	
$Ga_2Cl_4(g)$	-627*	590*	
$GaCl_3(g)$	-524.7[9]	142.3[9]	
$H_2(g)$	0 (0)	130.5[13] (166.1[13])	

Best values for the heat and entropy of reaction are collected below for the likely chemical reactions.

$$GaP(c) + HX(g) = GaX(g) + \tfrac{1}{4}P_4(g) + \tfrac{1}{2}H_2(g)$$

X = Cl

$\Delta H_{r\ 298} = 154.0$ kJmol^{-1}

$\Delta S_{r\ 298} = 137.7$ JK^{-1}mol^{-1}

$\Delta H_{r1000} = 147.8$ kJmol^{-1}

$\Delta S_{r1000} = 129.1$ JK^{-1}mol^{-1}

* estimated

X = Br

$\Delta H_{r\ 298} = 158.5\ kJmol^{-1}$

$\Delta S_{r\ 298} = 137.8\ JK^{-1}mol^{-1}$

$\Delta H_{r1000} = 152.3\ kJmol^{-1}$

$\Delta S_{r1000} = 125.0\ JK^{-1}mol^{-1}$

$$GaP(c) + 2HX(g) = GaX_2(g) + \tfrac{1}{4}P_4(g) + H_2(g)$$

X = Cl

$\Delta H_{r\ 298} = 121.0\ kJmol^{-1}$

$\Delta S_{r\ 298} = 78.4\ JK^{-1}mol^{-1}$

$\Delta H_{r1000} = 120.2\ kJmol^{-1}$

$\Delta S_{r1000} = 71.4\ JK^{-1}mol^{-1}$

X = Br

$\Delta H_{r\ 298} = 77.4\ kJmol^{-1}$

$\Delta S_{r\ 298} = 104.0\ JK^{-1}mol^{-1}$

$\Delta H_{r1000} = 76.6\ kJmol^{-1}$

$\Delta S_{r1000} = 95.7\ JK^{-1}mol^{-1}$

$$GaP(c) + 2HX(g) = \tfrac{1}{2}Ga_2X_4(g) + \tfrac{1}{4}P_4(g) + H_2(g)$$

X = Cl

$\Delta H_{r\ 298} = 3.7\ kJmol^{-1}$

$\Delta S_{r\ 298} = -1.7\ JK^{-1}mol^{-1}$

$\Delta H_{r1000} = 11.3\ kJmol^{-1}$

$\Delta S_{r1000} = -3.5\ JK^{-1}mol^{-1}$

X = Br

$\Delta H_{r\ 298} = 40.2\ kJmol^{-1}$

$\Delta S_{r\ 298} = 68.2\ JK^{-1}mol^{-1}$

$\Delta H_{r1000} = -7.0\ kJmol^{-1}$

$\Delta S_{r1000} = 20.3\ JK^{-1}mol^{-1}$

4.5 Phosphorus dissociation.

The dissociation of phosphorus distinctly influences the nature of the weight loss characteristics of GaP. The computer software takes account of this equilibrium by the inclusion of the parameter α. Now, in order to calculate α, the free energy of the dissociation reaction is required, so that K_p may be evaluated as a function of temperature. Three sources were examined to furbish this information.[18,19,20] The first of these leads to a value for ΔH_d of 225.1 $kJmol^{-1}$, and the more recent work, a value of 242.7 $kJmol^{-1}$. (For $P_4(g) = 2P_2(g)$).

Tables 4.2 and 4.3 list the equilibrium constant, K_p, and the degree of dissociation, β, over a wide temperature range using the two values for ΔH_d. Figure 4.5 shows these data in a graphical form. It is evident from the graph that the difference between the two values of β is exaggerated at low temperatures. Both values for ΔH_d have been used in computer simulations, but no difference in the final values of ΔH_r and ΔS_r is found (subtle differences in σ_{min} were however noted).

Table 4.4 and fig 4.6 illustrate good reason to ignore the $P_2(g) = 2P(g)$ equilibrium.

4.6 Computing results.

The gallium phosphide transport systems were both analysed using a scheme-1 regime. This simple approach was found not to adequately describe the results of the GaP:HBr study. These results were subsequently treated employing a scheme-2 regime.

Gallium phosphide : hydrogen chloride

Table 4.2

Equilibrium Constant for $P_4 = 2P_2$ Reaction as a Function of Temperature.

$\Delta H_d = 242.7\ kJmol^{-1}$

$\Delta S_d = 156.1\ JK^{-1}mol^{-1}$

T/K	K_p	β
675.0	2.36×10^{-11}	2.43×10^{-6}
700.0	1.10×10^{-10}	5.26×10^{-6}
725.0	4.65×10^{-10}	1.08×10^{-5}
750.0	1.78×10^{-9}	2.11×10^{-5}
775.0	6.25×10^{-9}	3.95×10^{-5}
800.0	2.03×10^{-8}	7.12×10^{-5}
825.0	6.13×10^{-8}	1.24×10^{-4}
850.0	1.74×10^{-7}	2.08×10^{-4}
875.0	4.63×10^{-7}	3.40×10^{-4}
900.0	1.17×10^{-6}	5.41×10^{-4}
925.0	2.81×10^{-6}	8.38×10^{-4}
950.0	6.45×10^{-6}	1.27×10^{-3}
975.0	1.42×10^{-5}	1.88×10^{-3}
1000.0	3.00×10^{-5}	2.74×10^{-3}
1025.0	6.10×10^{-5}	3.91×10^{-3}
1050.0	1.20×10^{-4}	5.48×10^{-3}
1075.0	2.29×10^{-4}	7.58×10^{-3}
1100.0	4.26×10^{-4}	1.03×10^{-2}
1125.0	7.67×10^{-4}	1.39×10^{-2}
1150.0	1.35×10^{-3}	1.84×10^{-2}
1175.0	2.32×10^{-3}	2.41×10^{-2}

Table 4.2 cont'.

T/K	K_p	β
1200.0	3.88×10^{-3}	3.11×10^{-2}
1225.0	6.38×10^{-3}	3.99×10^{-2}
1250.0	1.03×10^{-2}	5.06×10^{-2}
1275.0	1.62×10^{-2}	6.36×10^{-2}
1300	2.52×10^{-2}	7.92×10^{-2}
1325.0	3.85×10^{-2}	9.77×10^{-2}
1350.0	5.80×10^{-2}	1.20×10^{-1}
1375.0	8.59×10^{-2}	1.45×10^{-1}
1400	1.25×10^{-1}	1.74×10^{-1}

Table 4.3

Equilibrium Constant for $P_4 = 2P_2$ Reaction as a Function of Temperature.

$$\Delta H_d = 225.1 \text{ kJmol}^{-1}$$

$$\Delta S_d = 156.1 \text{ JK}^{-1}\text{mol}^{-1}$$

T/K	K_p	β
675.0	5.43×10^{-10}	1.16×10^{-5}
700.0	2.27×10^{-9}	2.38×10^{-5}
725.0	8.63×10^{-9}	4.64×10^{-5}
750.0	3.00×10^{-8}	8.65×10^{-5}
775.0	9.60×10^{-8}	1.55×10^{-4}
800.0	2.86×10^{-7}	2.67×10^{-4}
825.0	7.97×10^{-7}	4.46×10^{-4}
850.0	2.09×10^{-6}	7.23×10^{-4}
875.0	5.20×10^{-6}	1.14×10^{-3}

Table 4.3 cont'.

T/K	K_p	β
900.0	1.23×10^{-5}	1.75×10^{-3}
925.0	2.77×10^{-5}	2.63×10^{-3}
950.0	5.98×10^{-5}	3.87×10^{-3}
975.0	1.24×10^{-4}	5.57×10^{-3}
1000.0	2.49×10^{-4}	7.89×10^{-3}
1025.0	4.81×10^{-4}	1.10×10^{-2}
1050.0	9.03×10^{-4}	1.50×10^{-2}
1075.0	1.64×10^{-3}	2.03×10^{-2}
1100.0	2.92×10^{-3}	2.70×10^{-2}
1125.0	5.04×10^{-3}	3.55×10^{-2}
1150.0	8.50×10^{-3}	4.61×10^{-2}
1175.0	1.40×10^{-2}	5.91×10^{-2}
1200.0	2.27×10^{-2}	7.51×10^{-2}
1225.0	3.59×10^{-2}	9.44×10^{-2}
1250.0	5.59×10^{-2}	1.17×10^{-1}
1275.0	8.55×10^{-2}	1.45×10^{-1}
1300.0	1.29×10^{-1}	1.76×10^{-1}
1325.0	1.90×10^{-1}	2.13×10^{-1}
1350.0	2.78×10^{-1}	2.55×10^{-1}
1375.0	4.00×10^{-1}	3.02×10^{-1}
1400.0	5.69×10^{-1}	3.53×10^{-1}

Table 4.4

Equilibrium Constant for $P_2 = P$ Reaction as a Function of Temperature.

$$\Delta H_d = 489.1 \text{ kJmol}^{-1}$$

$$\Delta S_d = 108.1 \text{ JK}^{-1}\text{mol}^{-1}$$

T/K	K_p	β
1175.0	8.01×10^{-17}	4.47×10^{-9}
1200.0	2.27×10^{-16}	7.54×10^{-9}
1225.0	6.18×10^{-16}	1.24×10^{-8}
1250.0	1.62×10^{-15}	2.10×10^{-8}
1275.0	4.06×10^{-15}	3.18×10^{-8}
1300.0	9.87×10^{-15}	4.97×10^{-8}
1325.0	2.32×10^{-14}	7.61×10^{-8}
1350.0	5.27×10^{-14}	1.15×10^{-7}
1375.0	1.16×10^{-13}	1.71×10^{-7}
1400.0	2.50×10^{-13}	2.50×10^{-7}
1425.0	5.23×10^{-13}	3.61×10^{-7}
1450.0	1.06×10^{-12}	5.16×10^{-7}
1475.0	2.12×10^{-12}	7.28×10^{-7}
1500.0	4.11×10^{-12}	1.01×10^{-6}
1525.0	7.83×10^{-12}	1.40×10^{-6}
1550.0	1.46×10^{-11}	1.91×10^{-6}
1575.0	2.66×10^{-11}	2.58×10^{-6}
1600.0	4.78×10^{-11}	3.46×10^{-6}
1625.0	8.41×10^{-11}	4.59×10^{-6}
1650.0	1.46×10^{-10}	6.03×10^{-6}
1675.0	2.48×10^{-10}	7.87×10^{-6}
1700.0	4.15×10^{-10}	1.02×10^{-5}
1725.0	6.86×10^{-10}	1.31×10^{-5}
1750.0	1.11×10^{-9}	1.67×10^{-5}
1775.0	1.79×10^{-9}	2.12×10^{-5}
1800.0	2.84×10^{-9}	2.66×10^{-5}
1825.0	4.44×10^{-9}	3.33×10^{-5}
1850.0	6.87×10^{-9}	4.14×10^{-5}
1875.0	1.59×10^{-8}	5.12×10^{-5}
1900.0	1.59×10^{-8}	6.30×10^{-5}

Fig. 4.5 Dissociasion of Phosphorous

$P_4(g) = 2P_2(g)$

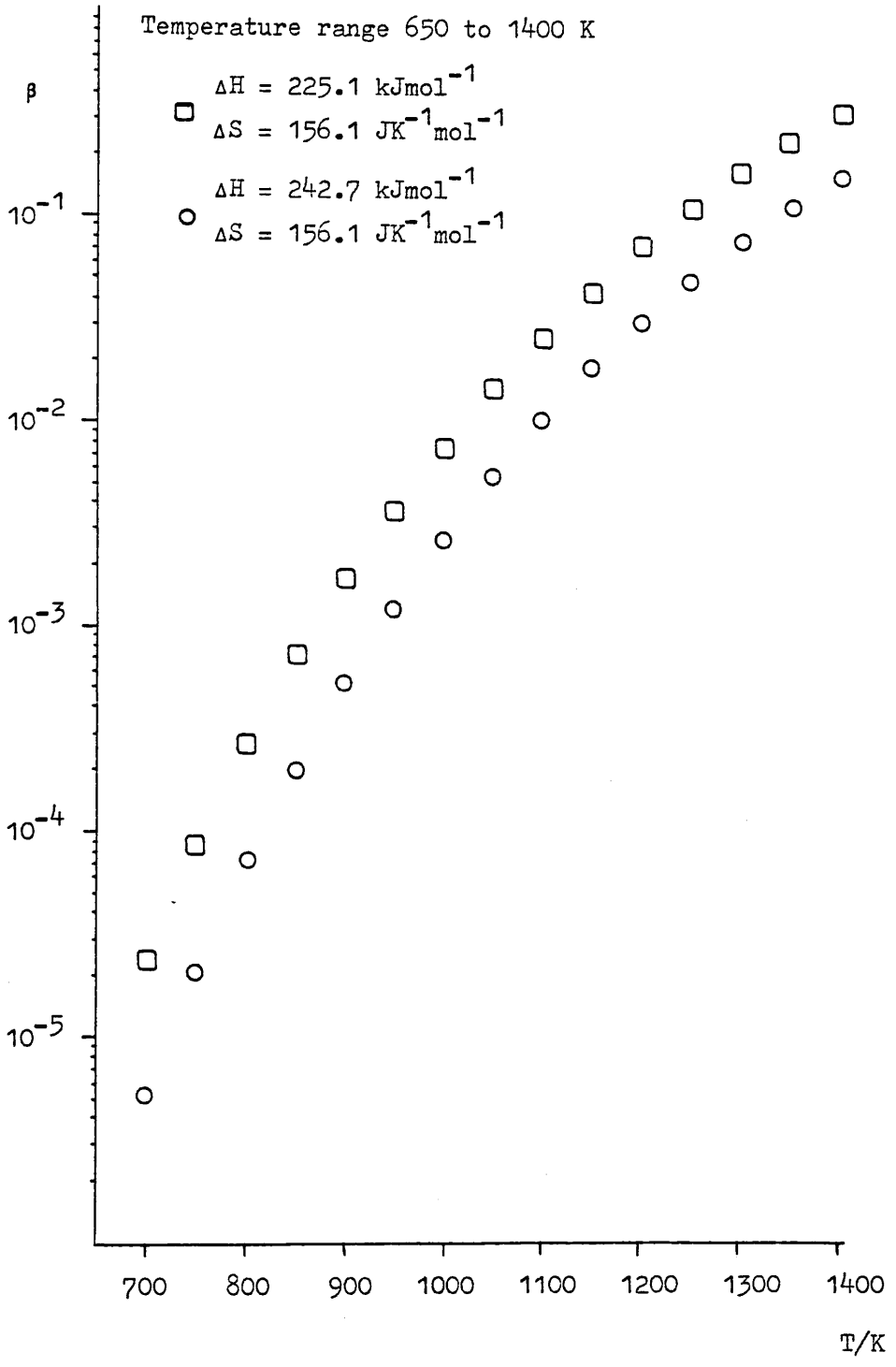

Fig. 4.6 Dissociasion of Phosphorous

$P_2(g) = 2P(g)$

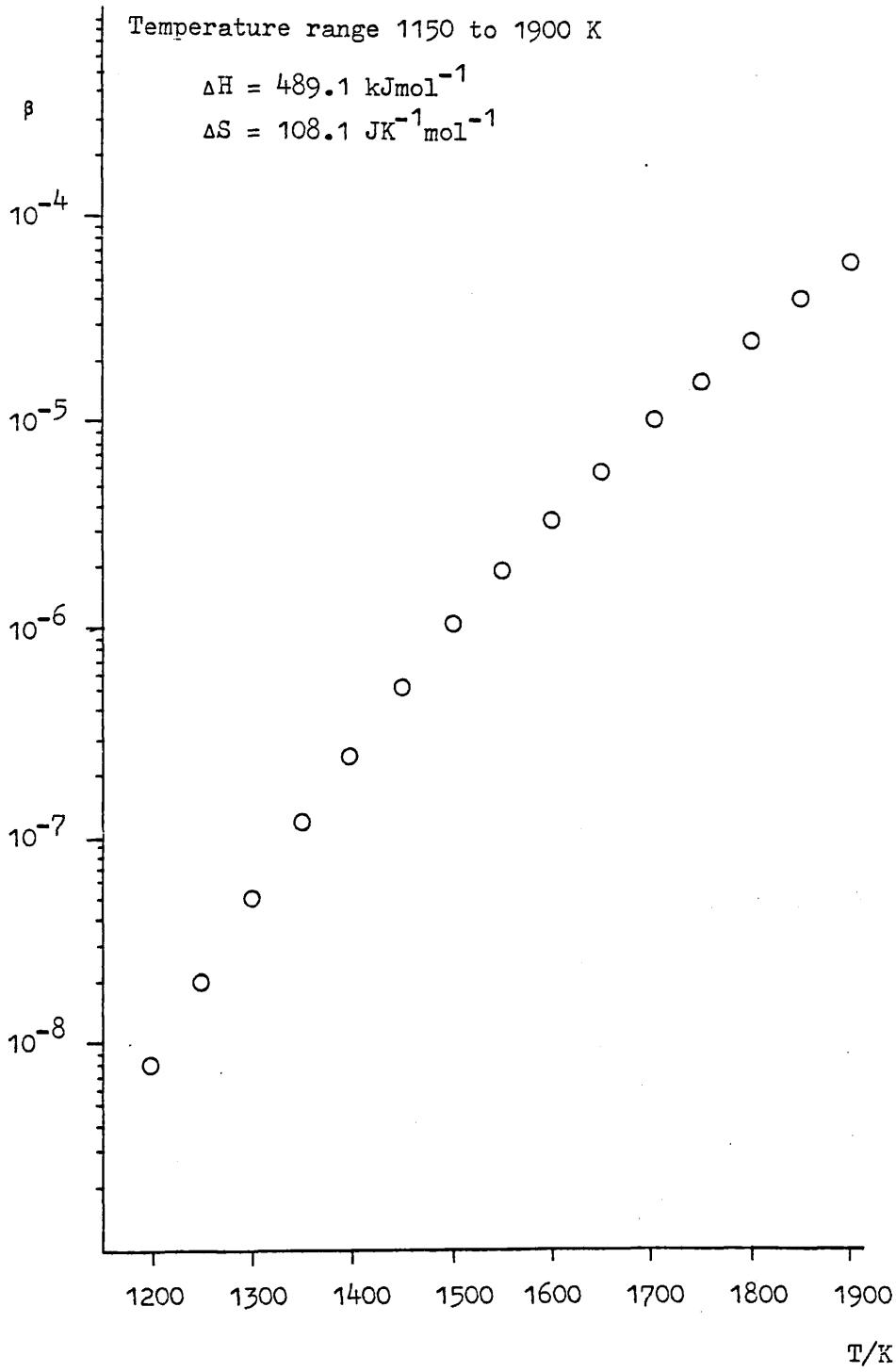

When fitting these results for GaP:HCl, it was found that the points below 950 K had a profound deletrious effect on the integrity of fit. In view of this, the appropriate data points have been omitted from the simulations.

The functions describing transport are usually well behaved and yield a single minimum. In this instance two minima were found. One, however, is chosen as the preferred result. Grounds for rejecting the alternative minimum include, a substantial reduction (≈20%) in D_o is required to attain σ_{min}, and significant differences in ΔH_r and ΔS_r for the two channel sizes result. The preferred results are summarised below:

channel Ø/mm	ε	ΔH_r/kJ mol^{-1}	ΔS_r/J K^{-1}mol^{-1}	$10^4 D_o$	s	σ
2	0.059	135.0	111.5	0.54	0.8	0.005
2	0.039	132.0	108.0	0.54	0.8	0.022
1	0.059	135.5	112.0	0.54	0.8	0.006
1	0.039	132.0	108.0	0.54	0.8	0.019
		133.6 ± 2	109.9 ± 2			

The alternative minimum yielded 140 ± 7 and 118 ± 7 for ΔH_r/kJmol^{-1} and ΔS_r/JK^{-1}mol^{-1} respectively. The expression

$$D_T/m^2s^{-1} = 0.54\times10^{-4}(T/273.15)^{1.8} \qquad (4.6.1)$$

is preferred since $D_o = 0.000054$ has been used in previous work[4] and lies within experimental error of the value determined at this laboratory[2]. Theoretical calculations give the following expression,

$$D_T/m^2s^{-1} = 0.646\times10^{-4}(T/273.15)^{1.65} \qquad (4.6.2)$$

These two expressions generate very similar values for D_T, see fig 4.7.

Graphs of $\ln(\dot{w}/kgs^{-1})$ v K/T appear in figs 4.8 to 4.11. The points plotted on these graphs represent the experimental data, and the line drawn the calculated results using the thermodynamic data yielding a minimum value for σ.

Previous computations using evolved forms of the British Telecom derived program had given the results summarised below.

channel	Ø/mm	ε	ΔH_r/kJ mol^{-1}	ΔS_r/J K^{-1}mol^{-1}	$10^4 D_o$	s	σ
2		0.059	142.5	120.4	0.48	0.8	0.135
2		0.039	152.0	131.9	0.42	0.8	0.080
1		0.059	143.5	121.5	0.48	0.8	0.090
1		0.039	149.2	128.6	0.43	0.8	0.150

In these analyses the contention of a second set of minima did not arise and the reduced values of D_o, most noticeable in the low ε instances, is required to attain a close approach to the experimental data. Using either program, difficulty is encountered in achieving a good fit at high temperature for both low experiments. This difficulty is so marked that using the latter program simulations were performed allowing some variation in ε. Small deviations in float height, representing the HCl flow-rate, could justify the reduced value employed here. In all instances a much improved fit, at high temperature, was obtained when ε was reduced from 0.039 to 0.031. The results are shown below and are plotted graphically in figs 4.12 and 4.13.

channel	Ø/mm	ε'	ΔH_r/kJmol^{-1}	ΔS_r/JK^{-1}mol^{-1}	$D_o \times 10^4$	s	σ
2		0.031	138.5	117.5	0.54	0.8	0.008

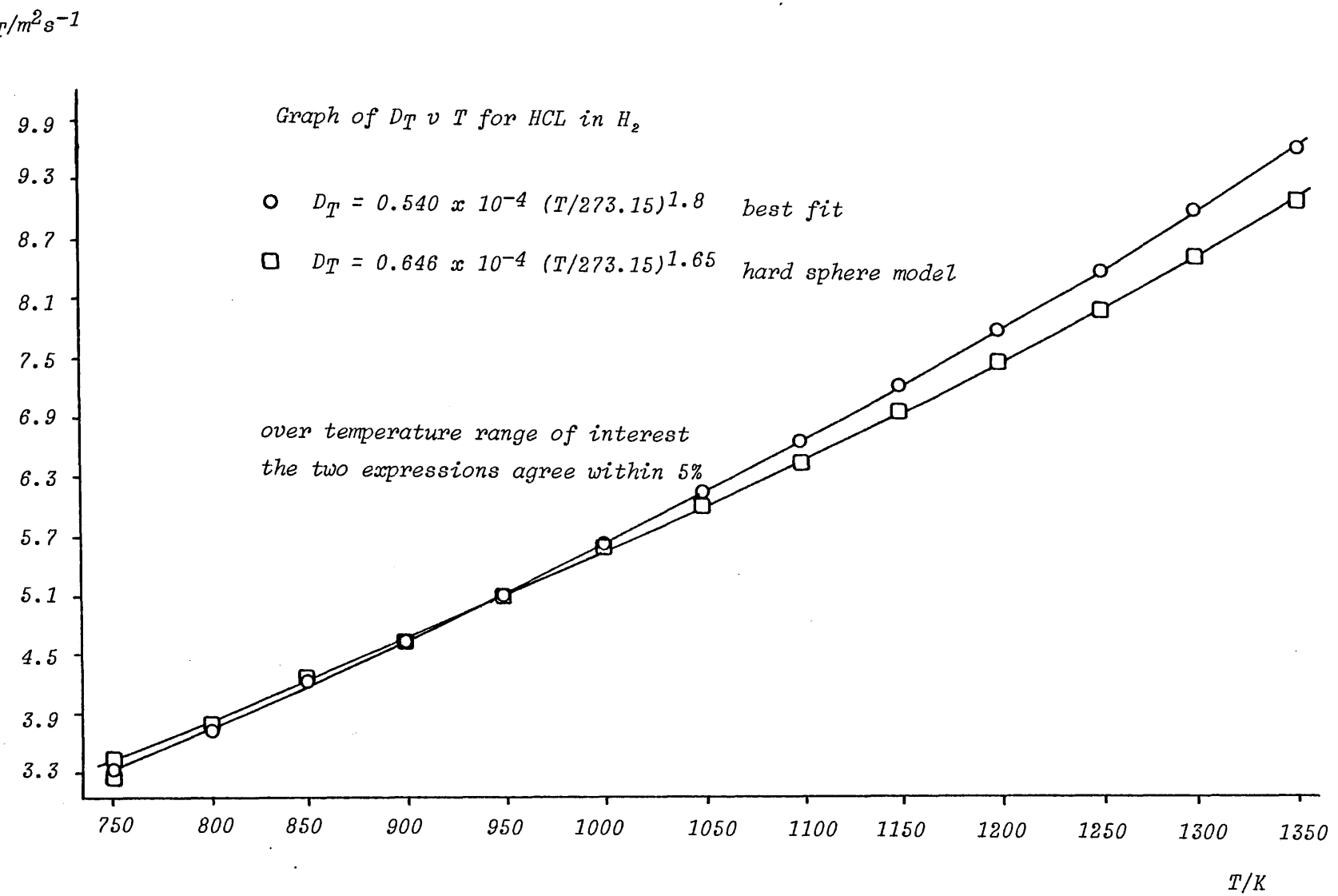
$10^4 D_T/m^2 s^{-1}$
Graph of D_T v T for HCL in H_2
$D_T = 0.540 \times 10^{-4} (T/273.15)^{1.8}$ best fit
$D_T = 0.646 \times 10^{-4} (T/273.15)^{1.65}$ hard sphere model
over temperature range of interest
the two expressions agree within 5%
9.9
9.3
8.7
8.1
7.5
6.9
6.3
5.7
5.1
4.5
3.9
3.3
750
800
850
900
950
1000
1050
1100
1150
1200
1250
1300
1350
T/K

Fig. 4.7

Fig 4.8 Graph of $\ln \dot{w}_{calc}$ v 10^4 K/T

Fitted Results for GaP:HCl, 0.002 m Ø, high ε.

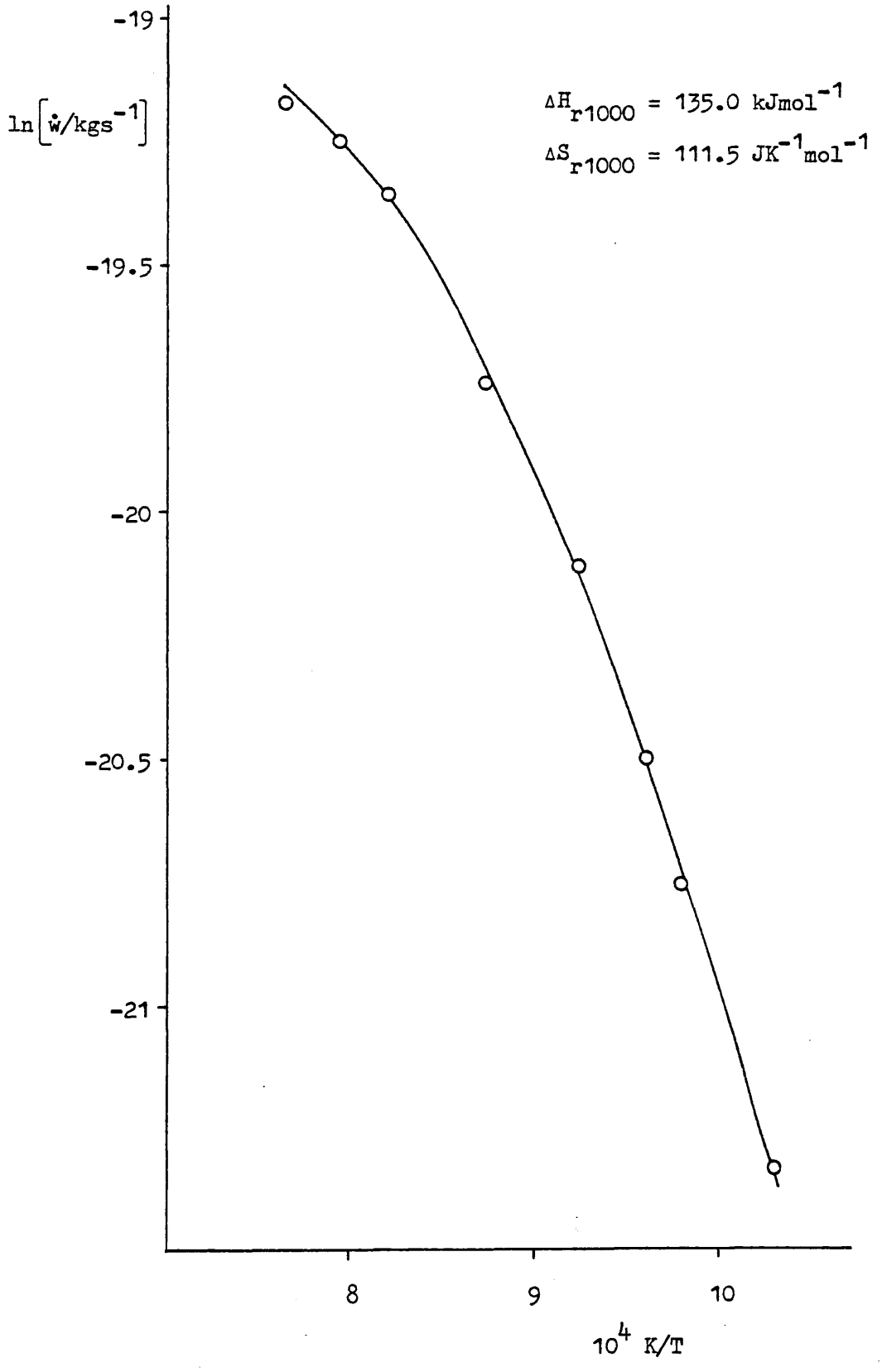

Fig 4.9 Graph of $\ln\dot{w}_{calc}$ v 10^4 K/T

Fitted Results for GaP:HCl, 0.002 m Ø, low ε.

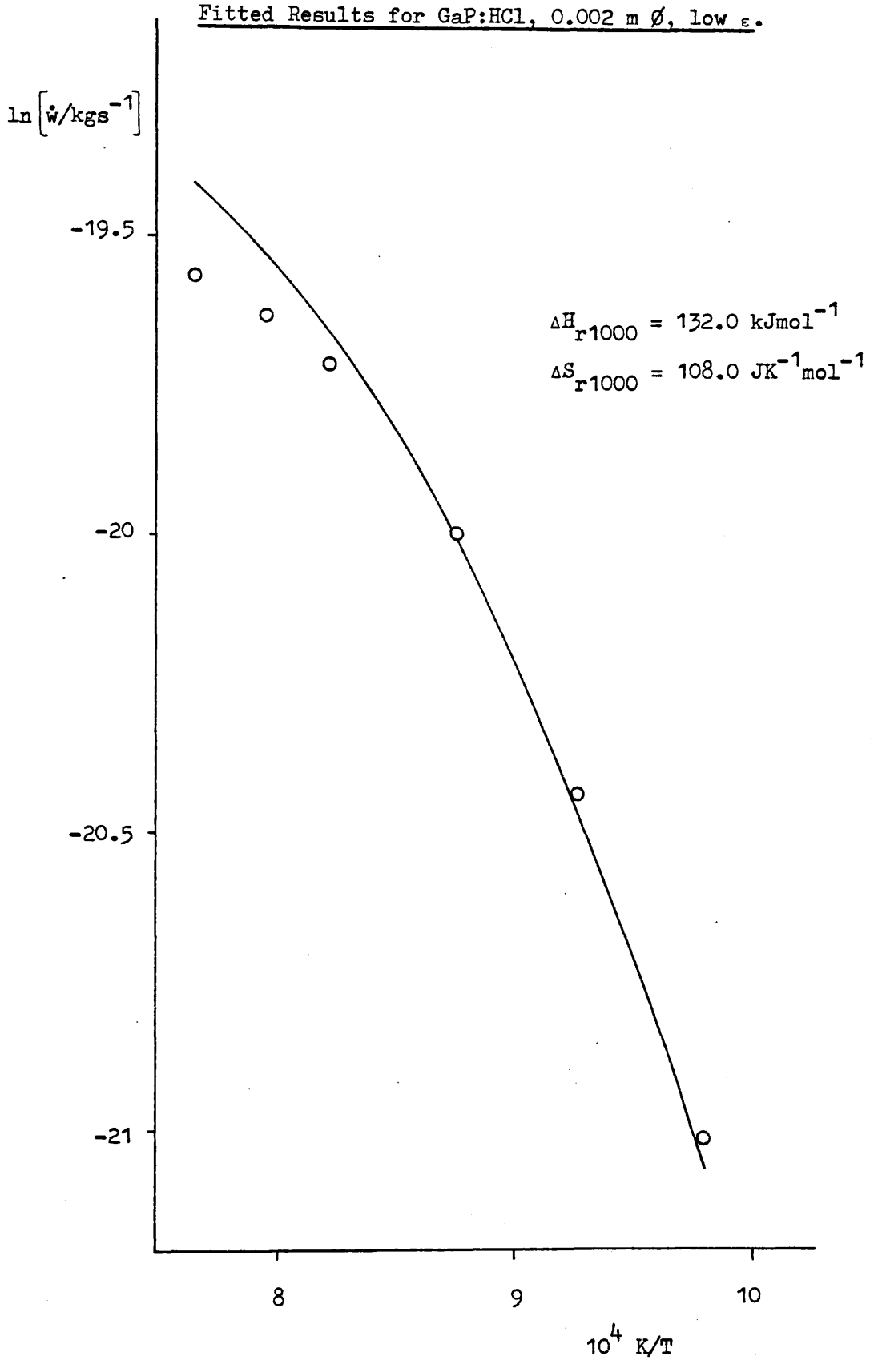

Fig 4.10 Graph of $\ln \dot{w}_{calc}$ v 10^4 K/T

Fitted Results for GaP:HCl, 0.001, high ε.

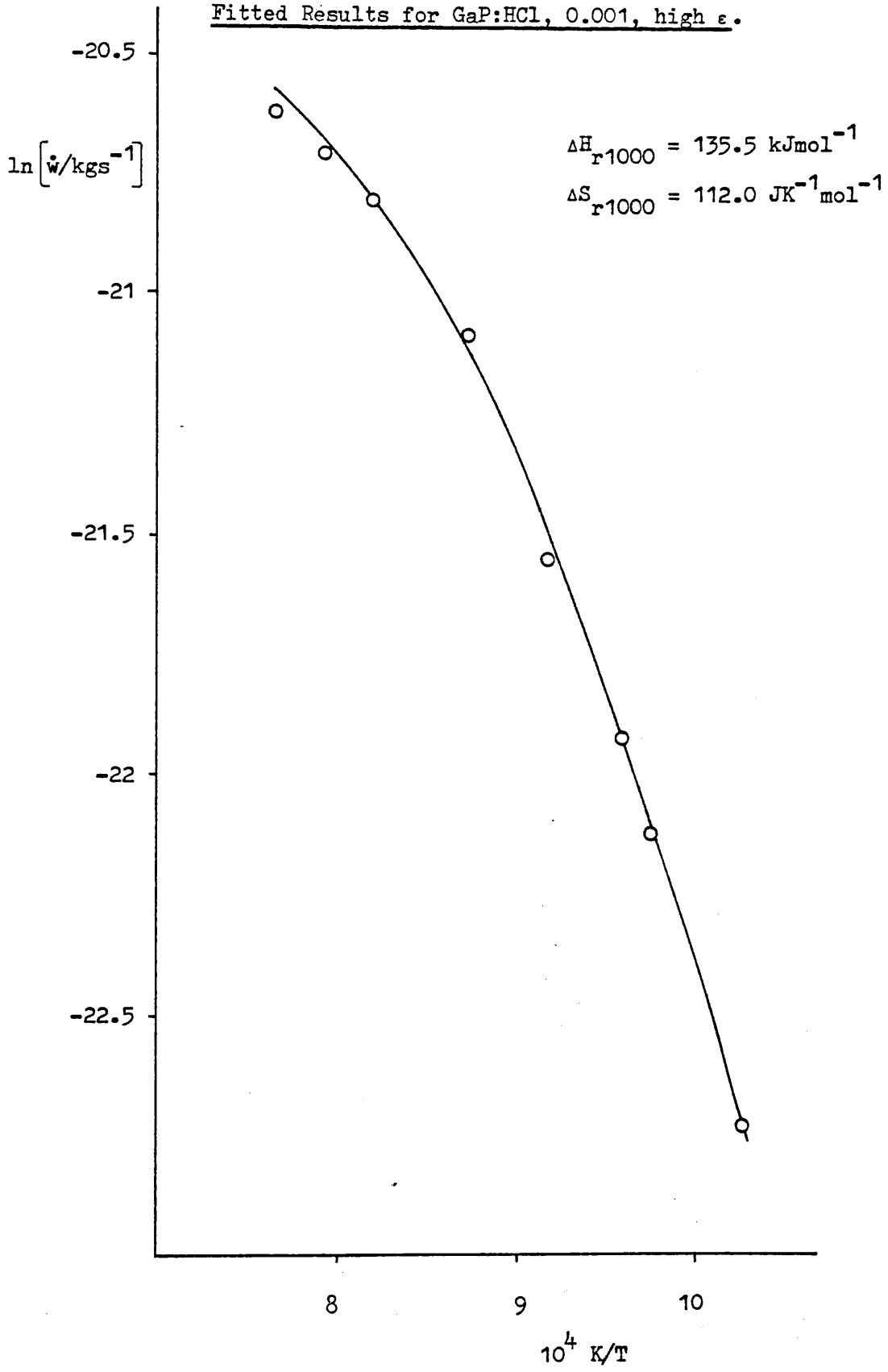

Fig 4.11 Graph of $\ln \dot{w}_{calc}$ v 10^4 K/T

Fitted Results for GaP:HCl, 0.001 m Ø, low ε.

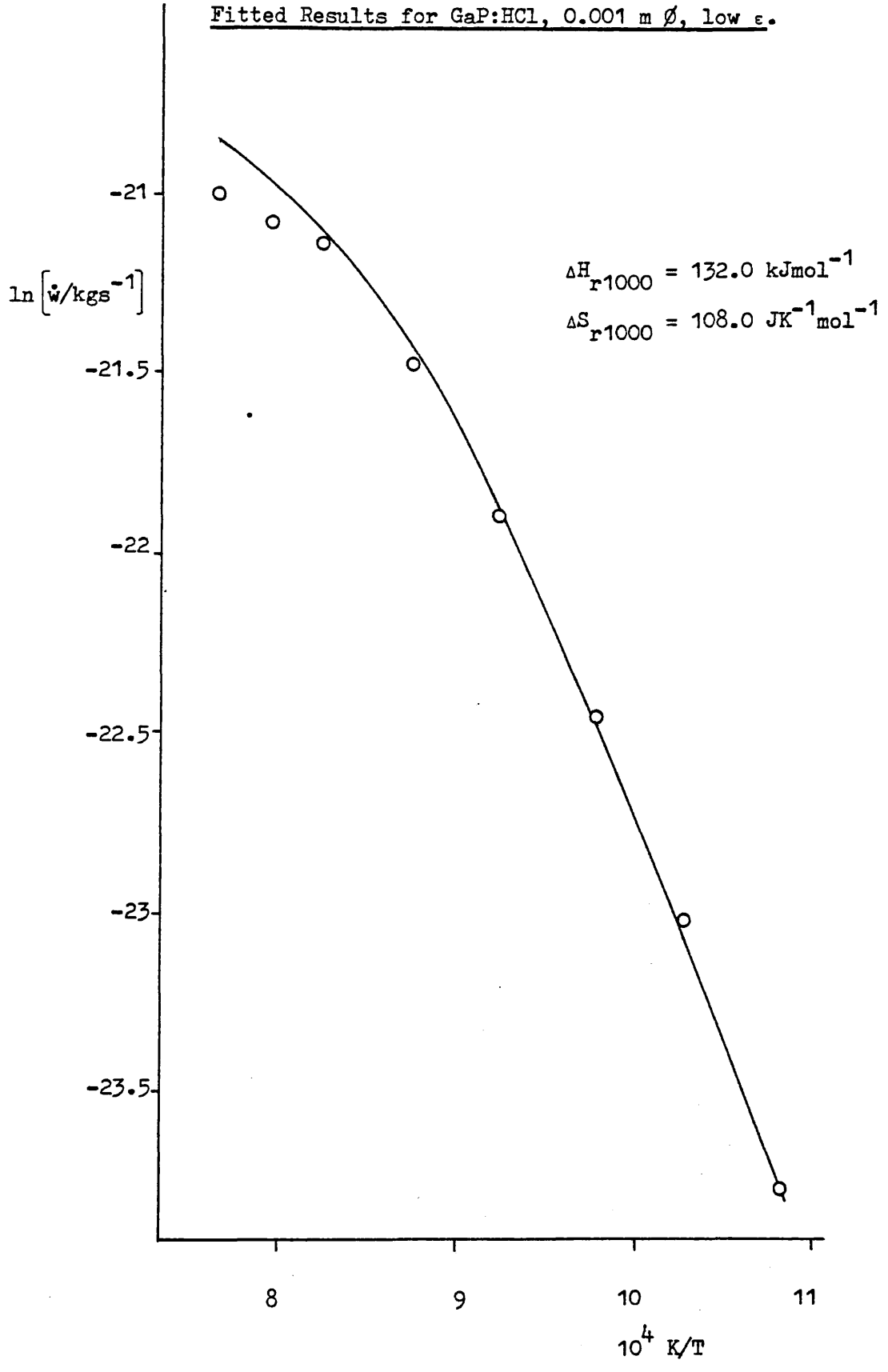

Fig 4.12 Graph of $\ln \dot{w}_{calc}$ v 10^4 K/T

Fitted Results, allowing ε to Take a Lower Value.

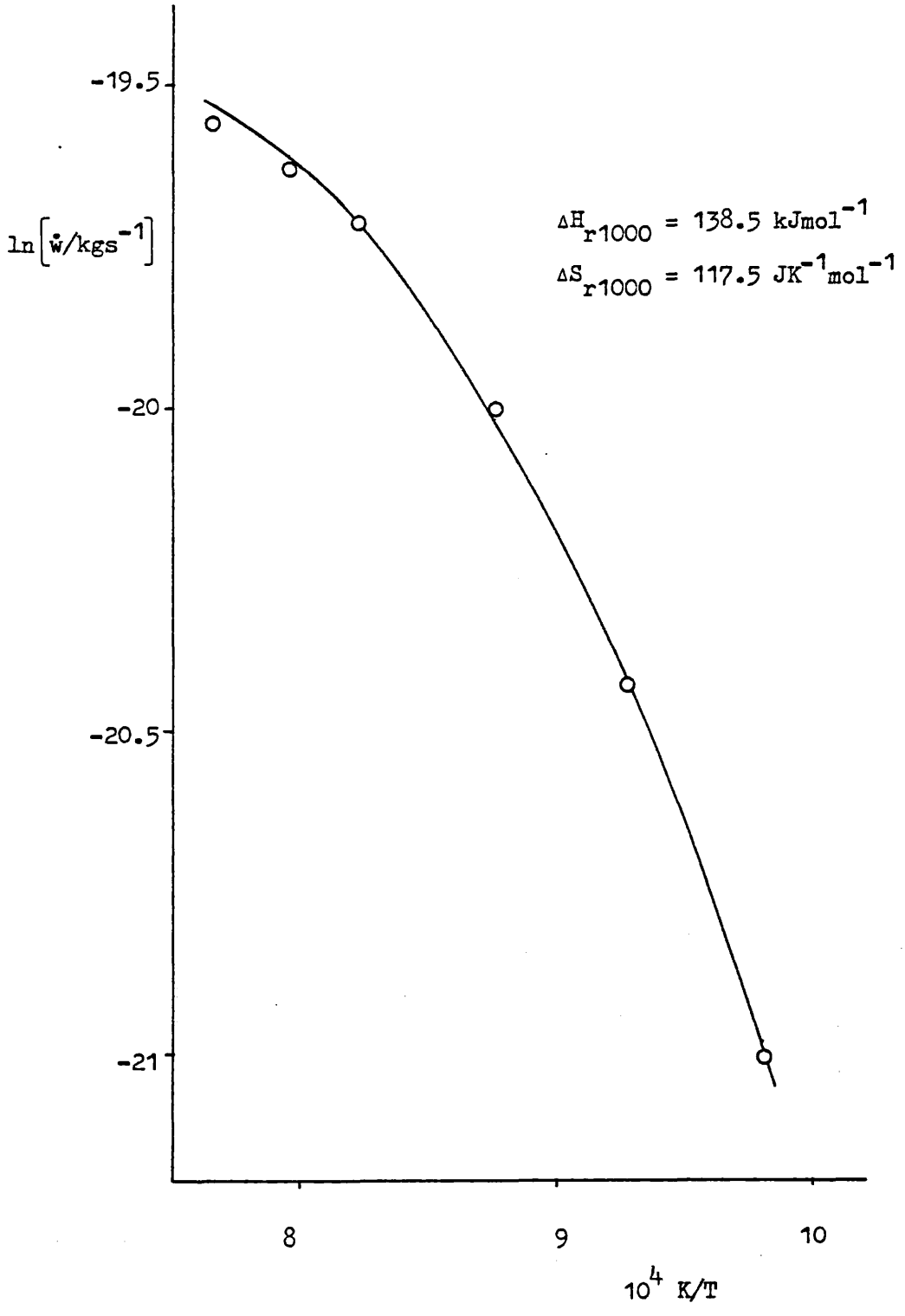

Fig 4.13 Graph of $\ln \dot{w}_{calc}$ v 10^4 K/T

Fitted Results, Allowing ε to Take a Lower Value.

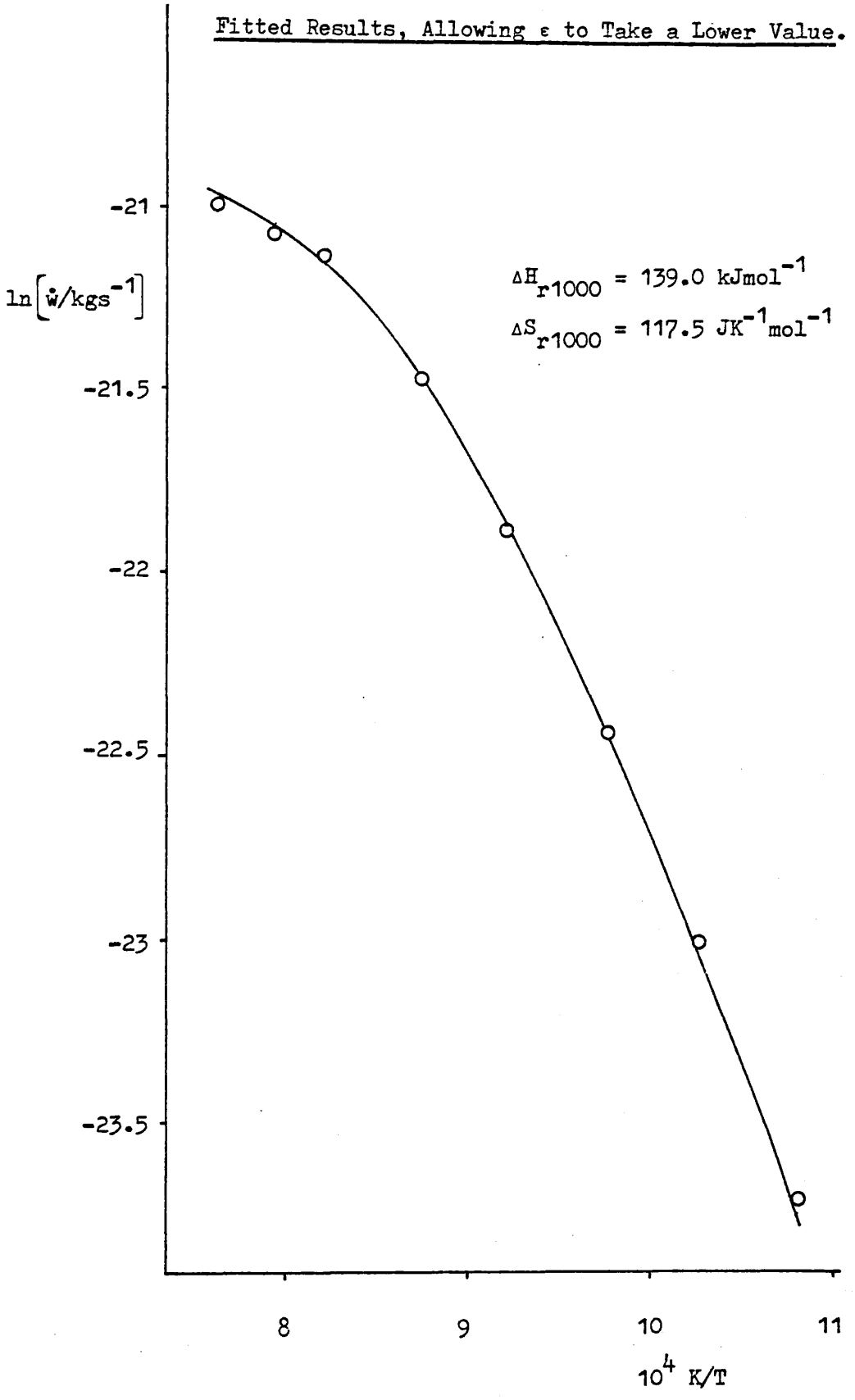

channel Ø/mm	ε'	ΔH_r/kJ mol^{-1}	ΔS_r/J K^{-1}mol^{-1}	$10^4 D_o$	s	σ
1	0.031	139.0	117.5	0.54	0.8	0.009

Gallium phosphide : hydrogen bromide

Figure 4.4 clearly illustrates that the experiments performed using the smaller channel bottle demonstrate the participation of two vapour transport reactions. Experimental results obtained using a bottle with approximately a four fold larger channel conductance would indicate that only a single transport reaction were operative.

Both the British Telecom derived programs and the more rigorous (RHC) procedures have been used. Simulation results in this instance do not produce dual minima, and for each system both program variants converge on essentially the same results.

Firstly consider the results obtained using the smaller channel, 0.001 m bottle. A scheme-2 type analysis was used here. The analysis was performed in three stages. In order to gain confidence in the value chosen for D_o and s in the expression for the diffusion coefficient, D_T, the high temperature region was fitted first. Values of D_o, s, ΔH_1, ΔH_2, ΔS_1 and ΔS_2 were then used to fit the low temperature region. Values for ΔH_1, ΔH_2, ΔS_1 and ΔS_2 were then chosen as starting data for the simulation over the whole temperature range. Figure 4.4 would suggest that for the transport of GaP using HBr, the rate of weight loss is supressed at the lowest temperatures, probably due to a kinetic influence at the substrate surface. The results are summarised below, and graphical representations appear in figs 4.14 and 4.15.

Fig 4.14 Graph of $\ln \dot{w}_{calc}$ v 10^4 K/T

Fitted Results for GaP:HBr, 0.001 m Ø, high ε.

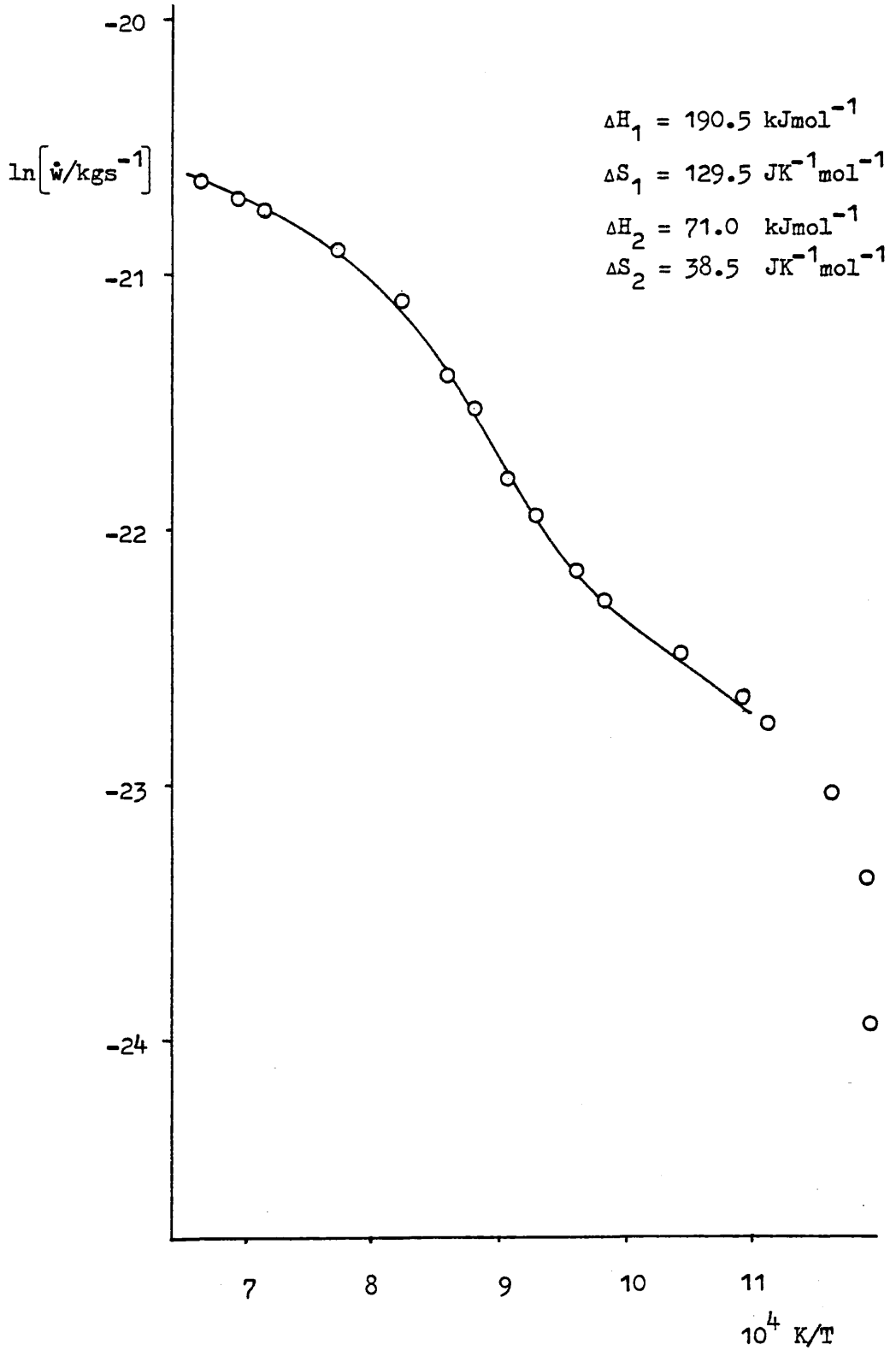

Fig 4.15 Graph of $\ln \dot{w}_{calc}$ v 10^4 K/T

Fitted Results for GaP:HBr, 0.001 m Ø, low ε.

$\Delta H_1 = 188.5 \text{ kJmol}^{-1}$

$\Delta S_1 = 128.8 \text{ JK}^{-1}\text{mol}^{-1}$

$\Delta H_2 = 70.5 \text{ kJmol}^{-1}$

$\Delta S_2 = 37.0 \text{ JK}^{-1}\text{mol}^{-1}$

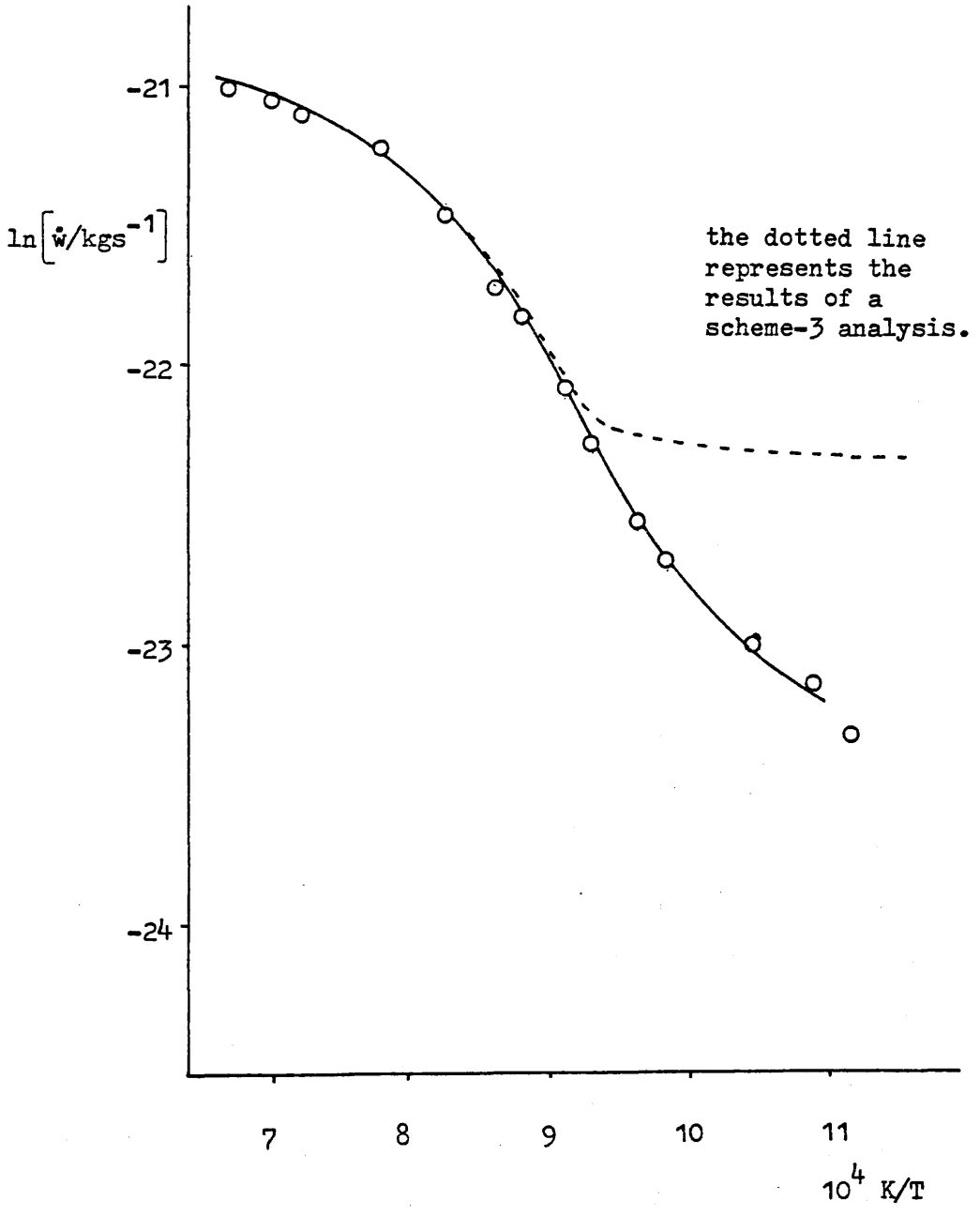

range	ε	ΔH_1	ΔH_2	ΔS_1	ΔS_2	D_o	s	σ
high temp	0.059	190	72.5	130.5	38	0.47×10^{-4}	0.78	0.06
low temp	0.059	192	70.5	129	38.5	0.47×10^{-4}	0.78	0.09
whole	0.059	190.5	71	129.5	38.5	0.47×10^{-4}	0.78	0.15
high temp	0.035	188	70	128	37	0.47×10^{-4}	0.78	0.09
low temp	0.035	190	70.5	128	36.5	0.47×10^{-4}	0.78	0.14
whole	0.035	188.5	70.5	128.5	37	0.47×10^{-4}	0.78	0.19

where ΔH_1 and ΔH_2 are expressed in $kJmol^{-1}$

ΔS_1 and ΔS_2 are expressed in $JK^{-1}mol^{-1}$

and D_o is expressed in m^2s^{-1}.

ΔH_1 and ΔS_1 refer to the reaction involving the formation of the monobromide, and ΔH_2 and ΔS_2 to the formation of the dibromide.

Various features of these results are note-worthy. ΔH_1 predicted by the simulation is appreciably larger than that estimated, and this is a little surprising as the estimate was thought to be more accurate. Good agreement for ΔS_1 is expected, as the entropy changes may be estimated with greater confidence. The large downward adjustment for ΔS_2 suggest that aggregation of the species "$GaBr_2$" in the vapour is likely.

An analysis, scheme-3 (see appendix 3) is available to take account of the presence of $Ga^{I}(Ga^{III}Br_4)$, but unfortunately, neither the BT or RHC programs produce a satisfactory simulation. Both regimes produce a good fit at high temperature, but as the break-point is approached at intermediate temperature, the simulations fail to follow the experimental results. Over the temperature region where the formation of $Ga^{I}(Ga^{III}Br_4)$ is

predicted, the computed results are too high (see fig 4.15). The slope of the graph over the low temperature range is found to be almost insensitive to changes in ΔH_2 and ΔS_2.

By printing various values of intermediate parameters in the calculation, it is seen that the values of $\dot{w}$ converge very rapidly, halting the reiterative refinement prematurely. No specific reason for this behaviour is evident from the numerical values of intermediate parameters. Simulations were performed over restricted temperature ranges inserting specific values for particular key parameters, such as α and θ, but these procedures failed to produce a more acceptable fit. The BT derived program was checked using test data from the GaAs/HBr system[2], but no problems arose in this simulation. Attempts to fit the GaP/HBr data using a scheme-3 analysis were subsequently abandoned.

In processing the 2 mm channel results, only points corresponding to the temperature range above the break-point were considered, since at lower temperatures it is unlikely that equilibrium partial pressures are attained in the bottle. Both BT and RHC variations of a scheme-1 analysis were used, and both gave very similar results. The results presented below, and in figs 4.16 and 4.17 are for the RHC formulation, which yielded a slightly better fit.

ε	ΔH_r/kJ mol^{-1}	ΔS_r/J K^{-1}mol^{-1}	$10^4 D_o$	s	σ
0.059	128	114	0.47	0.78	0.25
0.035	133	119	0.47	0.78	0.11

The "best fit" results for this larger channel are markedly different from those attained for the high temperature

Fig 4.16 Graph of $\ln \dot{w}_{calc}$ v 10^4 K/T

Fitted Results for GaP:HBr, 0.002 m Ø, high ε.

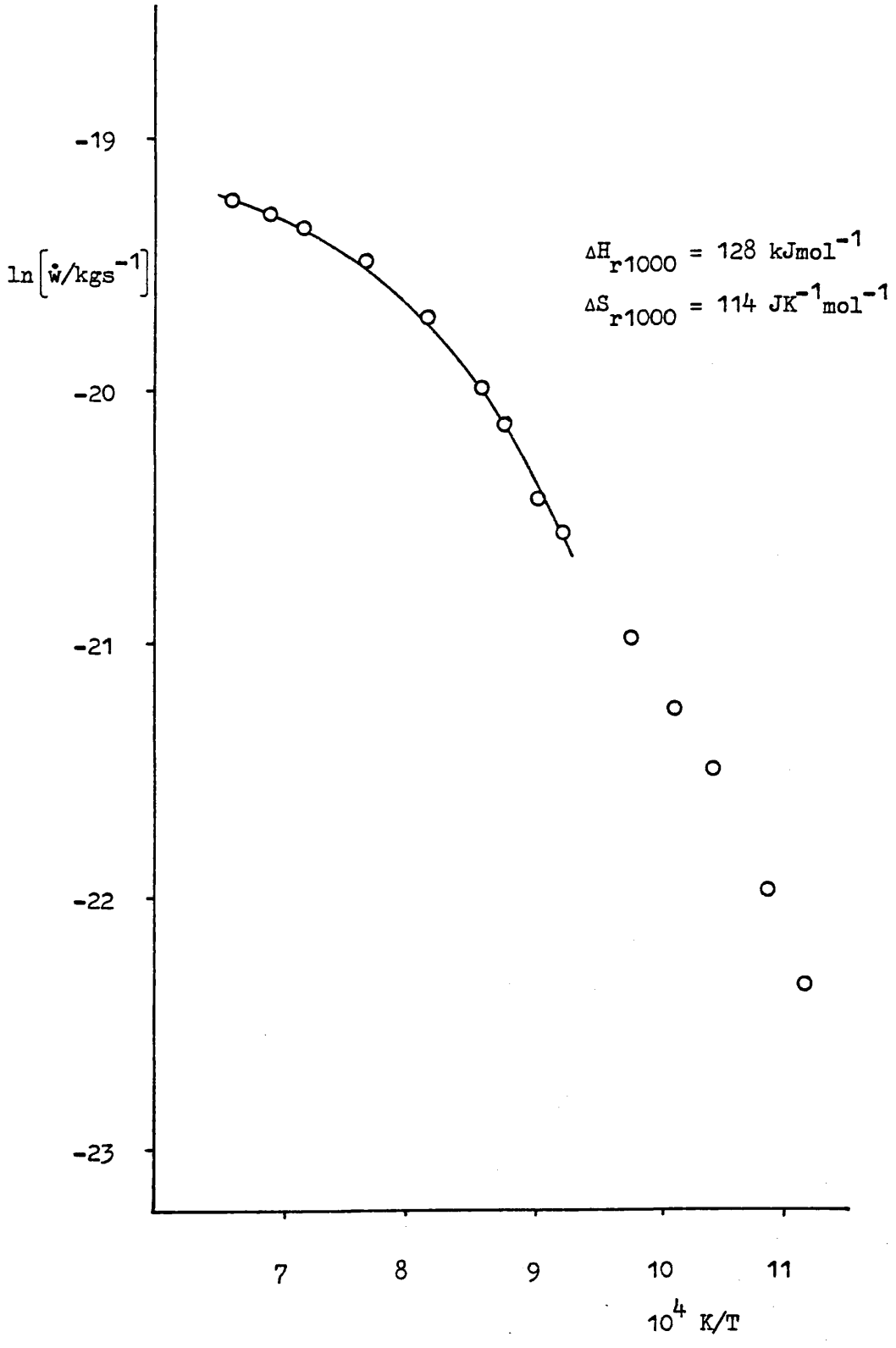

Fig 4.17 Graph of $\ln\dot{w}_{calc}$ v 10^4 K/T

Fitted Results for GaP:HBr, 0.002 m Ø, low ε.

$\Delta H_{r1000} = 133\ kJmol^{-1}$

$\Delta S_{r1000} = 119\ JK^{-1}mol^{-1}$

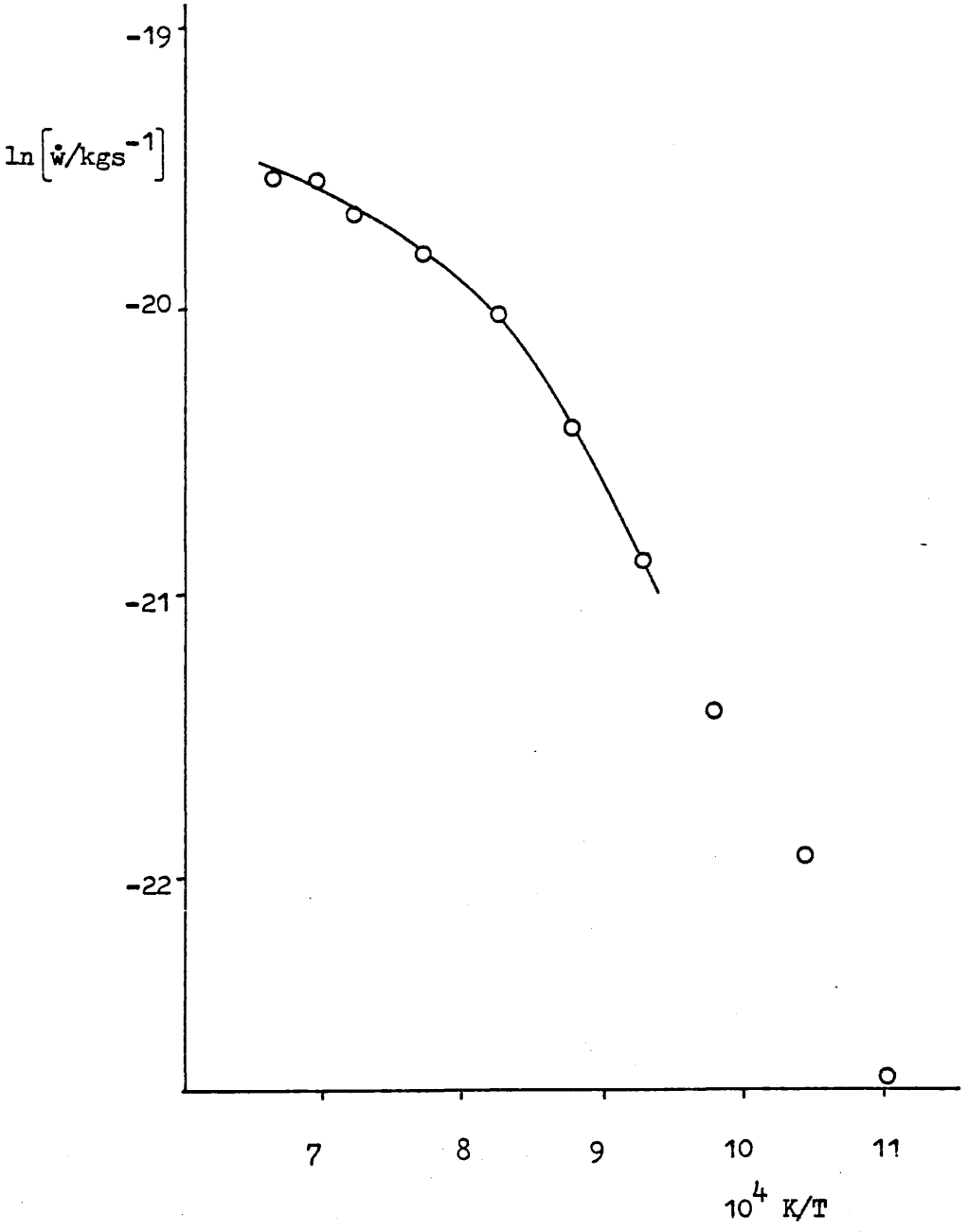

region using the smaller channel. Hence, either the computed values of the thermodynamic constants for the high temperature reaction are profoundly affected by the proximity of the second transport reaction (in this case not evident in the results, due to kinetic inhibition), or all data, both at high and low temperatures, is non-equilibrium.

Clearly, if the results attained using the larger channel were the only results available, then apparently acceptable thermodynamic constants for a single transport reaction would have been deduced. That such results are erroneous is demonstrated by the results for the smaller channel experiments, and emphasises the necessity for using more than one channel size in MEM work.

4.7 Derived thermodynamic functions

Using the second law values for the heats and entropies of reaction of the various CVT reactions, standard enthalpies and entropies of formation of the participating metal-halide species may be calculated. These values are summerised below, both at the mean experimental temperatures, and corrected to 298 K.

	H^{o}_{fT}	H^{o}_{f298}	S^{o}_{T}	S^{o}_{298}
GaCl(g)	-97.1	-67.5	268.9	230.0
GaBr(g)	-0.8	24.8	299.8	258
$GaBr_2$(g)	-173	-134	402	331

enthalpies are given in $kJmol^{-1}$, and entropies in $JK^{-1}mol^{-1}$.

To make the corrections to 298 K, the specific heat data calculated by Shaulov and Mosin[16] has been used for the

monochloride. For the monobromide the heat capacity quoted in Tech note 270-3[9] has been assumed. Specific heat data for the dibromide is not available so a heat capacity has been selected by comparison with values from a pseudo-homologous series.

Comparing these calculated values with those collected in table 4.1, good agreement is noted for the enthalpy of formation of GaCl(g). Good agreement is also seen between the value calculated here and from similar studies on the GaAs:HCl system.[4] The second law entropy of gallium monochloride calculated here would appear to be a little low by comparison with other data. Appreciable uncertainty in the enthalpy of formation of gallium monobromide is apparent. The value calculated here would suggest a confirmation of a value extracted from similar work.[5] Tech note 270-3 cites a value of 251.9 $JK^{-1}mol^{-1}$ for the entropy of the monobromide, so the value calculated here is in fair agreement. For the dibromide, an enthalpy was estimated for inclusion in table 4.1, and the value calculated is close to this. Again in this instance the second law entropy is low by comparison with other data.[15]

Table 4.5.

GaP : HCl 0.002 m channel ε = 0.059

T/K	$10^{10}\dot{w}/kgs^{-1}$
1141.2	27.00
1141.2	27.065
1141.2	26.801
1083.5	18.481
1083.8	19.084
1083.8	18.902
1083.8	19.046
1020.0	9.698
1020.0	9.708
1213.8	39.526
1213.8	39.098
1213.8	39.484
1253.7	43.117
1253.7	44.154
1253.7	44.159
1303.5	48.261
1303.5	46.157
1303.5	49.356
970.3	5.436
970.3	5.372
919.6	2.349
919.6	2.392
871.1	0.935
871.1	0.943

Table 4.5 cont'.

T/K	$10^{10}\dot{w}/kgs^{-1}$
1040.7	12.525
1040.7	12.487
819.3	0.402
819.3	0.397
819.3	0.386

Table 4.6

GaP : HCl 0.002 m channel $\varepsilon = 0.039$

T/K	$10^{10}\dot{w}/kgs^{-1}$
1305.2	31.688
1305.2	31.891
1215.5	27.569
1215.5	27.459
1215.5	27.667
1141.0	20.453
1141.0	20.945
1080.8	13.500
1080.8	13.495
1019.6	7.317
1019.6	7.685
971.8	3.790
971.8	3.588
971.8	3.685
922.0	1.546

Table 4.6 cont'.

T/K	$10^{10}\dot{w}/kgs^{-1}$
921.1	1.562
1255.8	29.585
1256.0	30.288

Table 4.7

GaP : HCl 0.001 m channel ε = 0.059

T/K	$10^{10}\dot{w}/kgs^{-1}$
1086.3	44.574
1086.3	45.068
1086.3	44.820
975.5	13.307
975.5	13.717
975.5	13.427
1145.2	70.426
1145.2	68.897
1145.2	68.966
923.8	6.453
1218.7	92.744
1218.7	92.500
1218.7	92.744
1042.2	29.970
1042.2	31.056
1258.7	101.950
1258.7	102.680

Table 4.7 cont'.

T/K	$10^{10}\dot{w}/kgs^{-1}$
1023.5	24.545
1023.5	25.139
1023.5	25.253
1306.1	110.780
1306.1	108.740
1306.1	110.170

Table 4.8

GaP : HCl 0.001 m channel ε = 0.039

T/K	$10^{10}\dot{w}/kgs^{-1}$
1142.6	50.404
1142.6	50.404
1022.0	18.444
1022.0	18.361
972.8	9.108
1217.5	66.467
1217.5	66.093
1085.5	35.265
1085.5	34.688
1258.3	71.541
1258.3	70.352
1258.3	70.530
923.1	4.995
1307.9	79.442

Table 4.8 cont'.

T/K	$10^{10}\dot{w}/kgs^{-1}$
1307.9	78.956
1307.9	79.283

Table 4.9

GaP : HBr 0.002 m channel $\varepsilon = 0.059$

T/K	$10^{10}\dot{w}/kgs^{-1}$
1023.7	18.193
1023.7	18.193
925.2	7.888
925.2	7.911
1088.0	27.978
1088.0	27.750
1145.5	35.035
1145.5	35.110
1145.5	34.755
975.2	11.926
975.2	11.881
874.9	4.642
874.9	4.656
1218.8	40.364
1218.8	40.161
1218.8	40.000
1308.8	44.027
1308.8	43.772

Table 4.9 cont'.

T/K	$10^{10}\dot{w}/kgs^{-1}$
1308.8	44.071
1260.2	42.068
1260.2	41.328
1260.2	41.245
992.4	13.661
992.4	13.640
992.4	13.681
822.2	1.947
822.2	1.965
822.2	1.998
772.8	0.755
1042.0	21.346
1042.0	21.034
897.6	5.848

Table 4.10

GaP : HBr 0.002 m channel $\varepsilon = 0.035$

T/K	$10^{10}\dot{w}/kgs^{-1}$
1023.0	13.764
1023.0	13.897
1023.0	13.792
922.2	4.960
922.2	4.901
922.2	4.926

Table 4.10 cont'.

T/K	$10^{10}\dot{w}/kgs^{-1}$
1084.3	20.579
1084.3	20.369
1084.3	20.535
1144.4	25.855
1144.4	25.855
1218.2	29.094
1218.2	29.524
1218.2	29.438
822.4	1.399
823.2	1.431
823.2	1.450
1258.7	31.783
1258.7	31.551
1258.7	31.688
973.5	8.879
973.5	8.702
973.5	8.720
873.2	3.030
873.2	3.040
1307.8	31.551
1307.8	31.923
1307.8	31.415
1307.8	31.689
772.6	0.366

Table 4.11

GaP : HBr 0.001 m channel $\varepsilon = 0.059$

T/K	$10^{11}\dot{w}/kgs^{-1}$
1308.1	112.009
1308.1	110.778
1308.1	109.43
1308.1	109.58
1024.5	45.446
1024.5	45.401
1024.5	45.583
1146.8	83.528
1146.8	85.360
1146.8	84.007
1222.1	97.656
1222.1	99.402
1222.1	98.419
1262.8	103.84
1262.8	103.10
1087.1	68.306
1087.1	67.799
975.6	29.556
975.6	30.353
975.6	29.886
975.6	30.414
1044.4	50.711
1044.4	50.404
925.4	21.261

Table 4.11 cont'.

T/K	$10^{11}\dot{w}/kgs^{-1}$
925.4	20.928
925.4	21.034
824.8	13.020
824.8	13.007
875.9	17.435
875.9	17.531
774.9	7.185
774.9	7.185
995.9	34.464
995.9	34.178
944.4	23.706
944.4	23.673
838.4	14.527
838.4	14.325
794.6	9.596
898.2	19.723

Table 4.12

GaP : HBr 0.001 m channel $\varepsilon = 0.035$

T/K	$10^{11}\dot{w}/kgs^{-1}$
1259.0	72.464
1259.0	73.066
1259.0	72.391
1143.1	60.920

Table 4.12 cont'.

T/K	$10^{11}\dot{w}/kgs^{-1}$
1143.1	61.543
1143.1	60.732
1022.8	33.267
1022.8	33.411
1022.8	33.524
923.2	13.994
923.2	13.905
923.2	13.861
1306.2	74.682
1306.2	74.757
1217.7	68.621
1217.7	69.441
1217.7	69.306
1217.7	69.167
1084.3	48.301
1084.3	48.213
973.7	21.303
973.7	20.922
973.7	21.062
875.1	10.561
1043.1	37.127
1043.1	37.871
1043.1	37.519
822.9	7.642
774.0	4.061
944.1	16.324

Table 4.12 cont'.

T/K	$10^{11}\dot{w}/kgs^{-1}$
944.1	16.100
991.7	25.575
843.2	9.328
843.2	9.199
844.6	9.541
898.2	11.113

REFERENCES TO CHAPTER FOUR

4.1 S.W. Yardley, unpublished work

4.2 E.J. Tarbox, PhD Thesis, London (1977)

4.3 R.H. Moss, PhD Thesis, London (1975)

4.4 D. Battat, M.M. Faktor, J. Garrett and R.H. Moss, J. Chem. Soc. Faraday I, 70, 2302 (1974)

4.5 M.M. Faktor, J. Garrett, M.H. Lyons and R.H. Moss, J. Chem. Soc. Faraday I, 73, 1446 (1977)

4.6 S. Chapman and T. Cowling, The Mathematical Theory of Non-uniform Gases (University Press, Cambridge, 1960)

4.7 D. Battat, M.M. Faktor, J. Garrett and R.H. Moss, J. Chem. Soc. Faraday I, 70, 2293 (1974)

4.8 D. Battat, unpublished work

4.9 Selected Values of Thermodynamic Properties, US National Bureau of Standards, Tech. Note 270-3 (1968)

4.10 S. Martosudirdjo and J.N. Prate, Thermal Analysis 10, 23 (1974)

4.11 M. Illegens, M.B. Panish and J.R. Arthur, J. Chem. Therm. 6, 157 (1974)

4.12 R.H. Cox and M.J. Pool, J. Chem. Eng. Data 12, 247 (1967)

4.13 JANAF, Thermochemical Tables, 2nd Ed., US Department of Commerce, National Bureau of Standards (1971)

4.14 A.V. Sandulova and M.I. Droneguk, Russ. J. Phys. Chem 47, 603 (1973)

4.15 O. Kubaschewski, E.L. Evans and C.B. Alcock, Metallurgical Thermochemistry (Pergamon, 1967)

4.16 M.G. Drake and G.M. Rosenblatt, J. Chem. Phys. 65, 4067 (1976)

4.17 Yu Kh Shaulov and A.M. Mosin, Zhur. Fiz. Khim. 47, 1131 (1973)

4.18 M.B. Panish and J.R. Arthur, J. Chem. Therm. 2, 299 (1970)

4.19 C.T. Foxon, B.A. Joyce, R.F.C. Farrow and R.M. Griffiths, J. Appl. Phys. D, 7, 2422 (1974)

4.20 R.F.C. Farrow, ibid. 7, 2436 (1974)

CHAPTER FIVE

Chemical Vapour Transport of Indium Phosphide

5.1 Introduction

The modified entrainment method (MEM) has been employed to study the chemical vapour transport (CVT) of indium phosphide using hydrogen bromide as the reactive gas. The experiments described here were performed using apparatus discussed previously[1].

Samples were loaded into integral bottles as a coarse powder. The rates of weight loss were recorded as a function of temperature within the range from 710 to 1250 K. Below 850 K a preheater was used to effect conversion of the bromine, entrained in the ballast hydrogen flow, into hydrogen bromide. The formation of hydrogen bromide, although favourable on thermodynamic grounds, becomes kinetically constrained below 850 K.[2]

Indium phosphide has a reported congruent melting point of 1326 K. At this temperature, it exhibits a dissociation pressure approaching 3040 kPa[3] (30 atmospheres). Open tube transport studies on indium phosphide have illustrated the presence of elemental indium at temperature as low as 650 K[4].

Fortunately, the separation of a second condensed phase (indium) will be supressed by the continous replenishment of hydrogen bromide, so effecting transportation of the indium. Eventually, however, with rising temperature, expectation would be that a point would be reached where a non-stoichiometric

phase would inevitably be generated. Such an instance would result once the flux of phosphorus excedes that of indium.

5.2 Calibration of hydrogen bromide flow rates

The procedures followed for this calibration were those used previously at this laboratory[1]. The furnace is set at an elevated temperature (800 - 1200 K), and the hydrogen flow rates adjusted to simulate a MEM experiment. Exhaust gases from the apparatus, instead of being vented directly to waste, pass through one of two columns connected in parallel. These columns are approximately half a metre in height and are packed with glass beads.

To determine the HBr flow rate, the exhaust gas stream is passed through one of these columns for a given time, while sodium hydroxide solution (1 M) is percolated down through it. Added to the alkali solution was phenolphthalein indicator to readily assess whether the HBr was being fully absorbed during its passage. Eluent and washings from the column are then back titrated to determine the quantity of unreacted alkali with hydrochloric acid (1 M).

25 ml aliquots of 1 M NaOH solution are taken and diluted to 100 ml with water, a few drops of indicator added, and the solution transferred to a dropping funnel. A steady stream of the solution is passed down the column while the exhaust gases pass up. The second column provides a by-pass with a similar resistance to flow, as the first.

After a predetermined time (20 - 30 minutes), the gas flow is stopped and the column is washed through with water, and the

eluent removed for titration.

	molecular weight of HBr	=	80.91697 $gmol^{-1}$
	specific volume @ 20 °C; 1 atm	=	299.6 $cm^3 g^{-1}$
	molar volume	=	24242.72 cm^3
	1 dm^3 of 1M NaOH	=	24242.72 cm^3 HBr
so	1 cm^3 Of 1M NaOH	=	24.243 cm^3 HBr

Float heights, for hydrogen flow, were maintained at 13.1 and 11.0. Table 5.1 lists the results using water thermostat temperatures of 27.0, 29.8, 35.0, 39.8 and 44.0 °C. The float heights of 13.1 and 11.0 correspond to flow rates of hydrogen of 119.1 and 86.1 $cm^3\ min^{-1}$ respectively at 293.0 K.

Table 5.1

Thermostat temp' /°C	HBr flow rate $cm^3 min^{-1}$	residual H_2 flow rate $cm^3 min^{-1}$	ε
27.0	6.51	216.97	0.0300
29.8	7.54	216.45	0.0348
35.0	10.23	215.11	0.0476
39.8	12.90	213.77	0.0604
44.0	16.23	212.11	0.0765

These results are plotted graphically in fig 5.1.

5.3 Results.

An initial sample of 0.3760 g was loaded in a 1 mm diameter channel bottle and suspended as described earlier (cf ch 2). The temperature was raised and held at 1107.2 K (in a gas

Fig 5.1 Calibration of the Hydrogen Bromide Flow Rate.

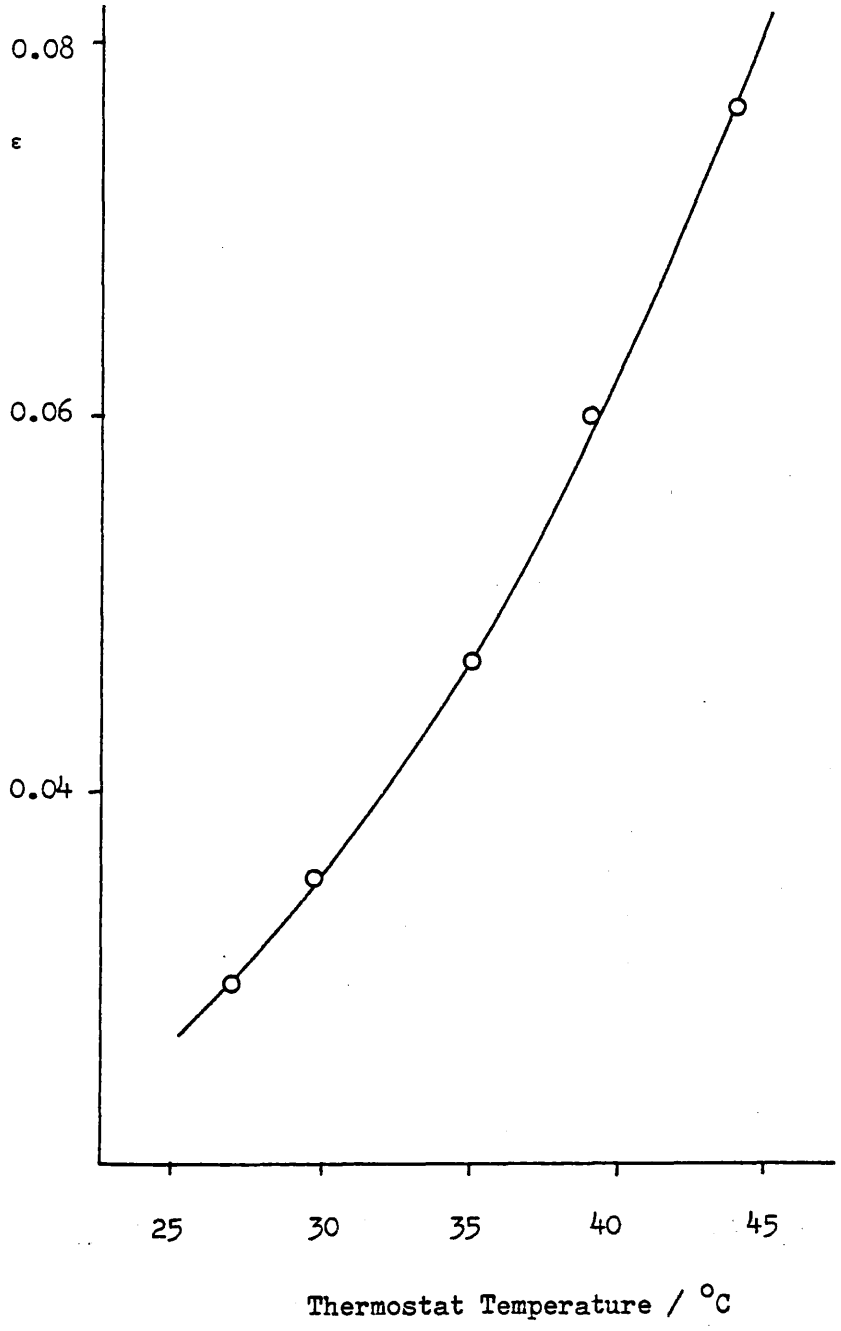

stream of hydrogen containing HBr, $\varepsilon = 0.0604$) in order to transport away a little of the sample so as to expose a fresh surface for the studies. The temperature was mainained for a duration commensurate with a loss of 50 mg in sample weight. During this period, the rate of weight loss remained constant. The temperature of the sample was then steadily raised, and the rate of weight loss monitered. With rising temperature, the rate of weight loss also increased until the sample reached 1259 K. At this temperature, a discontinuity in rate of weight loss occurred as the sample now began to lose weight more slowly.

On raising the furnace to afford visual inspection of the sample, a uniform sphere of material was observed, indicating that it had melted. The dramatic change in the rate of weight loss was then attributed to the change in surface area accompanying fusion of the sample.

In the ensuing experiments, care was taken not to exceed a temperature of 1230 K, thus avoiding the phenomena detailed above.

Two MEM experiments were now performed. In the first, a 0.4765 g sample was suspended in a gas flow, yielding $\varepsilon = 0.0348$. The numerical results are set out in table 5.2. The second experiment used a lighter sample (wt 0.2302 g), and a higher partial pressure of HBr, resulting in a value of $\varepsilon = 0.0604$. The numerical results appear in table 5.3. Graphical representation of these are plotted in fig 5.2.

In view of the premature melting of the first sample studied, beside limiting the temperature, it was decided not to heat the

Fig 5.2 Initial Results for InP:HBr,

0.001 m Ø channel.

ε = 0.0604 & (A)

ε = 0.0348 (B)

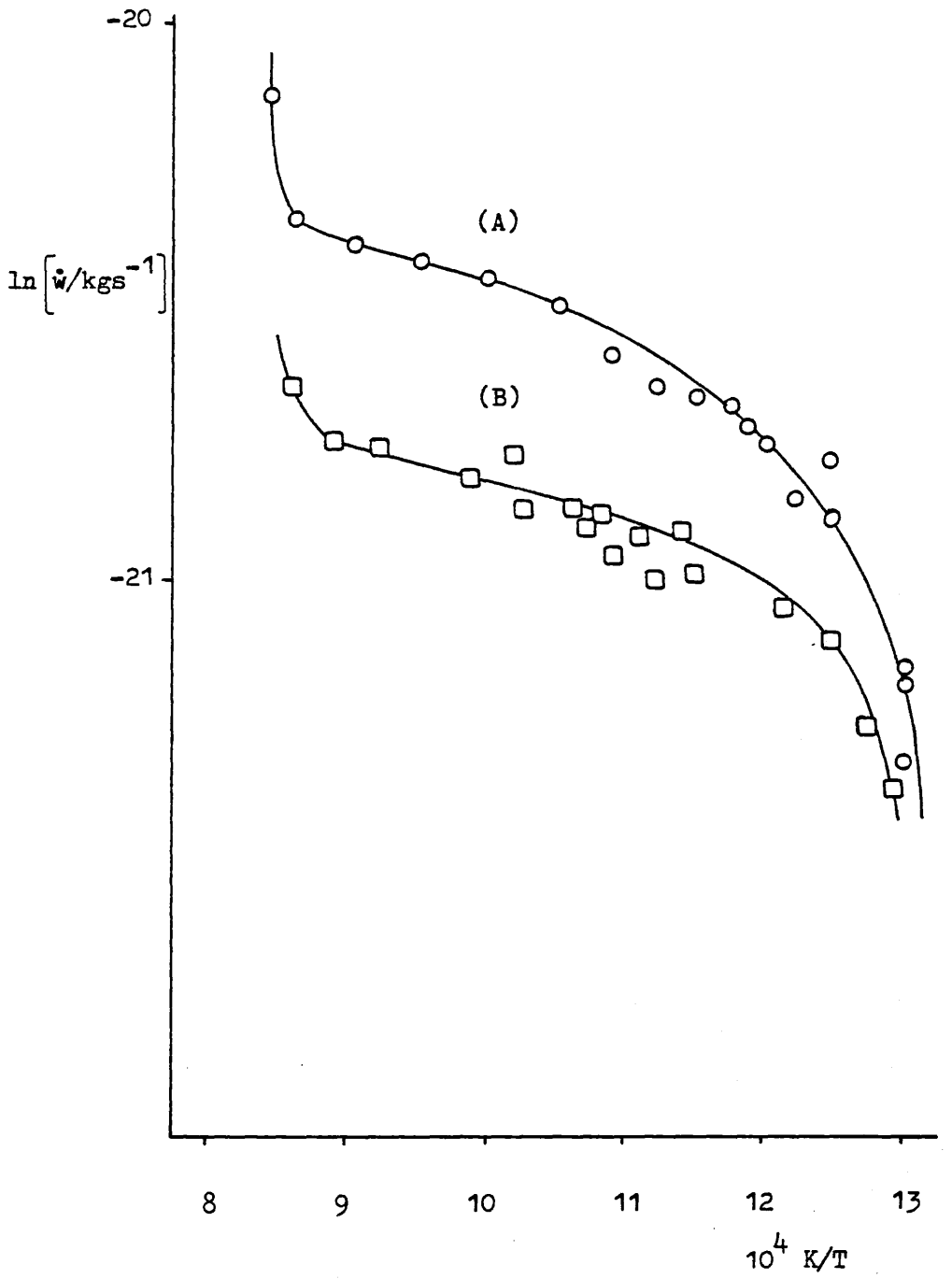

Table 5.2

Weight loss data for InP : HBr system, using a 0.001 m Ø channel, and $\varepsilon = 0.0348$.

T/K	$10^{10}\dot{w}$/kg s^{-1}	T/K	$10^{10}\dot{w}$/kg s^{-1}
1122.6	9.621	773.3	5.269
1122.7	9.946	773.3	5.242
1122.7	9.676	773.3	5.275
1122.7	10.074	773.3	5.259
1084.6	9.914	933.9	8.341
1084.5	9.407	933.9	8.424
1084.5	9.514	933.9	8.200
1084.5	9.665	933.9	8.477
1013.2	9.304	801.4	6.283
1013.2	9.183	801.4	6.237
1013.2	8.988	800.9	6.237
1013.2	9.263	800.9	6.191
924.2	8.079	974.9	8.675
923.3	8.693	974.6	8.997
922.7	8.501	975.1	9.183
922.1	8.467	974.7	9.084
1163.3	10.650	899.2	8.387
1163.3	10.341	899.2	8.383
1163.3	11.086	899.2	8.311
1163.3	10.837	899.2	8.313
874.0	8.280	844.4	7.641
874.0	8.268	844.2	7.479
825.4	6.997	844.2	7.587
825.4	7.576	844.2	7.533
825.4	7.115	808.5	6.720
825.4	7.115	810.5	6.828
876.7	7.782	809.2	6.906
875.2	7.782	809.2	6.828

Table 5.2 cont!

T/K	$10^{10}\dot{w}$/kg s^{-1}	T/K	$10^{10}\dot{w}$/kg s^{-1}
784.6	6.005	944.3	8.894
783.7	5.799	944.3	8.711
783.2	5.979	944.3	8.765
783.2	5.744	944.3	8.711
866.0	7.600	915.3	8.094
866.0	7.628	915.3	7.913
866.0	7.840	914.7	7.753
866.0	7.811	914.7	7.768

Table 5.3

Weight loss data for InP : HBr system, using a 0.001 m Ø channel, and ε = 0.0604.

T/K	$10^{10}\dot{w}$/kg s^{-1}	T/K	$10^{10}\dot{w}$/kg s^{-1}
834.3	9.243	890.4	11.050
834.3	9.961	841.3	9.901
834.3	9.556	841.3	9.950
834.3	9.687	841.3	10.217
870.0	10.504	841.3	10.101
870.0	10.275	766.4	5.482
870.0	10.492	766.4	6.289
870.0	10.717	766.4	6.508
819.4	8.912	919.7	11.412
819.6	8.766	919.7	11.132
819.7	9.143	919.7	11.696
819.7	8.639	919.7	10.723
890.8	11.086	858.4	10.417
890.4	10.554	858.4	10.142
890.4	11.158	858.4	10.384
890.4	11.050	858.4	10.040

Table 5.3 cont'.

T/K	$10^{10}\dot{w}$/kg s^{-1}
801.5	9.483
806.0	8.547
806.0	8.446
806.0	8.482
850.4	10.101
850.4	10.309
850.4	9.915
850.4	10.323
796.2	1.670
796.2	1.584
796.2	1.444
796.2	1.286
796.2	1.231
796.2	1.212
953.1	12.690
953.1	12.295
953.1	12.255
953.1	12.346
1001.9	13.021
1001.9	12.891
1001.9	12.920
1001.9	13.089
1053.0	13.477
1053.0	13.441
1053.0	13.387
1053.0	13.351
1101.8	14.045
1101.8	13.793
1102.0	14.006
1102.0	14.085
1162.8	14.409
1162.8	14.286
1162.8	14.663
1162.8	14.409
1162.0	14.535
1162.0	14.709
1162.0	14.620
1162.0	14.706
1182.0	17.731
1182.0	17.921
1182.9	18.587
1182.9	18.450
931.9	12.285
931.9	12.136
931.9	11.682
931.9	11.848

samples appreciably in the absence of the transporting gas. The samples were thus bathed in HBr at temperatures from 370 K upwards. During periods when the samples were held at their lower temperatures, a gain in weight was observed.

There are three notable features of these results that warrant immediate comment. Firstly, the upward turn in both graphs at high temperature. This feature has already been predicted in that indium phosphide does not melt congruently at atmospheric pressure. As expected, the upward turn of the curve occurs at a lower temperature in the lower epsilon experiment. The second observation concerns the gradients of the lines. Comparison with the results for the transport of gallium phosphide or gallium and indium arsenide illustrates that those for indium phosphide exhibit particularly shallow gradients. Below 830 K the graphs show a distinctive downward curvature. This feature displayed in a low temperature region has previously been attributed to kinetic influence at the phase interface.

We have found, then, that the transportation of indium phosphide via the vapour phase utilizing hydrogen bromide has several interesting aspects, some of which have not been previously encountered.

5.4 Thermodynamic aspects.

The results so far presented would suggest that a single CVT reaction is responsible for transport of indium phosphide. Reactions 5.1 and 5.2 should then be considered:

$$InP(c) + HBr(g) = InBr(g) + \tfrac{1}{4}P_4(g) + \tfrac{1}{2}H_2(g) \qquad (5.4.1)$$

$$P_4(g) = 2P_2(g) \qquad (5.4.2)$$

Listed in table 5.4 is the relevant thermodynamic data.

Using selected values for the thermodynamic functions involved, best-estimates for the heat and entropy of reaction 5.4.1 are calculated.

$$\Delta H_{r1000} = 110.9 \text{ kJ mol}^{-1}$$
$$\Delta S_{r1000} = 125.5 \text{ J K}^{-1}\text{mol}^{-1}$$

Inserting these values, in conjunction with a value for D_{oHBr} of 0.48×10^{-4} $m^2 s^{-1}$, gave an inadequate simulation of the experimentally observed findings.

In order to establish clear agreement between the experiment and the simulation, it was found necessary to reduce both ΔH_r and ΔS_r. Figure 5.3 shows the best correlation. Generally, however, sigma was rather insensitive to changes in ΔH and ΔS.

Let us briefly consider the value of the equilibrium constant for the transport reaction at 1000 K.

K_{p1000}	ΔH_{r1000}	ΔS_{r1000}
6	111	126
23	96	122
250	80	126

As already mentioned, the flux of material leaving the bottle through the narrow capillary may become limited by the rate of arrival of reactive gas. This constraint on weight loss manifests as the equilibrium constant becomes greater than unity. As a rule of thumb, $K_p = 10$ may be considered large. From such considerations, it would seem likely that the transport of InP is "diffusion limited" above 1000 K. This would explain the

Table 5.4

species	ΔH_f°/kJ mol^{-1}	S_f°/J K^{-1}mol^{-1}	C_p°/J K^{-1} mol^{-1}
InP(c)	75.3[11]	59.7[11]	51.9[12]
In(c)	0	57.8[11]	27.4[11]
(g)	242.7[11]	173.6[11]	
Br(g)	118.0[13]	174.9[13]	20.8[13]
Br_2(l)	0	152.2[13]	75.7[13]
(g)	30.9[11]	245.4[13]	36.0[13]
HBr(g)	-36.4[13] -36.4[14]	198.6[13]	29.2[13]
P(g)	314.6[13] 333.9[15]	163.1[13] 163.1[14]	
P_2(g)	144.3[13] 178.6[15]	218.0[13] 218.0[15]	31.8[11]
P_4(g)	58.9[13] 128.9[15]	279.9[13] 179.9[15]	66.9[11]
InBr(c)	-175.3[11] -173.6[16]	114.2[11] 113.8[17]	36.7[16]
(g)	-51.5[11] -54.8[16,17] -13.8[18]	259.5[11]	
$InBr_2$(c)	-410.9[11]	178.9[11]	
H_2(g)	0	130.5[15]	28.8[11]

All the above data is refered to a standard state temperature of 298.15 K.

Fig 5.3 Graph of $\ln \dot{w}_{calc}$ v 10^4 K/T

Initial Fit for the First Experiments.

ε = 0.0604 & (A)

ε = 0.0348 (B)

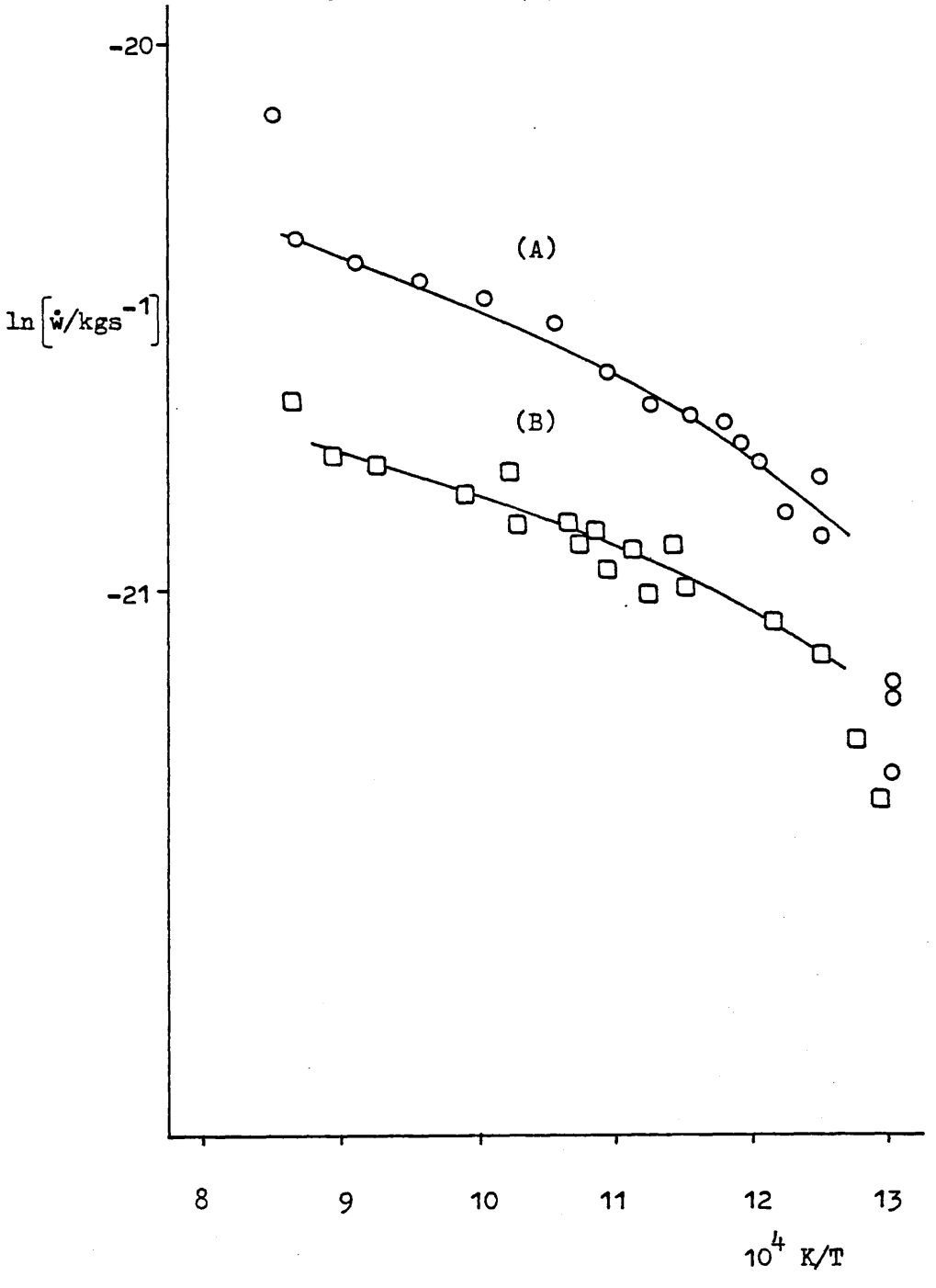

particularly shallow gradient of the graph, and also the insensitivity to changes in ΔH and ΔS encountered when computer modelling.

Armed with the foregoing appraisal, further experiments were planned and performed.

5.5 Dissociative sublimation of indium phosphide.

We are aware that InP does not melt congruently at atmospheric pressure. Experiment would suggest that at sufficiently elevated temperatures, preferential loss of phosphorus occurs despite a negative flux of HBr. In order to observe dissociative sublimation in isolation from reactive transport phenomena, a sample was investigated in the absence of HBr (ie $\varepsilon = 0.0$).

The results are documented in table 5.5 and are presented graphically in fig 5.4. Predictably, the graph displays a very steep gradient. Figure 5.5 shows the results for $\varepsilon = 0$, 0.0348 and 0.060 superimposed on a single set of axes.

Derivation of the weight loss equation.

We shall assume that the participating equilibria are:

$$InP(c) = In(l) + \tfrac{1}{2}P_2(g) \qquad (5.5.1)$$

and

$$P_4(g) = 2P_2(g) \qquad (5.5.2)$$

labelling the gas species as $2 = P_2$, and $4 = P_4$, and again defining α as the ratio of the fluxes of P_2 and P_4.

$$\alpha = j_2/j_4 \qquad (5.5.3)$$

and

$$j_P = 2j_2 + 4j_4 \qquad (5.5.4)$$

Table 5.5

Weight loss data for the dissociative sublimation of indium phosphide in a hydrogen atmosphere.

T/K	$10^{10}\dot{w}$/kg s^{-1}
1135.2	0.911
1135.2	0.921
1146.8	1.317
1147.4	1.412
1157.5	2.034
1157.5	2.141
1168.2	3.236
1168.2	2.892
1181.5	4.669
1181.5	4.803
1188.9	5.910
1188.3	6.224
1198.2	8.547
1198.2	7.968
1215.1	16.835
1215.1	17.153
1244.4	38.462
1241.4	26.774
1156.4	1.949

Fig 5.4 Results for the Dissociative Sublimation of Indium Phosphide, 0.001 m Ø channel.

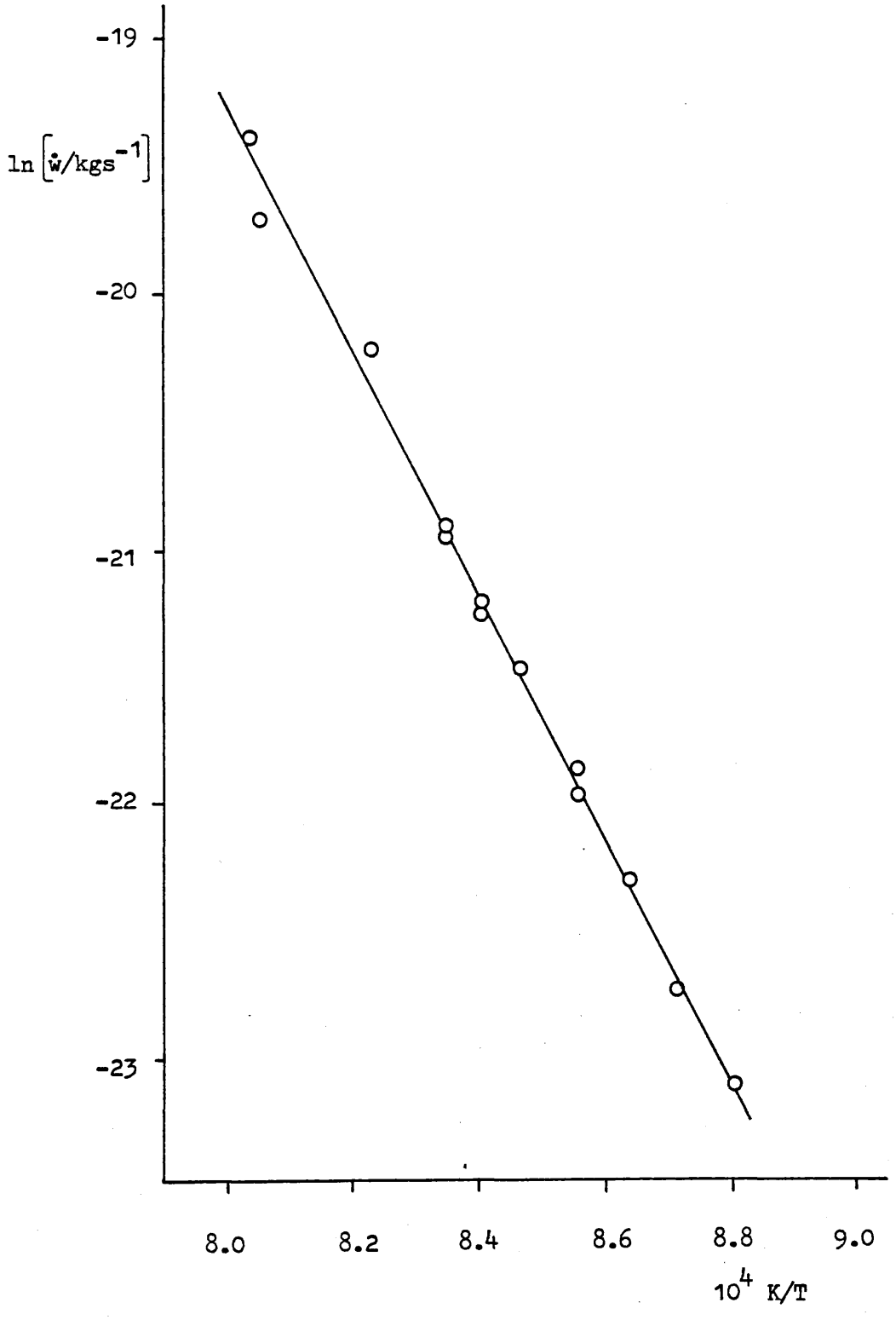

Fig 5.5 CVT and Dissociative Sublimation Results for Indium Phosphide.

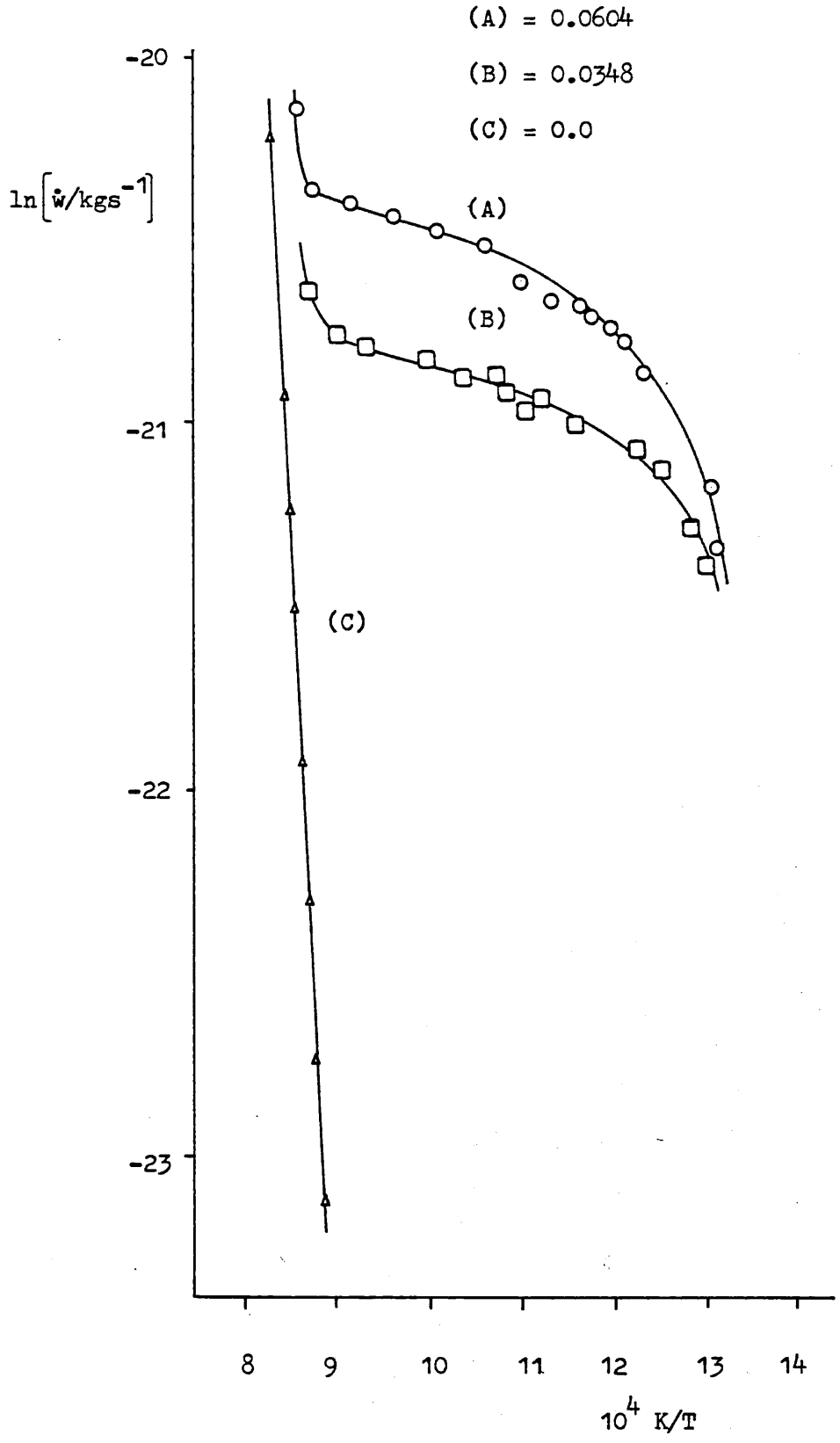

The total flux being:

$$J = \Sigma_i j_i = j_2 + j_4 = j_2 \frac{(\alpha+1)}{2} \qquad (5.5.5)$$

From equation 4.3.3 we may write,

$$\frac{p_2^o}{P} = \frac{j_2}{J} + \frac{P_2^{(1)}}{P} - \frac{j_2}{J} e^{-\xi_2} \qquad (5.5.6)$$

$$\approx \frac{\alpha \xi_2}{1+\alpha} \qquad (5.5.7)$$

Similarly, $$\frac{p_4^o}{P} \approx \frac{\xi_4}{\alpha+1} \qquad (5.5.8)$$

The weight loss, $\dot{w}$, is given by:

$$\dot{w} = A(M_2 j_2 + M_4 j_4) \qquad (5.5.9)$$

$$= A j_2 (M_2 + M_4/\alpha) \qquad (5.5.10)$$

Now substituting $j_2/J = \alpha/(\alpha+1)$ and $M_4 = 2M_2$

$$\dot{w} = AJM_2 \frac{\alpha+2}{\alpha+1} \qquad (5.5.11)$$

(M_2 and M_4 are the molecular **masses** of P_2 and P_4 and A is the cross-sectional area of the MEM channel).

Now combining the above equation with $\xi_2 = \frac{JRTl}{D_{(2,H_2)}P}$ (cf ch 4) we obtain:

$$\xi_2 = \frac{\dot{w}}{AM_2} \frac{\alpha+1}{\alpha+2} \frac{RTl}{D_{(2,H_2)}P} \qquad (5.5.12)$$

Now $$K_p = \sqrt{\frac{p_2^o}{P^{\ominus}}} \qquad (5.5.13)$$

Combining 5.5.7, 5.5.12 and 5.5.13

$$\dot{w} = \frac{K_p^2 P^o D_{(2,H_2)} AM_2}{RTlF} \qquad (5.5.14)$$

where $F = \alpha/(4+2\alpha)$

We shall use Graham's law for scaling the diffusion coefficient,

hence $D_2 = D_{(P_2,H_2)} = D_{(P_4,H_2)}\sqrt{M_4/M_2} = \sqrt{2}D$

therefore

$$\dot{w} = \frac{\sqrt{2}DP^{o}AM_2K_c^2}{RT1F} \qquad (5.5.15)$$

An expression for F.

$F = \alpha/(4+2\alpha)$ and $\alpha = j_2/j_4$

This term F takes account of the changing degree of dissociation in the $P_4 = 2P_2$ equilibrium with changing temperature. (At first reading the form seems unsound, because at low temperature $j_2 \to 0, \alpha \to 0$, so $F \to 0$ and $\dot{w} \to \infty$. This is illusorily, because as $j_2 \to 0$ then $p_2^o \to 0$ and then also $K_p \to 0$. The limiting behaviour of equations 5.5.7 and 5.5.12 is more predictable).

$$\alpha = j_2/j_4 \quad \frac{p_2^oD_2}{p_4^oD_4} \quad \frac{p_2^o}{p_4^o}\sqrt{\frac{M_4}{M_2}} = \sqrt{2}\,\frac{p_2^o}{p_4^o} \qquad (5.5.16)$$

Starting with n moles of P_4 at a given temperature, T, it is readily shown that the degree of dissociation, β, is independent of n, and is related to the equilibrium constant, K_p, for $P_4 = 2P_2$ by the expression:

$$\beta = \sqrt{\frac{K_p}{K_p+4(P/P^{\ominus})}} \qquad (5.5.17)$$

(cf ch 4)

where P = total pressure and $P^{\ominus}$ = standard state pressure.

Also

$$\frac{p_2^o}{p_4^o} = \frac{2\beta}{1-\beta} \qquad (5.5.18)$$

Hence the expression for F is evaluated from the following three equations:

$$F = \alpha/(4+2\alpha)$$

$$\alpha = 2\sqrt{2}\beta/(1-\beta)$$

$$\beta = (K_p/(K_p+4(P/P^{\ominus})))^{\frac{1}{2}}$$

Some numerical values for these are tabulated below in tables 5.6 and 5.7.

Table 5.6

T/K	K_p	α	β	F
700	2.3×10^{-9}	6.8×10^{-5}	2.4×10^{-5}	1.7×10^{-5}
800	2.9×10^{-7}	7.6×10^{-4}	2.7×10^{-4}	1.9×10^{-4}
900	1.2×10^{-5}	4.8×10^{-3}	1.7×10^{-3}	1.2×10^{-3}
1000	2.9×10^{-4}	2.4×10^{-2}	8.5×10^{-3}	5.9×10^{-3}
1100	2.9×10^{-3}	7.8×10^{-2}	2.7×10^{-2}	1.9×10^{-2}
1200	2.3×10^{-2}	2.3×10^{-1}	7.6×10^{-2}	5.2×10^{-2}
1300	1.3×10^{-1}	6.2×10^{-1}	1.8×10^{-1}	1.2×10^{-1}

where K_p is given by:

$$K_p = 1.4250\times10^{8}\ \exp(-27073.8/T) \qquad \text{and } P/P^{\ominus} = 1$$

Table 5.7

T/K	K_p	α	β	F
700	1.1×10^{-10}	1.5×10^{-3}	5.2×10^{-6}	3.7×10^{-6}
800	2.0×10^{-8}	2.0×10^{-4}	7.1×10^{-3}	5.0×10^{-5}
900	1.2×10^{-6}	1.6×10^{-3}	5.5×10^{-4}	4.0×10^{-4}
1000	3.0×10^{-5}	7.7×10^{-3}	2.7×10^{-3}	1.9×10^{-3}
1100	4.3×10^{-4}	2.9×10^{-2}	1.0×10^{-2}	7.2×10^{-3}
1200	3.9×10^{-2}	9.0×10^{-2}	3.1×10^{-2}	2.2×10^{-2}
1300	2.5×10^{-2}	2.4×10^{-1}	7.9×10^{-2}	5.4×10^{-2}

here K_p is given by:

$$K_p = 1.4250 \times 10^8 \exp(-29190.7/T) \qquad \text{and } P/P^{\ominus} = 1$$

5.6 Simulation results.

The weight loss equation derived above, 5.5.15, provides a most unsatisfactory interpretation of the experimental results. This is illustrated in fig 5.6, which shows the experimental line falling well below, and with a different gradient from, the line calculated using literature data[3] for the dissociative sublimation of InP.

5.7 Modification of equations.

One over sight of the above development is that the pressure dependence of the $P_4(g) = 2P_2(g)$ equilibrium has been ignored. The total pressure, P, has been assumed to be one atmosphere (101325 Pa). In fact it take greater values than this as the temperature approaches the melting point of InP(c). So now we write $P = p^o_{H_2} + p^o_{P_2} + p^o_{P_4}$.

Secondly the influence of the inert entrainment gas (H_2), was not considered.

Ignoring the $P_4(g) = 2P_2(g)$ equilibrium and assuming that the phosphorus exists soley as $P_2(g)$. Thus $\alpha \to \infty$ when $F \to \frac{1}{2}$ and hence,

$$\dot{w} = \frac{\sqrt{2DP^o AM_2 K_p^2}}{RTl} \qquad (5.7.1)$$

This equation shows a marked improvement in fitting the results, see fig 5.6.

Consider the equilibrium $P_4(g) = 2P_2(g)$, but now in the presence of m moles of hydrogen. At any temperature, T, let,

$$C = \frac{\text{number of moles of hydrogen (m)}}{\text{number of moles of phosphorus as } P_4}$$

Now recall from chapter 4,

$$K_p = 4\beta^2 P/((1-\beta)(1+\beta)P^o)$$

this now becomes,

$$K_p = 4\beta^2 P/((1+\beta+ C)(1-\beta)P^o) \qquad (5.7.2)$$

and β is given by:

$$\beta = \frac{-K_p C + \sqrt{(K_p^2 C^2 + 4(4+K_p)(K_p+K_p C))}}{2(K_p+4)} \qquad (5.7.3)$$

Equations relating $p^o_{P_2}$, $p^o_{P_4}$ and α are as before but now contain the revised formulation for β.

Now $P = p^o_2 + p^o_4 + p^o_{H_2}$

and $C = p^o_{H_2}/p^o_4$

It is now quite justified to let $P/P^{\ominus} = 1$.

It may be shown that with increasing temperature the decreasing molar ratio of H_2 to P_4, (falling from a value of 1.4×10^7 at 900 K to 28 at 1200 K), has the unexpected effect of decreasing the dissociation of $P_4(g)$.

Employing this modified treatment a good fit to the experimental data is obtained. Three constraints are imposed for this analysis:

1) ΔS_{ds} and ΔS_d are regarded as fixed (as well-established

literature data).

2) ΔH_{ds} and ΔH_d are altered in a dependent manner, ie a change of Δh in ΔH_d was accompainied by a corresponding change of $\frac{1}{4} h$ in H_{ds}.

3) D_o was treated as an arbitary variable, within reasonable limits.

In the above the subscript ds refers to the dissociative sublimation of InP, and the subscript d to the dissociation of P_4.

The results of the simulation are summarised below in table 5.8 and fig 5.6.

Table 5.8

fitted data	literature data	
$\Delta H_d = 242.7$ kJmol^{-1}	225.1 kJmol^{-1}	(ref.5)
	242.7 kJmol^{-1}	(ref.6)
$\Delta S_d = 156.1$ JK^{-1}mol^{-1}	156.1 JK^{-1}mol^{-1}	(ref.7)
$\Delta H_{ds} = 159.0$ kJmol^{-1}	154.0* kJmol^{-1}	(ref.8)
	160.2 kJmol^{-1}	(ref.6)
$\Delta S_{ds} = 113.8$ JK^{-1}mol^{-1}	113.4 JK^{-1}mol^{-1}	(ref.8)
	113.8 JK^{-1}mol^{-1}	(ref.7)
$D_o(HBr,H_2) = 3.3\times10^{-5}$ m^{2}s^{-1}	5×10^{-5}	(ref. 1)
	3.6×10^{-5}**	(ref.9)
	2.7×10^{-5}**	(ref.10)

* NB most of the data here was obtained with In(c) so a correction has been applied for ΔH_m (In).

** Values scaled using Graham's law.

5.8 Further transport experiments.

We have seen that the transport of InP using HBr is

Fig 5.6 Fitted lines for the dissociative sublimation of indium phosphide.

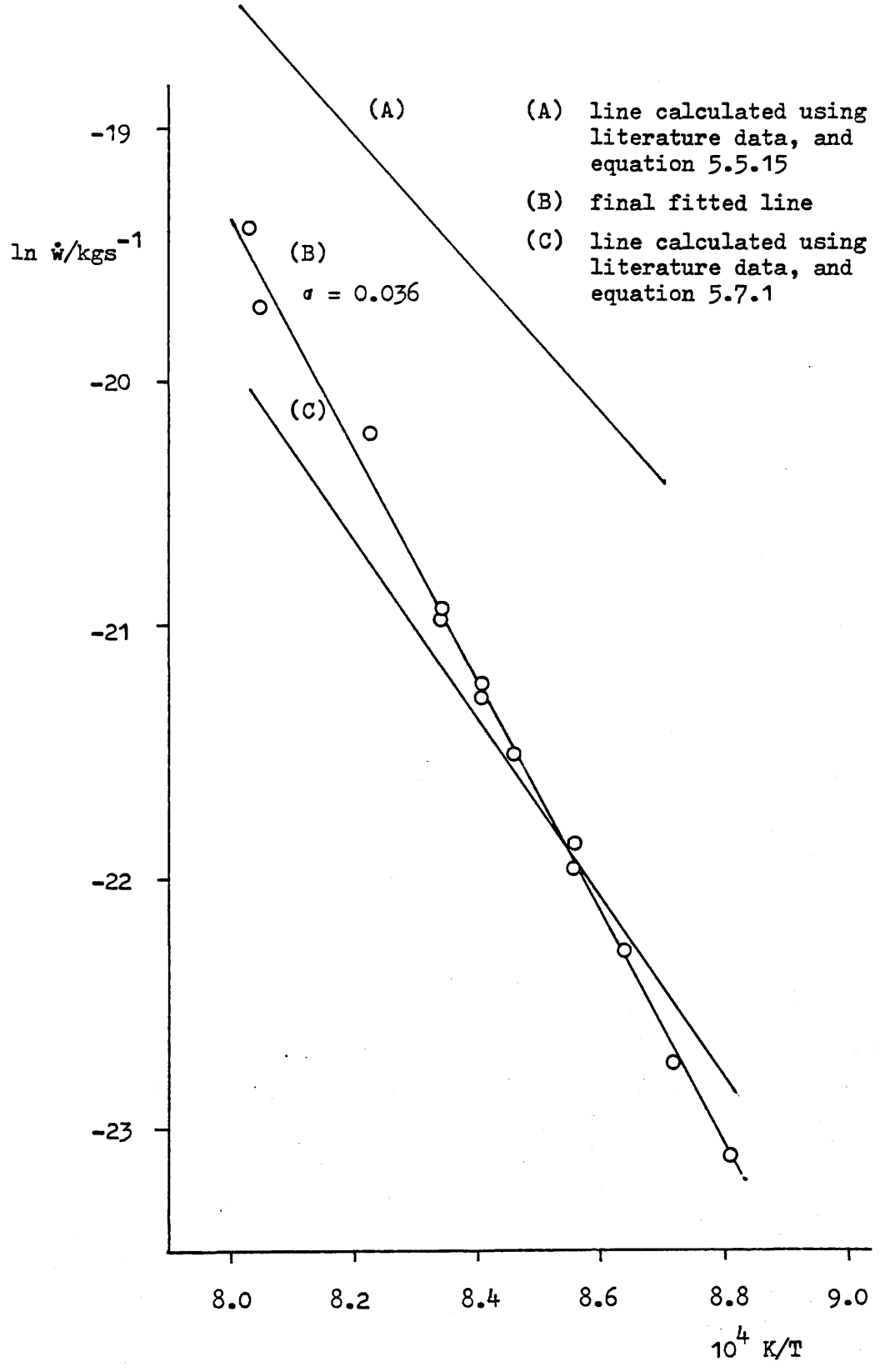

diffusion controlled over a wide temperature range. It is also observed that, in this experimental arrangement, the rate of weight loss due to the incongruent evaporation of phosphorus only becomes comparable with that through vapour transport (CVT) above 1170 K.

The next experiment undertaken was to repeat the study using $\epsilon = 0.0604$. The low temperature region was characterised with some care prior to heating the sample above 1140 K. To complete the experiment, as the calibrated weight range approached exhaustion, the temperature region above 1140 K was investigated. Following the experiment it was noted that the sample had not been melted, its granular aggregation remaining. Experimental results appear in table 5.9 and are graphically displayed in fig 5.7, also displayed in this figure is the data obtained from the dissociative sublimation study. Results from the $\epsilon = 0.0$ work have been normalised to the channel dimensions used for the CVT work.

A very sharp decline in the rate of weight loss is observed at the lower temperatures studied. In fact below 730 K weight loss became barely perceptible. Weight gain was evident when the temperature was lowered to 705 K (432 ^{o}C). A weight gain at the rate of 2.8×10^{-10} kgs^{-1} was recorded at 690.6 K. During the excursion below 730 K the sample gained a little over $\frac{3}{4}$ mg. At the end of this period the furnace was switched to ramp at maximum heating rate to a temperature of 1145 K. Whilst the temperature was rising the weight loss was continuously monitored. Initially evaporation of material from the sample bottle accounted for a weight loss rate four orders of magnitude greater than that normally expected. Approximately $5\frac{1}{2}$ mg were lost at a rate of

Table 5.9

Weight loss data for the second MEM experiment on the InP : HBr system, using a 0.001 m Ø channel, and ε = 0.0604.

T/K	$10^{10}\dot{w}$/kg s^{-1}	T/K	$10^{10}\dot{w}$/kg s^{-1}
1136.5	11.062	850.3	8.333
1136.0	11.377	850.3	8.386
1135.5	11.211	850.9	8.439
1135.8	11.369	849.9	8.503
1005.4	10.352	1083.8	10.989
1005.4	10.163	1083.7	10.823
1005.4	10.288	1083.8	11.123
1005.4	10.449	1084.0	11.034
904.7	9.158	787.8	6.079
904.7	9.311	785.9	6.236
905.4	9.662	785.5	6.400
905.4	9.346	785.5	5.977
875.6	8.790	737.1	2.544
875.6	8.961	737.1	2.569
875.7	8.658	737.1	2.604
875.7	8.677	737.1	2.650
828.9	8.052	744.4	4.039
828.9	8.052	744.4	4.167
828.9	7.968	744.4	4.197
828.9	8.048	744.2	4.259
795.8	6.993	946.9	9.416
794.7	6.601	946.7	9.578
793.4	6.498	946.7	9.416
792.9	6.826	946.7	9.634
756.7	5.170	1036.3	10.376
756.3	5.112	1035.8	10.515
756.3	5.283	1035.8	10.718
756.3	5.043	1036.0	11.062

Table 5.9 cont'.

T/K	$10^{10}\dot{w}$/kg s^{-1}	T/K	$10^{10}\dot{w}$/kg s^{-1}
811.8	7.380	1177.3	12.225
812.7	7.353	1177.3	12.225
812.7	7.366	1195.2	14.136
812.2	7.326	1195.2	15.385
771.7	5.747	1193.3	13.967
771.7	5.731	1193.3	13.774
777.4	5.731	1197.4	14.771
775.7	5.690	1197.4	14.327
753.3	5.066	1202.8	15.408
752.9	4.888	1203.2	15.838
754.1	4.888	1210.9	17.621
753.3	5.124	1210.9	16.807
1148.6	12.056	1216.3	18.323
1148.6	11.799	1216.3	18.692
1149.1	11.854	1221.7	20.915
1149.1	11.799	1221.7	20.915
734.8	1.883	1224.9	22.472
735.5	1.975	1224.9	22.792
734.8	2.109	1227.2	23.035
733.0	2.011	1227.2	23.774
1145.0	12.157		
1145.0	11.779		
1164.8	12.166		
1164.8	12.407		

Fig 5.7 Results of the Second Experiment on the CVT of Indium Phosphide : Hydrogen Bromide, 0.001 m Ø channel, ε = 0.0604.

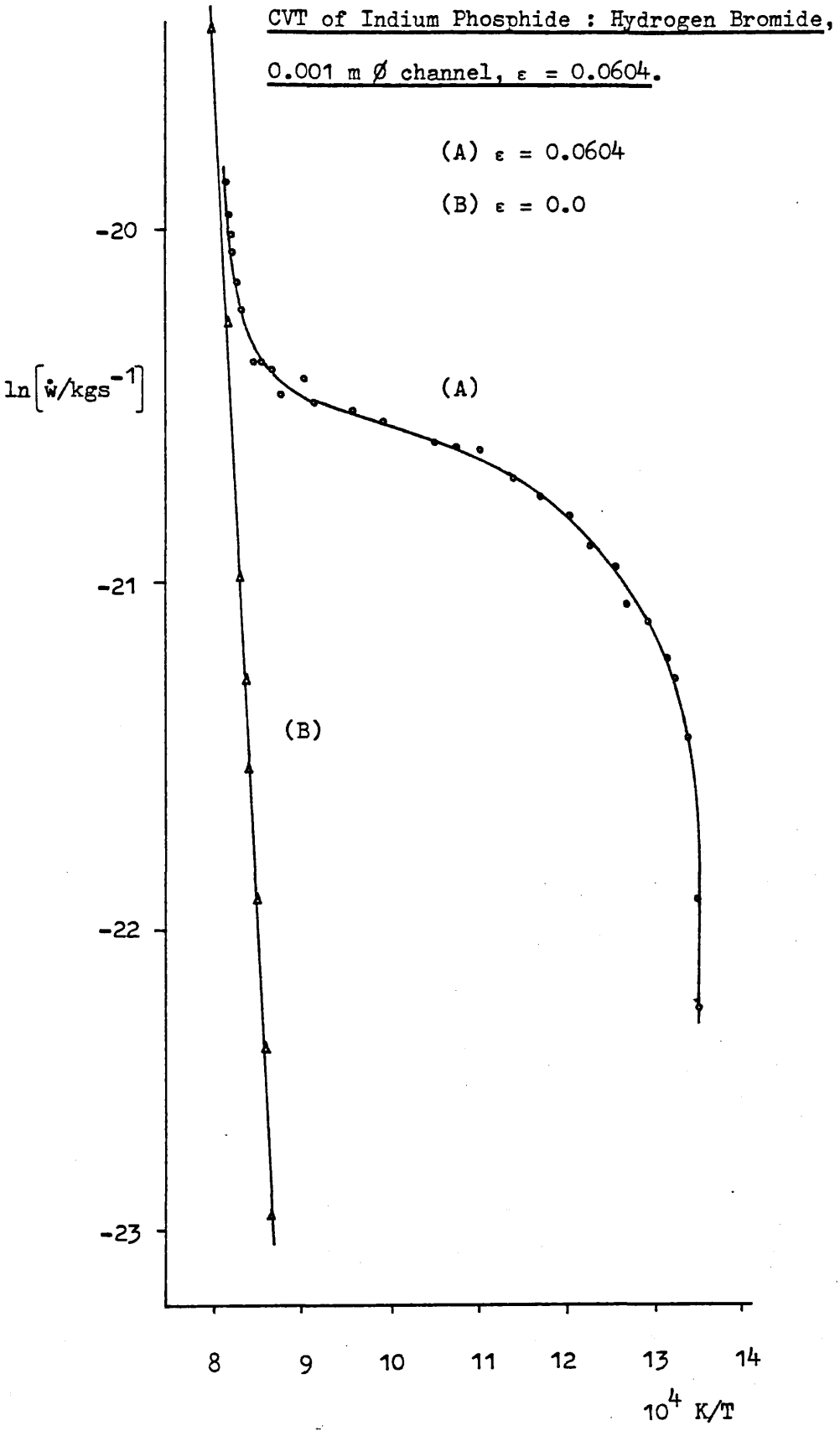

about $3x10^{-5}$ kgs^{-1}. Only when the sample temperature reached ≈1000 K did the rates return to normal proportions.

Downward curvature of a ln $\dot{w}$ v 1/T plot has been observed previously in other systems[1,10]. This effect has been shown generally to exhibit a time dependent nature, and is explained by kinetic limiting of the heterogeneous reactions responsible for weight loss. In this instance, however, no chronological dependence was noted. Another explanation of this phenomenon may be that an indium bromide of fairly low volatility may be generated in the capsule, thus giving rise to condensation.

In order to assess the involvement of kinetic constraints more rigorously the experiment was repeated, but using a capsule having a channel of lower diffusive resistance, (cf ch 4). Table 5.10 details these results, obtained using a nominal channel diameter of 0.002 m, and they are displayed in the usual manner in fig 5.8. If surface kinetics are to play a role in determining the rate of reaction, responsible for generating volatile species, or the rate of desorption of such species, then the rate of weight loss will become dependent upon crystal morphology and surface area. These properties change during the etching of a sample, and so give rise to time dependent results. Data presented in table 5.10 is listed chronologically. Rates of weight loss recorded late in the experiment, around 780 K, might have suggested that kinetic influences were operative. Having cycled the sample again to high temperature, and having lost appreciable further weight, attention was returned to the low temperature region. The final data collected, around 750 K, fall within the experimental scatter of earlier data.

Table 5.10

Weight loss data for InP : HBr system, using a 0.002 m Ø channel, and $\varepsilon = 0.0604$.

T/K	$10^9 \dot{w}$/kg s^{-1}	T/K	$10^9 \dot{w}$/kg s^{-1}
961.7	5.160	1062.8	5.556
961.7	5.189	1062.8	5.533
961.7	5.128	1061.9	5.571
961.7	5.181	1061.9	5.495
857.4	4.469	1095.2	5.747
857.4	4.396	1096.0	5.587
857.4	4.388	1096.0	5.714
857.4	4.571	1096.0	5.682
751.6	2.532	783.8	2.538
751.6	2.600	781.9	2.535
751.6	2.646	781.9	2.473
751.6	2.532	781.9	2.516
734.3	8.091	1112.6	5.882
733.4	8.097	1112.6	5.882
733.4	7.092	1111.8	5.848
733.4	8.130	1111.8	5.900
750.2	2.092	1169.2	6.006
750.2	2.136	1169.2	6.270
750.2	2.072	1166.4	5.882
750.2	2.105	1164.9	6.098
803.7	3.247	1198.8	7.080
803.7	3.551	1198.8	7.299
803.7	3.509	1198.8	7.117
803.7	3.478	1207.3	7.874
915.6	4.854	1211.5	8.772
914.7	4.854	1214.2	8.696
914.7	4.902	751.6	2.558
914.7	4.831	751.6	2.612
1015.7	5.305	751.6	2.530
1012.9	5.420		
1012.9	5.391		
1012.9	5.362		

Fig 5.8 Results for the CVT of Indium Phosphide : Hydrogen Bromide, using a 0.002 m Ø channel, and $\varepsilon = 0.0604$.

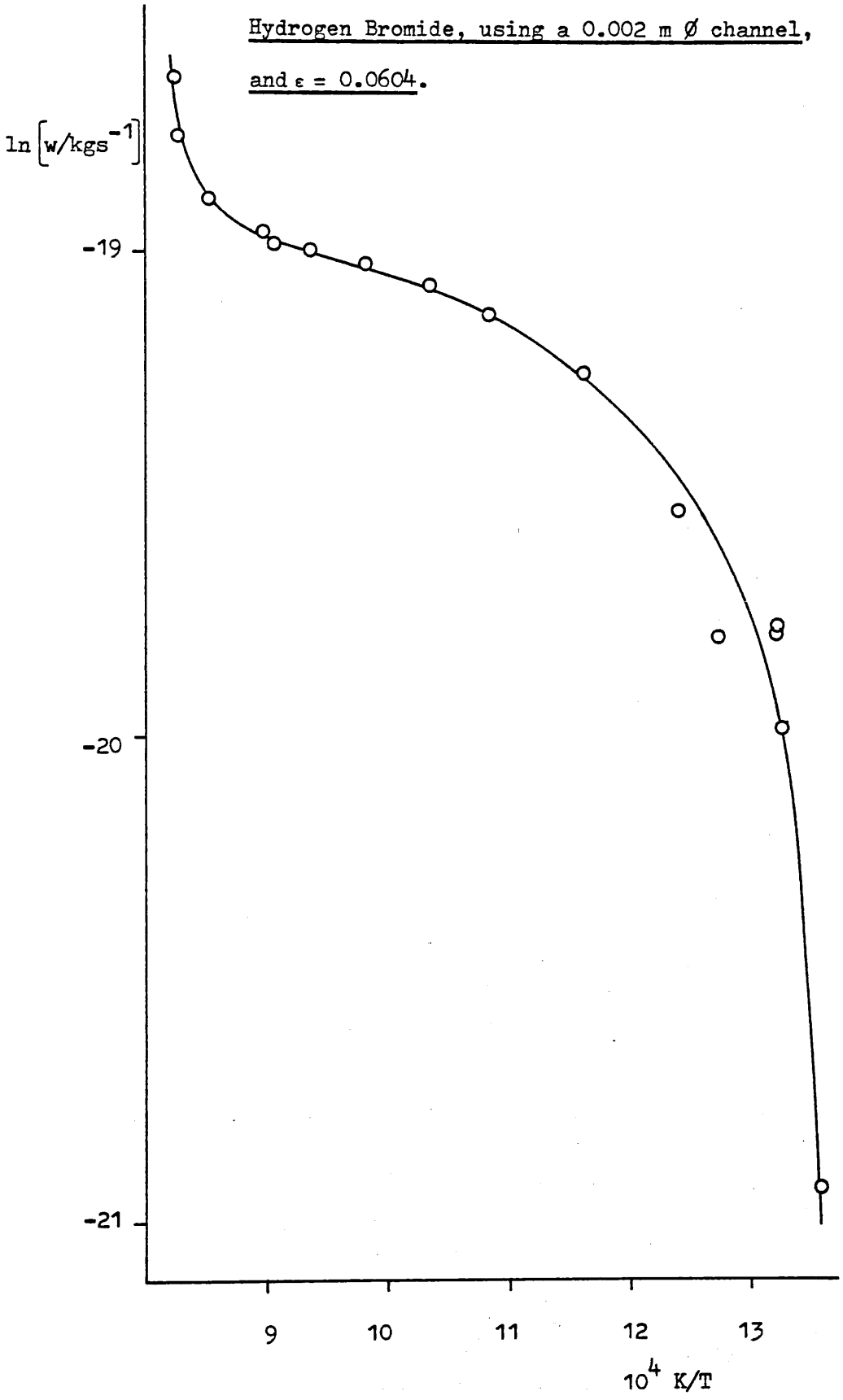

In order to make a direct comparison between the results obtained using 0.001 and 0.002 m channels, one or other sets of data must be dimensionally scaled. Both sets of data appear superimposed in fig 5.9. Evidently, once the differences in channel conductances has been taken into account there is little difference between the two. Had surface kinetics been a contributing factor in deteriming the rate of weight loss at lower temperatures, a marked deviation between the two lines would have been expected in this region.

5.9 Incongruent evaporation.

Let us consider the InP : HBr system. We shall employ the following nomenclature,

InBr = 1, P_2 = 2, HBr = 3, H_2 = 4, and In = 5

The normal transport equilibrium at high temperature is:

$$InP(c) + HBr(g) = InBr(g) + \tfrac{1}{2}P_2(g) + \tfrac{1}{2}H_2(g) \qquad (5.9.1)$$

$$K_p = p_1^o\sqrt{p_2^o p_4^o}/p_3^o = K_1 \qquad (5.9.2)$$

Incongruent evaporation is,

$$InP(c) = In(l) + \tfrac{1}{2}P_2(g) \qquad (5.9.3)$$

$$K_p = a_5\sqrt{p_2^o} = K_2 \qquad (\text{Let } a_5 = 1) \qquad (5.9.4)$$

Phase rule considerations

1) With no liquid phase, F=4-2+2=4

We take, P,T,ε and $j_{In}=j_P$ as the degrees of freedom.

2) In the presence of a liquid phase, F=3.

So for arbitary values of P,T and ε , then $j_{In}=j_P$ and a

Fig 5.9 Superposition of the $\ln\dot{w}$ v $10^4/T$ Plots for InP:HBr, Employing 0.001, and 0.002 m Ø MEM channels.

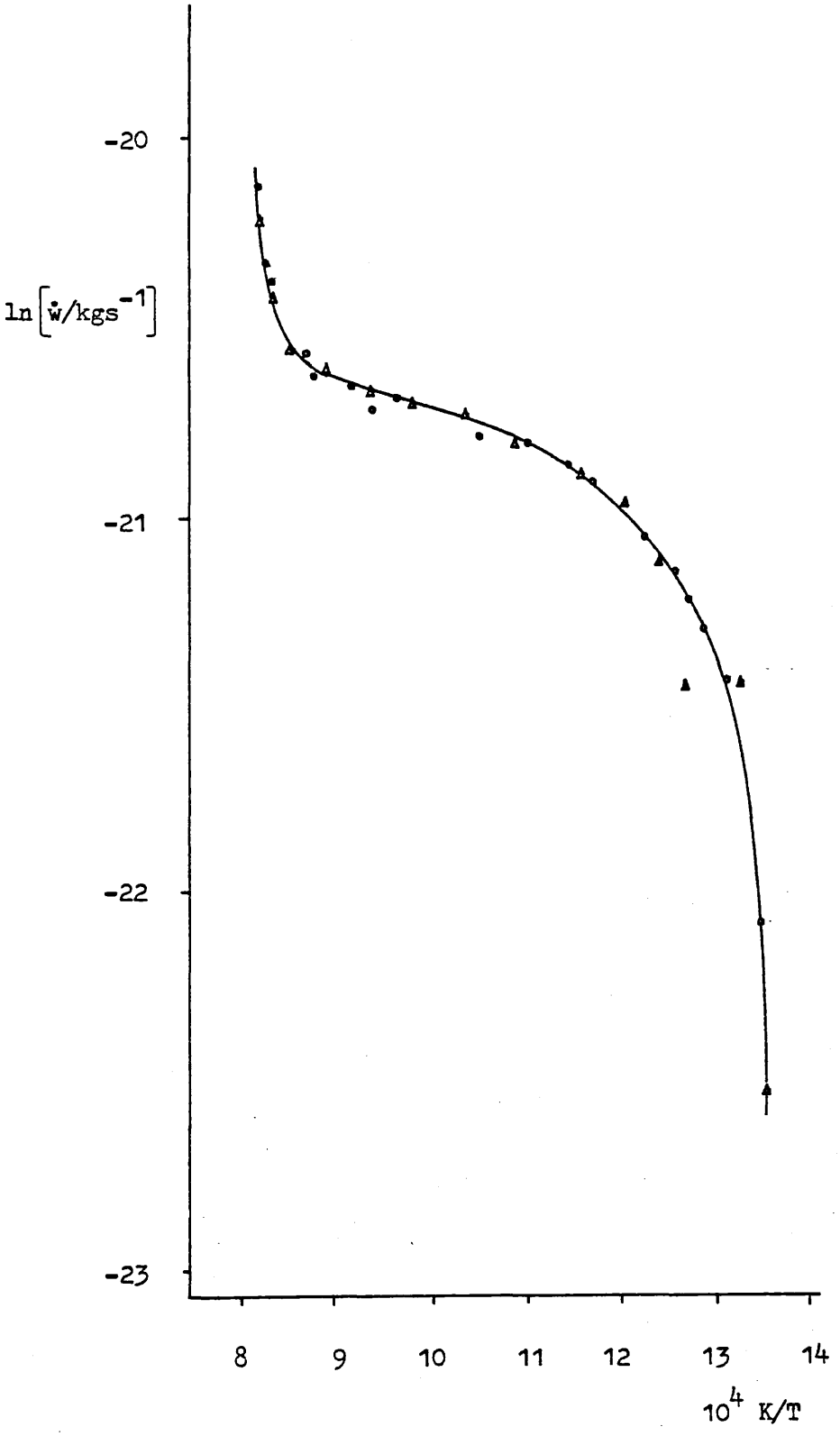

steady state does not exist. There exists a $T(P,\varepsilon)$ for which $j_{In}=j_P$, and at that temperature the amount of liquid indium remains constant. At this temperature the liquid phase does not influence the rate of weight loss, and the point corresponding to this position lies on the normal curve.

Transport considerations

Now let j_i denote the flux of species i, and J the sum of all such fluxes.

Then
$$\frac{p_i^{o(0)}}{P} = \frac{j_f}{J} + \left[\frac{p_i^{o(1)}}{P} - \frac{j_i}{J}\right] e^{-\xi_i} \qquad (5.9.5)$$

where $\xi = JRTl/DP$

Flux relationships

Let $j_2 = j_1\psi$ (normally $j_2=\frac{1}{2}j_1$ ie $\psi=\frac{1}{2}$) (i)

Then
$$j_5 = j_1 \qquad \text{(ii)}$$
$$j_P = 2j_2 = 2\psi j_1 \qquad \text{(iii)}$$
$$j_{Br} = j_1 + j_3 = 0 \qquad \text{(iv)}$$

therefore
$$j_3 = -j_1 \qquad \text{(v)}$$
$$j_H = j_3 + 2j_4 = 0 \qquad \text{(vi)}$$

therefore
$$j_4 = -j_3/2 = \tfrac{1}{2}j_1 \qquad \text{(vii)}$$

also
$$J = \Sigma_i j_i = (\psi+\tfrac{1}{2})j_1 \qquad \text{(viii)}$$

Partial pressures
$$p_1^o(1) = 0 \qquad \text{(ix)}$$
$$p_2^o(1) = 0 \qquad \text{(x)}$$
$$p_3^o(1) = \varepsilon P \qquad \text{(xi)}$$

and $$p_4^o(1) = P(1-\varepsilon) \qquad \text{(xii)}$$

for the channel exit, and for the bottle cavity:

$$p_1^{o(0)} = P\xi/(\psi+\tfrac{1}{2}) \qquad \text{(xiii)}$$

$$p_2^{o(0)} = P\xi\psi/(\psi+\tfrac{1}{2}) \qquad \text{(xiv)}$$

$$p_3^{o(0)} = P((\varepsilon-\xi)/(\psi+\tfrac{1}{2})) \qquad \text{(xv)}$$

$$p_4^{o(0)} = P(1-\varepsilon) - \xi P\psi/(\psi+\tfrac{1}{2}) \qquad \text{(xvi)}$$

Weight loss

Now using 5.9.5 and the flux relationships we find:

$$\dot{w} = A(M_1 j_1 + M_2 j_2) = Aj_1(M_1 + \psi M_2) = Aj_1\mu \qquad (5.9.6)$$

where M_1 and M_2 are the molecular **masses** of InBr and P_2 respectively, and μ is the "ψ - weighted mass".

Thus $$\xi = \dot{w}RT1(\psi+\tfrac{1}{2})/(APD\mu) \qquad (5.9.7)$$

Now $$K_2 = P\xi\psi/(\psi+\tfrac{1}{2}) \qquad (5.9.8)$$

or $$\psi^2(ADK_2^2M_2-\dot{w}RT1) + \psi(ADK_2^2M_1+\tfrac{1}{2}K_2^2ADM_2-\tfrac{1}{2}\dot{w}RT1) + \tfrac{1}{2}K_2^2ADM_1 = 0 \qquad (5.9.9)$$

which is a quadratic for ψ in terms of $\dot{w}$.

5.9.2 now becomes:

$$2K_1^2(\varepsilon^2-2\varepsilon\gamma\xi+\gamma^2\xi^2) = P^2\xi^3\gamma^2(2-\gamma) \qquad (5.9.10)$$

with $\gamma = 1/(\psi+\tfrac{1}{2})$

For the general case we have to solve 5.9.9 and 5.9.10 simultaneously.

Reaction 5.9.1 extreme

At sufficiently elevated temperatures reaction 5.9.1

proceeds almost to completion. In this instance,

$$p_3^{o(0)} = 0 \quad \text{and} \quad p_1^{o(0)} = \varepsilon P$$

But $$p_1^{o(0)} = P\xi/(\psi+\tfrac{1}{2})$$

therefore $$\xi = \varepsilon(\psi+\tfrac{1}{2}) = \dot{w}RT1(\psi+\tfrac{1}{2})/(APD\mu) \qquad (5.9.11)$$

so $$\mu = \dot{w}RT1/(APD\varepsilon) = M_1 + M_2 \qquad (5.9.12)$$

Thus we have a relationship between $\dot{w}$ and , substituting into equation 5.9.9 a cubic equation in ψ is generated.

$$-P\varepsilon M_2\psi^3 + (K_2^2M_2 - P\varepsilon M_1\frac{M_2}{2})\psi^2 + (K_2^2M_1 + \tfrac{1}{2}K_2^2M_2 - \frac{P\varepsilon M_1}{2})\psi + \tfrac{1}{2}K_2^2M_1 = 0 \qquad (5.9.13)$$

which factorises to give,

$$(\psi+\tfrac{1}{2})(M_2\psi+M_1)(K_2^2-P\psi\varepsilon) = 0 \qquad (5.9.14)$$

It is the third of these roots only that seems to have any real significance.

$$P\varepsilon\psi = K_2^2 \qquad (5.9.15)$$

Since no Graham's law terms have been included, ie all diffusion coefficients have been taken as equal, (this is so to a first approximation), $j_2 = \psi j_1$. With extreme reaction this becomes P . So, equation 5.9.15 follows from 5.9.4. For the special case, when $\psi=\frac{1}{2}$ we must have a value for T such that $K_2^2=\frac{1}{2}P\varepsilon$. For weight loss then we may write:

$$\dot{w} = \frac{ADM_2K_2^2}{RT1} \qquad (5.9.16)$$

Critical temperature

Let T_c be the temperature such that the following equality

is applicable,

$$K_2^2(T_c) = \tfrac{1}{2}P\varepsilon \qquad (5.9.17)$$

Then:
$$\ln\varepsilon = -\Delta H_2/T_c + (\Delta S_2 - \ln\tfrac{1}{2}P) \qquad (5.9.18)$$

If T_c could be found experimentally as a function of $\ln\varepsilon$, then a graph of $\ln\varepsilon$ v $1/T_c$ would enable ΔH_2 and ΔS_2 to be found. The gradient of the line yielding ΔH_2, and the intercept taking the form $(\Delta S_2 - \ln\frac{1}{2}P)/\Delta H_2$. In order to locate T_c on the normal weight loss line, data points are required close to and above T_c.

5.10 Investigation of weight loss at various partial pressures of hydrogen bromide.

So far the experimental results have been discussed for two non zero values of epsilon, and a further discussion related to a zero value. In order to test the foregoing section on incongruent evaporation four further experiments were performed. Additional investigations were undertaken using the following values for ε: 0.030, 0.0348, 0.0476 and 0.0765. The numerical data appears in tables 5.11, 5.12, 5.13 and 5.14 respectively. All sets of data are collected and displayed in fig 5.10.

Attempts to extract values for T_c, to insert in the incongruent evaporation treatment described, from the emperical results were frustrated by the large scatter of data in this temperature region. Some considerable time was invested in trying to derive a working computer simulation in order to extract values for $T_c(\varepsilon)$. These efforts were not very fruitful. It was found possible to predict a temperature where ψ reverted to an almost constant value with decreasing temperature, but this value

Table 5.11

Weight loss data for InP : HBr system, using a 0.001 m Ø channel, and $\varepsilon = 0.0765$.

T/K	$10^9 \dot{w}$/kg s^{-1}	T/K	$10^9 \dot{w}$/kg s^{-1}
998.5	1.286	1150.9	1.423
997.7	1.237	1151.4	1.404
997.7	1.202	1157.3	1.396
997.8	1.224	1156.2	1.413
1038.1	1.269	1161.4	1.429
1037.9	1.268	1161.4	1.148
1037.9	1.269	1167.0	1.423
1038.0	1.287	1166.1	1.462
1088.7	1.336	1170.0	1.434
1088.6	1.323	1170.0	1.408
1088.6	1.316	1175.0	1.449
1088.6	1.316	1175.0	1.421
1123.1	1.393	1181.2	1.504
1122.4	1.337	1181.2	1.460
1122.4	1.348	1185.1	1.533
1122.4	1.348	1185.1	1.530
934.7	1.179	1190.6	1.615
934.7	1.161	1190.6	1.603
933.9	1.180	1198.4	1.670
933.0	1.129	1197.7	1.628
1128.8	1.326	1210.8	1.918
1128.3	1.374	1210.8	1.900
1138.0	1.401	1222.4	2.319
1137.6	1.401	1222.4	2.260
1143.0	1.412		
1142.2	1.453		
1148.2	1.299		
1148.2	1.437		

Table 5.12

Weight loss data for InP : HBr system, using a 0.001 m Ø channel, and $\varepsilon = 0.0476$.

T/K	$10^9 \dot{w}$/kg s^{-1}	T/K	$10^9 \dot{w}$/kg s^{-1}
995.7	0.914	1125.8	1.047
995.7	0.919	1126.0	0.985
995.7	0.948	1126.0	1.023
995.7	0.903	1126.0	0.990
1088.6	0.972	1137.7	1.031
1087.8	0.988	1136.9	1.039
1087.8	0.989	1148.4	1.051
1087.1	0.970	1147.2	1.032
931.2	0.889	1157.4	1.019
932.0	0.877	1156.9	1.010
932.0	0.885	1168.0	1.058
932.0	0.860	1167.2	1.011
1037.9	0.930	1177.1	1.107
1037.0	0.924	1176.2	1.102
1037.0	0.943	1185.8	1.205
1037.0	0.930	1185.8	1.198
1106.3	1.003	1206.6	1.530
1106.3	0.966	1205.4	1.515
1106.3	1.005	1222.3	2.132
1105.5	1.004	1221.6	2.107

Table 5.13

Weight loss data for InP : HBr system, using a 0.001 m Ø channel, and $\varepsilon = 0.0348$.

T/K	$10^{10}\dot{w}$/kg s^{-1}	T/K	$10^{10}\dot{w}$/kg s^{-1}
996.9	7.220	1124.1	8.016
996.9	7.326	1124.9	7.952
996.9	7.055	1124.9	8.039
996.9	7.117	1124.9	7.859
1038.4	7.435	1126.8	7.968
1039.9	7.181	1126.8	8.130
1039.1	7.346	1152.2	8.163
1039.1	7.394	1152.2	8.180
919.8	6.644	1171.1	9.185
919.8	6.780	1171.1	9.229
919.8	6.472	1195.4	11.905
919.8	6.634	1193.8	12.308
1087.4	7.491	1205.6	14.598
1087.4	7.988	1205.6	15.152
1087.4	7.767		
1115.4	7.752		
1115.4	8.052		
1115.4	7.874		
1115.4	8.097		

Table 5.14

Weight loss data for InP : HBr system, using a 0.001 m Ø channel, and ε = 0.0300.

T/K	$10^{10}\dot{w}$/kg s^{-1}	T/K	$10^{10}\dot{w}$/kg s^{-1}
965.3	5.923	1115.2	6.734
965.3	5.865	1115.2	6.623
965.3	5.900	1123.2	6.826
965.3	5.908	1123.2	7.117
994.9	6.384	1136.7	6.920
994.9	6.061	1135.1	6.993
994.9	6.042	1144.9	7.143
994.9	5.970	1144.0	7.050
1036.5	6.192	1158.4	8.147
1035.7	6.173	1158.4	7.813
1035.7	6.103	1173.5	8.493
1035.7	6.135	1173.5	8.569
1083.7	6.452	1194.7	12.327
1083.7	6.369	1192.4	9.302
1104.0	6.623		
1104.0	6.745		

Fig 5.10 Graphs of $\ln\dot{w}$ v $10^4/T$ for all Values of ε.

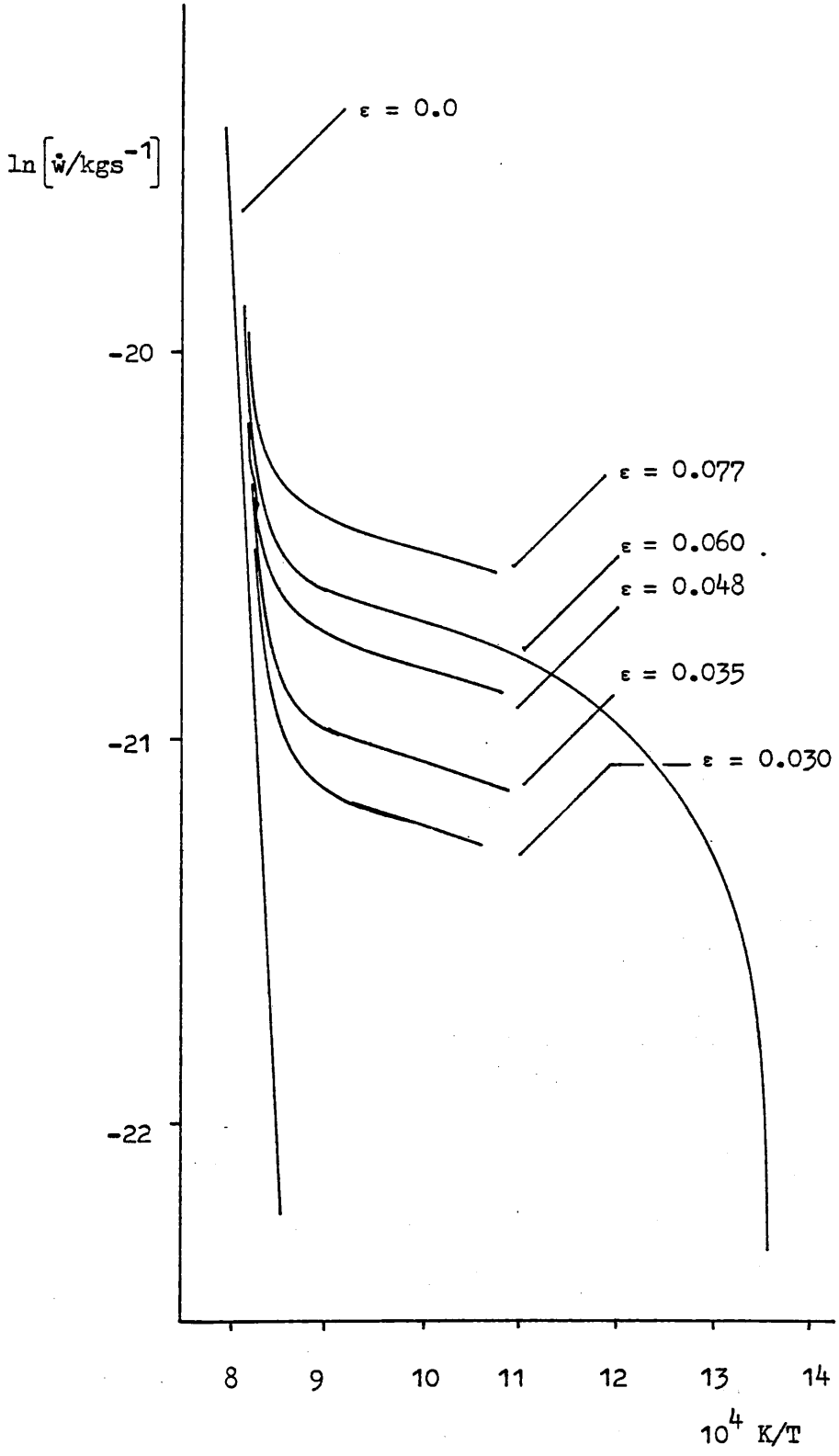

was not $\frac{1}{2}$. Neither did any of the simulations adequately describe the general form of the results. This avenue of approach was therefore abandoned.

To analyse the results in any useful manner it was found necessary to separate the dissociative sublimation treatment (section 5.7) from the CVT treatment.

5.11 Simulation results.

The best-fit simulation results for dissociative sublimation have already been presented in section 5.7. In summary:

$$InP(c) = In(l) + \tfrac{1}{4}P_2(g) \qquad (5.11.1)$$

$$P_4(g) = 2P_2(g) \qquad (5.11.2)$$

$$\Delta H_{ds} = 159.0 \text{ kJ mol}^{-1}$$

$$\Delta S_{ds} = 113.8 \text{ J K}^{-1}\text{mol}^{-1}$$

$$\Delta H_{d} = 242.7 \text{ kJ mol}^{-1}$$

$$\Delta S_{d} = 156.1 \text{ J K}^{-1}\text{mol}^{-1}$$

Both BT and RHC formulations of the MEM simulations have been applied. The results presented here are for the RHC treatment, although the results of one BT analysis are given for comparison.

The results obtained in section 5.10 have not been fitted rigorously to the model, but the thermodynamic parameters resulting from the other experiments have been shown to simulate these results well.

Firstly, the initial experiments reported in section 5.3 were fitted. Initially, the linear region, where transport is

Fig 5.11 Graphs of $\ln \dot{w}_{calc}$ v $10^4/T$

Fitted Results for the Initial Experiments.

ε = 0.0604 & (A)

ε = 0.0348 (B)

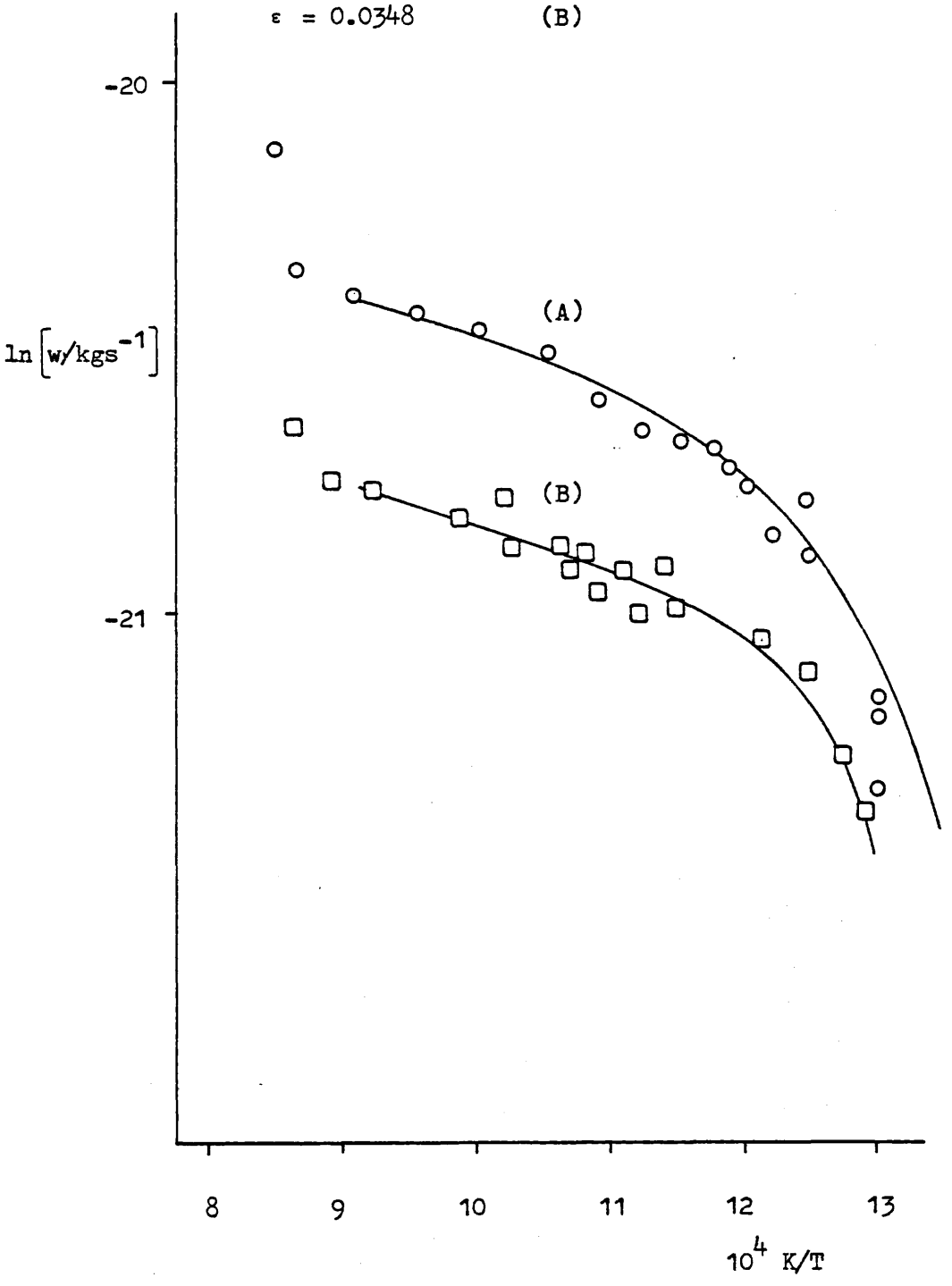

believed to occur via the formation of the monobromide, (and K_p is large), was fitted. Considering this region in isolation enables the best choice for D_o to be made. A value for D_o of 0.44×10^{-4} $m^2 s^{-1}$ gave the best fit here. Further data was then included in the simulation, spanning the temperature range ca 1100 to ca 750 K. For the higher value of ϵ, (0.060), the following values for the enthalpy and entropy of reaction were extracted:

$$\Delta H_r = 120.0 \text{ kJ mol}^{-1}$$

$$\Delta S_r = 159.5 \text{ J K}^{-1}\text{mol}^{-1}$$

$$\sigma = 0.074$$

and for ϵ = 0.035:

$$\Delta H_r = 123.0 \text{ kJ mol}^{-1}$$

$$\Delta S_r = 159.5 \text{ J K}^{-1}\text{mol}^{-1}$$

$$\sigma = 0.004$$

The values of enthalpy and entropy changes are reference to the mean operating temperature of 930 K. These best-fits are illustrated in fig 5.11.

The remaining two experiments cover the widest temperature range (735 to 1230 K), and were both performed using ϵ set to 0.060, but using MEM capsules with different diameter channels. Again, setting D_o to 0.44×10^{-4} $m^2 s^{-1}$ gives the most satisfactory fit. The best-fit value for the thermodynamic parameters are given below, (again for 930 K):

channel	ΔH_r/kJ mol^{-1}	ΔS_r/J K^{-1}mol^{-1}	ε
0.001 m Ø	120.0	158.0	0.004
0.002 m Ø	126.0	160.0	0.015

The temperature range of points included in these simulations spanned 1085 to 740 K for the 0.001 m Ø result, and 1100 to 750 K for the 0.002 m Ø result.

A good correlation between the fitted values for these four experiments is seen, although the value for the enthalpy of reaction is found some 5 % higher using the 0.002 m channel than using the 0.001 m channel. Using the BT formulation to analyse the second ε = 0.060 experiment (0.001 m channel), the following results were obtained:

$$\Delta H_r = 117.5 \text{ kJ mol}^{-1}$$

$$\Delta S_r = 168.5 \text{ J K}^{-1}\text{mol}^{-1}$$

$$D_o = .44 \times 10^{-4} \text{ m}^2\text{s}^{-1}$$

$$\sigma = .004$$

$$\text{for T} = 930 \text{ K}$$

It is of some interest that the computer program predicts the rapid down-turn of the logarithm of the rate of weight loss plot against inverse temperature. This suggests that the interpretation of the experiments is correct, ie that kinetic limiting of transport is not a dominant feature in this system at modest temperature elevations.

Using the mean values of ΔH_r and ΔS_r from the four experiments, it may be seen how rapidly K_p becomes large with

Fig 5.12 Graph of $\ln \dot{w}_{calc}$ v $10^4/T$ for InP:HBr, Using Both 0.001 & 0.002 m Ø MEM Channels.*

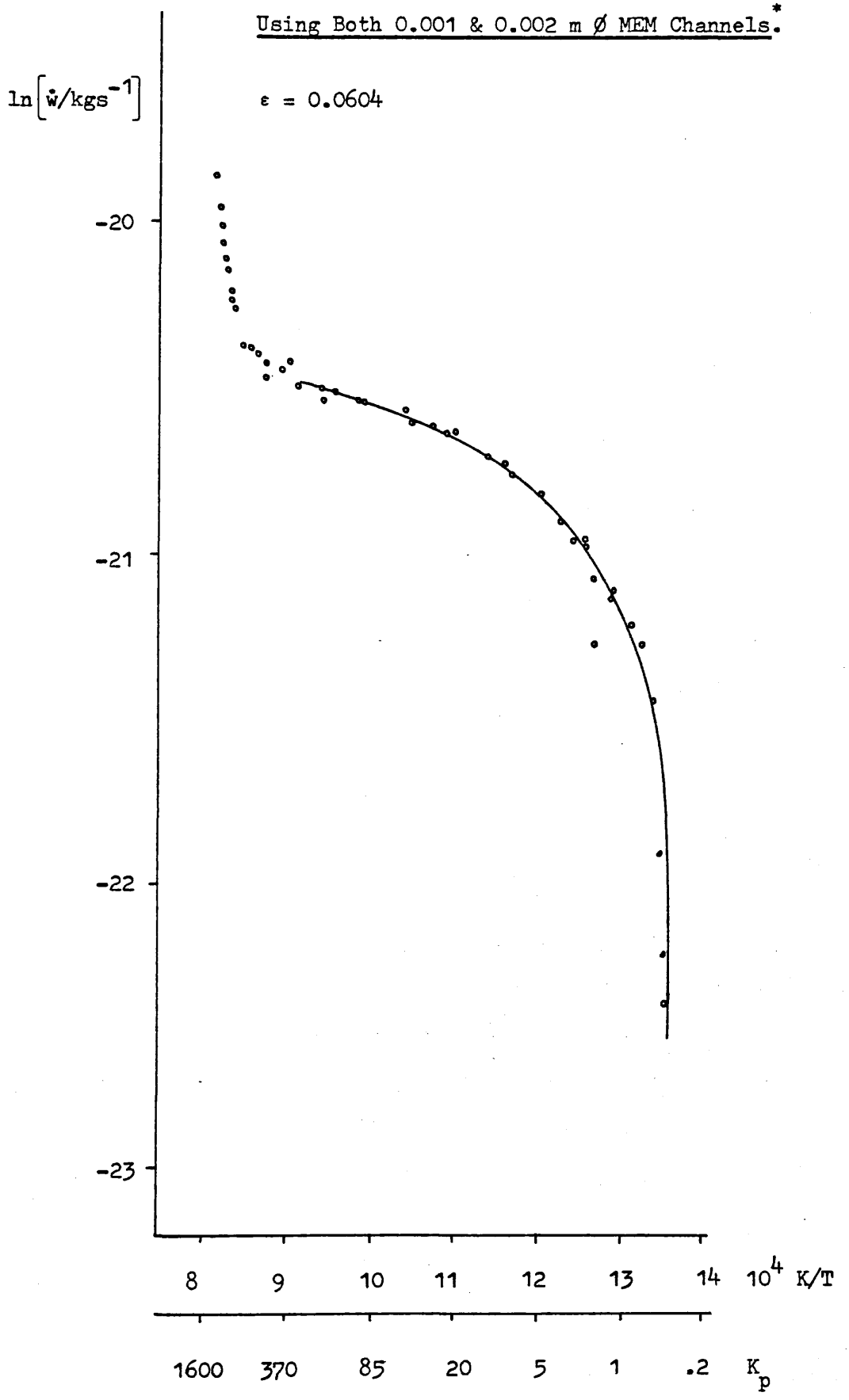

increasing temperature. Figure 5.12 gives the simulation results for the latter two experiments, and included as an **abscissa** is the value of K_p for the CVT reaction.

5.12 Discussion.

While enthalpy and entropy changes for the transport reactions may be obtained from the results of MEM experiments, a more practical spin-off for the crystal grower accompanies this information. The $\ln\dot{w}$ v $1/T$ plots give a direct quantitative measure of the thermodynamic efficiency of a transport system. In a pure CVT growth experiment, efficient growth is achieved when K_p is close to unity (this constraint arises from the reversible nature of the CVT reactions). Although the exercise of extracting thermodynamic constants is useful, the results themselves give an immediately useful appraisal of the transport system.

In section 5.4, estimates were made for the values of ΔH and ΔS for the transport reaction under consideration. The best-fit value of ΔH_r lies within 10 % of the estimated value, and is encouraging. On the negative side, however, the large upward adjustment (30 %) of the estimate for ΔS_r is surprising. Entropy changes may generally be predicted more accurately than corresponding changes of enthalpy. Bearing in mind the lower temperatures that are being considered in this system, it is important to pursue an alternative interpretation of the results from that so far assumed. It is sensible to consider a single transport reaction predominating mass transfer, but this reaction may not necessarily, however, involve the formation of the monobromide. The low temperature region is the area in which

the participation of the di-halides has been demonstrated in other systems[1]. Larger entropy changes associated with the di-halide formation would give rise to the onset of diffusion control at modest temperatures; this is a feature that dominates these results. Estimations of ΔH_r and ΔS_r, assuming the involvement of $InBr_2$, lead to values of 115 $kJmol^{-1}$ and 300 $J\ K^{-1}\ mol^{-1}$ respectively. Clearly, ΔS_r is far larger than the value extracted for these simulations. Adopting a scheme-2 analysis, a most unsatisfactory simulation results. It is therefore concluded that the formation of the di-bromide is not prominent in this system.

Assuming that the thermodynamic data for all the species except InBr(g) is reliable, and using the heat of reaction from the best-fit simulation, a value of ΔH^{o}_{f298} InBr(g) $= -50.3\ kJ\ mol^{-1}$ and a corresponding value of S^{o}_{f298} InBr(g) $= 271.4\ J\ K^{-1}mol^{-1}$ are calculated.

REFERENCES TO CHAPTER FIVE

5.1 E.J. Tarbox, PhD Thesis, London (1977)

5.2 A. Levy, J. Phys. Chem. 62, 570 (1958)

5.3 K. Weiser, J. Phys. Chem. 61, 513 (1957)

5.4 M.M. Faktor, Private Communication

5.5 M.B. Panish and J.R. Arthur, J. Chem. Therm. 2, 299 (1970)

5.6 R.F.C. Farrow, J. Appl. Phys. D. 7, 2422 (1974)

5.7 R. Hultgren, P.D. Desai, D.T. Hawkins, M. Gleiser, K.K. Kelley and D.D. Wagman, Selected Values of Thermodynamic Properties of the Elements (American Society for Metals, 1973)

5.8 Bachman and Buchler, J. Electrochem. Soc. 121, 835 (1974)

5.9 D. Battat, M.M. Faktor, J. Garrett and R.H. Moss, J. Chem. Soc. Faraday I 70, 2293 (1974)

5.10 D. Battat, M.M Faktor, J. Garrett and R.H. Moss, J. Chem. Soc. Faraday I, 70, 2302 (1974)

5.11 O. Kubaschewski and C.B. Alcock, Metallurgical Thermochemistry, 5th Ed. (Pergamon, 1979)

5.12 Pankratz, U.S. Bureau of Mines 6592 (1965)

5.13 Selected Values of Thermodynamic Properties, U.S. National Bureau of Standards, Technical Note 270-3 (1968)

5.14 M. Illegens, M.B. Panish and J.R. Arthur, J.Chem. Therm. 6, 157 (1974)

5.15 JANAF, Thermochemical Tables 2nd Ed., US Department of Commerce, National Bureau of Standards (1971)

5.16 F.J. Smith and R.F. Barrow, Trans. Faraday Soc. 51, 1478 (1955)

5.17 R.F. Barrow, A.C.P. Pugh and F.J. Smith, Trans. Faraday Soc. 51, 1657 (1955)

5.18 A.V. Sandulova, E.G. Zaidowskii, V.A. Prokhorov, Russ. J. of Phys. Chem. 47, 429 (1973)

CHAPTER SIX

High temperature Raman spectroscopy of group III halides

6.1 Introduction

The modified entrainment method (MEM), has been applied to the study of numerous heterogeneous reaction equilibria involving binary III-V semiconductors. The results for the experiments on GaAs[1,2] and GaP[3] would suggest that two gallium halide species are involved in the transport of the binary materials.

From the slope of the graphs, it is evident that both the transport reactions involved are endothermic. In the upper temperature range, gallium monohalide is the most probable reaction product. The gallium/halogen species dominating transport in the low temperature region must either be the di- or tri-halide (or polymeric forms of these). The formation of GaX_3 via the equation:

$$GaA + 3HX = GaX_3 + \tfrac{1}{4}A_4 + \tfrac{1}{2}H_2 \qquad (6.1.1)$$

would be exothermic, and may therefore be disregarded. This leaves gallium dihalide:

$$GaA + 2HX = GaX_2 + \tfrac{1}{4}A_4 + H_2 \qquad (6.1.2)$$

$$GaA + 2HX = \tfrac{1}{2}Ga_2X_4 + \tfrac{1}{4}A_4 + H_2 \qquad (6.1.2)$$

There is, however, very little independent evidence supporting the existence of group III dihalides in the vapour.

Interest in the halides of group III metals has been

heightened in recent years by studies on binary electronic materials, where hydrogen halides are used to enhance the volitility of the metal by formation of the halides. Generally, however, interest in the valancies displayed by such halides may be traced back almost a century. In 1888, Nilson and Patterson[4] reported that their vapour density measurements provided inconclusive evidence to support the existence of indium dichloride in the vapour phase at 879 K. This work was reported twenty five years after the discovery of indium.

Phase studies may be cited[5] that refute the existence of indium dichloride as a compound. To quote from a well known inorganic chemistry text[6], "Indium dichloride does not appear to exist as a distinct compound". And in more recent years, "Phase studies have re-established the existence of indium dichloride"[7].

Fused indium dichloride has been shown to have the structure $In^{I}\ In^{III}Cl_4$, using Raman scattering[8]. Similarly, $Ga^{I}\ Ga^{III}Cl_4$ has been shown to be the structure of the gallium dichloride in both solid[9] and liquid[10] states. Bromine containing salts appear to have attracted far less attention.

The existence of $TlInCl_4$ molecules in the vapour is supported by electron defraction studies[11]. Mass spectrometric work reveals evidence for the existence of vapour phase In_2Cl_4 over molten indium chloride salts[12]. In a series of papers published by Yasuo Kuniya,[13] a number of **vapour phase reactions** in group III-VII systems have been studied. Within this work, electronic spectroscopy has been used in conjunction with vapour pressure measurements to identify the composition of the vapours. These studies support the existence of In_2Cl_4 in the vapour at

appreciably elevated temperatures.

Group III halides lend themselves, as a group of compounds, admirably to study by Raman spectroscopy, as the molecules are good scatterers due to their large polarisability.

Since the advent of the laser, Raman spectroscopy has enjoyed a renaissance. It provides a non-destructive technique which may be employed to interrogate solid, liquid and gaseous samples. Raman spectroscopy may be used to excite both rotational and vibrational transitions within molecules, and is therefore frequently used as a complementary technique to microwave or infra red spectroscopy. The molecular weights of most of the group III halides place the vibrational frequencies below 400 cm^{-1}. This imposes a constraint if infra red spectroscopy is to be used, since the far infra red region demands the use of specialised equipment (frequently intraferrometric), and is far from being a routine technique, particularly at elevated temperatures.

The Raman process being a scattering phenomenon allows the study of vibrations in the energy band 10 - 400 cm^{-1} with ease. The excitation source and detection photo-tube may be chosen to best advantage. Raman scattering intensity is proportional to the fourth power of frequency, so light towards the blue end of the electromagnetic spectrum is often used to excite the transitions of interest. In many instances, use of light of too high an energy stimulates fluoresence of the sample, and any advantage is lost. In this instance, some instruments allow measurements to be made on the anti-Stokes (augmented frequency) side of the excitation line. Normally, Stokes lines are recorded, as these

are more intense at room temperature. With elevation of temperature, however, the situation improves with respect to the intensity of the anti-Stokes side, at the expense of the Stokes.

6.2 Results

Preliminary results were obtained at the Chemistry Department, University of Southampton, in April 1977. A Spectra Physics 170 Argon ion laser, operating at 4880 Å (photon energy, 20491.8 cm^{-1}), and delivering approximately 4 W of power at the sample, was used in conjunction with a Spex 1401 double monochromator and a RCA photomultiplier tube.

The samples were contained in cylindrical ampoules, which generated some problems, as described in chapter 2. Three ampoules were prepared for study, although one unfortunately, (for technical reasons), yielded no results.

The first ampoule was sealed containing Ga (0.1 g), GaBr, (0.4 g) and 300 mbar of H_2. However, attempts to obtain gas phase spectra in the temperature range 470 - 570 K, failed. Despite the fact that both the laser and the monochromater collection lens were focused at the centre of the ampoule, the incident beam passed through the melt (mpt $GaBr_3$ 394.7 K).

Further experiments at higher temperature (720 - 1020 K), were hindered by vigorous boiling of the ampoule contents in the vicinity of the laser beam, and condensation on the ampoule wall cold spots (at the furnace beam exit, and observation ports). The boiling caused rapid fluctuations in the intensity of scattered light, causing high noise levels. Figure 6.1 illustrates the Raman spectra recorded at 770 and 970 K. Although each spectrum is rather noisy, the three bands between

Fig 6.1

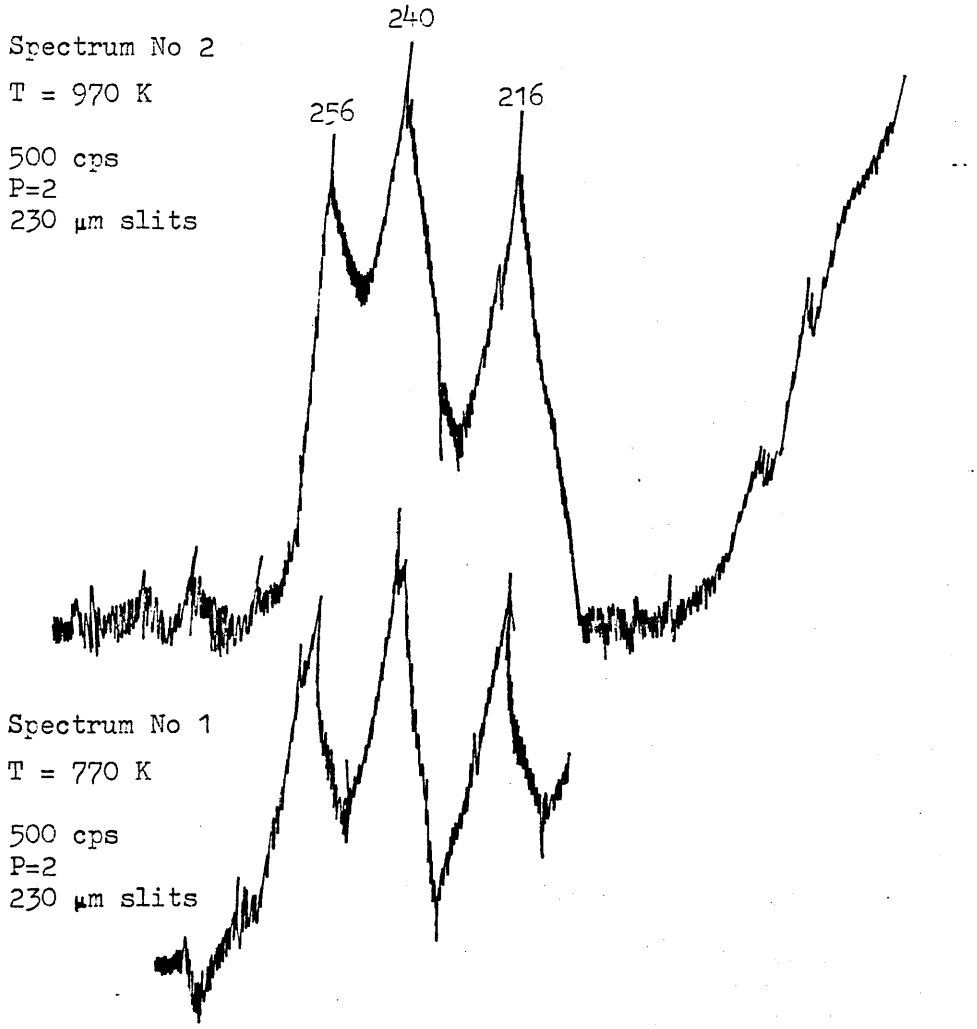
Spectrum No 2
T = 970 K
500 cps
P=2
230 µm slits
256
240
216
Spectrum No 1
T = 770 K
500 cps
P=2
230 µm slits

200 - 300 cm^{-1} were found to be reproducible.

As the temperature was raised further, the problem with noise began to abate. At 1070 K and above, clean high level Raman signals were obtained. Spectra from 70 - 400 cm^{-1} at 1070 and 1170 K were recorded, (see figs 6.2 and 6.3). Each of these spectra exhibit bands at the following Raman shifts: 83, 216, 240, 256, and a weak broad feature around 340 cm^{-1}. All of these except 256 cm^{-1} have been previously assigned to gallium tribromide. The additional band at 256 cm^{-1} is attributed to gallium monobromide. No evidence for any other gallium-bromine species was noted.

The second ampoule was sealed containing GaAs (0.2 g), $GaBr_3$ (0.5 g), 300 mbar H_2, and 60 mbar Br_2. Similar problems with respect to noise at moderate temperatures were encountered here, as with the previous ampoule. Spectra at 870 and 1070 K were recorded from 40 - 500 cm^{-1}, and both yielded good results, (see figs 6.4 and 6.5). The bands in these two spectra have all been assigned to $GaBr_3$. No scatter attributable to the monobromide was observed, although spectrum 6.5 does perhaps exhibit a shoulder to the high frequency side of the 240 cm^{-1} band. It is possible that less than the desired quantity of bromine was in fact sealed in the ampoule. In this instance, possibly insufficient HBr was present in the system to generate volatile species from GaAs, (even at high sensitivity, the characteristic spectrum of HBr, 2559 cm^{-1} could not be detected). No dissociation or disproportionation of $GaBr_3$ was detected, and the spectra were unaffected by the presence of GaAs, in which the activity of gallium was presumably sufficiently

Fig 6.2

Spectrum No 3

T = 1070 K

2000 cps
P=1
80 μm slits

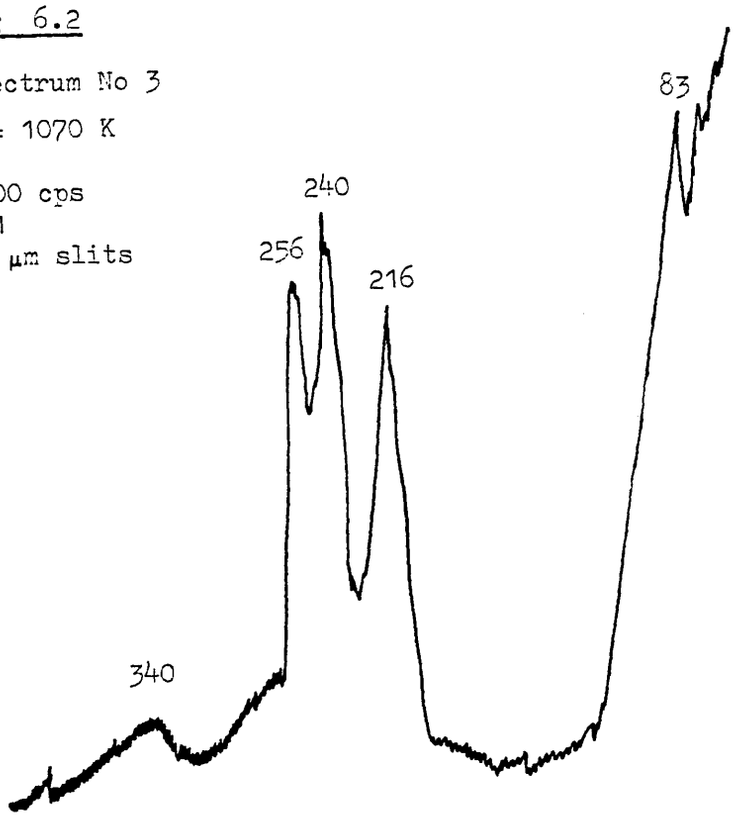

Fig 6.3

Spectrum No 4

T = 1170 K

2000 cps
P=1
80 μm slits

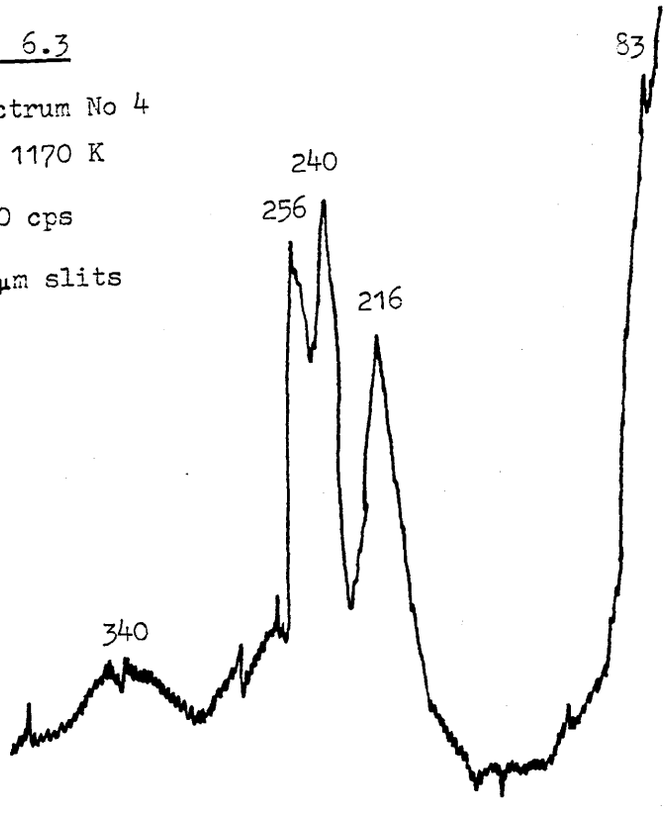

Fig 6.4

Spectrum No 5

T = 870 K

5000 cps
P=2
70 μm slits

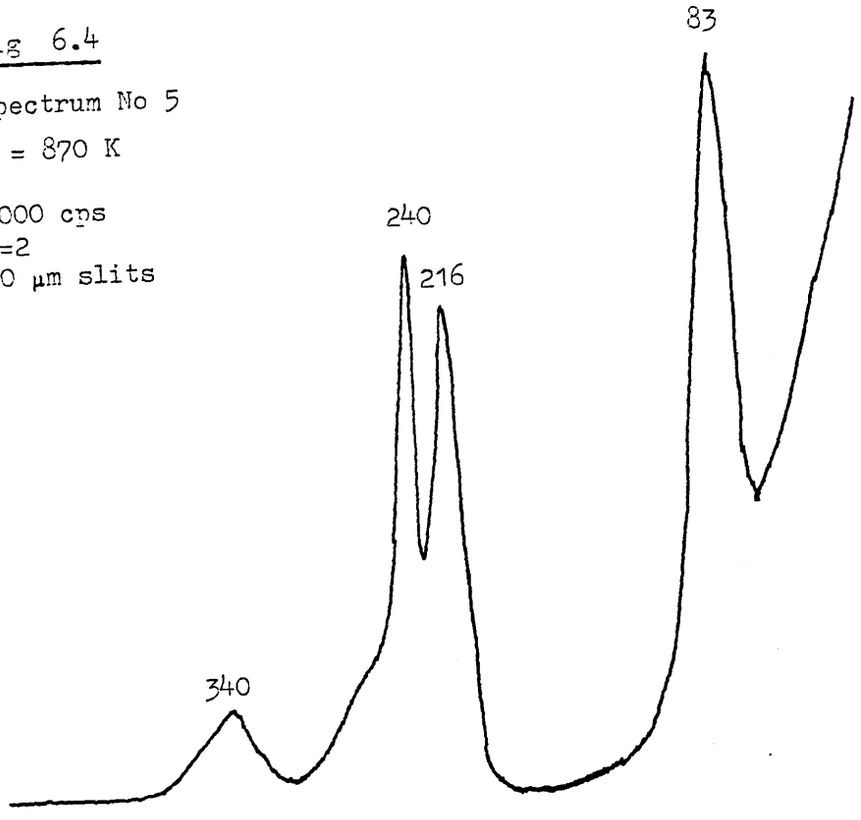

Fig 6.5

Spectrum No 6

T = 1070 K

5000 cps
P=2
70 μm slits

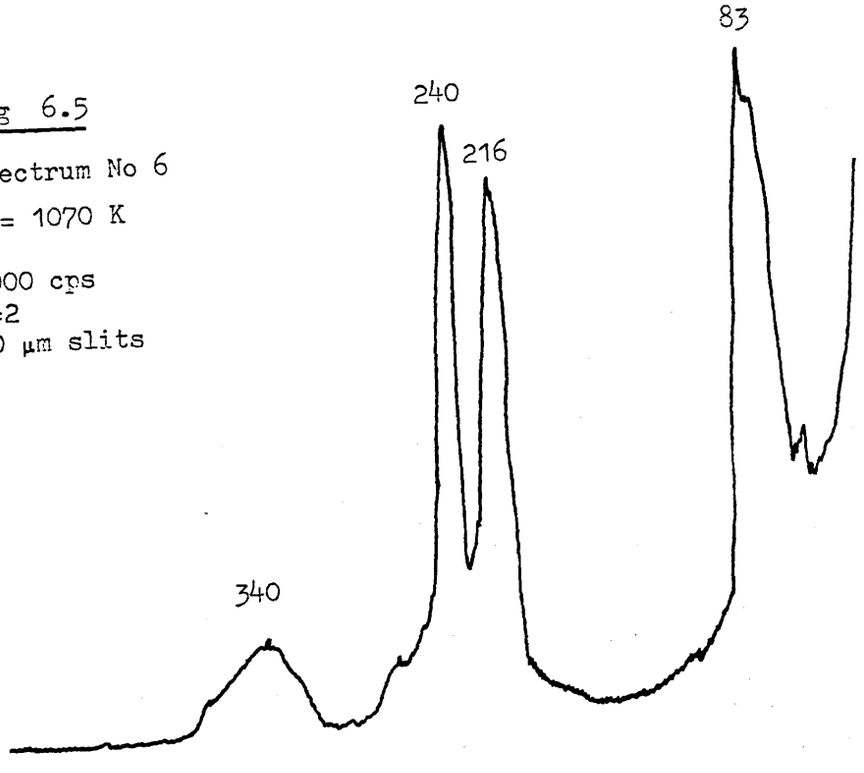

supressed to preclude the formation of GaBr.

The rest of the Raman work presented here was conducted at the Chemistry Department, University College, London, during May and June, 1978. A Coherent Radiation CR-12 Argon ion laser, operating at 514.5 nm (photon energy, 19436.3 cm^{-1}) and delivering 7 W of power at source, was used in conjunction with a Spex Ramalog 6 double monochromator.

In each of these experiments, a revised ampoule design was used, (see chapter two). Seven further ampoules were investigated. Details of the loadings of these ampoules are given below:

a) 2:1 molar quantities of gallium and gallium tribromide, sealed under vacuum.

b) Excess gallium arsenide, sealed in the presence of 800 mbar hydrogen.

c) As a), but sealed in the presence of 300 mbar hydrogen.

d) 2:1 molar quantities of gallium and gallium tribromide, sealed in the presence of 400 mbar hydrogen at 77 K.

e) 2:1 molar quantities of indium and indium tribromide, sealed in the presence of 400 mbar hydrogen at 298 K.

f) As e), but with indium trichloride substituted for the tribromide.

g) As e), but with indium triiodide substituted for the tribromide.

Ampoule a).

Spectrum number 7 was recorded at 783 K. This was the lowest temperature at which the collection port was free from condensing material. Raman shifts were recorded at 216, 240, 257, and 340 cm^{-1}. Additional spectra were recorded at 870, 923, and 990 K, and are labelled 8,9, and 10 respectively.

As the temperature is elevated, it is seen that the relative intensity of the monobromide peak at 257 cm^{-1}, increases at the expense of those peaks due to the tribromide. At the highest temperature, a rotational band contour (O, Q, S), is seen superimposed on the vibrational signal of the monohalide.

The low frequency band at 83 cm^{-1} does not appear in these spectra, since the high level of Rayleigh scatter precluded a scan below 100 cm^{-1}.

Ampoule b).

Spectrum number 11 was recorded at 579 K over the range 50 - 400 cm^{-1}. A good quality spectrum was obtained, displaying Raman shifts at the following frequencies: 53, 83, 118, 197, 216, 240, 295 and 347 cm^{-1}. The temperature was then lowered to 516 K and spectrum number 12 was recorded. Shifts are again seen at those frequencies quoted above, although the relative intensities of those due to $GaBr_3$ (83, 216, 240 and 347 cm^{-1}), have decreased with respect to those at 53, 118, 197 and 295 cm^{-1}. Spectra numbers 13, 14 and 15 were recorded at 470, 623 and 726 K respectively. At the lowest temperature, (470 K), the peaks at 53, 118, 197 and 295 cm^{-1} display their greatest intensity relative to those due to the tribromide. The highest temperature spectrum exhibits bands due to the tribromide alone, although

Fig 6.6

Spectrum No 7

T = 783 K

1000 cps
.2 $cm^{-1}s^{-1}$
IT=1
TC=1
400 μm slits

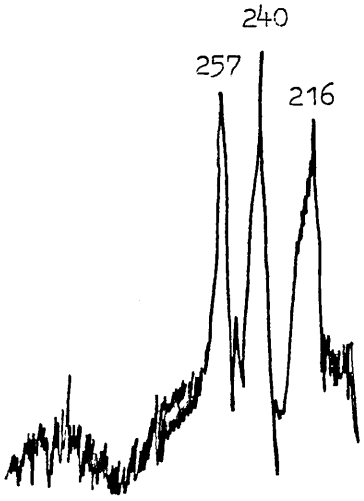

Fig 6.7

Spectrum No 8

T = 870 K

1000 cps
.2 $cm^{-1}s^{-1}$
IT=1
TC=1
400 μm slits

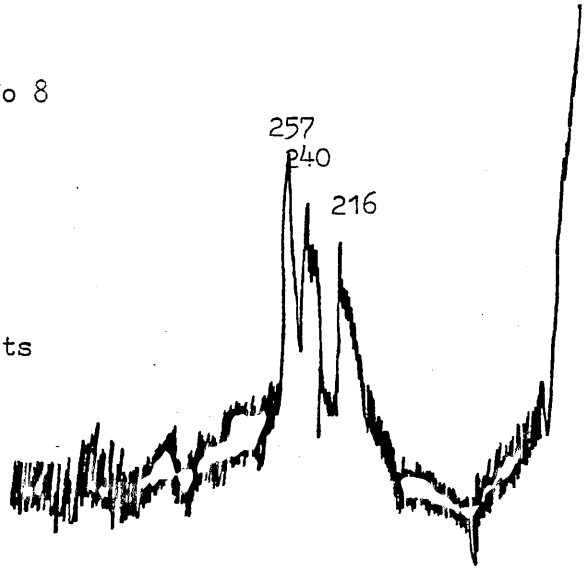

Fig 6.8

Spectrum No 9

T = 923 K

1000 cps
.2 $cm^{-1}s^{-1}$
IT=1
TC=1
400 μm slits

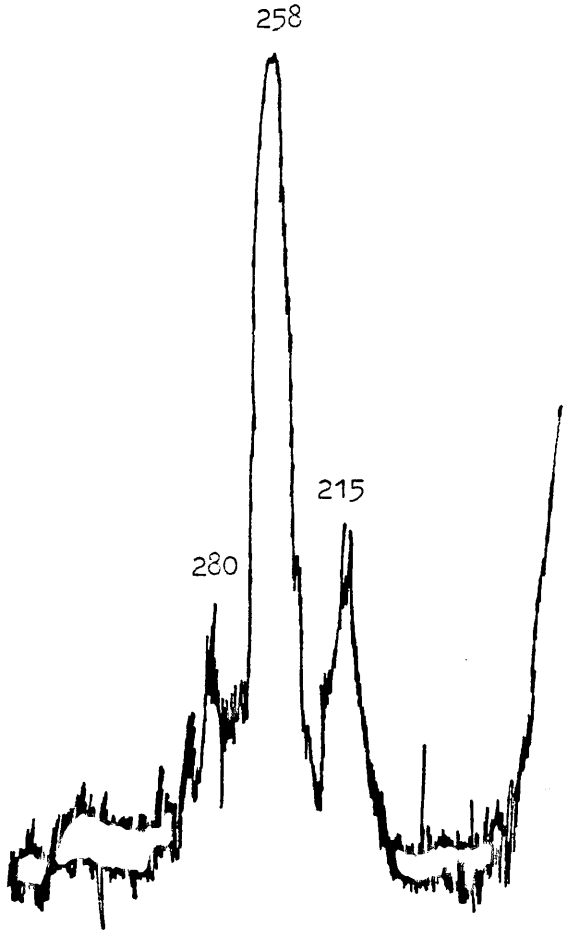

Fig 6.9

Spectrum No 10

T = 990 K

1000 cps
.2 $cm^{-1}s^{-1}$
IT=1
TC=1
400 μm slits

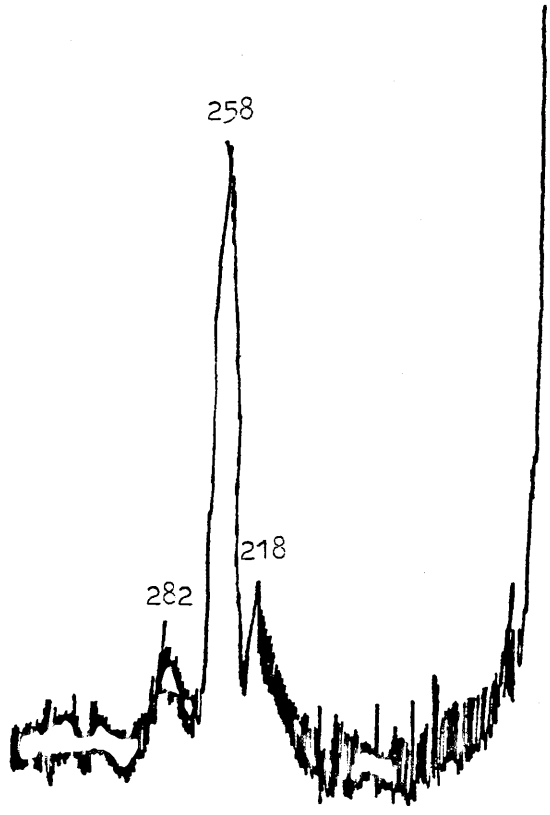

Fig 6.10

Spectrum No 11

T = 579 K

10000 cps
.5 $cm^{-1}s^{-1}$
IT=.2
TC=.5
400 μmslits

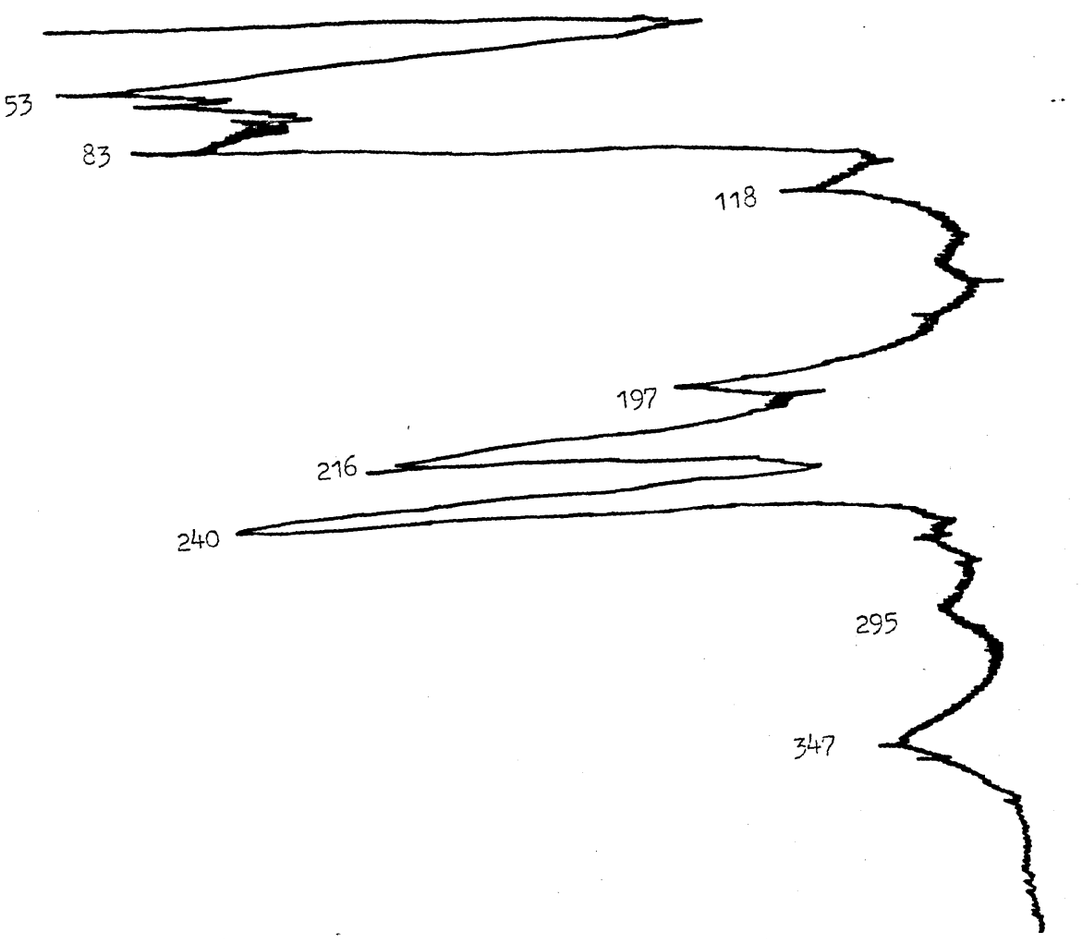

Fig 6.11

Spectrum No 12

T = 516 K

10000 cps
.5 $cm^{-1}s^{-1}$
IT=.2
TC=.5
400 µm slits

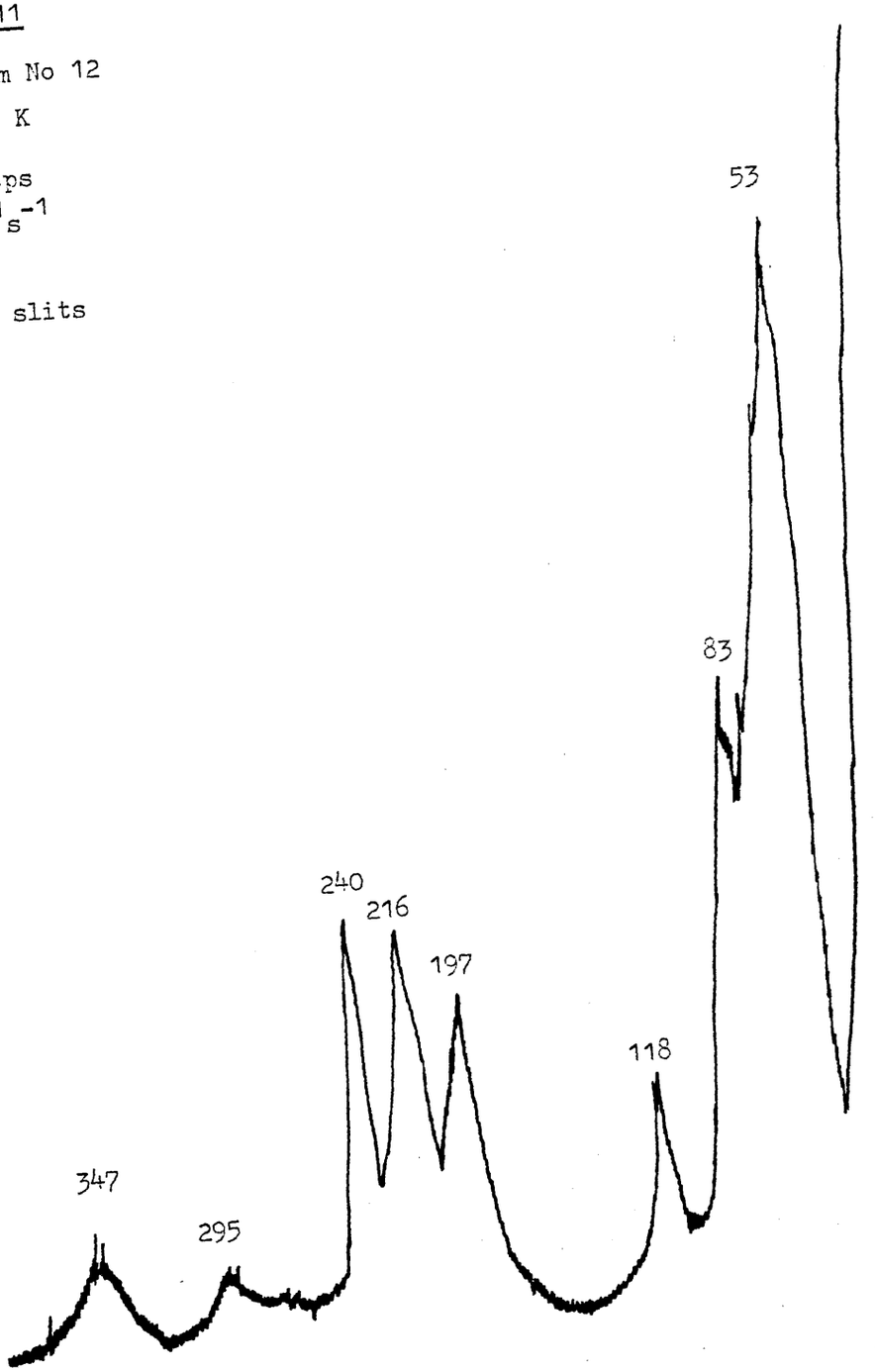

Fig 6.12

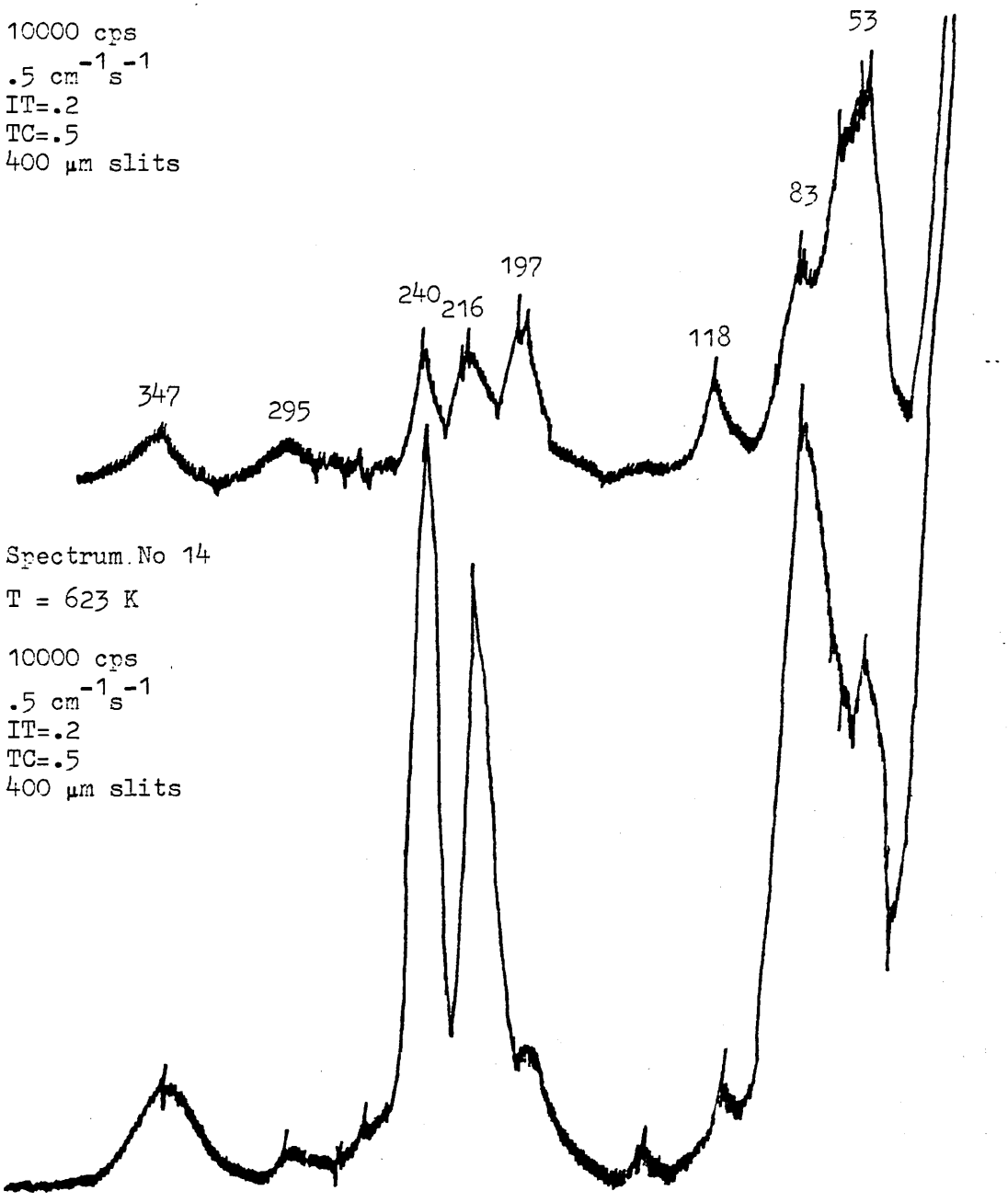
Spectrum No 13
T = 470 K
10000 cps
.5 cm-1s-1
IT=.2
TC=.5
400 µm slits
347
295
240
216
197
118
83
53
Spectrum No 14
T = 623 K
10000 cps
.5 cm-1s-1
IT=.2
TC=.5
400 µm slits

Fig 6.13

Spectrum No 15

T = 726 K

10000 cps
.5 $cm^{-1}s^{-1}$
IT=.2
TC=.5
400 μm slits

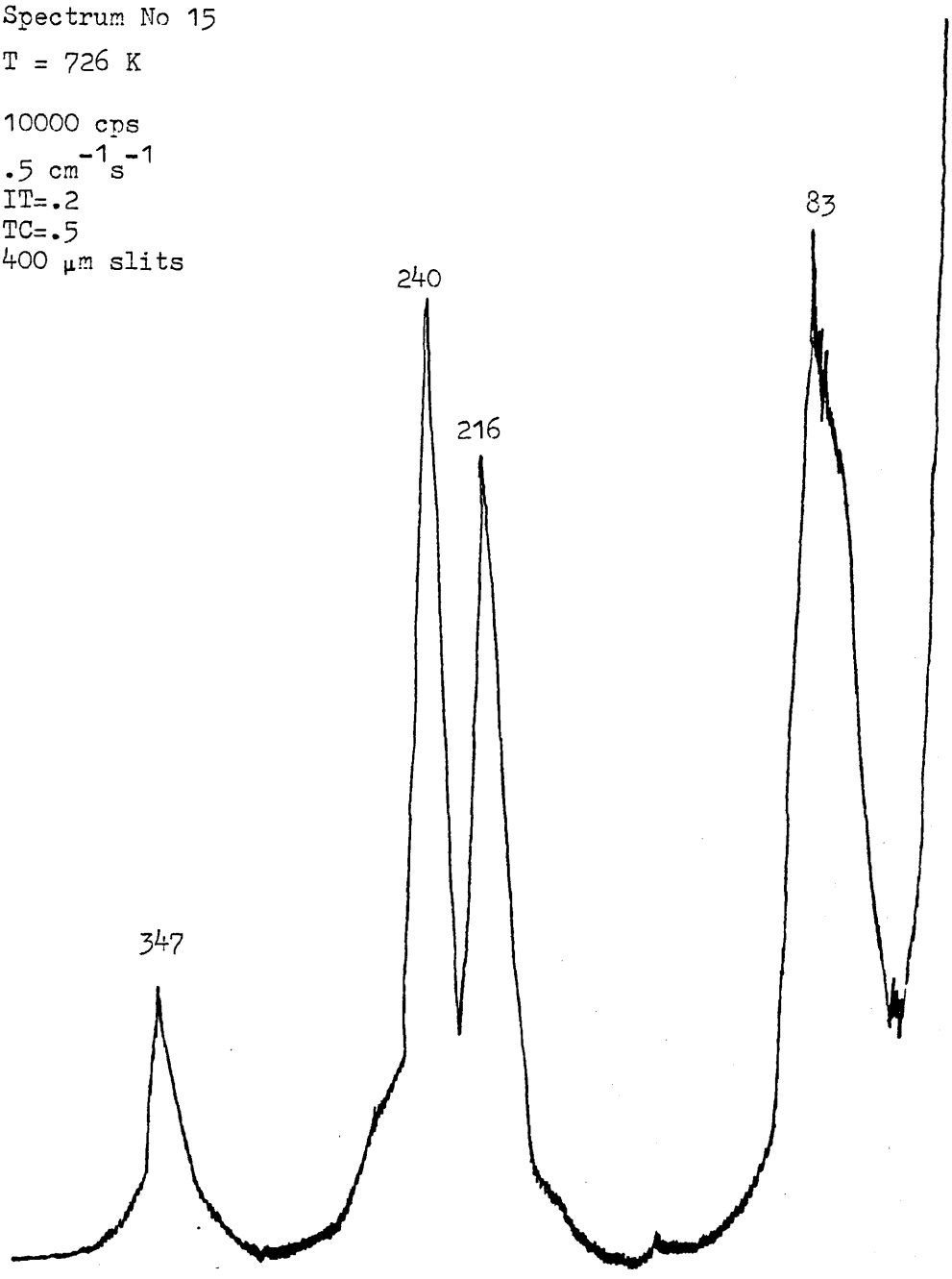

evidence does appear to be present of a slight shoulder to the high frequency side of the 240 cm^{-1} band. This shoulder can probably be attributed to the monobromide. The other four bands noted may be assigned to Ga_2Br_6.

Ampoule b) was loaded with polycrystalline GaAs. After temperature cycling, to ensure mechanical integrity of the ampoule, regrowth of the GaAs to form a single crystal was noted. It is evident then, that conditions prevail within the ampoules that are conducive to CVT of the GaAs, from a hot to a cooler zone.

Ampoule c)

Spectra numbers 16, 17, and 18 were recorded at 1053, 683, and 683 K respectively. Number 16 shows Raman scatter from GaBr alone, and the O,Q,S structure is evident, although the O branch is obscured by hot bands. For a diatomic molecule, the vibrational - rotational selection rules for Raman scattering are as follows; J = -2, 0 and +2, corresponding to the O,Q and S branches. The Q band centre occurs at 266 cm^{-1}, and the S branch maximum at 290 cm^{-1}.

Spectrum number 17 (683 K), was recorded from 60 - 380 cm^{-1}. Raman shifts are observed at 83, 210, 220, 240, 262 and 346 cm^{-1}. To record spectrum number 18 (683 K), the region 190 - 230 cm^{-1} was scanned with scale expansion: bands are seen at 207 cm^{-1} (centre of shoulder), and 218 cm^{-1}.

The last experiments were conducted on ampoules loaded with a group III metal halide, and hydrogen.

Fig 6.14

Spectrum No 16

T = 1053 K

.2cm^{-1}s^{-1}

IT=1

TC=1

400 μm slits

20000 cps

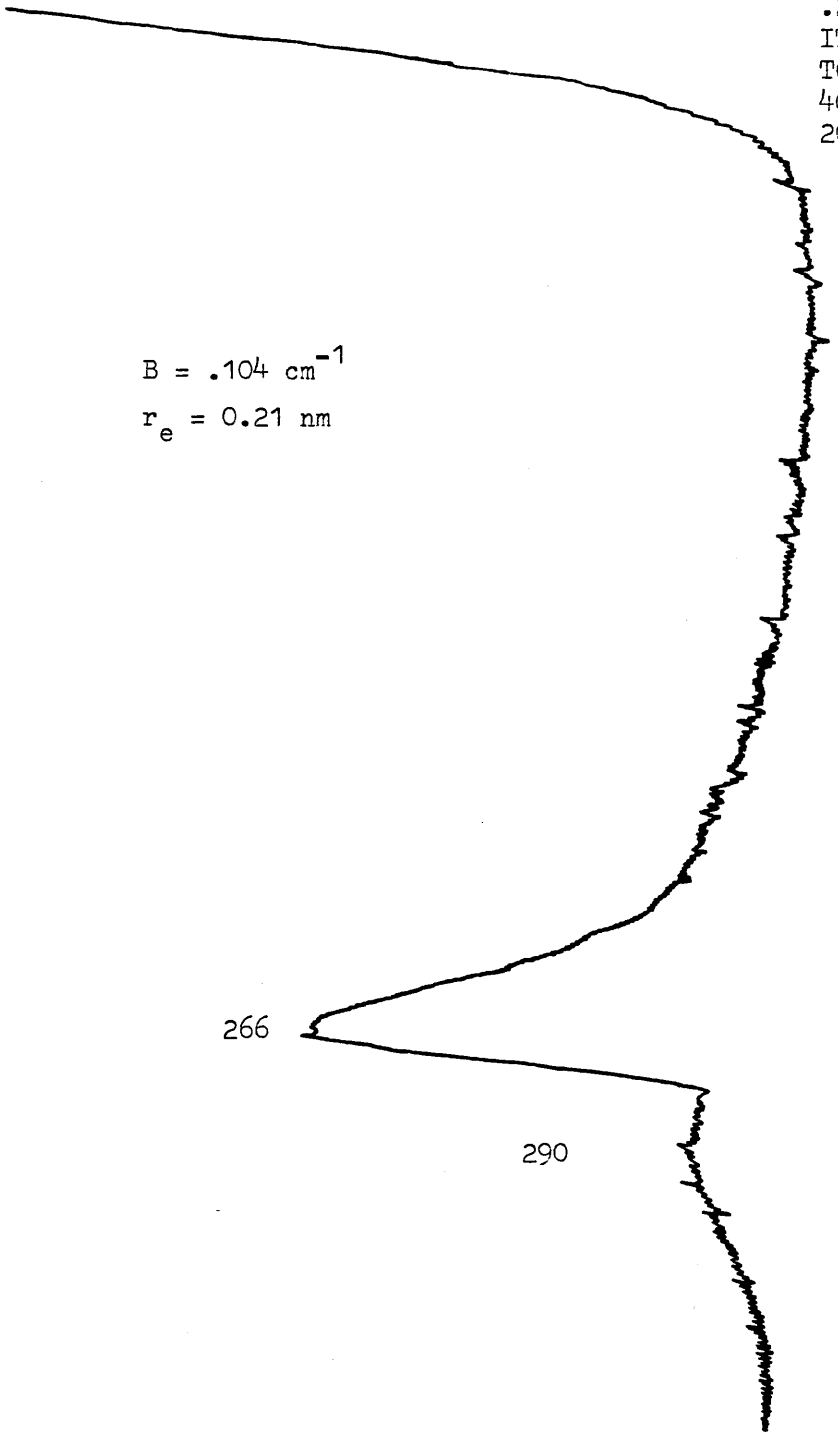

Fig 6.15

Spectrum No 17

T = 683 K

2000 cps
.2 $cm^{-1}s^{-1}$
IT=1
TC=1
400 μm slits

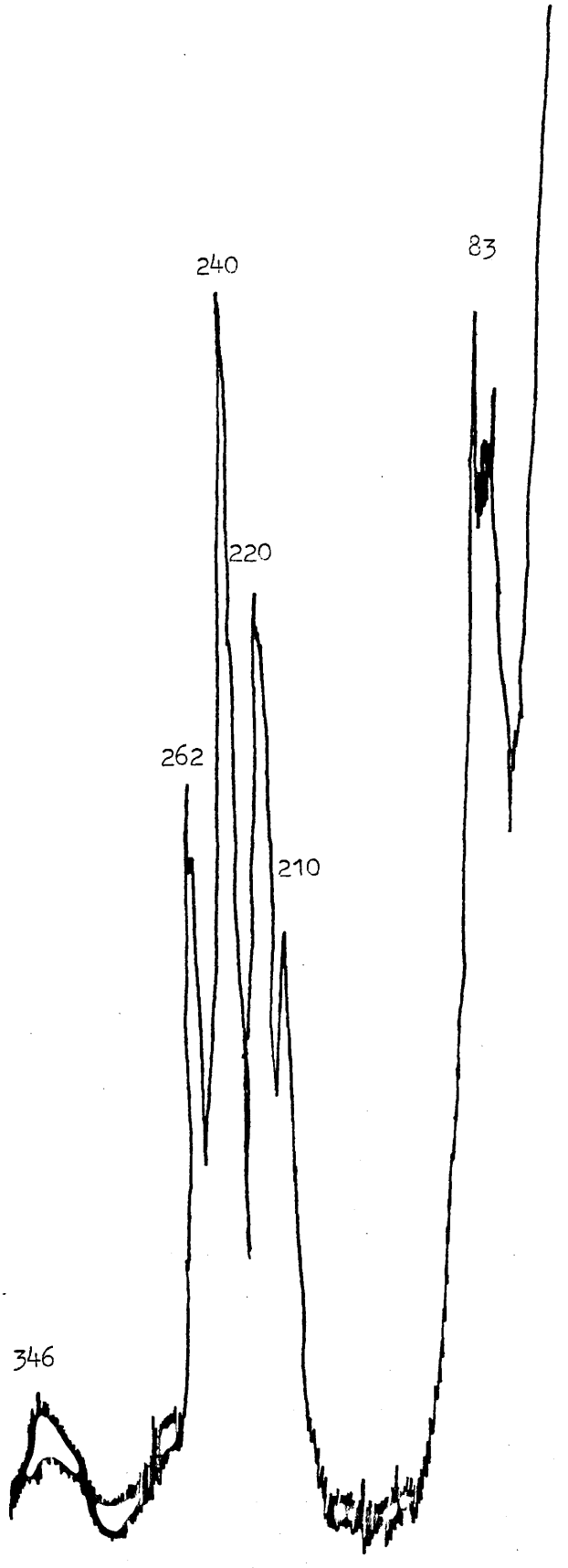

Fig 6.16

Spectrum No 18

T = 683 K

2000 cps
.2 $cm^{-1}s^{-1}$
IT=1
TC=1
400 μm slits

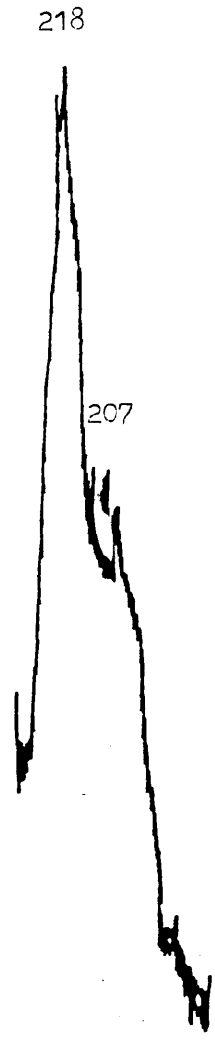

Ampoule d)

Spectrum number 19 was recorded at 718 K, which is the lowest temperature the collection port was free from condensing material. Raman shifts were recorded at 83, 208, 216, 240, 260, 346 and 357 cm^{-1}. The peaks at 208 and 357 cm^{-1} were found to be reproducible, but their resolution could not be improved. This is illustrated in spectrum number 20. Further spectra (numbers 21 and 22), were recorded at 787 and 973 K respectively. Progressive depletion of $GaBr_3$, and enhancement of GaBr is noted for the sequential spectra 20,21 and 22. This represents a shift to the right of the equilibrium:

$$GaBr_3(g) + 2Ga(l) = 3GaBr(g)$$

for which $\Delta H^{\circ} = 130\ kJmol^{-1}$.

Ampoule e)

Spectrum number 23 was recorded at 1086 K. Raman shifts occur at 214 and 235 cm^{-1}, corresponding to the Q and S branches of InBr. The O branch is again obscured by hot bands. Spectra of $InBr_3$ were not obtained, since as the temperature was lowered, material started to condense on the cooler collection port.

Ampoule f)

Spectrum number 24 was recorded at 1093 K. Q and S branches of the In Cl vibrational - rotational spectrum are noted at 310 and 335 cm^{-1} respectively. For reasons already stated above, no spectra were obtained at lower temperatures.

Fig 6.17

Spectrum No 19

T = 718 K

2000 cps
.2 $cm^{-1}s^{-1}$
IT=1
TC=1
400 μm slits

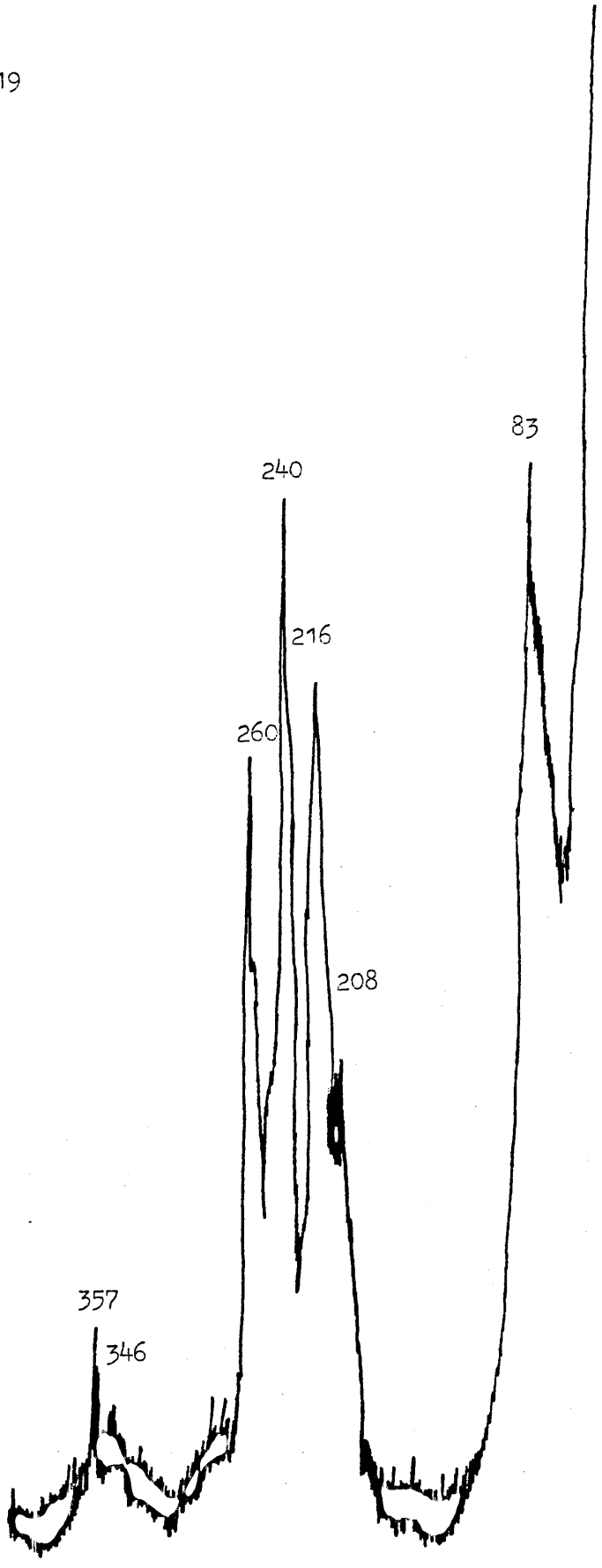

Fig 6.18

Spectrum No 20

T = 718 K

2000 cps
.2 $cm^{-1}s^{-1}$
IT=1
TC=1
400 μm slits

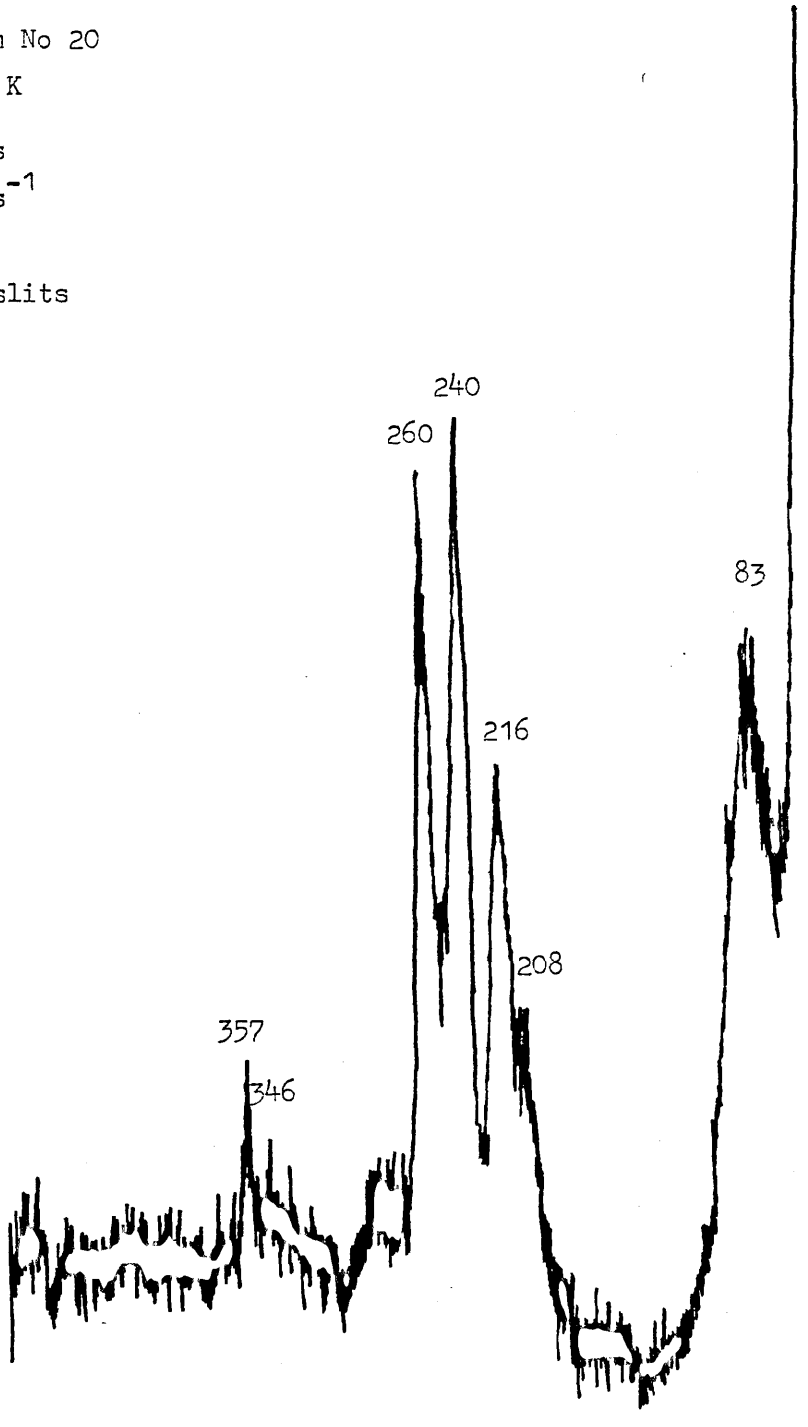

Fig 6.19

Spectrum No 22

T = 973 K

2000 cps
.2 $cm^{-1}s^{-1}$
IT=1
TC=1
400 μm slits

Spectrum No 21

T = 787 K

2000 cps
.2 $cm^{-1}s^{-1}$
IT=1
TC=1
400 μm slits

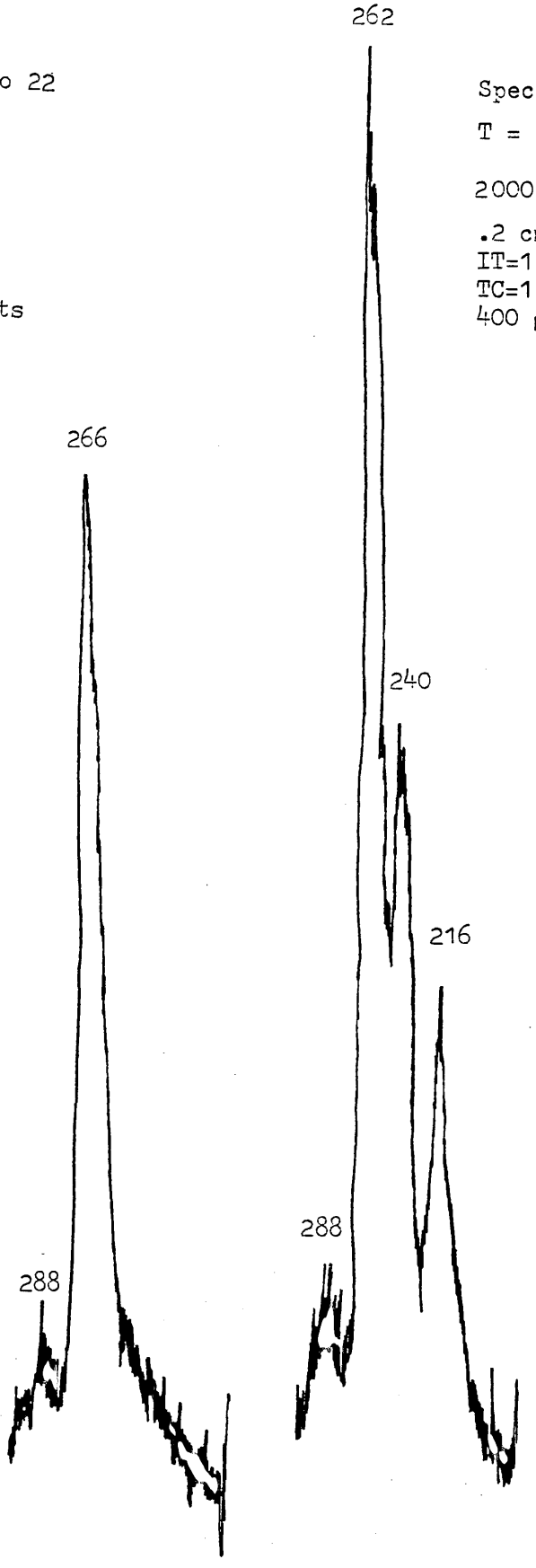

Fig 6.20

Spectrum No 23

T = 1086 K

2000 cps
.2 $cm^{-1}s^{-1}$
IT=1
TC=1
400 μm slits

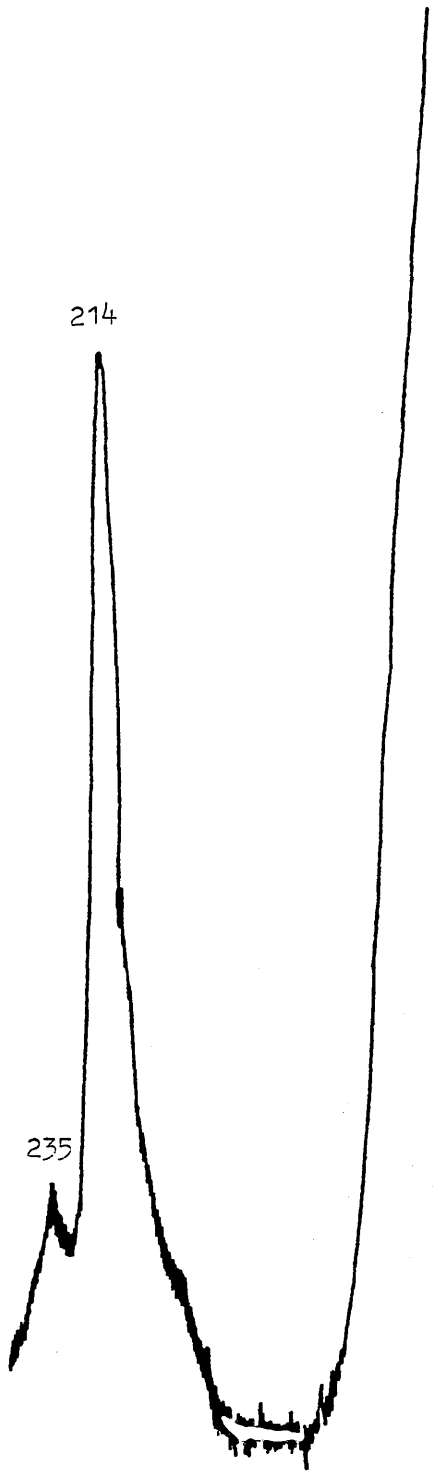

Fig 6.21

Spectrum No 24

T = 1093 K

2000 cps

.2 $cm^{-1}s^{-1}$
IT=1
TC=1
400 μm slits

Spectrum No 25

T = 875 K

2000 cps

.2 $cm^{-1}s^{-1}$
IT=1
TC=1
400 μm slits

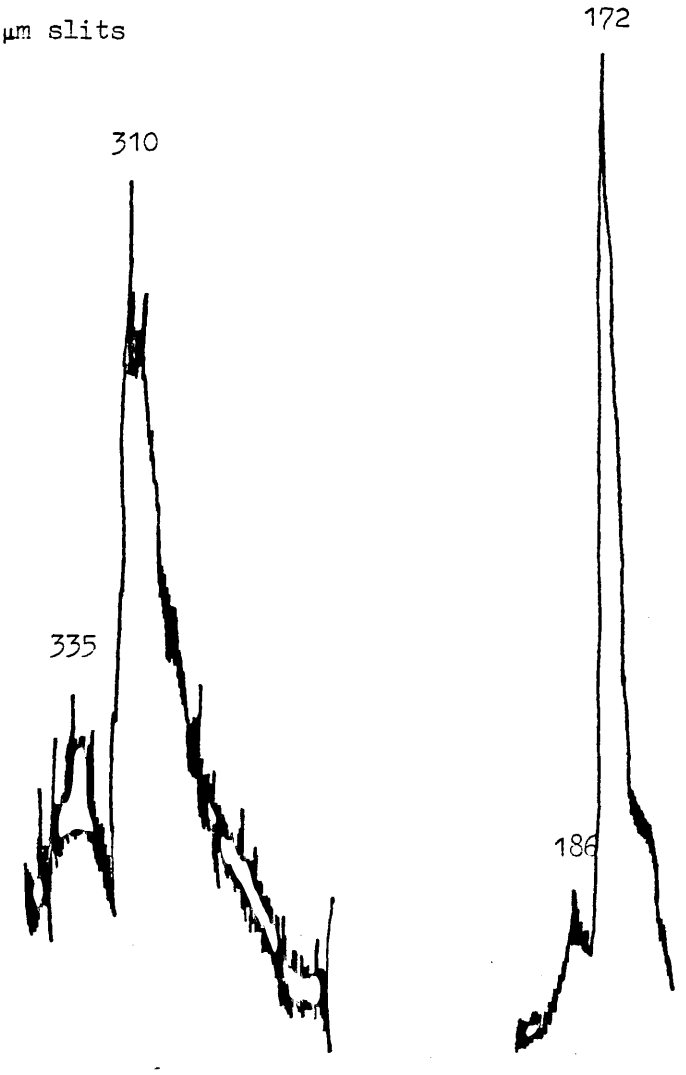

Ampoule g)

Spectrum number 25 was recorded at 875 K, and displays the Q (172 cm^{-1}) and S (186 cm^{-1}) branches of the vibrational - rotational spectrum of InI. Again no spectra were recorded at lower temperatures. In this instance, this was due to an intense fluorescence background.

6.3 Discussion

Many people in the electronics industry today are interested in the composition of CVT vapours. Some elegant work has been performed where Raman spectroscopy is used to moniter the gas composition over a growing crystal.[14,15,16] Various laboratories have performed more fundemental studies directly on the vapours above the metal halides of interest.[17.18] At the time that the decision was made to undertake this Ramna study, investigations on the vapour over "MX_2" melts had failed to yield any evidence of "MX_2" species in the vapour.

In was decided, then, to adopt an intermediate approach, and to study the vapours in "mini systems", including sealed ampoules where CVT might reasonably be in progress.

The MEM experiments that precipitated this interest were performed in a reducing ambient of a hydrogen atmosphere. Many of the ampoules were therefore sealed containing hydrogen.

The preliminary experiments yielded spectra of gallium mono- and tri-halides. The gaseous spectra of these molecules are well documented, and the observed bands may be unequivocally assigned. The band at 256 cm^{-1}, allowing for the presence of "hot" bands and a small isotope effect, is close to that predicted for GaBr from electronic spectroscopy.[19]

The second ampoule was loaded with a coarsely ground sample of GaAs. Following numerous temperature excursions, the condensed phase remained as discreet polycrystallites. In view of this, it may be concluded that chemical vapour transport mechanisms were not active in the system.

Group theory[20] predicts three Raman active bands for the D_{3h} point group (see appendix 4), of $GaBr_3$.

$$\Gamma_{GaBr_3} = A_1' + A_2' + A_2'' + 3E' + E''$$

			No vib'	Activity	
A_1'	1		1		R
A_2'	1	R_z	0		
A_2''	2	z	1	ir	
E'	3(6)	x,y	2(4)	ir	R
E''	1(2)	R_x,R_y	0		

$3N - 6 = 6$

We expect, then, a Raman spectrum consisting of two depolarised, degenerate modes, and one polarised mode. The fourth line has been attributed to Fermi resonance. In order to explain this fourth line, it is necessary for either a combination band, or an overtone to fall into accidental degeneracy with the $\tilde{\upsilon}_1$ fundemental. The only contender in this instance is the second overtone of $\tilde{\upsilon}_4$, at 83 cm^{-1}.

The symmetry restrictions governing the probability of an interaction between two wave functions, such that Fermi resonsnce might arise, are as follows: The overtone, or combination band, must contain the symmetry elements of the higher frequency fundemental; that is, the second overtone of $\tilde{\upsilon}_4$ must contain the

totally symmetric species A_1'.

The representation of the second overtone of E' $\tilde{\upsilon}_4$ is given by:

$$\chi_3(S) = \tfrac{1}{2}\ (\chi(S)\chi_2(S) + \chi(S^3)) \qquad (6.3.1)$$

where $\chi_2(S) = \tfrac{1}{2}\ (\chi(S)\chi(S) + \chi(S^2))$ (6.3.2)

$\chi(S)$, $\chi(S^2)$ and $\chi(S^3)$ are given below:

D_{3h}	E	$2C_3$	$3C_2'$	σ_h	$2S_3$	$3\sigma_v$
$\chi E'(S)$	2	-1	0	2	-1	0
$\chi(S^2)$	E	C_3	E	E	C_3^-	E
$\chi(S^3)$	E	E	C_2	σ_h	σ_h	σ_v
$\chi E'(S^2)$	2	-1	2	2	-1	2
$\chi E'(S^3)$	2	2	0	2	2	0

Now from 6.3.2

$\chi_2 E'(S)$	3	0	1	3	0	1

and from 6.3.1

$\chi_3 E'(S)$	4	1	0	4	1	0
χ_j^{cont}	3	0	-1	1	-2	1

using $n^{\Gamma} = 1/g\ \Sigma_j g_j\ \chi_j^{\Gamma}\chi_j$ (A4.1)

$$n^{A_1'} = 1/12\ (12 + 0 - 3 + 4 - 4 + 3) = 1$$

The second overtone of $\tilde{\upsilon}_4$ is theoretically then "allowed" to enter into Fermi resonance with the totally symmetric species. Three times 83 = 249, allowing for some "heavy metal anharmonicity" this frequency would drop and might approach 232 cm^{-1}. This is the frequency of the unperturbed $\tilde{\upsilon}_1$ mode estimated by Drake and

Rosanblatt.[18] Fermi resonance also appears to account for an additional peak in the spectrum of GaI_3, when excited by 488.0 nm radiation.

The remaining experiments were made using ampoules loaded with significantly smaller quantities of material. Less material was loaded for two reasons:

a) The furnace made available by Southampton University for these experiments accommodated 12 mm Ø ampoules, (as opposed to 20 mm Ø, previously used).

b) Trouble had been encountered with large volumes of melt in the ampoules.

The ampoule loaded with Ga and $GaBr_3$ again failed to yield spectra of intermediate gallium/bromine species. Another ampoule was sealed containing excess GaAs and a bromine-hydrogen mixture, in the hope of promoting CVT of the condensed phase by reaction with HBr. This ampoule was initially loaded with a coarsely ground sample of GaAs. Following temperature cycling to ensure mechanical integrity of the ampoule, the GaAs was observed to have regrown as a single crystal. On cooling, the characteristic brown colouration, indicating the presence of molecular bromine, was absent.

Spectra were obtained from ampoule b) at appreciably lower temperatures than previously possible. With the lower temperatures, came the opportunity to generate Ga_2Br_6 which was clearly present, as illustrated by the spectrum obtained.

Raman active features of the Ga_2Br_6 spectrum have been reported to occur at 56, 118 and 197 cm^{-1}.[21] After accounting for other known gallium bromides,[21] there remain two features still

to be assigned. These are the shifts observed at 150 and 297 cm^{-1}. The intensity of these two bands appear to increase with temperature. At the highest temperature, (726 K), however, the shift at 297 cm^{-1} is absent. In spectrum number 15, the peak at 347 cm^{-1} appears particularly sharp and intense. This is probably caused by a contribution from As_4, which exhibits a Raman active vibrational mode in this region.[22,23] Tetrameric arsnic has a further active mode at 270 cm^{-1}, and if present, this may either account for, or be obscured by the shoulder to high frequency (shift) of the Fermi resonance pair.

Molecular species likely to be contenders in accounting for the remaining scattering include $AsBr_3$, $SiBr_4$, and Si_2Br_6. However, none of these molecules scatter in the required shifts. The particular bands of interest were only present in spectra recorded from an ampoule containing arsnic. Tentatively, then, it is suggested that these bands arise from an arsnic containing molecule. $AsBr_3$ is reported to exhibit scatter at the following shifts: 289.7, 125.4, 284.0 and 92.5 cm^{-1}.[24]

The spectra recorded from ampoules c) and d), containing $Ga/GaBr_3/H_2$, are of particular interest. These ampoules provide spectra containing a well defined and reproducible peak to the low (Raman shift) frequency side of the Fermi resonance pair, due to $GaBr_3$. This additional band at 208 cm^{-1} is very likely to arise from a gallium-bromide molecule, although not one of those already discussed.

The Q-S separation in the spectra of the indium monohalides allows bond lengths to be calculated, but uncertainties in the band centre of the S branch introduce significant errors. These

calculations are collected in the table below:

molecule	observed $\tilde{\upsilon}/cm^{-1}$ Q	S	$\tilde{\omega}_e$	literature r_e/nm	calculated* r_e/nm
InCl	310	335	317[19]	0.242[25,26]	0.251±0.025
InBr	214	235	221[19]	0.257[25,27]	0.200±0.021
InI	172	186	177[19]	0.286[25]	0.257±0.027

* the uncertainties shown are calculated assuming an error of ±2 cm^{-1} in $\tilde{\upsilon}_S$.

Fairly recently, the existence of $InCl_4^-$ and $InBr_4^-$ has been reported in the vapour.[28] The evidence presented in reference 28 does not, however, appear to be totally conclusive, since the Raman frequencies assigned to these species have previously been assigned to In_2Cl_6 and In_2Br_6 respectively.[21]

If the interpretation of the spectra reported in reference 27 is correct, then it might be argued that some of the Raman bands reported here as attributable to Ga_2Br_6, may in fact arise from $GaBr_4^-$.

REFERENCES TO CHAPTER SIX

6.1 D. Battat, M.M. Faktor, J. Garrett and R.H. Moss J. Chem. Soc. Faraday I, 70, 2302 (1974)

6.2 E.J. Tarbox, PhD Thesis, London (1977)

6.3 This Work

6.4 L.F. Nilson and O. Petterson, Z. Physik Chem. 2, 657 (1888)

6.5 C.C. Addison and N.N. Greenwood, Ann. Rep. Chem. Soc. 55 122 (1958)

6.6 F.A. Cotton and G. Wilkinson, Advanced Inorganic Chemistry, pp 344 (Wiley 1962)

6.7 J.R. Chadwick, A.W. Atkinson and B.G. Huckstepp, J. Inorg. Nucl. Chem. 28, 1021 (1966)

6.8 J.H.R. Clarke and R.E. Hester Chem. Comm. pp. 1042 (1968)

6.9 G. Garton and H.M. Powell, J. Inorg. Nucl. Chem. 4, 84 (1957)

6.10 L.A. Woodward, G. Garton and H.L. Roberts, J. Chem. Soc. 3723 (1956)

6.11 V.P. Spinidonov, Yu. A. Brezgin and M.J. Shakhparonov, Russ. J. Struc. Chem. 13, 293 (1972)

6.12 A. Sultanov, Russ. J. Inorg. Chem. 17, 309 (1972)

6.13 Y. Kuniya and T. Chino, Denki Kagaku 40, 858 (1972)

Y. Kuniya, Y. Tanizawa and M. Hosaka, ibid. 41, 108 (1973)

Y. Kuniya and M. Hosaka, ibid. 616 (1973)

Y. Kuniya, S. Hasada and M. Hwaka, ibid. 42, 20 (1974)

Y. Kuniya and M. Hosaka, ibid. 616 (1974)

Y. Kuniya, M. Hasaka and I. Shindo, ibid. 43, 373 (1975)

Y. Kuniya and M. Hosaka, J. Cryst. Growth 28, 385 (1975)

6.14 T.O. Sedgwick, J.E. Smith, R. Ghez and M.E. Coaker, J. Cryst. Growth 31, 264 (1975)

6.15 T.O. Sedgwick and J.E. Smith, J. Electrochem. Soc. 123, 254 (1976)

6.16 Ja.Kh. Grinberg, J. Inorg. Nucl. Chem. 38, 383 (1976)

6.17 J.R. Beatlie and J.R. Horder, J. Chem. Soc. A 2433 (1970)

6.18 M.C. Drake and G.M. Rosenblatt, J. Chem. Phys. 65, 4067 (1976)

6.19 G. Herzberg, Spectra of Diatomic Molecules (Von Nostrand, 1967)

6.20 E. Bright Wilson, J.C. Decius and P.C. Cross, Molecular Vibrations : The Theory of Infrared and Raman Vibrational Spectra (Constable 1980)

6.21 J.R. Beatlie and J.R. Horder, J. Chem. Soc. A 17, 2655 (1969 1969)

6.22 R.J. Capwell and G.M. Rosenblatt, J. Mol. Spec. 33, 525 (1970)

6.23 A. Rogstad, J. Mol. Structure 14, 421 (1972)

6.24 R.J.H. Clark and D.M. Rippon, J. Mol. Spec. 52, 58 (1974)

6.25 H. Brode, Ann. Physik 37, 344 (1940)

6.26 G.H.L. Delvigise and H.W. de Wijn, J. Chem. Phys. 45, 3318 (1966)

6.27 E. Tiemann, U. Kölher and J. Hoeft, Z. Naturforsch A 32, 6 (1977)

6.28 P.L. Radloff and G.N. Papatheodoroug, J. Chem. Phys. 72. 992 (1980)

CHAPTER SEVEN

Thermochemistry of indium bromide

7.1 Introduction

In order to process the results obtained from MEM experiments, it has been seen that thermodynamic data relating to the likely species involved is required (viz chapters 4 and 5). Studies involving the transport of InAs and InP, via the volatile bromides of indium would suggest the involvement of InBr(g).[1,2]

Unfortunately, there is some uncertainty as to the value of ΔH^{o}_{f} InBr(g) at 298 K, and hence also a similar value at 1000 K. Collating data from the literature, and using estimates derived from bond energies, it would seem that:

$$-80 < \Delta H^{o}_{f1000}\ \mathrm{InBr(g)} < 0$$

In view of this unsatisfactory situation, it was decided that some measurements might usefully be made in this area. To this end, the following work was undertaken: determination of ΔH^{o}_{f298} InBr(c), ΔH_{vap} InBr(l), C_p InBr(c), ΔH_{fus} InBr(c). It was originally intended also to measure the heat capacity of InBr(l). This was, however, precluded for reasons explained later. The heat capacity of InBr(g) is readily calculated, using a statistical approach.

Now:

$$\Delta H^{o}_{f1000} = \Delta H^{o}_{f298} + \int_{T_{298}}^{T_{mpt}} \Delta C_p(c)\,dT + \Delta H_{fus} + \int_{T_{mpt}}^{T_{fus}} \Delta C_p(l)\,dT$$

$$+ \Delta H_{vap} + \int_{T_{vap}}^{1000} \Delta C_p(g)dT \qquad (7.1.1)$$

The first term may be determined calorimetrically.

The second, third and fourth terms may be measured by DSC.

The fifth term may be determined by MEM experiments.

The sixth term may be calculated using statistical thermodynamics.

7.2 Solution calorimetry

7.2.1 Procedure.

The heat of formation of InBr(c) at 298.15 K was determined by repeating the measurements of Barrow et al,[3] using the isoperibol solution calorimeter described in chapter two. This particular method of determination was first employed by Klemm and Brautigam.[4]

The heat of solution of InBr(c), $InBr_3$(c) and In(c) were measured in a 33% solution of potassium bromide saturated with bromine. The heats of formation of InBr(c) and $InBr_3$(c) are obtained from the heats of solution by application of Hess' Law. Cycles of the appropriate reactions appear in figures 7.1, and 7.2.

Prior to the calorimetric study on the indium bromides, the accuracy and precision of the calorimeter was assessed. This assessment is made by measuring the heat of solution of a standard material. Tris-hydroxymethylamioethane (THAM), was the standard material chosen for this purpose. The neutralisation of THAM in 0.1 mol dm^{-3} hydrochloric acid is widely used in this

Fig 7.1

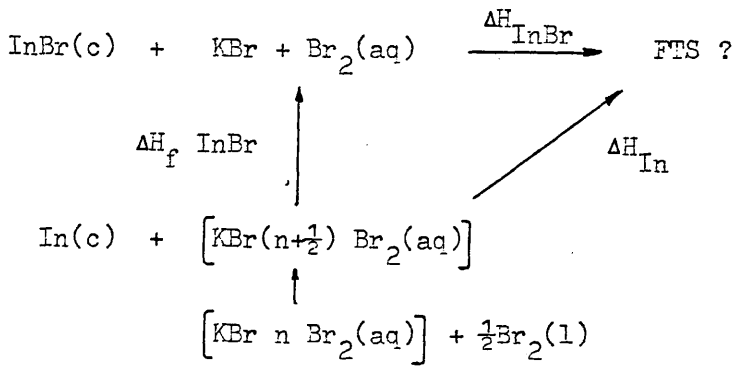

$$\Delta H_f\ InBr(c) = \Delta H(In) - \Delta H(InBr) + \Delta H(Br)$$

Fig 7.2

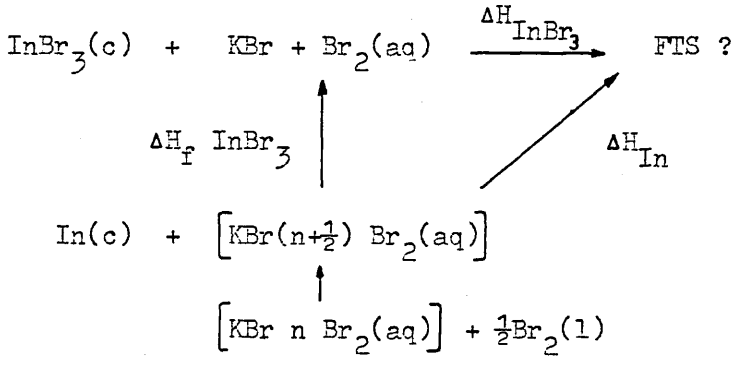

$$\Delta H_f\ InBr_3(c) = \Delta H(In) - \Delta H(InBr_3) + \Delta H(Br)$$

context. THAM is a white crystalline solid, non-hydroscopic, which is available in high purity.

In order that the above assessment is a valid indication of the overall accuracy in heats of solution (reaction) of other materials, certain constraints must be applied. The weight of material for which the heat of solution (reaction) is being determined, is chosen such that the "reaction" generates a similar temperature change in the reaction vessel as does the test THAM reaction.* This ensures that the calorimeter is not operated beyond the limits of temperature change, calibration etc, as observed for the test reaction. The assessment procedure was also repeated following any modifications to the calorimeter, (eg, adoption of alternative calibration curcuits and/or heaters).

Ampoules and THAM were oven dried at 400 K, cooled under vacuum, and bathed in dry nitrogen prior to use.

7.2.2 Results

The assessment of the calorimeters' performance took place in three stages. The preliminary work simply illustrated that the calorimeters' calibration cicuit required objective scrutiny. Having made the necessary modification to the calibration curcuit, an assessment was then made using the commercially available, PTFE encapsulated heaters. The final appraisal involved the use of home-made heaters, and further revision of the calibration circuits.

* (NB. The neutralisation of THAM by 0.1 M hydrochloric acid is exothermic. This standard, then, is only attributable, as an assessment, to exothermic reactions. An endothermic reaction standard must be adopted if endothermic reactions are to be studied).

The Tronac heaters proved unreliable when immersed in the bromine saturated solution required for the work on the indium salts. Failure of the heaters, although not in a catastrophic manner, resulted as bromine permeated the PTFE cladding. Further problems arose from the corrosive nature of the solution in use. The hermatic seal used to secure the thermistors also yielded to attack. This problem was overcome by tightly wrapping the thermistors in PTFE tape, prior to sealing in silicone rubber.

Table 7.1 shows the overall results for the neutralisation of THAM in 0.1 M hydrochloric acid (ie, including all three stages of the assessment). Table 7.2 lists those results obtained with the calibration circuit in its final form.

The results for the measurements of the heats of solution of indium monobromide, indium tribromide and indium metal appear in tables 7.3, 7.4 and 7.5 respectively.

Having obtained values for the various heats of solution involved in the thermodynamic cycles shown previously, ΔH^{o}_{f298} InBr(c) and ΔH^{o}_{f298} $InBr_3$(c) may be extracted.

Now: ΔH^{o}_{f298} InBr(c) = ΔH In(c) - ΔH InBr(c) + ΔH Br(l)

the heats of solution of a very small quantity of bromine, ΔH Br, in a solution already saturated with bromine is assumed to be negligibly small.

Hence ΔH^{o}_{f298} InBr(c) = -140.2 ± 10 kJ mol^{-1}

and ΔH^{o}_{f298} $InBr_3$(c) = -399.8 ± 6 kJ mol^{-1}

Table 7.1

Heats of neutralisation of THAM in 0.1 M hydrochloric acid.

vessel indentification	weight of sample/g	Heat of solution /kJ mol^{-1}
left	0.7277	30.03
left	0.7060	31.16
left	0.7319	29.56
left	0.9088	29.05
left	0.7733	29.63
left	0.9334	29.62
right	0.7982	29.53
right	0.6932	29.65
right	0.7544	30.14
right	0.7830	29.35
right	0.9410	29.77
right	0.7210	29.99
right	0.8886	30.26
right	0.7096	29.50
right	0.6154	30.21
right	0.6465	30.72
right	0.8637	29.86
left	0.6449	30.86
left	0.6222	30.96
left	0.7530	29.33
left	0.7012	29.99
right	0.6234	30.63
right	0.5847	29.56
right	0.6716	29.49
right	0.9212	29.62
left	0.8065	29.38
left	0.6986	29.89
left	0.6292	30.26
left	0.5856	30.37
left	0.8758	29.65

Table 7.1 continued.

vessel indentification	weight of sample/g	Heat of solution /kJ mol^{-1}
left	0.8586	29.84
left	0.7802	29.88
right	0.6204	30.27
right	0.6363	30.29
right	0.7078	29.66
right	0.6559	29.52
right	0.7399	29.76
right	0.6827	29.74
n = 38		29.92 ± 0.16
n = 17 left		29.97 ± 0.29
n = 21 right		29.88 ± 0.17

Table 7.2

Heats of neutralisation of THAM in 0.1 M hydrochloric acid, with the calibration circuit in its final form.

vessel indentification	weight of sample/g	Heat of solution /kJ mol^{-1}
left	0.8065	29.38
left	0.6986	29.89
left	0.6292	30.26
left	0.5856	30.37
left	0.8758	29.65
left	0.8586	29.84
left	0.7802	29.88
right	0.6204	30.27
right	0.6363	30.29
right	0.7078	29.66
right	0.6559	29.52
right	0.7399	29.76

Table 7.2 continued.

vessel identification	weight of sample/g	Heat of solution /kJ mol^{-1}
right	0.6827	29.74
n = 13		29.89 ± 0.18
n = 7 left		29.90 ± 0.26
n = 6 right		29.87 ± 0.27

These values may be compared with a difinitive value taken as 29.77 ± 0.03 kJ mol^{-1}.*

Table 7.3

Heats of solution of indium monobromide.

vessel identification	weight of sample/g	Heat of solution /kJ mol^{-1}
left	0.1105	341.5
left	0.1007	349.3
left	0.1519	364.4
left	0.0572	352.2
left	0.1133	337.6
left	0.0732	344.3
right	0.2939	346.9
right	0.0691	362.7
right	0.0847	339.4
right	0.0669	364.6
right	0.1172	351.2
n = 11		350.4 ± 5.9
n = 6 left		348.2 ± 7.8
n = 5 right		353.0 ± 9.5

* E J Prosen and M V Kilday, J Res Natl Bur Stand 77A, 581 (1973)

Table 7.4

Heats of solution of indium tribromide.

vessel identification	weight of sample/g	Heat of solution /kJ mol^{-1}
left	0.1394	90.28
left	0.7381	93.47
right	0.9329	93.07
right	1.2371	91.93
right	0.6262	90.23
right	0.4973	90.63
n = 6		91.60 ± 1.18

Table 7.5

Heats of solution of indium metal.

vessel identification	weight of sample/g	Heat of solution /kJ mol^{-1}
left	0.1283	498.8
left	0.0310	496.8
left	0.0394	495.0
left	0.0292	480.1
left	0.0382	490.4
right	0.1120	487.5
right	0.0333	479.6
right	0.0392	490.1
right	0.0434	495.2
right	0.0398	484.1
right	0.0315	498.8
n = 11		490.6 ± 4.2
n = 5 left		492.2 ± 6.7
n = 6 right		489.2 ± 5.8

(NB the heat of solution, $\Delta H(In)$, found in this work compares favourably with values obtained by both Barrow & Smith, and Klemm & Brautigam).

7.2.3 Discussion

Comparing the heats of solution for indium and indium monobromide in this work with that performed by Smith and Barrow[3], it is clear that good agreement is obtained for indium, but not the monobromide.

Comparison of the heats of solution appear below:

	Barrow & Smith	This Work
ΔH_s InBr(c)	-313.4 ± 12	-350.4 ± 5.9
ΔH_s In(c)	-486.6 ± 8	-490.6 ± 4.2 *

This difference in ΔHInBr gives rise to a significant deviation in the calculated values for ΔH^o_{f298} InBr(c) :

Barrow & Smith	This Work
-173.6 ± 20	-140.2 ± 10.1

The value of ΔH^o_{f298} $InBr_3$(c) of -399.8 kJ mol^{-1} lies within 8% of the value published in NBS Tech Note 270 - 3, of -428.9, and lies within experimental error of the value in reference 5.

7.3 Heat capacity of indium monobromide

7.3.1 InBr(g)

Statistical thermodynamics provides the tool by which thermodynamic properties of gases may be calculated. For an ideal diatomic molecule, the treatment is relatively simple, as the experimental parameters required are normally available from the

* (NB The heat of solution, ΔHIn, found within this work also compares favourably with the value obtained by Klemm and Brautigam)[4].

literature.

Essentially, the treatment involves the evaluation of the translational, rotational and vibrational partition functions. Since indium monobromide is not included in JANAF tables, a generalised computer program was written using the calculational methods of Mayer and Mayer (as used by JANAF), and the calculations performed by a CDC 6600 electronic computer.

The program was tested by comparing the data output on selected test molecules that are included in the JANAF computation. The molecules chosen for the comparison were AlCl, AlBr and InCl. Good agreement was found in each case. Tables were then generated for InBr. Spectroscopic data were taken from Herzberg in each case. Atomic weights and relative abundences were assumed from Tennent.[6] Table 7.6 illustrates the results. The values for C_p^o may be fitted to an expression of the form:

$$C_p = a - (bT^{-2}) \quad JK^{-1}mol^{-1}$$

the values

$$a = 37.415$$

$$b = 65000$$

satisfy the calculations over the temperature range 273 to 2000 K.

7.3.2 InBr(c)

A Perkin-Elmer differential scanning calorimeter (model DSC-2), was used as described in chapter two. Temperature scans (40 K intervals) were made at a heating rate of 5 K min^{-1} and a

Table 7.6

Thermodynamic functions of indium monobromide gas over the temperature range 100 to 2000 K.

T/K	C_p°	S°	$-(G^\circ-H^\circ_{298})/T$	$H^\circ-H^\circ_{298}$
100	32.93	221.0	291.5	-7.03
200	35.86	245.0	262.8	-3.56
273.2	36.53	256.3	259.6	-0.92
298.2	36.65	259.5	259.5	0.0
300	36.69	259.7	259.5	0.08
400	36.99	270.3	261.0	3.77
500	37.15	278.6	263.7	7.44
600	37.23	285.4	266.8	11.17
700	37.28	291.1	269.8	14.90
800	37.32	296.1	272.8	18.62
900	37.32	300.5	275.6	22.34
1000	37.36	304.4	278.3	26.11
1100	37.36	308.0	280.9	29.83
1200	37.36	311.2	283.3	33.56
1300	37.36	314.2	385.5	37.32
1400	37.36	317.0	287.7	41.05
1500	37.36	321.4	289.7	44.77
1600	37.40	322.2	291.7	48.53
1700	37.40	324.2	293.5	52.26
1800	37.40	326.4	295.3	55.98
1900	37.40	328.4	297.0	59.75
2000	37.40	330.3	298.6	63.47

range setting corresponding to a deflection of 8.368×10^{-4} Js^{-1} (for 10 mV fsd). From the traces obtained, heat capacities were calculated at 10 K intervals in the range 330 to 530 K. At the chosen heating rate, the following temperature correction is appropriate:

$$T_{true}/K = ((T_{obs}/K) - 3.5722)\ 1.0087$$

The results are tabulated in table 7.7. This experimental data was fitted to a straight line by a linear regression routine, and the following expression results:

$$C_p/JK^{-1}mol^{-1} = 4.24 \pm 0.02 + (10.792 \pm 0.004) \times 10^{-2}\ (T/K)$$

7.4 Transition enthalpies of indium monobromide

7.4.1 Fusion

When the DSC was used to record the heat of fusion of InBr(c), an unexpected additional thermal transition was discovered. There is conflicting literature data on the melting point of InBr, (values of 493[7], 548,[5] and 563[8] K have been reported).

Temperature scans from 330 to 600 K display two features of interest. In the range 470 to 510 K, a small endothermic transition is evident, as the thermogram displays multiple* irreproducible peaks in this region. At around 550 K, a larger, far more reproducible endothermic peak occurs. This larger peak is interpreted as the melting transition. When the lower temperature transition occurs as a single peak, the temperature is reproducible at 506.8 K. The exothermic event that results

* (NB Frequently, a single peak was recorded in this temperature region, although in many instances, multiple peaks were observed).

Table 7.7

The measured heat capacity of InBr(c).

C_p/J $K^{-1}mol^{-1}$	T/K	C_p/J $K^{-1}mol^{-1}$	T/K
39.84	330	50.65	430
40.93	340	51.75	440
42.02	350	52.80	450
43.16	360	53.86	460
44.16	370	54.98	470
45.25	380	56.07	480
46.34	390	57.12	490
47.45	400	58.21	500
48.46	410	60.35	520
49.52	420	61.46	530

Table 7.8

The measured transition enthalpies of InBr(c).

ΔH_1/kJ mol^{-1}	T_1/K	ΔH_2/kJ mol^{-1}	T_2/K
3.64	470-510	11.62	551
3.56	480-507	11.90	550.5
3.41	460-505	12.78	548.5
3.47	460-505	12.51	550
3.57	455-505	12.95	551
3.53 ± 0.08		12.4 ± 0.5	

T_1 and ΔH_1 refer to the crystal-crystal transition, and T_2 and ΔH_2 refer to the melting transition.

on cooling falls some 6 K lower. This low temperature endotherm is probably a crystal-crystal transition, and the irreproducibility probably arises from imperfect thermal contact between the pan and the crystals it contains. During melting, of course, good thermal contact is quickly obtained.

The results of five experiments performed at a heating rate of 10 K min^{-1} are collected in table 7.8. T_1 denotes the crystal-crystal transition, and T_2 the melting transition. A typical trace appears in fig 7.3.

Further traces were recorded at half the heating rate previously used to determine the transition temperatures.
In summary:

$$\Delta H_1 = 3.53 \pm 0.08 \quad kJ\,mol^{-1}$$
$$T_1 = 506.8\ K$$
$$\Delta H_2 = 12.4 \pm 0.5 \quad kJ\,mol^{-1}$$
$$T_2 = 550\ K$$

This value for ΔH_2 is in poor agreement with a figure quoted in reference 5, of 24.3 $kJmol^{-1}$. The appearance of a crystal-crystal transition was initially surprising, since no reports of such dimorphism are evident in the literature. Three differing values spanning 70 K for the melting point of InBr(c) are documented. (These are 493,[7] 548,[5] and 563[8] K). The values for T_2 from this work may be seen to be in good agreement with that from reference 5. It is known that $Ga_2Br_4(c)$ is dimorphic,[9] and the two crystalline forms display different colours, with melting points of 426 and 438 K.

Fig 7.3 Typical thermogram, displaying two transitions.

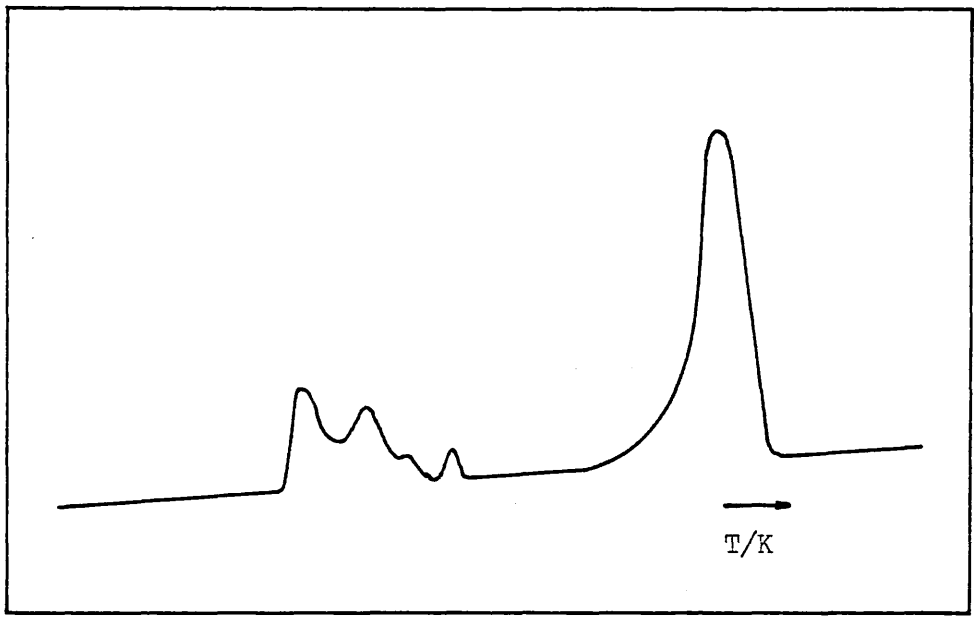

7.4.2 Vaporisation

It was deemed useful to carry out a MEM study on indium monobromide for two reasons. Firstly, from the results, the enthalpy and entropy of evaporation may be extracted. Further interest results from the MEM study on indium phosphide/hydrogen bromide. At low temperatures, the plot of $\ln\dot{w}$ v $1/T$ curves steeply downward, and below 730 K weight gain was evident (vis chapter five). A possible explanation for the low temperature behaviour of the InP/HBr system may be that indium monobromide formed during transport may have insufficient volatility to escape from the bottle.

Now, in chapter three, it was shown that for the evaporation of a single species:

$$P_A^o = P(1 - e^{-\xi_i}) \qquad (7.4.1)$$

Where: P_A^o is the pressure of species A.

P is the total pressure.

ξ_i is the transport function of species A.

If the weight loss is not too large, we may approximate the experimental in 7.4.1, and obtain:

$$P_A^o = \dot{w}RTl/(DM_AAP) \qquad (7.4.2)$$

Here: $\dot{w}/kgs^{-1}$ is the observed rate of weight loss.

$R/JK^{-1}mol^{-1}$ is the gas constant.

T/K is the temperature.

l/m is the length of the channel.

D/m^2s^{-1} is the diffusion coefficient of InBr in H_2.

$M/kgmol^{-1}$ is the molecular weight of InBr.

A/m^2 is the cross sectional area of the channel.

P/Pa is the total pressure.

It is preferable to carry out measurements of weight loss over as wide a temperature range as possible, and it is necessary to correct for the temperature dependence of the diffusion coefficient. Over a range of temperature, the expression:

$$D_T = D_o(T/273.15)^{1+s} \qquad (7.4.3)$$

as used in chapters four and five. Equation 7.4.2 may now be rewritten:

$$p_A^o = \dot{w}RT_o^{1+s}1/(D_oT^sM_AAP) \qquad (7.4.4)$$

A plot of $R\ln(\dot{w}/T^s)$ against $1/T$ will have a slope of $-\Delta H_v$, and an intercept at $1/T$ of $\Delta S_v - R\ln(1RT_o^{1+s}/(D_oPM_AA))$.

Any values of enthalpy and entropy of evaporation extracted from such work will be dependent on uncertainties in the diffusion coefficient. The parameter D_o appears only in the expression for the entropy, and then only as a logorithm. An error of 6 $Jmol^{-1}K^{-1}$ will then be introduced by an uncertainty of a factor of two in D_o. Although the value of D_o may not be known accurately, a reasonable estimate may usually be made.

The index s affects both ΔH and ΔS. The error $\delta(\Delta H)$ introduced by an error $\delta(s)$ may be found:

$$-\Delta H = \frac{d}{d(1/T)}(R\ln\dot{w} - Rs\ln T)$$

$$= \frac{d}{d(1/T)}(R\ln\dot{w}) + RsT$$

and hence $$\delta(\Delta H) = -RT\delta(s)$$

Table 7.9

Recorded rates of weight loss for indium monobromide from a MEM capsule over the temperature range 626 to 816 K.

T/K	$10^9 \dot{w}/kgs^{-1}$	T/K	$10^9 \dot{w}/kgs^{-1}$
626.9	0.0975	734.2	1.2270
626.3	0.0875	734.2	1.2346
626.3	0.0914	734.2	1.2232
642.5	0.1341	734.2	1.2270
642.5	0.1358	743.6	1.5444
681.3	0.3899	743.6	1.5504
681.3	0.3842	743.6	1.5474
705.9	0.6127	743.6	1.5326
703.1	0.6039	766.4	2.4353
701.2	0.5952	765.4	2.4206
701.2	0.5882	765.4	2.4242
711.5	0.7567	765.4	2.3881
711.5	0.7435	775.7	3.0189
711.5	0.7605	774.8	3.0019
711.5	0.7491	774.8	2.9091
722.8	1.0030	774.8	2.8986
722.8	0.9950	816.1	6.6445
722.8	0.9926	816.1	6.7114
722.8	0.9950	816.1	6.7114
		816.1	6.6556
		676.1	3.3168
		676.1	3.2520

Fig 7.4 MEM results for the evaporation of indium monobromide in hydrogen.

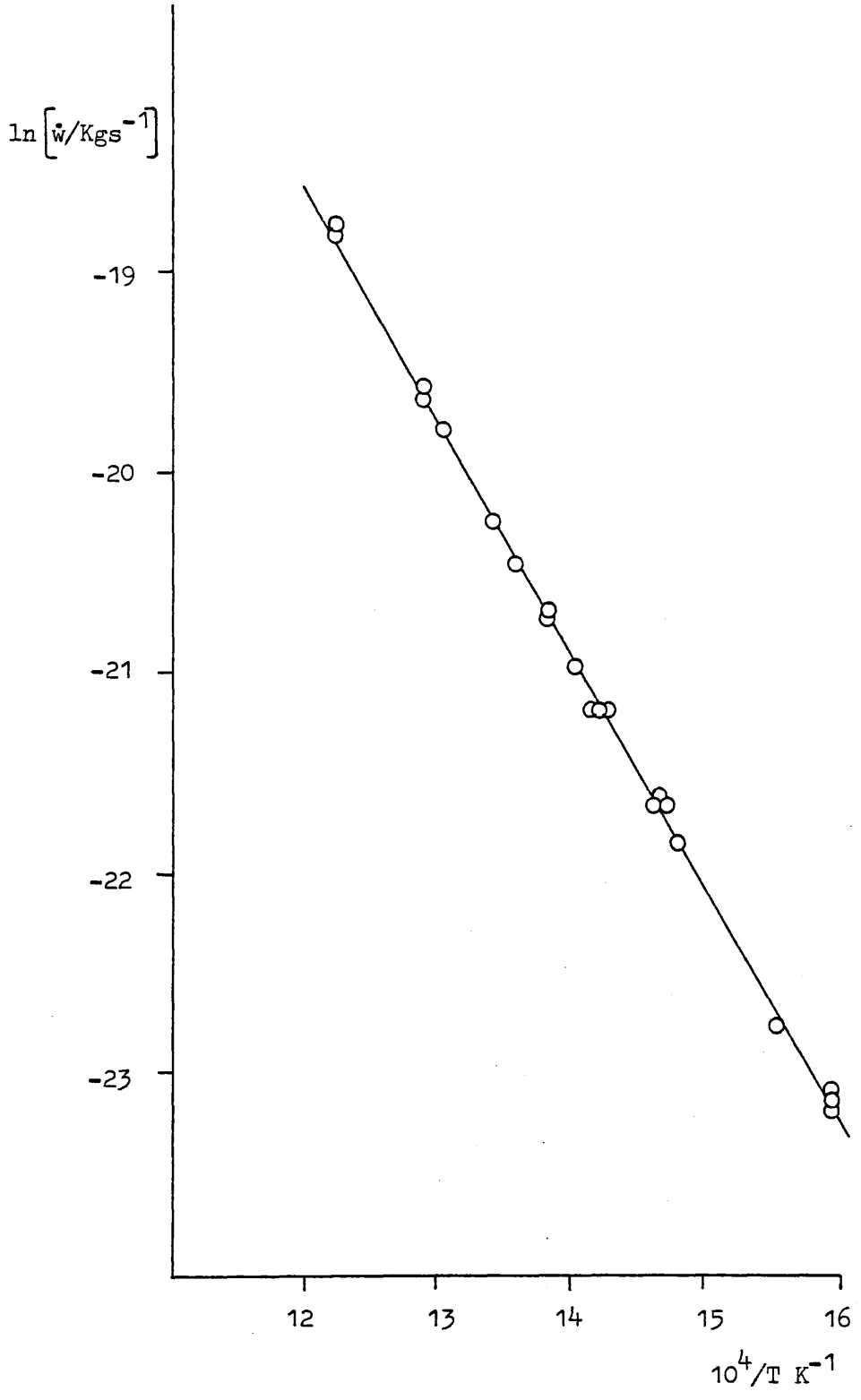

Thus an error of 0.1 in s at 1200 K produces an error of 1 $kJmol^{-1}$ in ΔH. Similarly the error $\delta(\Delta S)$ caused by an error $\delta(s)$ in the index s may be found:

$$\delta(\Delta S) \quad -R\delta(s)(1 + \ln(T/T_o))$$

Thus an error of 0.1 in s introduces an error in ΔS of 1 $JK^{-1}mol^{-1}$ at 320 K, and 2 $JK^{-1}mol^{-1}$ at 1200 K, if T_o = 273 K.

Results

The rate of weight loss of indium monobromide was measured over the temperature range 626 to 816 K. The results are given in table 7.9, and are displayed graphically in fig 7.4. From the results, the following enthalpy and entropy of vaporisation, at the mean experimental temperature of 720 K, are extracted:

$$\Delta H_v = 68.6 \text{ kJ mol}^{-1}$$

$$\Delta S_v = 74.7 \text{ J K}^{-1}\text{mol}^{-1}$$

7.5 Summary

From solution calorimetry, a value of -140.2 $kJmol^{-1}$ is calculated for ΔH^{o}_{f298} InBr(c) . The heat capacity of the crystal from 298 to 550 K may be represented by the expression $4.24 + 0.108T \; JK^{-1}mol^{-1}$ An additional additive term may be introduced to 7.1.1 to take account of the crystal-crystal transition revealed by the DSC work, ΔH_T = 3.5 $kJmol^{-1}$ The heat of fusion has been measured as 12.4 $kJmol^{-1}$ Estimating the heat capacity of InBr(l) as a constant quantity equal to the heat capacity of the solid at its melting point, then C_p InBr(l) = 63.6 $JK^{-1}mol^{-1}$ (NB Measurement of this quantity was precluded

due to the fact that the DSC head was damaged during the final measurements made on the crystal). The mean temperature of the MEM evaporation study on InBr(l) was 720 K, so ΔH_v InBr(l) = 68.6 $kJmol^{-1}$ is referred to this temperature. Finally, the expression $37.4 - (65000\ T^{-2})\ JK^{-1}mol^{-1}$ may be used to represent the heat capacity of the vapour from 720 to 1000 K.

Using the values set out above, the heat of formation of indium monobromide vapour may be calculated at 1000 K:

$$\Delta H_{f1000}\ InBr(g) \quad = \quad -10.4\ kJ\ mol^{-1}$$

This value does not compare very well with the value calculated from the "best-fit" reaction enthalpy, for reaction 5.4.1, of $-26.6\ kJmol^{-1}$. These figures correspond to values of -33.9 and -50.3 at 298 K respectively. Both the above values lie within the range of literature data detailed in table 5.4.

7.6 Melting point determination

Below are documented the observations made on two samples of indium monobromide while being heated in a laboratory melting point apparatus.

Sample one, heated in an open tube:

25°C bright orange colour crystals

45°C metalic? specks appeared

65°C sample started to darken, remaining orange

77°C small black specs increasing in size, but only near air pockets

80°C growth of dark specs appeared to cease

120°C sample darkening further, becoming reder

200°C the dark pockets appear to have gained a metalic lustre

230°C the sample continues to darken

240°C the sample is now very dark brown

270°C the sample very quickly turns black, apparently accompanied by slight shrinkage

328°C melt? liquid above the bulk of the sample appeared colourless

Sample two, sealed anhydrously:

30°C orange as bulk

100°C no noticable change

210°C the sample begining to darken from the base

240°C the sample has become brick-red in colour

250°C dark red glitterey appearence, shrinkage noted, coalescence?

273°C very dark red, lustrous speckeled surface

275°C sample turned black, metalic appearence (probably mpt)

300°C sample has the appearence of a pencil lead

REFERENCES TO CHAPTER SEVEN

7.1 E.J. Tarbox, PhD. Thesis, London (1977)

7.2 This Work

7.3 F.J. Smith and R.F. Barrow, Trans. Faraday Soc. 51, 1478 (1955)

7.4 W. Klemm and Brautigam, Z. Anorg. Chem. 163, 225 (1927)

7.5 O. Kubaschewski and C.B. Alcock, Metallurgical Thermochemistry (Pergamon 1979)

7.6 R.M. Tennent, Science Data Book (Oilver and Boyd, 1972)

7.7 C.R.C. Handbook of Chemistry and Physics, R.C. Weast (Ed.) (C.R.C. Press 60th Edition, 1980)

7.8 O. Kubaschewski, E.L. Evans and C.B. Alcock, Metallurgical Thermochemistry (Pergamon, 1967)

Appendix 1

Temperature profiles of the furnaces used in the MEM and Raman studies.

The furnace used in conjunction with the Cahn R-100 balance, for the evaporation experiment performed on the Zn/H_2 system, was of a tubular design 250 mm in length and 200 mm in diameter. The single resistance winding was powered by a low voltage (25 V) transformer controlled by a Stanton Redcroft linear temperature variable rate programmer. The power rating of this furnace is 2.5 kW.

The furnace employed for all experiments using the Cahn RG balance is specified as follows. A tubular furnace, type 2A (Severn Sciences Ltd.) 300 mm long, having an internal diameter of 38 mm, and an external diameter of 150 mm. This furnace comprises of sillimanite tube gradient,wound, in two zones, with "Kanthal A1" wire. Fitted between the windings and the central tube is a sheath to accept a control thermocouple. The outer case is of aliminium and "Sindanyo" end plates are fitted. The power rating of this furnace is 825 W at 100 V.

Precise constructional details for the furnace used for the high temperature Raman work are not available. A drawing of the furnace appears in chapter 2. Platinum wire is employed as the resistance winding, (cold resistance≈2Ω), and the end plates are water cooled.

Temperature profiles of the above furnaces appear in Figs A1, A2 and A3.

Fig A1. Selected temperature profiles of furnace used with the Cahn RG balance.

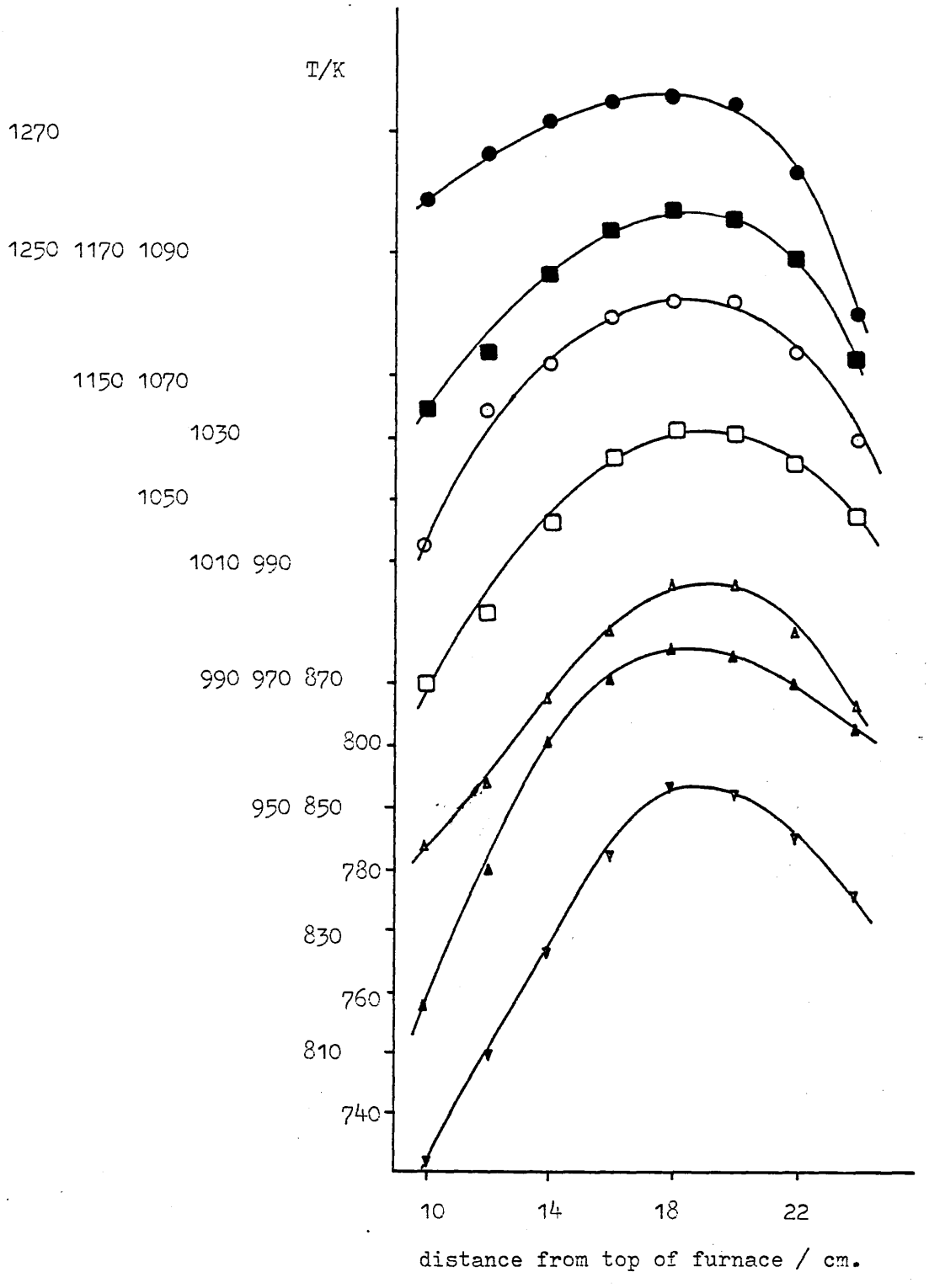

Fig A2. Selected temperature profiles of furnace used with Cahn R-100 balance.

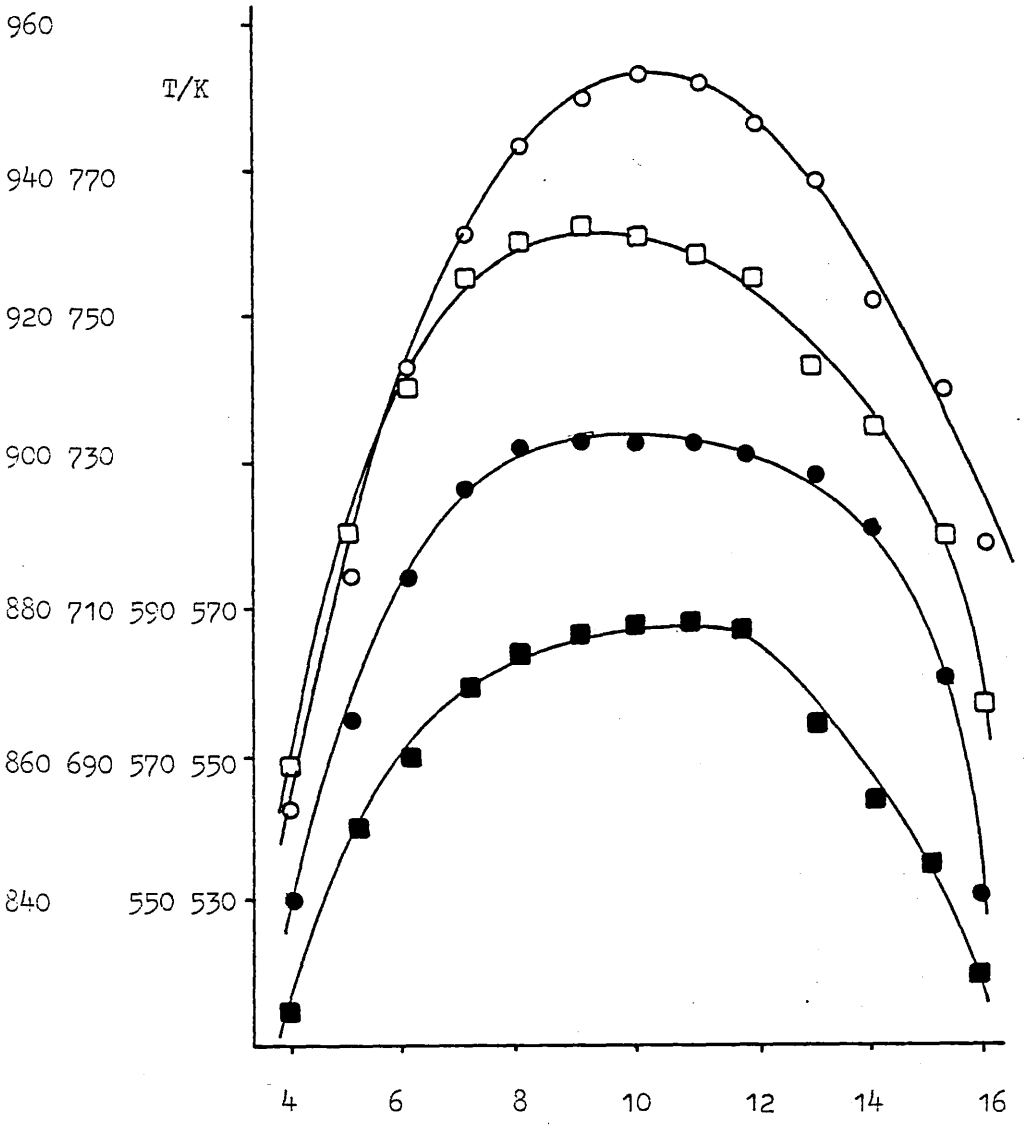

Fig A3. Typical temperature profile of furnace used for high temperature Raman study of group III halides.

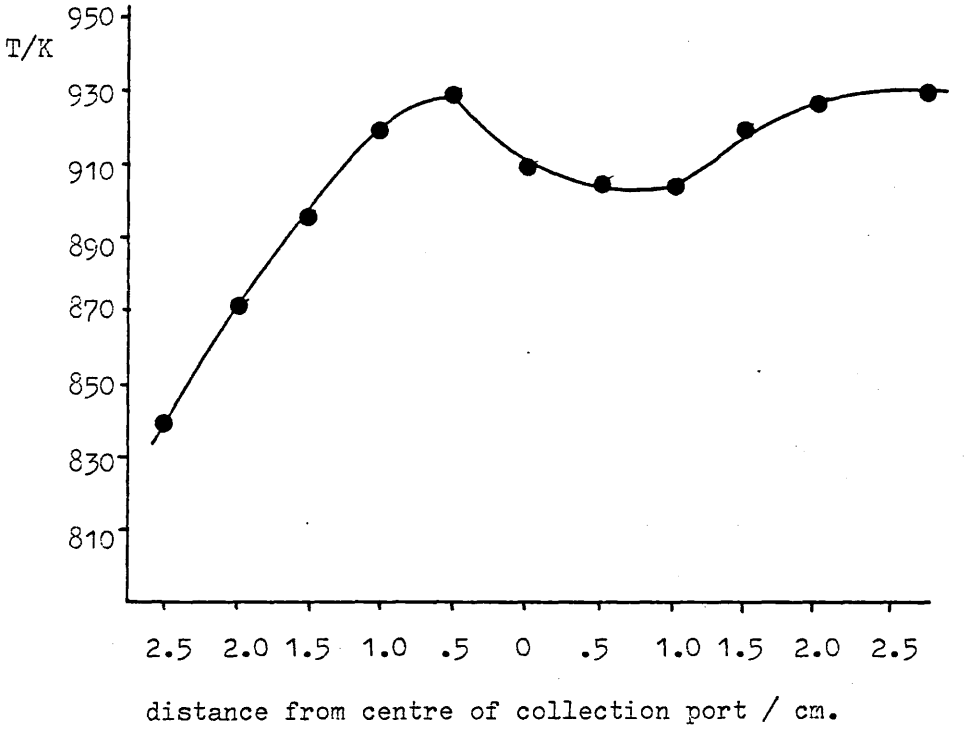

Appendix 2

Channel dimensions.

A number of different bottles were used in the MEM experiments described in this thesis. A travelling microscope was employed to measure their channel (or stopper) dimensions. Several measurements of length and diameter were made of each channel, and from these a mean and standard deviation formulated. End corrections, l_c, were established to account for the flaring of the channel at the lower end.

Correction for transport in a tapered channel.

On elimination of the Stefan velocity, U, from the flow equations (see chapter 3) and substitution of UP=JRTs, where s denotes the sum of the stoichiometric coefficients in the transport equation, the following expression results:

$$\left\{\frac{p_i^o - P/s}{p_i^l - P/s}\right\} = \exp\left\{-\frac{RTs}{DP}\int_l^o J\,dx\right\} \qquad (A2.1)$$

this is in terms of the boundary conditions, x=0, and x=1. If r(x) is known (r being the radius of the channel) then the above equation may be integrated.

a) for a uniform taper

$r = ax + b$ where $b = r(0)$, and $a = \dfrac{r(1) - r(0)}{l}$

Then $$\int_0^l \frac{dx}{r^2} = \frac{1}{r(1)r(0)} \qquad (A2.2)$$

b) <u>for a mixed tube</u>

Region I: $r = ax + b$
as above

Region II : $r = r(1)$
which is constant.

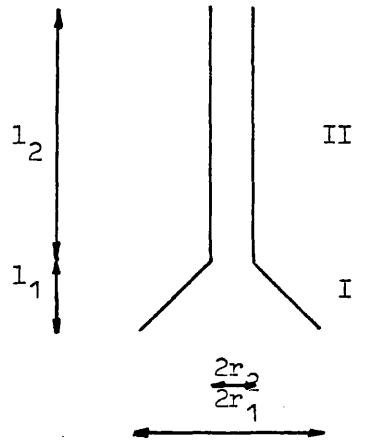

Now for region I

$$\left\{\frac{p_i^{0} - P/s}{p_i^{l_1} - P/s}\right\} = \exp\left\{-\frac{RTQl_1 s}{PDr_2 r_1}\right\}$$

where $Q = Jr^2$
this value is costant,
due to conservation
of mass.

and for region II

$$\left\{\frac{p_i^{l_1} - P/s}{p_i^{l_2} - P/s}\right\} = \exp\left\{-\frac{RTQl_2 s}{PDr_2^2}\right\}$$

multiplying these expressions gives,

$$\left\{\frac{p_i^{0} - P/s}{p_i^{l} - P/s}\right\} = \exp\left\{-\frac{RTsQ}{PD}\ \frac{l_1 r_2 + l_2 r_1}{r_1 r_2^2}\right\}$$

The measured rate of weight loss, $\dot{w} = J(1)\ r_2^2 M$

so $\dot{w} = QM$

or $Q = \dot{w}/M$

To a first order approximation :

$$p^{0} = (p^{l} - P/s)\left\{1 - \frac{\dot{w}RTs}{MPD}\ \frac{l_1 r_2 + l_2 r_1}{r_1 r_2^2}\right\} + P/s$$

therefore,

$$= \frac{\dot{w}RT(l_2 + l_1)}{DNPA}\ \frac{l_1 r_2 + l_2 r_1}{r_1(l_1 + l_2)}$$

$$\text{or} \qquad = \frac{\dot{w}RTl_2}{DMPA} \quad 1 + \frac{r_2 l_1}{r_1 l_2}$$

$$\text{Hence} \qquad l_c = \frac{r_2 l_1}{r_1 l_2} + 1 \qquad \text{(A2.3)}$$

A similar correction term may be derived for the channel geometry shown below.

$$\text{Here} \qquad = \frac{\dot{w}RTl_2}{DMPA} \quad 1 + \frac{r_2^2 l_1}{r_1^2 l_2}$$

$$\text{and} \qquad l_c = \frac{r_2^2 l_1}{r_1^2 l_2} + 1 \qquad \text{(A2.4)}$$

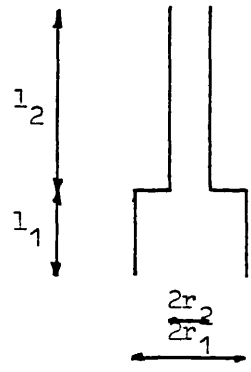

Dimensions of the MEM channels used.

All dimensions are quoted in m.

For the evaporation of zinc in a hydroge ambient,

$l = 0.0204 \pm 0.0009$

$d = 0.00206 \pm 0.00004$

$l_c = 1.0$ (NB in this experiment a stoppered bottle was used)

For the study of the heterogeneous eqilibria of the GaP/HCl and GaP/HBr systems,

$l = 0.0172 \pm 0.0001$

$d = 0.00098 \pm 0.00004$ nominally 0.001

$l_c = 1.0167$

and

$l = 0.01631 \pm 0.00008$

$d = 0.00199 \pm 0.00002$ nominally 0.002

$l_c = 1.1020$

For the initial studies of the heterogeneous equilibria of the InP/HBr and the dissociative sublimation systems,

$l = 0.0138 \pm 0.0002$

$d = 0.00092 \pm 0.00003$ nominally 0.001

$l_c = 1.0336$

and for the further studies,

$l = 0.0169 \pm 0.0004$

$d = 0.00093 \pm 0.00002$ nominally 0.001

$l_c = 1.0335$

and

$l = 0.01631 \pm 0.00008$

$d = 0.00199 \pm 0.00002$ nominally 0.002

$l_c = 1.0394$

For the evaporation of indium monobromide in a hydrogen ambient,

$l = 0.01277 \pm 0.00052$

$d = 0.00108 \pm 0.00002$ nominally 0.001

$l_c = 1.0664$

Appendix 3

Computer Programing for the Results from the GaP and InP systems.

Both BT evolved and RHC formulations of computer software have been used to analyse the results of various MEM studies in this thesis. The basis of the BT derived programs appear elsewhere[1]. Computer programs representing a scheme-1 and scheme-2 analysis of CVT reaction equilibria are presented in this appendix. Also given is the treatment for dissociative sublimation. The programs here are designated "best-fit sig routines", since they calculate values for $\dot{w}$ and then compare these calculated values with those obtained from experiment. The values of the enthalpy and entropy changes for the CVT reactions considered are altered by the program, over predetermined ranges, and the "best-fit" indicated.

The criterion used to judge the closest approach between the calculated and experimental data, ie the best-fit, was that σ should be a minimum. Where:

$$\sigma = \sigma_2 = (\sigma_1/N)^{\frac{1}{2}}$$

and

$$\sigma_1 = \Sigma_N \left[\ln \frac{\dot{w}_{cal}}{\dot{w}_{obs}} \right]^2 /N$$

Nomencluture

DHI = $\Delta H_I/kJmol^{-1}$

DSI = $\Delta S_I/JK^{-1}mol^{-1}$

PRE = D_o/m^2s^{-1}

SPLUS1 = 1+s

$$\left\{ D_T = D_o(T/273.15)^{1+s} \right.$$

EPS = ε

GAPRI = γ_i approx' ie ignoring terms in $\dot{w}$

D(I,J) = $D_{(I,J)}$, binary diffusion coefficient

DIST = channel length/m of the MEM bottle

AREA = cross-sectional area/m^2 of the MEM channel

W(I) = molecular weight of species I / $kgmol^{-1}$

R = gas constant / $JK^{-1}mol^{-1}$

T = T/K

ALPHA = α

THETA = θ

GA(I) = γ_i

A further scheme of analysis is available, not used here, designated scheme-3. This scheme is formulated in a similar manner to 1 & 2, and accomodates the formation of M_2X_4. Using the terminology:

1 = MX, 2 = A_2, 3 = M_2X_4, 4 = A_4, 5 = HX, and 6 = MA

then the flux relations take the form:

with $\alpha = j_2/j_4$ and $\theta = j_1/j_3$

also $j_d = 2 - \theta(3 + 2\alpha)$

$$j_1/J = -\theta(4 + 2\alpha)/j_d \qquad j_2/J = -\alpha(2 + \theta)/j_d$$

$$j_3/J = -(4 + 2\alpha)/j_d \qquad j_4/J = -(2 + \theta)/j_d$$

$$j_5/J = (4 + 2\alpha)(4 + \theta)/j_d \qquad j_6/J = -(4 + 2\alpha)(2 + \theta)/j_d$$

```
      PROGRAM FWSIG (INPUT,OUTPUT,TAPE5=INPUT)
*
      COMMON/CMFORM/DH1,DS1,PRE,SPLUS1,CONST,EPS
      COMMON/GAMMAS/D(6,6),GAPR2,GAPR3,GAPR5,GAPR6
      DIMENSION W(7)
      DIMENSION EXPTTT(100),EXPWDT(100),TTR(100),WCALC(100)
      DIMENSION Y(10),TITLE(10)
      REAL LNWEXP(100),LNWCALC(100)
      REAL MINDH,MINDS
      DATA P,R/101325.0,8.3143/
      DATA TITLE/10*' '/
*
* INPUT DATA
*
      READ *,EPS
      READ *,W
      READ *,DIST,AREA
*        DH1 AND DS1 ARE FOR  INP + HX = INX + 0.25P4 + 0.5H2
      READ *,DH1,DS1,PRE,SPLUS1
      READ *,THI,TLOW
      READ *,NINC,SIZINC
*
* PRINT INPUT DATA
*
      PRINT 100 £ PRINT 110 £ PRINT 120 £ PRINT 130
      PRINT 120 £ PRINT 140,DH1,DS1
      PRINT 120 £ PRINT 160,DIST,AREA,P,EPS
      PRINT 120 £ PRINT 170,PRE,SPLUS1
      PRINT 120 £ PRINT 190,(I,I=1,7),W
      PRINT 120 £ PRINT 110
      PRINT 200 £ PRINT 210,NINC,SIZINC
*
*        D(I,J) ARE MODIFIED GRAHAM'S LAW SCALING TERMS IN THE FORM
*        ROOT RATIO MOLECULAR MASSES MINUS ONE
*        1=H2,2=INX,3=P2,4=INX2,5=P4,6=HX,7=INP
*
      DO 40 J=1,6
      DO 40 I=1,6
   40 D(I,J)=SQRT(W(J)/W(I))-1.0
*
* APPROXIMATE GAMMAS
*
      GAPR2=1.0+D(1,6)*EPS
      GAPR3=GAPR2
      GAPR5=GAPR2
      GAPR6=1.0+(D(1,2)+0.25*D(1,5))*EPS+EPS/(4.0/3.0)
      CONST=R*DIST/(AREA*W(7)*P)
*
* READ EXPTAL DATA (DECR TEMP)
*
      I=1
    1 READ(5,*,END=2) EXPTTT(I),EXPWDT(I)
      TTR(I)=10000.0/EXPTTT(I)
      LNWEXP(I)=ALOG(EXPWDT(I))
      I=I+1
      GO TO 1
    2 IMAX=I-1
```

```
*
* DH1 AND DS1 CYCLES INITIALIZED AND INCREMENTED
*
      PRINT 9
      MINDH=DH1-(FLOAT(NINC/2)+1.0)*SIZINC*1000.0
      MINDS=DS1-(FLOAT(NINC/2)+1.0)*SIZINC
      DH1=MINDH
      DO 30  IH=1,NINC
      DH1=DH1+SIZINC*1000.0
* DS1 ZEROED WHENEVER DH1 INCREASED
      DS1=MINDS
      DO 30  JS=1,NINC
      DS1=DS1+SIZINC
      SIG=0.0
*
* SIG CALCULATED FOR EACH H AND S PERMUTATION
*
      DO 22  I=1,IMAX
      T=EXPTTT(I)
      CALL FORM(T,WCALC,ALPHA,ID)
      LNWCALC(I)=ALOG(WCALC(ID))
   22 SIG=SIG+(LNWCALC(I)-LNWEXP(I))*(LNWCALC(I)-LNWEXP(I))
*
      SIG2=SQRT((SIG/IMAX)/(IMAX-1))
      PRINT 8,DH1,DS1,SIG2,IH,JS
      IF(IH.EQ.1.AND.JS.EQ.1)  SIGMIN=SIG2
*
* SIGS COMPARED AND POSSIBLY EXCHANGED
*
      IF(SIG2.GT.SIGMIN)  GO TO 30
      SIGMIN=SIG2
      DHMIN=DH1
      DSMIN=DS1
   30 CONTINUE
*
* OPTIMUM VALUES PRINTED AND CARRIED FORWARD TO GRAPH
*
      DH1=DHMIN
      DS1=DSMIN
      PRINT 12
      PRINT 11,DH1,DS1,SIGMIN
      PRINT 13
*
* CALCULATION TO PRODUCE TABLE
*
      PRINT 220
      SIG=0.0
*
      DO 20 I=1,IMAX
      T=EXPTTT(I)
      CALL FORM(T,WCALC,ALPHA,ID)
      LNWCALC(ID)=ALOG(WCALC(ID))
      PRINT 50,LNWEXP(I),EXPWDT(I),EXPTTT(I),TTR(I),WCALC(ID),LNWCALC(I
     *D),ALPHA,ID
      LNWCALC(I)=LNWCALC(ID)
```

```
      SIG=SIG+(LNWCALC(I)-LNWEXP(I))*(LNWCALC(I)-LNWEXP(I))
   20 CONTINUE
*
      SIG1=SIG/IMAX
      SIG2=SQRT(SIG1/(IMAX-1))
      PRINT 60
      PRINT 70,SIG,SIG1,SIG2
      PRINT 7
      PRINT 11,DH1,DS1,SIG2
*
    7 FORMAT(///,48X,'DH1',14X,'DS1',13X,'SIG2',/)
    8 FORMAT(46X,F8.1,10X,F5.1,10X,F7.5,10X,I2,5X,I2)
    9 FORMAT(///,48X,'DH1',14X,'DS1',13X,'SIG2',12X,'IH',05X,'JS',/)
   11 FORMAT(46X,F8.1,10X,F5.1,10X,F7.5)
   12 FORMAT(//,48X,'MINIMUM SIG PARAMETERS',/)
   13 FORMAT(///)
*
* 2ND CALC. TO PRODUCE GRAPH
* DETERMINE ALMAX AND ALMIN
      T=THI
      CALL FORM(T,WCALC,ALPHA,ID)
      ALMAX=ALOG(WCALC(ID))
      IF(ALMAX.LT.LNWEXP(1))  ALMAX=LNWEXP(1)
*
      T=TLOW
      CALL FORM(T,WCALC,ALPHA,ID)
      ALMIN=ALOG(WCALC(ID))
      IF(ALMIN.GT.LNWEXP(IMAX)) ALMIN=LNWEXP(IMAX)
*
      PRINT 80,THI,ALMAX,TLOW,ALMIN
   80 FORMAT(///,30X,'THI = ',F7.1,2X,'LNWCALC = ',F9.4,5X,'TLOW = ',
     *F7.1,2X,'LNWCALC = ',F9.4)
*
      PRINT 90,IMAX
   90 FORMAT(///,30X,'NO OF EXPTL PTS = ',I2)
*
      TTTLO=10000./THI
      TTTHI=10000./TLOW
      NINC=120
      TTTINC=(TTTHI-TTTLO)/NINC
      CALL LPPLOT(0,'LOG WDOT','10000/T',ALMAX,ALMIN,TITLE,TTT)
*
      TTT=TTTLO
      DO 61 I=1,NINC
         T=10000.0/TTT
         CALL FORM(T,WCALC,ALPHA,ID)
         Y(1)=ALOG(WCALC(ID))
*        SEARCH FOR EXPERIMENTAL VALUES LYING CLOSE TO THIS POINT
         NPOINT=1
         DO 62 IE=1,IMAX
               EXPTTT(IE)=TTR(IE)
            IF(EXPTTT(IE).GE.TTT-.5*TTTINC .AND.
```

```
     *          EXPTTT(IE).LT.TTT+.5*TTTINC .AND. NPOINT.LT.100) THEN
                NPOINT=NPOINT+1
                Y(NPOINT)=ALOG(EXPWDT(IE))
              ENDIF
   62     CONTINUE
          CALL LPPLOT(1,NPOINT,'*COOOOOOOO',ALMAX,ALMIN,Y,TTT)
          TTT=TTT+TTTINC
   61  CONTINUE
       STOP
*
   60  FORMAT('0',53X,' SIG         SIG1         SIG2')
   70  FORMAT(49X,3F11.5)
   50  FORMAT(22X,F9.4,X,E11.4,2X,F7.1,2X,F8.4,X,E11.4,3X,F9.4,X,E11.4,
     ↱I9)
  100  FORMAT(1H1)
  110  FORMAT(39X,59('*'))
  120  FORMAT(39X,'*',57X,'*')
  130  FORMAT(39X,'*',23X,'INPUT DATA',24X,'*'/
     1       39X,'*',23X,'----------',24X,'*')
  140  FORMAT(39X,'*',20X,'DH1',10X,'DS1',21X,'*'/
     1       39X,'*',20X,'---',10X,'---',21X,'*'/
     2       39X,'*',13X,F13.1,F11.1,20X,'*')
  160  FORMAT(39X,'*',6X,'LENGTH',7X,'AREA',7X,'PRESSURE',6X,'EPSILON',6X
     1,'*'/  39X,'*',6X,'------',7X,'----',7X,'--------',6X,'-------',6X
     2,'*'/  39X,'*',2X,2E12.5,F12.1,F12.4,7X,'*')
  170  FORMAT(39X,'*',10X,'DD(6) = ',F9.7,'*(T/273.15)**',F5.3,12X,'*')
  190  FORMAT(39X,'*',7(3X,'W',I1,3X),' *'/
     1       39X,'*',7(3X,'--',3X),' *'/
     2       39X,'*',7(F7.5,1X),' *')
  200  FORMAT('0',65X,'RESULTS'/' '65X,'-------'//)
  210  FORMAT('0',48X,'NINC = ',I2,10X,'SIZINC = ',F3.1)
  220  FORMAT(22X,'  LNWEXP    WEXP(KG/SEC)  T(K)     10000/T  WCALC(KG/SEC
     ↱)   LNWCALC      ALPHA        CYCLES')
       END


       SUBROUTINE FORM(T,WCALC,ALPHA,ID)
       COMMON/CMFORM/DH1,DS1,PRE,SPLUS1,CONST,EPS
       COMMON/GAMMAS/D(6,6),GAPR2,GAPR3,GAPR5,GAPR6
       COMMON/PARAMS/ CA1,CA2
       DIMENSION WCALC(100)
       DIMENSION DD(6),GA(6),DDG(6)
       EXTERNAL F
       REAL J2J,J3J,J5J,J6J,J7J,K1,KA
       DATA R/8.3143/
*
* EVALUATE K CONSTANTS
*         K1 IS FOR CVT REACTION
*         KA IS FOR P4=2P2
       K1=EXP(DS1/R-DH1/R/T)
       KA=EXP(18.772-29190.0/T)
```

```
      DUMP=CONST*T
      DD(6)=PRE*(T/273.15)**SPLUS1
      ID=0
*
    5 ID=ID+1
      DO 10 N=2,5
      IF(ID.EQ.1)  GA(N)=GAPR2
   10 DDG(N)=(D(N,6)+1.0)*DD(6)/GA(N)
      IF(ID.EQ.1)  GA(6)=GAPR6
      DDG(6)=DD(6)/GA(6)
*
* DETERMINE PARAMETERS FOR, AND ZERO OF, FUNCTION F
      CA0=K1*DDG(2)*SQRT(DDG(5))/(SQRT(1.0-EPS)*KA**0.25*SQRT(DDG(3)))
      CA1=CA0*DDG(5)*EPS/(KA*DDG(3)*DDG(3))
      CA2=CA0/DDG(6)
      CALL C05AAF(0.0,10.0,1.0E-14,1.0E-14,F,ALPHA,0)
*
* SUBSTITUTE ALPHA IN 2ND EQN AND SOLVE FOR WCALC
      WCALC(ID)=KA*DDG(3)*DDG(3)*(4.0+2.0*ALPHA)/(DDG(5)*ALPHA*ALPHA
     +**DUMP)
      IF(ID.EQ.1)  GO TO 15
      IF(ABS(ALOG(WCALC(ID-1))/ALOG(WCALC(ID))-1.0).LT.0.00001)GO TO 111
*
*        ALPHA IS THE FLUX RATIO OF P2 TO P4
*        NOTATION JIJ MEANS FLUX JI OVER TOTAL FLUX J
   15 J2J=(4.0+2.0*ALPHA)/(3.0+2.0*ALPHA)
      J3J=ALPHA/(3.0+2.0*ALPHA)
      J5J=1.0/(3.0+2.0*ALPHA)
      J6J=-J2J
      J7J=J2J
*
*        REDUCED TRANSPORT FUNCTIONS ARE CALLED EBARI
*        TRANSPORT FUNCTIONS ARE CALLED EI
      EBAR2=DUMP*WCALC(ID)/DDG(2)
      EBAR3=DUMP*WCALC(ID)/DDG(3)
      EBAR5=DUMP*WCALC(ID)/DDG(5)
      EBAR6=DUMP*WCALC(ID)/DDG(6)
      E2=EBAR2/J7J
      E3=EBAR3/J7J
      E5=EBAR5/J7J
      E6=EBAR6/J7J
      C2=-D(2,3)*D(1,3)*J3J-D(2,5)*D(1,5)*J5J-D(2,6)*D(1,6)*J6J
      C3=-D(3,2)*D(1,2)*J2J-D(3,5)*D(1,5)*J5J-D(3,6)*D(1,6)*J6J
      C5=-D(5,2)*D(1,2)*J2J-D(5,3)*D(1,3)*J3J-D(5,6)*D(1,6)*J6J
      C6=-D(6,2)*D(1,2)*J2J-D(6,3)*D(1,3)*J3J-D(6,5)*D(1,5)*J5J
      A6=1.0-(D(1,2)*J2J/J6J+D(1,3)*J3J/J6J+D(1,5)*J5J/J6J)*EPS
      GBET2=GAPR2-(1.0+C2)*E2/2.0
      GBET3=GAPR3-(1.0+C3)*E3/2.0
      GBET5=GAPR5-(1.0+C5)*E5/2.0
      GBET6=A6-(1.0+C6)*E6/2.0-EPS/J6J
*
* EXACT GAMMA CORRECTIONS
```

```
      GA(2)=GBET2
      GA(3)=GBET3
      GA(5)=GBET5
      GA(6)=GBET6
      GO TO 5
  111 RETURN
      END


      FUNCTION F(ALPHA)
      COMMON/PARAMS/ CA1,CA2
      F=((CA1*ALPHA-2.0*CA2)*ALPHA-4.0*CA2)*SQRT(ALPHA)-2.0*ALPHA-4.0
      RETURN
      END


      SUBROUTINE LPPLOT(IQ,IA,IB,PRA,PRB,PY,X)
      INTEGER P(13)
      DIMENSION Y(13),PY(10)
      IF(IQ.EQ.0) ICALL=0
      IF(ICALL.NE.0)GOTO7
C
C SETTING AXES
C
      DO 11 J=1,10
   11 Y(J)=PY(J)
      Y(11)=1H
      CALL DATE(Y(12))
      CALL CLOCK(Y(13))
      RA=PRA
      RB=PRB
      PRINT1,Y
    1 FORMAT(1H1,135('*')/' *  ',13A10,' *'/1H ,135('*'))
      PRINT2,IA
    2 FORMAT(1H0,63X,A10/64X,10('-'))
      RA=RA-RB
      T=RA/12.0
      Y(1)=RB
      DO3I=2,13
    3 Y(I)=Y(I-1)+T
      PRINT4,Y
    4 FORMAT(6X,13F10.4)
      PRINT5,IB
    5 FORMAT(1H ,A10,1X,12('.         '),'.')
      PRINT6
    6 FORMAT(12H ---------- ,121('.'))
      RA=120.0/RA
      RB=0.5-RA*RB
      ICALL=1
      IQ=1
    7 RETURN
C
```

```
C
C PLOTTING
      7 CONTINUE
        DO 13 J=1,IA
     13 Y(J)=PY(J)
        K=10H.
        IF(MOD(ICALL,10).EQ.0)K=10H..........
        DO8I=1,13
      8 P(I)=K
        DO9I=1,IA
        J=INT(Y(I)*RA+RB)
        IF(J.LT.0)J=0
        IF(J.GT.120)J=120
        K=J/10+1
        J=60*K-6*J-6
      9 P(K)=AND(P(K),SHIFT(-63,J))+SHIFT(AND(SHIFT(IB,6*I),77B),J)
        PRINT10,X,P
     10 FORMAT(1H ,E10.4,1X,12A10,A1)
        IF(IQ.EQ.2) PRINT12,(PY(I),I=1,IA)
     12 FORMAT(12X,10(1PE12.4))
        ICALL=ICALL+1
        RETURN
        END
```

```
      PROGRAM FA2SC (INPUT,OUTPUT,TAPE5=INPUT)
C
C     ----------------------------------------------------------------
C
      COMMON/CAFCON/DH1,DS1,DH2,DS2,PRE,SPLUS1,CONST,EPS,FLOW
      COMMON/GAMMAS/D(5,5),GAPR2,GAPR3,GAPR4,GAPR5,GAPR6
      DIMENSION W(7)
      DIMENSION EXPTTT(100),EXPWDT(100),TTR(100),WCALC(200)
      DIMENSION Y(10),TITLE(10)
      REAL LNWEXP(100),LNWCALC(200)
      REAL MINDH1,MINDS1,MINDH2,MINDS2
      DATA P,R/101325.0,8.3143/
      DATA TITLE/10*' '/
C
C     ----------------------------------------------------------------
C     INPUT DATA
C     ----------------------------------------------------------------
C
      READ *,EPS
      READ *,W
      READ *,DIST,AREA
      READ *,DH1,DS1,DH2,DS2,PRE,SPLUS1
      READ *,THI,TLOW
      READ *,NINC,SIZINC,NNINC,SSIZINC
C
C     ----------------------------------------------------------------
C     PRINT INPUT DATA
C     ----------------------------------------------------------------
C
      PRINT 100 $ PRINT 110 $ PRINT 120 $ PRINT 130
      PRINT 120 $ PRINT 140,DH1,DS1,DH2,DS2
      PRINT 120 $ PRINT 160,DIST,AREA,P,EPS
      PRINT 120 $ PRINT 170,PRE,SPLUS1
      PRINT 120 $ PRINT 190,(I,I=1,7),W
      PRINT 120 $ PRINT 110
      PRINT 200 $ PRINT 210,NINC,SIZINC,NNINC,SSIZINC
C
C     ----------------------------------------------------------------
C
      DO 40 J=1,5
      DO 40 I=1,5
   40 D(I,J)=SQRT(W(J)/W(I))-1.0
C
C     ----------------------------------------------------------------
C
      GAPR2=1.0+D(1,6)*EPS
      GAPR3=GAPR2
      GAPR4=GAPR2
      GAPR5=GAPR2
      GAPR6=GAPR2
      CONST=R*DIST/(AREA*W(7)*P)
C
C     ----------------------------------------------------------------
C     READ EXPERIMENTAL DATA
C     ----------------------------------------------------------------
C
      I=1
    1 READ(5,*,END=2) EXPTTT(I),EXPWDT(I)
      TTR(I)=1000.0/EXPTTT(I)
      LNWEXP(I)=ALOG(EXPWDT(I))
      I=I+1
```

```
      LNWEXP(I)=ALOG(EXPDT(I))
      I=I+1
      GOTO1
    2 IMAX=I-1
C
C     ------------------------------------------------------------------
C     ENTHALPIES AND ENTROPIES CYCLED
C     ------------------------------------------------------------------
C
      PRINT9
      MINDH1=DH1-(FLOAT(NINC/2)+1.0)*SIZINC*1000.0
      MINDH2=DH2-(FLOAT(NINC/2)+1.0)*SSIZINC*1000.0
      MINDS1=DS1-(FLOAT(NINC/2)+1.0)*SIZINC
      MINDS2=DS2-(FLOAT(NINC/2)+1.0)*SSIZINC
      DH1=MINDH1
      DO 30 IH=1,NINC
      DH1=DH1+SIZINC*1000.0
      DS1=MINDS1
      DO 30 JS=1,NINC
      DS1=DS1+SIZINC
      DH2=MINDH2
      DO 30 IHH=1,NNINC
      DH2=DH2+SSIZINC*1000.0
      DS2=MINDS2
      DO 30 JSS=1,NNINC
      DS2=DS2+SSIZINC
      SIG=0.0
C
C     ------------------------------------------------------------------
C     NEW VALUE OF SIG CALC.....  AND MAYBE REPLACED
C     ------------------------------------------------------------------
C
      DO 22 I=1,IMAX
      T=EXPTIT(I)
      CALL FORM(I,WCALC,ALPHA,THETA,ID)
      LNWCALC(I)=ALOG(WCALC(I))
   22 SIG=SIG+(LNWCALC(I)-LNWEXP(I))*(LNWCALC(I)-LNWEXP(I))
C
C     ------------------------------------------------------------------
C
C
C     ------------------------------------------------------------------
      SIG2=SQRT((SIG/IMAX)/(IMAX-1))
      PRINT 8,DH1,DS1,DH2,DS2,SIG2,IH,JS,IHH,JSS
      IF(IH.EQ.1.AND.JS.EQ.1.AND.IHH.EQ.1.AND.JSS.EQ.1)  SIGMIN=SIG2
C
C     ------------------------------------------------------------------
C     VALUES OF SIG AND DIFFERED
C     ------------------------------------------------------------------
C
      IF(SIG2.GT.SIGMIN) GO TO 30
      SIGMIN=SIG2
      DHMIN=DH1
      DSMIN=DS1
      DHMIN2=DH2
      DSMIN2=DS2
   30 CONTINUE
C
C     ------------------------------------------------------------------
C     OPTIMUM VALUES ARE PRINTED AND CARRIED FORWARD
C     ------------------------------------------------------------------
C
```

```
C
      DH1=DHMIN1
      DS1=DSMIN1
      DH2=DHMIN2
      DS2=DSMIN2
      PRINT 13
      PRINT 11,DH1,DS1,DH2,DS2,SIG2
      PRINT 13
C     ------------------------------------------------------------------
C     CALCULATIONS TO PRODUCE TABLE
C     ------------------------------------------------------------------
C
      PRINT 220
      SIG=0.0
      DO 20 I=1,IMAX
      T=EXPTIT(I)
      CALL FCAL(T,WCALC,ALPHA,THETA,ID)
      LNWCALC(ID)=ALOG(WCALC(ID))
      PRINT 50,LNWEXP(I),EXPWGT(I),EXPTIT(I),TTR(I),WCALC(ID),LNWCALC(ID
     1),ALPHA,THETA,ID
      LNWCALC(I)=LNWCALC(ID)
      SIG=SIG+(LNWCALC(I)-LNWEXP(I))*(LNWCALC(I)-LNWEXP(I))
   20 CONTINUE
      SIG1=SIG/IMAX
      SIG2=SQRT(SIG1/(IMAX-1))
      PRINT 60
      PRINT 70,SIG,SIG1,SIG2
      PRINT 7
      PRINT 11,DH1,DS1,DH2,DS2,SIG2
    7 FORMAT(///,40X,'DH1',10X,'DS1',10X,'DH2',10X,'DS2',10X,'SIG2',/,
     1          40X,'---',10X,'---',10X,'---',10X,'---',10X,'----',/)
    8 FORMAT(40X,F8.1,05X,F5.1,05X,F8.1,05X,F5.1,05X,F7.5,05X,I2,5X,I2,5
     1X,I2,5X,I2)
    9 FORMAT(///,42X,'DH1',12X,'DS1',12X,'DH2',12X,'DS2',11X,'SIG2',6X,'
     1IH',5X,'JS',4X,'IHH',3X,'JSS',/)
   11 FORMAT(40X,F8.1,10X,F5.1,10X,F8.1,10X,F5.1,10X,F7.5)
   12 FORMAT(//,50X,'MINIMUM SIG PARAMETERS',/
     1          50X,'------------------------',/)
   13 FORMAT(/////)
*
* 2ND CALC. TO PRODUCE GRAPH
* DETERMINE ALPHA AND ALPHA
      T=TH1
      CALL FCAL(T,WCALC,ALPHA,THETA,ID)
      ALMAX=ALOG(WCALC(ID))
      IF(ALMAX.LT.LNWEXP(1)) ALMAX=LNWEXP(1)
*
      T=TL0W
      CALL FCAL(T,WCALC,ALPHA,THETA,ID)
      ALMIN=ALOG(WCALC(ID))
      IF(ALMIN.GT.LNWEXP(IMAX)) ALMIN=LNWEXP(IMAX)
*
      PRINT 40,TH1,ALMAX,TL0W,ALMIN
   40 FORMAT(///,30X,'TH1 = ',F7.1,2X,'LNWCALC = ',F9.4,5X,'TLOW = ',
     1F7.1,2X,'LNWCALC = ',F9.4)
*
      PRINT 90,IMAX
   90 FORMAT(///,30X,'NO OF EXPTL PTS = ',I2)
*
      TTL0W=TL0W/TH1
      TTTH1=TH1/TL0W
```

```
      PRINT 90,IMAX
   90 FORMAT(///,30X,'NO OF EXPTL PTS = ',I2)
*
      TTTLO=10000./THI
      TTTHI=10000./TLOW
      NINC=120
      TTTINC=(TTTHI-TTTLO)/NINC
      CALL LPPLOT(0,'LOG WOUT','10000/T',ALMAX,ALMIN,TITLE,TTT)
*
      TTT=TTTLO
      DO 61 I=1,NINC
        T=10000.0/TTT
        CALL FORM(T,WCALC,ALPHA,THETA,ID)
        Y(1)=ALOG(WCALC(ID))
*       SEARCH FOR EXPERIMENTAL VALUES LYING CLOSE TO THIS POINT
        NPOINT=1
        DO 62 IE=1,IMAX
            EXPTTT(IE)=TTT(IE)
          IF(EXPTTT(IE).GE.TTT-.5*TTTINC .AND.
     *       EXPTTT(IE).LT.TTT+.5*TTTINC .AND. NPOINT.LT.10) THEN
            NPOINT=NPOINT+1
            Y(NPOINT)=ALOG(EXPWOT(IE))
          ENDIF
   62   CONTINUE
        CALL LPPLOT(1,NPOINT,'*000000000',ALMAX,ALMIN,Y,TTT)
        TTT=TTT+TTTINC
   61 CONTINUE
      STOP
*
   60 FORMAT('0',53X,' SIG          SIG1          SIG2')
   70 FORMAT(49X,3F11.5)
   50 FORMAT(22X,F9.4,X,E11.4,2X,F7.1,2X,F8.4,X,E11.4,3X,F9.4,X,E11.4,
     1E11.4,I9)
  100 FORMAT(1H1)
  110 FORMAT(39X,59('*'))
  120 FORMAT(39X,'*',57X,'*')
  130 FORMAT(39X,'*',23X,'INPUT DATA',24X,'*'/
     1       39X,'*',23X,'----------',24X,'*')
  140 FORMAT(39X,'*',7X,'DH1',10X,'DS1',10X,'DH2',10X,'DS2',8X,'*'/
     1       39X,'*',7X,'---',10X,'---',10X,'---',10X,'---',8X,'*'/
     2       39X,'*',F13.1,F11.1,F14.1,F12.1,7X,'*')
  160 FORMAT(39X,'*',6X,'LENGTH',7X,'AREA',7X,'PRESSURE',6X,'EPSILON',6X
     1,'*'/  39X,'*',6X,'------',7X,'----',7X,'--------',6X,'-------',6X
     2,'*'/  39X,'*',2X,E12.5,F12.1,F12.4,7X,'*')
  170 FORMAT(39X,'*',10X,'CD(5) = ',F9.7,'*(T/273.15)**',F5.3,12X,'*')
  190 FORMAT(39X,'*',7(3X,'W',I1,3X),' *'/
     1       39X,'*',7(3X,'--',3X),' *'/
     2       39X,'*',7(F7.3,1X),' *')
  200 FORMAT('0',55X,'RESULTS'/' ',55X,'-------'//)
  210 FORMAT(' 0',35X,'NINC =',I2,5X,'SSSTAS =',F3.1,5X,'NNINC =',I2,5X,
     1'SSIZINC =',F3.1)
  220 FORMAT(22X,'  LNWEXP    WEXP(KG/SEC)   T(K)     10000/T  WCALC(KG/SEC
     +)  LNWCALC      ALPHA          THETA      CYCLES')
      END


      SUBROUTINE FORM(T,WCALC,ALPHA,THETA,ID)
      COMMON/COMFORM/DH1,DS1,DH2,DS2,PRE,SPLOS1,CONST,EPS,TLOW
      COMMON/GAPVALS/C(5,7),GAPR2,GAPR3,GAPR4,GAPR5,GAPR6
      DIMENSION WCALC(20)
      DIMENSION DH(6),DS(6),DGH(6)
```

```
      SUBROUTINE FORM(T,WCALC,ALPHA,THETA,ID)
      COMMON/CMFORM/DH1,DS1,DH2,DS2,PRE,SPLUS1,CONST,EPS,TLOW
      COMMON/GAMMAS/D(5,6),GAMR2,GAMR3,GAMR4,GAMR5,GAMR6
      DIMENSION WCALC(200)
      DIMENSION DD(6),GA(5),DDG(6)
      REAL J2J,J3J,J4J,J5J,J6J,J7J,K[illegible],K1,K2
      DATA R/8.3143/
      TL=TLOW+25.0
C
C     ----------------------------------------------------------------
C     EVALUATE EQUILIBRIUM CONSTANTS
C     ----------------------------------------------------------------
C
      KA=EXP(37.3*4.184/R-56000.0*4.184/R/T)
      K1=EXP(DS1/R-DH1/R/T)
      K2=EXP(DS2/R-DH2/R/T)
C
C     ----------------------------------------------------------------
C
      DUMP=CONST*T
      DD(6)=PRE*(T/273.15)**SPLUS1
      ID=0
C
C     ----------------------------------------------------------------
C
    5 ID=ID+1
      DO 10 N=2,5
      IF(ID.EQ.1)  GA(N)=GAMR[illegible]
   10 DDG(N)=(D(N,5)+1.0)*DD(6)/GA(N)
      IF(ID.EQ.1)  GA(6)=GAMR6
      DDG(6)=(DD(6)+1.0)/GA(6)
C
C     ----------------------------------------------------------------
C     COEFFICIENTS OF POLYNOMIAL ARE CALCULATED
C     ----------------------------------------------------------------
C
      A=K1*DDG(2)*DDG(5)**0.25/(1.0-EPS)**0.5
      B=KA*DDG(3)**2/DDG(5)
      C=K2*DDG(4)/(DDG(2)*(1.0-EPS)**0.5)
      CK=4.0*[illegible]*DDG(6)
      CM=CK*C**[illegible]
      V=EPS*C
      CN=-2.0*[illegible]*C*C*DDG(6)**[illegible]/A
      S=CN*C**3
      CL=C**4*DDG(6)**[illegible]/A**4
      A0=-32.0*CM
      A1=32.0*CM*V-112.0*CM
      A2=112.0*CM*V-1[illegible].0*CM+8.0*S
      A3=150.0*CM*V-120.0*CM-CL-2[illegible].0*V*S+20.0*S
      A4=120.0*CM*V-50.0*CM+8.0*V*CL-2.0*CL+24.0*S*V**2+18.0*S-60.0*V*S
      A5=50.0*CM*V-11.0*CM-1[illegible].0*CL*V**2-12.0*V*CL-CL-6.0*S*V**3+60.0*S*V
     1*V-54.0*V*S+7.0*S
      A6=11.0*CM*V-CM+[illegible].0*CL*V**3-[illegible].0*CL*V*V+6.0*V*CL-20.0*S*V**3+54.0
     1*S*V*V-21.0*V*S-[illegible]
      A7=CM*V-15.0*CL*V**4+[illegible].0*CL*V**3-15.0*CL*V*V-18.0*S*V**3-21.0*S*V
     1*V-3.0*V*S
      A8=6.0*CL*V**5-[illegible]*CL*V**4+20.0*CL*V**3-7.0*S*V**3+3.0*S*V*V
      A9=-CL*V**6+[illegible]*CL*V**5-15.0*CL*V**4-S*V**3
      A10=-2.0*CL*V**[illegible]+[illegible].0*CL*V**5
      A11=-CL*[illegible]
```

```
      A9=-CL*V**2+12*CL*V**3-15.0*CL*V**4-5*V**5
      A10=-2.0*CL*V**6+6.0*CL*V**5
      A11=-CL*V**6
C
C     ------------------------------------------------------------------
C     NEWTON METHOD SOLUTION
C     ------------------------------------------------------------------
C
      NN=0
      M=0
      IF(T.GT.TL) GO TO 501
      THETA=2000.0
      GO TO 502
  501 THETA=1.0/THETA
  502 F0THETA=A11+A10*THETA+A9*THETA*THETA+A8*THETA**3+A7*THETA**4+A6*TH
     1ETA**5+A5*THETA**6+A4*THETA**7+A3*THETA**8+A2*THETA**9+A1*THETA**1
     20+A0*THETA**11
      F1THETA=A10+2.0*A9*THETA+3.0*A8*THETA*THETA+4.0*A7*THETA**3+5.0*A6
     1*THETA**4+6.0*A5*THETA**5+7.0*A4*THETA**6+8.0*A3*THETA**7+9.0*A2*T
     2HETA**8+10.0*A1*THETA**9+11.0*THETA**10
      THETAN=THETA-(F0THETA/F1THETA)
      IF(ABS(THETA/THETAN-1.0).LT.0.000000001) GO TO 500
      THETA=THETAN
      M=M+1
      IF(M.EQ.1000) GO TO 111
      GO TO 502
  500 THETA=1.0/THETA
      IF(NN.EQ.0)  THETA1=THETA
      IF(NN.EQ.1)  THETA2=THETA
      NN=NN+1
      IF(NN.EQ.2)  GO TO 504
C
C     ------------------------------------------------------------------
C     BISECTION ROUTINE USED TO LOCATE REGION FOR THETA2
C     ------------------------------------------------------------------
C
      M=0
      THETA1=1.0/THETA1
      SI=-0.01*THETA1
      F1=THETA1+SI
      F0=F1
      THETA=F0
      F0THETA=A11+A10*THETA+A9*THETA*THETA+A8*THETA**3+A7*THETA**4+A6*TH
     1ETA**5+A5*THETA**6+A4*THETA**7+A3*THETA**8+A2*THETA**9+A1*THETA**1
     20+A0*THETA**11
  505 F=F0THETA
      F0=F0+SI
      THETA=F0
      F0THETA=A11+A10*THETA+A9*THETA*THETA+A8*THETA**3+A7*THETA**4+A6*TH
     1ETA**5+A5*THETA**6+A4*THETA**7+A3*THETA**8+A2*THETA**9+A1*THETA**1
     20+A0*THETA**11
      FF=F0THETA
      FFF=F*FF
      IF(FFF)502,506,505
  506 THETA1=1.0/THETA1
      THETA2=THETA1
C
C     ------------------------------------------------------------------
C     WEIGHT LOSSES CALCULATED
C     ------------------------------------------------------------------
```

```
C     ----------------------------------------------------------------
C     WEIGHT LOSSES CALCULATION
C     ----------------------------------------------------------------
C
  504 X=DOG(6)*(THETA2+1.0)*(C*THETA2*EPS-1.0)/(C*THETA2*(THETA2+2.0))
      THETA=THETA2
      ALPHA=(2.0*[illegible]+S[illegible](4.0*[illegible]))/2.0/X
      WCALC(ID)=X/[illegible]
      IF(ID.EQ.1)  GO TO 15
      IF(ABS(ALOG(WCALC(ID-1))/ALOG(WCALC(ID))-1.0).LT.0.00001)GO TO 111
C
C     ----------------------------------------------------------------
C
   15 DENOMJ=(ALPHA+1.0)*(1.0+2.0*THETA)+THETA
      J2J=THETA*(4.0+2.0*ALPHA)/DENOMJ
      J3J=ALPHA*(1.0+THETA)/DENOMJ
      J4J=(4.0+2.0*ALPHA)/[illegible]
      J5J=(1.0+THETA)/[illegible]
      J6J=-(4.0+2.0*ALPHA)*(THETA+2.0)/DENOMJ
      J7J=(THETA+1.0)*(4.0+2.0*ALPHA)/DENOMJ
      EBAR2=DUMP*WCALC(ID)/DOG(2)
      EBAR3=DUMP*WCALC(ID)/DOG(2)
      EBAR4=DUMP*WCALC(ID)/DOG(2)
      EBAR5=DUMP*WCALC(ID)/DOG(2)
      EBAR6=DUMP*WCALC(ID)/DOG(2)
      E2=EBAR2/J7J
      E3=EBAR3/J7J
      E4=EBAR4/J7J
      E5=EBAR5/J7J
      E6=EBAR6/J7J
      C2=-D(2,3)*D(1,3)*J3J-D(2,4)*D(1,4)*J4J-D(2,5)*D(1,5)*J5J-D(2,6)*D
     1(1,6)*J6J
      C3=-D(3,2)*D(1,2)*J2J-D(3,4)*D(1,4)*J4J-D(3,5)*D(1,5)*J5J-D(3,6)*D
     1(1,6)*J6J
      C4=-D(4,2)*D(1,2)*J2J-D(4,3)*D(1,3)*J3J-D(4,5)*D(1,5)*J5J-D(4,6)*D
     1(1,6)*J6J
      C5=-D(5,2)*D(1,2)*J2J-D(5,3)*D(1,3)*J3J-D(4,5)*D(1,4)*J4J-D(5,6)*D
     1(1,6)*J6J
      C6=-D(6,2)*D(1,2)*J2J-D(6,3)*D(1,3)*J3J-D(6,4)*D(1,4)*J4J-D(6,5)*D
     1(1,5)*J5J
      GBET2=GAMA2-(1.0+C2)*E2/2.0
      GBET3=GAMA3-(1.0+C3)*E3/2.0
      GBET4=GAMA4-(1.0+C4)*E4/2.0
      GBET5=GAMA5-(1.0+C5)*E5/2.0
[illegible]
      GA(2)=GBET2
      GA(3)=GBET3
      GA(4)=GBETA
      GA(5)=GBET5
      GA(6)=GBET6
      GOTO 5
  111 RETURN
      END

      SUBROUTINE [illegible]
      INTEGER [illegible]
      [illegible]
      IF(I[illegible]
      IF(I[illegible]
C
```

```
      SUBROUTINE LPPLOT(IO,IA,IB,PRA,PRB,PY,A)
      INTEGER P(13)
      DIMENSION Y(13),PY(10)
      IF(IO.EQ.0) ICALL=0
      IF(ICALL.NE.0)GO TO 7
C
C SETTING AXES
C
      DO 11 J=1,10
   11 Y(J)=PY(J)
      Y(11)=IB
      CALL DATE(Y(12))
      CALL CLOCK(Y(13))
      RA=PRA
      RB=PRB
      PRINT1,Y
    1 FORMAT(1H1,135('*')/' *  ',13A10,' *'/1H ,135('*'))
      PRINT2,IA
    2 FORMAT(' ',3X,A10/4X,130('-'))
      RA=RA-RB
      T=RA/12.0
      Y(1)=RB
      DO 3 I=2,13
    3 Y(I)=Y(I-1)+T
      PRINT4,Y
    4 FORMAT(6X,13F10.4)
      PRINT5,IB
    5 FORMAT(1H ,A10,1A,12('          '),'.')
      PRINT6
    6 FORMAT(12X,' ---------- ',12('.'))
      RA=120./A
      RB=0.5-RB*RA
      ICALL=1
      IO=1
      RETURN
C
C PLOTTING
    7 CONTINUE
      DO 13 J=1,1A
   13 Y(J)=PY(J)
      K=10H.
      IF(MOD(ICALL,10).EQ.0)K=10H..........
      DO 8 I=1,13
    8 P(I)=K
      DO 9 I=1,1A
      J=INT(Y(I)*RA+RB)
      IF(J.LT.1)J=1
      IF(J.GT.120)J=120
      K=J/10+1
      J=J-10*K+10
    9 P(K)=AND(P(K),NOT(SHIFT(77B,6*J)))+OR(SHIFT(I,6*J),SHIFT(SHIFT(15,6*1),77B),J)
      PRINT10,(P
   10 FORMAT(1H ,13A10,A1,A10,A1)
      IF(IO.EQ.2) PRINT11,(P(I),I=1,I-1)
   11 FORMAT(' ',13A10)
      ICALL=ICALL+1
      RETURN
      END
-----------------------------------IN CHANGE OF IO CORRECT - SEE ARGUMENT IN C
------ALSO USE IA FOR
```

```
      PROGRAM IPDS(INPUT,OUTPUT,TAPE5=INPUT)

      COMMON/CMFORM/DH1,DS1,PRE,SPLUS1,D(6,6),CONST,W(7)
      DIMENSION TEXP(100),RTEXP(100),WEXP(100)
      REAL LNWEXP(100)
      DIMENSION Y(10),TITLE(10)
      DATA TITLE/10*' '/
      DATA P,R/101325.0,8.3143/

      READ *,W
      READ *,DIST,AREA,BETA
      DIST=DIST*BETA
      READ *,DH1,DS1,PRE,SPLUS1
      DH1=DH1*4.184
      DS1=DS1*4.184
      READ *,THI,TLOW

      I=1
    1 READ (5,*,END=2) TEXP(I),WEXP(I)
      RTEXP(I)=10000.0/TEXP(I)
      LNWEXP(I)=ALOG(WEXP(I))
      I=I+1
      GO TO 1
    2 IMAX=I-1

      PRINT 100 £ PRINT 110 £ PRINT 120 £ PRINT 130
      PRINT 120 £ PRINT 140,DH1,DS1
      PRINT 120 £ PRINT 160,DIST,AREA,P
      PRINT 120 £ PRINT 170,PRE,SPLUS1
      PRINT 120 £ PRINT 190,(I,I=1,7),W
      PRINT 120 £ PRINT 110

  100  FORMAT(1H1)
  110 FORMAT(39X,59('*'))
  120 FORMAT(39X,'*',57X,'*')
  130 FORMAT(39X,'*',23X,'INPUT DATA',24X,'*'/
     1       39X,'*',23X,'----------',24X,'*')
  140 FORMAT(39X,'*',20X,'DH1',10X,'DS1',21X,'*'/
     1       39X,'*',20X,'---',10X,'---',21X,'*'/
     2       39X,'*',13X,F13.1,F11.1,20X,'*')
  160 FORMAT(39X,'*',6X,'LENGTH',7X,'AREA',7X,'PRESSURE',6X,'EPSILON',6X
     1,'*'/  39X,'*',6X,'------',7X,'----',7X,'--------',6X,'-------',6X
     2,'*'/  39X,'*',2E12.5,F12.1,F12.4,7X,'*')
  170 FORMAT(39X,'*',10X,'DD(6) = ',E10.4,'*(T/273.15)**',F5.3,11X,'*')
  190 FORMAT(39X,'*',7(3X,'W',I1,3X),' *'/
     1       39X,'*',7(3X,'--',3X),' *'/
     2       39X,'*',7(F7.5,1X),' *')

      DO 40 J=1,6
      DO 40 I=1,6
   40 D(I,J)=SQRT(W(J)/W(I)-1.0
      CONST=R*DIST/(AREA*P)

      PRINT 87
   87 FORMAT(///,40X,'ID',10X,'ZO',11X,'GA3',12X,'GA5',12X,'WCALC',/)
      PRINT 220
  220 FORMAT(22X,'  LNWEXP  WEXP(KG/SEC)  T(K)  10000/T  WCALC(KG/SEC)
```

```
     LNWCALC      ALPHA      CYCLES',/)
   SIG=0.0

   DO 22 I=1,IMAX
   T=TEXP(I)
   CALL FORM(T,ALPHA,XCALC,ID,1)
   PRINT 50,LNWEXP(I),WEXP(I),TEXP(I),RTEXP(I),XCALC,ALOG(XCALC),
   ALPHA,ID
50 FORMAT(/,22X,F9.4,X,E11.4,2X,F7.1,2X,F8.4,X,E11.4,3X,F9.4,X,E11.4,
   I9,//)
   SIG=SIG+(ALOG(XCALC)-LNWEXP(I))*(ALOG(XCALC)-LNWEXP(I))
22 CONTINUE

   SIG2=SQRT((SIG/IMAX)/(IMAX-1))
   PRINT 11, DH1,DS1,SIG2
11 FORMAT(/,40X,'DH1 =',F9.1,10X,'DS1 =',F5.1,10X,'SIG2 =',F7.5)

   CALL FORM(THI,ALPHA,XCALC,ID,0)
   ALMAX=AMAX1(ALOG(XCALC),LNWEXP(1))

   CALL FORM(TLOW,ALPHA,XCALC,ID,0)
   ALMIN=AMIN1(ALOG(XCALC),LNWEXP(IMAX))

   PRINT 80,THI,ALMAX,TLOW,ALMIN
80 FORMAT(///,30X,'THI =',F7.1,2X,'LNWCALC =',F9.4,5X,'TLOW =',
   F7.1,2X,'LNWCALC =',F9.4)

   RTLO=10000.0/THI
   RTHI=10000.0/TLOW
   NINC=120
   RTINC=(RTHI-RTLO)/NINC
   CALL LPPLOT(0.'LN WDOT','1000/T',ALMAX,ALMIN,TITLE,RT)
   RT=RTLO
   DO 61 I=1,NINC
         T=10000.0/RT
         IP=0
         CALL FORM(T,ALPHA,XCALC,ID,IP)
         Y(1)=ALOG(XCALC)
         NPOINT=1
         DO 62 IE=1,IMAX
               IF(RTEXP(IE).GE.RT-.5*RTINC.AND.
                  RTEXP(IE).LT.RT+.5*RTINC.AND.NPOINT.LT.10) THEN
         NPOINT=NPOINT+1
         Y(NPOINT)=ALOG(WEXP(IE))
         END IF
62       CONTINUE
         CALL LPPLOT(1,NPOINT,'*0000000000',ALMAX,ALMIN,Y,RT)
         RT=RT+RTINC
61 CONTINUE
   STOP
   END

   SUBROUTINE FORM(T,ALPHA,XCALC,ID,IP)

   COMMON/CMFORM/DH1,DS1,PRE,SPLUS1,D(6,6),CONST,W(7)
   DIMENSION WCALC(100)
   REAL K1,KA,J3J,J5J
```

```
      DATA R/8.3143/

      K1=EXP(DS1/R-DH1/R/T)
      KA=EXP(37.3*4.184/R-58000.0*4.184/R/T)

      ID=0
      ZO=0.0
      GA3=1.0
      GA5=1.0
      DD3=PRE*(T/273.15)**SPLUS1

  540 ID=ID+1
      DG3=DD3/GA3
      DG5=DD3*SQRT(W(3)/W(5))/GA5
      ALPHA=KA*DG3/(K1*K1*DG5)
      WCALC(ID)=K1*K1*DG3*W(3)*(ALPHA+2.0)/(ALPHA*CONST*T)
      XCALC=WCALC(ID)

      IF(ID.EQ.1)GOTO550
      ZO=AMIN1(WCALC(ID),WCALC(ID-1))/AMAX1(WCALC(ID),WCALC(ID-1))
  550 IF(IP.EQ.0)GOTO 560
      PRINT 88,ID,ZO,GA3,GA5,WCALC(ID)
   88 FORMAT(40X,I2,5X,F10.8,5X,F9.6,5X,E13.7)

  560 IF(ZO.GT.0.99999) RETURN

      J3J=ALPHA/(ALPHA+1.0)
      J5J=1.0/(ALPHA+1.0)
      E3=WCALC(ID)*T*CONST*(ALPHA+1.0)/((ALPHA+2.0)*W(3)*DG3)
      E5=WCALC(ID)*T*CONST*(ALPHA+1.0)/((ALPHA+2.0)*W(5)*DG5)
      GA3=1.0+(D(1,5)*D(3,5)*J5J-1.0)*E3/2.0
      GA5=1.0+(D(1,3)*D(5.3)*J3J-1.0)*E5/2.0

      GOTO 540

      END


      SUBROUTINE LPPLOT(IQ,IA,IB,PRA,PRB,PY,X)
      INTEGER P(13)
      DIMENSION Y(13),PY(10)
      IF(IQ.EQ.0) ICALL=0
      IF(ICALL.NE.0) GOTO 7

      DO 11 J=1,10
   11 Y(J)=PY(J)
      Y(11)=1H
      CALL DATE(Y12))
      CALL CLOCK(Y(13))
      RA=PRA
      RB=PRB
      PRINT1,Y
    1 FORMAT(1H1,135('*')/' * ',13A10,' * '/1H ,135('*'))
      PRINT2,IA
    2 FORMAT(1HO,63X,A10/64X,10('-'))
      RA=RA-RB
      T=RA/12.0
```

```
      Y(1)=RB
      DO 3 I=2,13
    3 Y(I)=Y(I-1)+T
      PRINT4,Y
    4 FORMAT(6X,13F10.4)
      PRINT5,IB
    5 FORMAT(1H ,A10,1X,12('.          '),'.')
      PRINT6
    6 FORMAT(12H ---------- ,121('.'))
      RA=120.0/RA
      RB=0.5-RA*RB
      ICALL=1
      IQ=1
      RETURN

    7 CONTINUE
      DO 13 J=1,IA
   13 Y(J)=PY(J)
      K=10H.
      IF(MOD(ICALL,10).EQ.0)K=10H.........
      DO 8 I=1,13
    8 P(I)=K
      DO 9 I=1,IA
      J=INT(Y(I)*RA+RB)
      IF(J.LT.0)J=0
      IF(J.GT.120)J=120
      K=J/10+1
      J=60*K-6*J-6
    9 P(K)=AND(P(K),SHIFT(-63,J))+SHIFT(AND(SHIFT(IB,6*I),77B),J)
      PRINT 10,X,P
   10 FORMAT(1H ,E10.4,1X,12A10,A1)
      IF(IQ.EQ.2) PRINT 12,(PY(I),I=1,IA)
   12 FORMAT(12X,10(1PE12.4)
      ICALL=ICALL+1
      RETURN
      END
```

Appendix 4

Group theory and molecular vibrations

If the abstract symmetry operations of a molecular point group are replaced by the transformation matricies that represent the effect of those operations on the base vectors of a co-ordinate system within the domain of the molecule, we may say that the matricies corresponding to the symmetry operations form a representation of the molecular point group. Furthermore, the set of base vectors of the co-ordinate system to which the matricies are defined, forms the basis of the representation. The trace of such a matrix is known as the character of the operation.

Allowing such co-ordinates to form the basis of a representation of a molecular point group, the appropriate characters corresponding to the applicable symmetry operations form a reducible representation. A reducible representation may be reduced by the appropriate similarity matricies. The following formula allows such analysis:

$$n^{\Gamma} = 1/g \; \Sigma_j g_j \chi_j^{\Gamma} \chi_j \qquad \text{(A4.1)}$$

where g = the number of operations in the group.

g_j = the number of operations in the j^{th} class.

χ_j = the character for the reducible representation for any operation in the j^{th} class.

χ_j^{Γ} = the character of the j^{th} irreducible representation from character tables.

and n^{Γ} = the number of times the irreducible representation appears in the reducible representation.

Contribution to character per unshifted atom,

Proper operations		Improper operations	
R	χ^R	R	χ^R
C_n^k	$1 + 2\cos(2\pi k/n)$	S_n^k	$-1 + 2\cos(2\pi k/n)$
$E = C_1^k$	3	$\sigma = S_1^1$	1
C_2^1	-1	$i = S_2^1$	-3
C_3^1 C_3^2	0	S_3^1 S_3^5	-2
C_4^1 C_3^3	1	S_4^1 S_4^3	-1
C_6^1 C_6^5	2	S_6^1 S_6^5	0

The useful properties of group representations and their characters in the problem of molecular vibrations can be derived from a basic theorm. The theorm concerns the elements of the matricies which constitute the irreducible representation of a group. This theorm is stated below and is known as the "great orthogonality theorm:"

$$\Sigma R \left[\Gamma_i(R)_{mn}\right]\left[\Gamma_j(R)_{m'n'}\right]^* = g/\sqrt{d_i d_j}\ \delta_{ij}\delta_{mn'}\delta_{mn'} \qquad (A4.2)$$

where R denotes the various operations in the group. The elements in the m^{th} row and the n^{th} column of the matrix corresponding to an operation R in the i^{th} irreducible representation is denoted $\Gamma_i(R)_{mn}$.

g denotes the order of the group

and d denotes the dimension of the irreducible representation.

This means that in the set of matricies constituting any one irreducible representation, any set of corresponding matrix elements, one from each matrix behaves as the component of a

vector in d-dimensional space such that all these vectors are mutually orthogonal, and each is normalised so that the square of its length is g/d_i.

Five important rules concerning irreducible representations and their characters are stated below without proof. The derivation of these rules may be found in a text by F A Cotton.[1]

1) The sum of the squares of the dimensions of the irreducible representations of a group is equal to the order of that group:

$$\Sigma_i d_i^2 = g \qquad \text{(A4.3)}$$

2) The sum of the squares of the characters in any irreducible representation equals g:

$$\Sigma_R \left[\chi_i(R)\right]^2 = g \qquad \text{(A4.4)}$$

3) The vectors whose components are the characters of two different irreducible representations are orthogonal:

$$\Sigma_R \chi_i(R)\chi_j(R) = 0 \qquad \text{where } i \neq j \qquad \text{(A4.5)}$$

4) In a given representation (reducible or irreducible) the characters of all matricies belonging to operations in the same class are identical.

5) The number of irreducible representations of a group is equal to the number of classes in the group.

Any reducible representation can be reduced by some similarity transformation to a completely reduced form. This transformation leaves the characters of the elements unchanged and therefore we may write:

$$x(R) = \Sigma_j n_j x_j^{\Gamma}(R) \qquad (A4.6)$$

where n_j is the number of times the j^{th} irreducible representation x_j^{Γ} appears in the reduced form. Multiplying by x_i^{Γ}, and summing over all R we have:

$$\Sigma x(R) x_i^{\Gamma}(R) = \Sigma_i \Sigma_j n_j x_j^{\Gamma}(R) x x_j^{\Gamma}(R) \qquad (A4.7)$$

In the sum over j only j=i is non zero, so:

$$= \Sigma_R x_j^{\Gamma}(R) x(R) \qquad \text{from} \quad (A4.5)$$

$$= g n_j \qquad \text{from} \quad (A4.4)$$

Hence we may write:

$$n^{\Gamma} = 1/g \; \Sigma_j g_j x_j^{\Gamma} x_j \qquad (A4.1)$$

Now let us consider some molecules:

1) MX $C_{\infty h}$ $\Gamma(MX) = A_1^*$

1 Raman active band.

2) M_2X_2 D_{2h} $\Gamma(M_2X_2) = 2A_{1g}^* + B_{1g}^* + 2B_{1u} + B_{2g}^* + 2B_{2u} + 2B_{3g}^* + 2B_{3u}$

6 vibrational modes,

3 Raman active

stretching modes transform as $A_{1g} + B_{1u} + B_{2u} + B_{3g}$

and deformation modes transform as $A_{1g} + B_{3u}$

3) MX_2 $D_{\infty h}$ $\Gamma(MX_2) = A_{1g}^* + A_{2u} + E_{1g}^* + E_{3u}^*$

4 vibrational modes

3 Raman active

stretching modes transform as $A_{1g} + A_{2u} + E_{1g}$

and deformation modes transform as E_{1u}

4) MX_2 C_{2v} $\Gamma(MX_2) = 3A_1^* + A_2 + 3B_1^* + 2B_2$

3 vibrational modes all Raman active

5) M_2X_4 C_{2v} $\Gamma(M_2X_4)_{cis} = 6A_1^* + 2A_2^* + 6B_1^* + 4B_2^*$

$\Gamma(M_2X_4)_{tran} = 6A_1^* + 2A_2^* + 5B_1^* + 5B_2^*$

12 vibrational modes all Raman active

terminal stretching modes transform as $A_1 + B_2$

bridging stretching modes transform as $2A_1 + 2B_1$

and deformation modes transform as $3A_1 + 2A_2 + 3B_1 + 4B_2$

6) M_2X_4 D_{2h} $\Gamma(M_2X_4) = 3A_{1g}^* + 1B_{1g} + 3B_{1u} + 2B_{2g}^* + 3B_{2u} + 3B_{3g}^* + 3B_{3u}$

12 vibrational modes

6 Raman active

terminal stretching modes transform as $A_{1g} + B_{2u}$

bridging stretching modes transform as $A_{1g} + B_{1u} + B_{2u} + B_{3g}$

and deformation modes transform as $A_{1g} + B_{1u} + B_{2g} + B_{3g} + 2B_{3u}$

7) MX_3 D_{3h} $\Gamma(MX_3) = A_1'^* + A_2' + 2A_2'' + 3E'^* + E''$

6 vibrational modes

5 Raman active

stretching modes transform as $A_1' + 2E'$

and deformation modes transform as $A_2'' + 2E'$

8) M_2X_6 D_{2h} $\Gamma(M_2X_6) = 4A_{1g}^* + A_{1u} + 2B_{1g}^* + 4B_{1u} + 3B_{2g}^* + 4B_{2u} + 3B_{3g}^* + 3B_{3u}$

17 vibrational modes

9 Raman active

terminal stretching modes transform as $A_{1g} + B_{1u} + B_{2u} + B_{2g}$

bridging stretching modes transform as $A_{1g} + B_{1g} + B_{2u} + B_{3u}$

and deformation modes transform as $2A_{1g} + A_{1u} + 2B_{1u} + 2B_{2g} + B_{2u} + B_{3g} + B_{3u}$

Asterisked terms are Raman active.

Errata

Page	Line	
14	9	for "nuclear" read "molecular"
17	17	for "rate" read "route"
30	8	for "quantative" read "quantitative"
35	2	for "Western" read "Weston"
36	5	for "R/ " read "R/Ω"
41	23	for "atscissa" read "abscissa"
42	7	for "isthermal" read "isothermal"
45	20	for "Coberg" read "Coderg"
46	1	for "Spectre" read "Spectra"
46	16	for "monitered" read "monitored"
57		ref 2.3 "London University"
72	16	for "peroid" read "period"
79		ref 3.5, for "(979)" read "(1979)"
86	9	for " $P \approx \varepsilon/n$" read "$\xi P \approx \varepsilon/n$"
92	10	for LHS of (xvii) read "ξ_i"
95	7	for " H" read "ΔH"
95	8	for " S" read "ΔS"
102	9	for " S_{1000} " read "ΔS_{1000} "
110/111	1	for "Dissociasion" read "Dissociation"
113	18	for "low " read "low ε"
128	19	for " H°_{fT} " read "ΔH°_{fT}" and for " H°_{f298} " read "ΔH°_{f298} "
145	2	for "80.91697" read "80.917"
145	11	for "293.0 K" read "273 K"
178	6	for "$\dot{w}$ and " read "$\dot{w}$ and ψ"
178	17	for " P " read "$\psi P \varepsilon$"
187	11	for " = 0.035" read "ε = 0.035"
194	6	for "Patterson" read "Petterson"
194	21	for "defraction" read "diffraction"
195	15	for "intraferrometric" read "interferometric"
220	14	for "Ramna" read "Raman"
221	24	for "resonsnce" read "resonance"
227	-	ref 6.21, for "Beatlie" read "Beattie"
229	23	for "Tris-hydroxymethylamioetane" read "Tris-hydroxymethylaminomethane"
236	7	for "difinitive" read "definitive"
239	14	for "abundences" read "abundances"
246	16	for "logorithm" read "logarithm"
251	7/27	for "metalic" read "metallic"
260	3	for "hydroge" read "hydrogen"
284	12/14/15	for "theorm" read "theorem"

Addenda

Ref 7.9 J D Corbett and A Hershaft, J. Am. Chem. Soc. 80, 1530 (1958).

Ref A4.1 F A Cotton, Chemical Applications of Group Theory (Wiley-Interscience, 1971).

It has been pointed out that some ambiguity may arise as to exactly which MEM channel was used in each experiment. An attempt to clarify this appears below:

Channel A, l = 0.0204 m, d = 0.00206 m, was used to record the data collected in table 3.1 (pp 64 to 66), and represented graphically in fig 3.2 (p 67).

Channel B, l = 0.0172 m, d = 0.00098 m, was used to record the data collected in tables 4.7 (pp 132, 133), 4.8 (pp 133, 134), 4.11 (pp 137, 138), and 4.12 (pp 138 to 140).

Channel C, l = 0.01631 m, d = 0.00199 m, was used to record the data collected in tables 4.5 (pp 130, 131), 4.6 (pp 131, 132), 4.9 (pp 134, 135), and 4.10 (pp 135, 136).

Channel D, l = 0.0138 m, d = 0.00092 m, was used to record the data collected in tables 5.2 (pp 149, 150), 5.3 (pp 150, 151), and 5.5 (p 157), and represented graphically in figs 5.2 to 5.6 and 5.11.

Channel E, l = 0.0169 m, d = 0.00093 m, was used to record the data collected in tables 5.9 (pp 168, 169), 5.11 (p 180), 5.12 (p 181), 5.13 (p 182), and 5.14 (p 183), and represented graphically in figs 5.7, 5.9, 5.10, and 5.12. Appropriate data in the graphs (usig channels D and G) have been scaled accordingly.

Channel F, l = 0.01631 m, d = 0.00199 m, was used to record the data collected in table 5.10 (p 172), and represented graphically in fig 5.8. The data has been scaled in figs 5.9 and 5.12.

Channel G, l = 0.01277 m, d = 0.00108 m, was used to record the data collected in table 7.9 (p 247), and represented graphically in fig 7.4.